In Situ/Operando Electrocatalyst Characterization by X-ray Absorption Spectroscopy

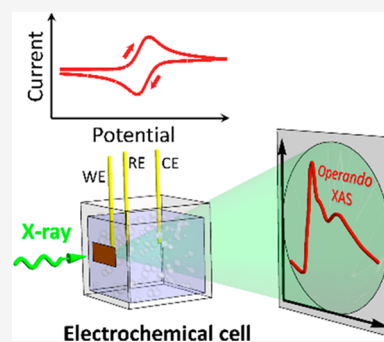Janis Timoshenko* and Beatriz Roldan Cuenya*

Read Online

ACCESS | Metrics & More | Article Recommendations

ABSTRACT: During the last decades, X-ray absorption spectroscopy (XAS) has become an indispensable method for probing the structure and composition of heterogeneous catalysts, revealing the nature of the active sites and establishing links between structural motifs in a catalyst, local electronic structure, and catalytic properties. Here we discuss the fundamental principles of the XAS method and describe the progress in the instrumentation and data analysis approaches undertaken for deciphering X-ray absorption near edge structure (XANES) and extended X-ray absorption fine structure (EXAFS) spectra. Recent usages of XAS in the field of heterogeneous catalysis, with emphasis on examples concerning electrocatalysis, will be presented. The latter is a rapidly developing field with immense industrial applications but also unique challenges in terms of the experimental characterization restrictions and advanced modeling approaches required. This review will highlight the new insight that can be gained with XAS on complex real-world electrocatalysts including their working mechanisms and the dynamic processes taking place in the course of a chemical reaction. More specifically, we will discuss applications of *in situ* and *operando* XAS to probe the catalyst's interactions with the environment (support, electrolyte, ligands, adsorbates, reaction products, and intermediates) and its structural, chemical, and electronic transformations as it adapts to the reaction conditions.

CONTENTS

1. INTRODUCTION

The last decades have been marked by drastic developments in experimental *in situ* and *operando* characterization techniques as well as great progress in theory. Such advanced new methods have allowed us to gain deeper insight into the complex processes that take place in thermal- and electro-catalysts while at work.[1−9] The concept of catalysts being dynamic systems that actively transform and respond to the reaction conditions, rather than just a static arrangement of atoms, is almost commonplace now. However, this shift of paradigm results in an even more pressing need for experimental tools that would allow one to probe the composition, structure, and dynamics of catalysts under realistic reaction conditions. An additional challenge here is that catalysts are commonly complex, heterogeneous, disordered systems with multiple species coexisting. In many cases, the nature of the actual active site is still a matter of heated

debate, and cooperative effects involving multiple-sites for different reaction steps might also have to be considered.

X-ray absorption spectroscopy (XAS) is as a premier method for *in situ/operando* studies of catalysts in a broad range of experimental conditions. Since it is an element-specific method, it is well-suited to single out the active sites in multielement systems and can be applied to the investigation of a broad range of materials (ordered, disordered, nano-structured, liquids, etc.)[10,11] The prominent role of XAS in catalyst research is also based on its ability to provide very diverse information about a given sample in a single experiment. Through the in depth analysis of XAS features, one can gain access to minute variations in bond lengths (picometer scale) due to only thermal expansion, surface relaxation, and interactions with the support, ligands, and adsorbates but also probe the changes in the material's nanoscale morphology, the macroscopic evolution of its composition and crystallographic structure, and even map heterogeneous distributions of different species in macroscopic samples.[10,12,13] When carried out under *operando* conditions, such studies can provide key information about the identity of the active species and their activation/deactivation under reaction conditions, the reaction intermediates and preferred reaction mechanisms, and the role of the reaction environment.[7,10] At the same time, *operando* spectroscopic studies often require new developments in the instrumentation as well as data analysis and software. The solutions that worked well for decades in the studies of well-defined samples under ambient conditions can be inadequate for the characterization of dynamic processes in realistic heterogeneous and disordered samples in contact with diverse environments. The unique challenges of *operando* XAS studies, and new approaches undertaken to address them, are the main topics of this Review.

While many of the problems and examples considered here are common for both XAS investigations of electrocatalysts and of thermal catalysts, we chose to especially highlight the former ones. One of the reasons for this selection is that there is still a reduced base of fundamental knowledge available on electrocatalysts while at work. Furthermore, there are also pressing environmental concerns coupled with the need of developing a sustainable energy economy, which have brought to the forefront of fundamental and applied research the understanding of electrocatalytic processes that might lead to cost-effective and environmental friendly chemicals and fuels. Indeed, technologically important electrochemical processes such as alcohol oxidation reactions in fuel cells, the electrochemical water splitting for the production of green hydrogen, the electrochemical reduction of CO$_2$ (CO$_2$RR) to valuable chemicals and a number of additional electrochemical reactions still require more efficient catalysts. In many cases, fundamental understanding of the working principles of existing catalysts is still lacking, which also hinders the development of novel catalytic materials.[14]

Another reason for the emphasis on electrocatalysis in this Review includes the additional challenges in the XAS studies under an electrochemical environment. Factors such as the chemical composition of the catalyst, its oxidation state, relative concentration and distribution of different atomic species, the crystallographic structure, morphology (particle size, shape, exposed facets), lattice strain, surface roughness, defects, and interparticle distance can affect the performance of all heterogeneous catalysts. Nevertheless, the presence of the
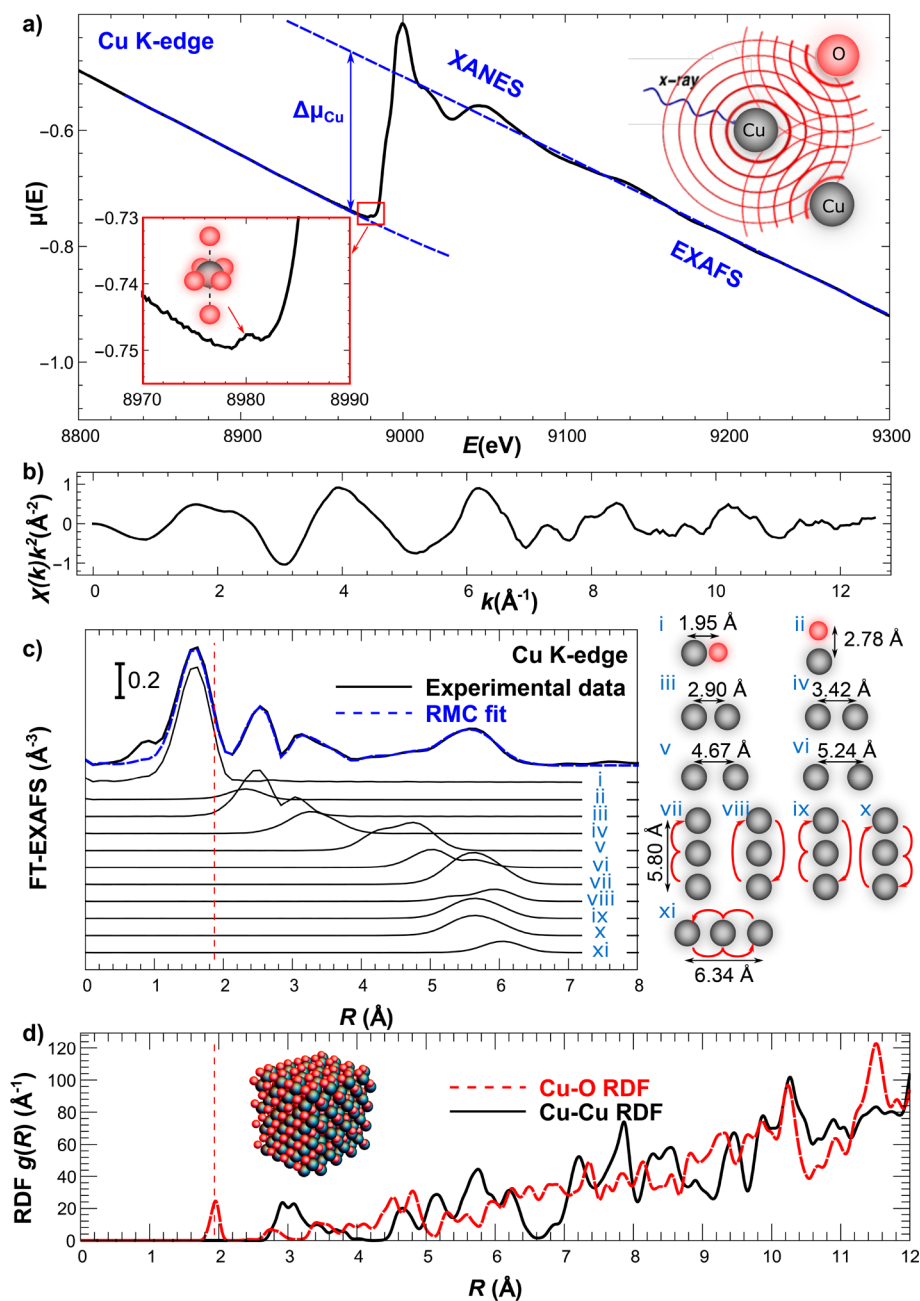
Figure 1. (a) Cu K-edge XAS data for an as-prepared Cu nanocatalyst used for CO2RR (from ref 25). Schematics of the photoelectron scattering process, and pre-edge at the Cu K-edge are shown in the insets. (b) Cu K-edge EXAFS data extracted from the XAS spectrum shown in panel a. (c) Fourier-transformed (FT) Cu K-edge EXAFS spectrum for bulk Cu(II) oxide, its fit with the reverse Monte Carlo (RMC) method (see Section 4.4), and the contributions of the 11 most important photoelectron scattering paths, whose geometries are shown on the right. (d) Cu−O and Cu−Cu partial radial distribution functions in bulk CuO as obtained from RMC-EXAFS analysis. The structure model, optimized in RMC simulations is shown in the inset. The vertical dashed lines in panels c and d show the R-value corresponding to an average nearest neighbor Cu−O distance. See ref 25 for RMC details.

electrolyte, its composition, and pH pose additional difficulties for the data acquisition, interpretation, and modeling, motivating the current focus on problems and examples that are more specific to electrochemical catalytic processes. Note that most of the aforementioned properties can change under reaction conditions. Therefore, *in situ* and *operando* studies are indispensable for establishing structure−property relationships in this class of materials.[2,15,16]

This Review thus complements the recent excellent work by Bordiga, Lamberti, et al.,[10] which discussed the XAS method and the recent experimental developments in XAS in the context of studies of heterogeneous thermal catalysts. Here we build up and expand the focus of previous reviews by Russel and Rose on the use of XAS for low temperature fuel cell characterization,[17] or that of Lassalle-Kaiser[18] and Fabri et al.[19] on electrochemical water splitting, Jia et al. on the oxygen reduction reaction (ORR),[20] Marinkovic et al.[21] on the electrochemical ethanol oxidation, and Wang et al.[22] describing XAS application for the study of nanoscale electrocatalysts. Moreover, we will use this opportunity to summarize and put into context the various XAS data analysis methods available for the investigation of heterogeneous, complex, disordered

systems under diverse environmental conditions. The interpretation of XAS data in these cases is often nontrivial, and the proper choice of data analysis tools can be just as important as the advancements and proper care implemented in the acquisition of the experimental data.[12,23] The former aspect is also less well represented in the previous reviews about the *in situ* XAS method.

After the necessary introduction of the basic concepts of XAS in Section 2, and a brief overview of important experimental aspects of the method in Section 3, we will dedicate Sections 4 and 5 to the discussion of data analysis methods, with special attention being paid to the common pitfalls of the XAS analysis and new advanced analysis approaches. In Section 6, the application of XAS for *in situ* and *operando* electrochemical studies will be demonstrated based on selected stories highlighting the diverse information that can be extracted from XAS data and how such new knowledge has helped to improve our understanding of the working mechanisms and structure−property relationships in electrocatalysis. In particular, examples related to the CO_2RR are shown in Section 6.1, ORR in Section 6.2, and the oxygen evolution reaction (OER) in Section 6.3. A brief discussion of the usage of the XAS method to study other electrochemical processes is given in Section 6.4. Concluding remarks and future outlook are given in Section 7.

2. XAS: PHYSICAL PRINCIPLES

2.1. Absorption and Absorption Edge

The absorption of any portion of the electromagnetic spectrum is described by the Beer−Lambert law that states that the intensity of the radiation after the sample (I_T) is exponentially reduced as the sample thickness d is increased in comparison to the intensity of the incident radiation (I_0) due to the interactions of the incident photons with atoms in the material:

$$I_T = I_0 \exp(-\mu d) \tag{1}$$

Here μ is the linear absorption coefficient, which depends on the energy of the incident radiation E. In the X-ray range for a homogeneous monatomic material, an empirical relation links the $\mu(E)$ dependency to the density of the material ρ, atomic number Z, and relative atomic mass A:[24]

$$\mu(E) \sim \frac{\rho Z^4}{A E^3} \tag{2}$$

However, at certain energies, when the energy of the incident photon matches the binding energy of an electron in one of the deep core levels of the atom, the behavior of $\mu(E)$ deviates from the smooth dependency described by eq 2, and a sharp increase in the absorption is observed, the so-called absorption edge or absorption jump. For example, Figure 1a shows an absorption edge at ~9.0 keV due to the absorption of X-ray photons by K-shell (1s) electrons of Cu in an oxidized Cu nanoparticle (NP).[25] In this case, the X-ray photons absorbed excite the core electrons of Cu to available unoccupied states in the valence band, resulting in the absorption edge, which then is referred to as Cu K-edge. The position of the absorption edge E_0 is element-specific, with the corresponding energies scaling approximately as Z^2. The amplitude of the absorption edge is determined by the number of atoms of a given type in the way of the X-ray beam, that is, by the sample thickness and the concentration of the absorbing element. The shape of the absorption edge and that of the features before

and after the absorption edge are determined by the details of the electronic structure of the material (density of unoccupied states available for the excited core-level electron, further on referred to as photoelectron) as well as its atomistic structure due to the interactions between the photoelectron and the neighboring atoms. The oscillations of the absorption probability before and after the absorption edge are referred to as X-ray absorption fine-structure (XAFS) and are thus a very sensitive probe of the material structure and properties.

XAFS features before and immediately after the edge are known as X-ray absorption near edge structure (XANES), or near edge XAFS (NEXAFS), and are sensitive to the details of the density of electronic states near the Fermi level, including the presence of localized and hybridized states, thus providing information about the chemical state of the absorbing atoms, local symmetry, and chemical bonding.[26] This region of the absorption spectra is followed by the extended X-ray absorption fine structure (EXAFS), which extends into the range of a few thousands eV above the absorption edge energy. Because of the high density of available electronic states, and high energy of the photoelectrons, the EXAFS region is much less affected by the details of the electronic structure but is a sensitive probe of spatial arrangements of nearest neighbors around the absorbing atoms.[27] XANES and EXAFS portions of the absorption spectra thus provide highly complementary information.

X-ray absorption is intimately linked to X-ray fluorescence and emission. The vacant state created in the core level of the absorbing atom after the electron is excited by the X-ray photon is eventually filled by an electron from some occupied level with higher energy. Subsequently, the excess energy is released through the emission of a photon, or by creating secondary excitations in the electronic system (e.g., the emission of Auger electrons). In the case of radiative transitions, due to the large energy difference between the core levels, the emitted photon will also have its energy in the X-ray range, and the intensity of the resulting X-ray fluorescence I_F can be used as an indirect measure of the absorption probability:

$$I_F \sim I_0 \mu(E) \tag{3}$$

The same relation describes also the intensity of the Auger electron emission and enables XAS experiments in total fluorescence and total electron yield modes.[24] The spectrum of the X-ray fluorescence depends on the density of occupied states and the created secondary excitations, which may be captured in complementary X-ray emission spectroscopy (XES) and resonant elastic and inelastic X-ray scattering (REXS and RIXS) experiments.[28,29]

2.2. XANES Basics

As in the case of other spectroscopies, the absorption of X-rays is described by Fermi's Golden Rule:[30]

$$\mu(E) \approx \sum_f |\langle f|\hat{T}|i\rangle|^2 \delta(\epsilon_f - \epsilon_i - E) \tag{4}$$

where $|i\rangle$ is the initial (ground) state of the absorbing atom and the summation is carried out over all available final states $|f\rangle$. They correspond to the situation with one electron (photoelectron) excited to a higher energy level (localized or delocalized) and all other electrons in the atom rearranged due to the presence of positively charged holes in the core state. A Dirac function $\delta(\epsilon_f - \epsilon_i - E)$ describes the

conservation of energy. The operator $\hat{T}$ describes the interaction of the electron with the photon and for practical calculations can be treated in a common dipole or more complex quadrupole approximation. The intensity and shape of the XANES features is thus affected by the density of unoccupied localized and delocalized states as well as by the selection rules for a particular transition.

The position of the absorption edge is defined as the onset of transitions to delocalized continuum states. The corresponding energy is very sensitive to the oxidation state of the atom and can change by several eVs when the valence state of the atom changes by one electron. The XANES spectrum after the absorption edge (post-edge region) changes relatively smoothly, and the observed features can be understood within a full multiple scattering (FMS) formalism as a result of the interactions between the photoelectron and the neighboring atoms.[26,31−33] Similarly to the EXAFS features, the postedge XANES features are sensitive to the materials crystallographic structure, interatomic distances, and particle sizes, although their quantitative interpretation may be even more challenging.[31,34−38]

The transitions to localized states result in XANES features in the region below the main absorption edge. The dipole-allowed transitions to vacant localized states result in a very sharp and intense feature (so-called white line (WL)), as observed, for instance, at the L_3 and L_2 absorption edges for transition metals with unoccupied d-states (for example, Pt and Ir). In the case of K-edges, the s to d transition is dipole-forbidden, while the intensity of the allowed quadrupole transitions is orders of magnitude weaker; thus, such an intense WL is not observed for pure metals. At the same time, if the absorbing atom forms chemical bonds, due to the hybridization effect, the vacant d-orbital may assume the character of p-type states, and the corresponding photoelectron transition becomes dipole-allowed, resulting in sharp features (so-called pre-edges). The hybridization depends on the symmetry of the absorbing site and is allowed, for example, in tetrahedral bonding motifs, while it is prohibited in octahedral coordination.[26] Because of the distortions of the octahedral structural units due to the Jahn−Teller effect, weak pre-edges can be observed, as shown in Figure 1a for the Cu K-edge in oxidized Cu nanoparticles (NPs). In this case, the environment around the absorbing Cu^{2+} species is similar to that in CuO, featuring a strongly distorted CuO_6 octahedron with axial Cu−O bonds being ~0.8 Å longer than 4 in-plane Cu−O bonds (see the inset in Figure 1a).[25] The resolution of the XANES features strongly depends on the absorption edge energy and for heavy elements is reduced significantly due to the high energy of the excitation and the short lifetime of the core-hole created. Improved resolution of the XANES features can be achieved in the so-called high energy resolution fluorescence detected (HERFD) mode, where instead of measuring transmission or fluorescence due to filling-in the created core hole, the fluorescence associated with a state with a longer lifetime is monitored.[28,39]

Overall, the XANES features contain very rich information about the atomic and electronic structure of a material. XANES analysis is also well suited for *in situ* and *operando* investigations due to the high signal-to-noise ratio in this portion of the X-ray absorption spectrum, its relative insensitivity to thermal disorder (which affects EXAFS data interpretation), and the short acquisition times required. These factors allow one to collect good quality XANES data with good time resolution and under harsh experimental conditions.[40,41] The quantitative analysis, however, has been limited by the lack of analytical models that would allow linking the XANES features to a particular structure motif. The interpretation of XANES spectra has thus remained in many cases qualitative, by adhering to a comparison of the obtained spectra with those for reference materials with known structure, or semiquantitative, when methods such as linear combination analysis were employed to fit the concentrations of different species contributing to the averaged spectrum of a mixture.[26] This situation has begun to change in the last years due to the advancements in XANES data modeling within different approximations[34] such as FMS,[33,42] time-dependent density-functional theory,[43,44] Bethe-Salpeter method,[45,46] and others.[47−50] Codes like FitIt[51] and MXAN[52] now provide the possibility to efficiently fit the parameters of simple structures and match theoretically simulated spectra to experimental data, while the recently developed machine learning approaches enable automatic spectra matching[53,54] and regression of structure parameters[12,34,38] based on the recognition of patterns in large data sets.

2.3. EXAFS Basics

The origin of the EXAFS signal is the interactions between the photoelectron excited from a deep core level of the absorbing atom by an incident X-ray photon, with the electrostatic potentials of neighboring atoms. The presence of neighboring atoms perturbs slightly the absorption probability, resulting in the oscillatory structure of the absorption coefficient $\mu(E)$ on top of smooth variations of the absorption probability $\mu_0(E)$ that are not related to the sample structure, Figure 1a. Commonly, the normalization of the EXAFS component $\chi(E)$ is carried out as

$$\chi(E) = \frac{\mu(E) - \mu_0(E)}{\Delta\mu_0(E_0)} \tag{5}$$

where $\mu(E)$ is the experimentally measured spectrum, and $\mu_0(E)$ is the smooth background function that can be constructed by smoothing the experimental signal via polynomial fitting or spline interpolation.[55,56] $\Delta\mu_0(E_0)$ is the absorption jump value, calculated as the difference between two smooth functions that describe the background before the absorption edge (pre-edge region) and after the absorption edge (postedge region), respectively, calculated at the reference energy value E_0.[55] As discussed above, E_0 corresponds to the minimal necessary energy required to excite the photoelectron to a delocalized state. Commonly, the maximum point of the first derivative of $\mu(E)$ is used as the approximation for the E_0 value, although other conventions also may be employed. Next, the EXAFS signal is converted from energy space to photoelectron wavenumber (k-) space by using the relation:

$$k = \sqrt{\frac{2m_e}{\hbar^2}(E - E_0)} \tag{6}$$

Here $\hbar$ is Planck's constant, and m_e is the electron mass. As an example, Figure 1b shows Cu K-edge EXAFS spectra for oxidized Cu NPs.[25] The choice of background fitting procedure and the E_0 value selected can affect the appearance of the EXAFS features significantly, especially at low k-values, and therefore, it should be carried out systematically for all spectra in the analyzed series.

The border between the XANES and EXAFS regions of the XAS spectra is not strictly defined and is related to the effective mean-free path for the excited electron $\lambda(k)$. The latter accounts for two different effects: finite lifetime of the core-hole, created by the X-ray absorption processes, and the inelastic interactions of the excited photoelectron. In the EXAFS region, that is, at large photoelectron energies (larger than the effective plasmon excitation energy), $\lambda(k)$ decreases significantly; thus, interactions with relatively few nearest neighbors need to be considered.[30] This limits the sensitivity of the EXAFS spectra to contributions of distant atoms and makes it essentially a very local method. On the other hand, it simplifies the mathematical description of the EXAFS part of the absorption spectrum. Using a commonly employed scattering formalism, the EXAFS signal can be expressed as a sum of contributions of different possible photoelectron scattering paths:

$$\chi(k) = \sum_p \chi_p(k) \tag{7}$$

Because of the low value of $\lambda(k)$ in the EXAFS region, only the shortest scattering paths need to be considered. Furthermore, due to disorder effects, the contributions of many long scattering paths are suppressed. As a result, the series in eq 7 convergences quickly.[57] While formally the same approach can also be used to describe the postedge features in the XANES spectra, due to the significantly larger $\lambda(k)$ value, the presence of strong scattering events at low photoelectron energies, as well as the lower importance of disorder effects in the XANES region, the sum in eq 7 converges poorly. Therefore, full multiple scattering approaches are needed to describe the XANES features accurately.[27,33,57] Note also that an alternative expansion of the $\chi(k)$ function in terms of many-body distribution functions rather than scattering paths is possible and realized in the so-called GNXAS approach.[58,59]

The summation in eq 7 is carried out both over single-scattering (SS) terms, which involve only interactions of the photolelectron with a single atomic neighbor, as well as more complex multiple-scattering (MS) terms, see Figure 1c. Commonly, the contributions of similar paths are grouped together, for example, single-scattering paths arising from neighboring atoms within a single coordination shell. $\chi_p(k)$ for SS terms can then be conveniently described in terms of a partial radial distribution function (RDF) $g_p(R)$ as[60,61]

$$\chi_p(k) = S_0^2 \int_0^{+\infty} g_p(R) F_p(k, R) e^{-2R/\lambda(k)} \sin(2kR + \phi_p(k, R)) \frac{dR}{kR^2} \tag{8}$$

The material-specific terms in eq 8 (S_0^2, $F_p(k,R)$, $\lambda(k)$, $\phi_p(k,R)$) describe the interactions of the X-ray-excited photoelectron with other electrons and atoms within the material and are discussed below. The key characteristics of the local structure of the material, however, are captured by $g_p(R)$, which expresses the probability density to find an atom of a given type at a distance R from the absorbing atom. RDF contains information about the number of nearest neighbors, interatomic distances, and degree of structural disorder. In particular, the number of atoms of a given type within the distance interval between R_1 and R_2 is given by an integral:

$$C_p = \int_{R_1}^{R_2} g_p(R) \, dR \tag{9}$$

Partial $g_p(R)$ functions corresponding to Cu–O and Cu–Cu RDFs in copper(II) oxide are shown in Figure 1d.[25] The width of the $g_p(R)$ features is determined by the structural disorder. Note here that due to the very short lifetime of the excitation created by the incident X-ray photon ($\sim$1 fs), which is much shorter than the characteristic atomic thermal vibration times (on the order of picoseconds), EXAFS probes the "frozen" snapshot of the structure (averaged over all absorbing atoms) and does not distinguish between atomic deviations due to static distortions and dynamic thermal motion.[27]

Because of the sinusoidal nature of the $\chi_p(k)$ components, obvious from eq 8, a Fourier transform (FT) is commonly used to analyze and visualize the information encoded in the EXAFS signals. The total Fourier-transformed EXAFS $\chi(k)k^2$ for copper(II) oxide, together with Fourier transforms of the most important partial contributions $\chi_p(k)k^2$, is shown in Figure 1c. Geometries of the corresponding scattering paths are also shown.[25]

The chemical sensitivity (e.g., the ability to distinguish between Cu and O neighbors) of the EXAFS method is ensured by the fact that the functions $F_p(k,R)$ and $\phi_p(k,R)$, which describe the changes in the photoelectron wave amplitude and phase upon scattering from a neighboring atom, respectively, depend on the type of neighboring atom. The terms $e^{-2R/\lambda(k)}$ and $\frac{1}{kR^2}$ reduce the contribution of atoms at large interatomic distances from the absorbing atom, and are responsible for the decreased importance of more distant coordination shells, and make the EXAFS a local method, with a characteristic structure probing length less than 1 nm. Interestingly, the possibility of quantitative EXAFS data analysis up to 10 Å was recently demonstrated by Jonane, Kuzmin et al.[62,63]

Finally, let us note that eq 8 describes the photoelectron interactions with the neighboring atoms in one-electron approximation; thus, the additional term S_0^2 is necessary here to account for the reduction of the EXAFS amplitude due to many electronic excitations.[30,64] Typically the S_0^2 value is between 0.7 and 1.0, and it can be obtained from the analysis of reference materials with known structure.

Eq 8 can be generalized to account for the contributions of MS paths as well. In this case, the radial distribution function $g_p(R)$ should be replaced by a many-atom distribution function, and the dependencies of the F_p and ϕ_p functions on the relative positions of all atoms involved (e.g., on bonding angles) need to be taken into account. The number of MS paths surpasses significantly the number of SS paths. The MS path amplitudes, especially in the structures with near-linear chains of atoms (e.g., fcc and bcc cubic structures, rock salt-type structures, perovskite-type structures, etc.), can be comparable or even higher to those for SS paths.[27,65] The contribution of the first-coordination shell (and, sometimes the second) has a significantly lower frequency (lower R value, see eq 8) than that of other SS and MS paths and thus can be singled out using Fourier-filtering and analyzed separately. Nevertheless, contributions of more distant coordination shells always overlap with the contributions of MS paths, and they need to be considered together with SS contributions. While the presence of MS paths complicates significantly the interpretation of EXAFS spectra, the sensitivity of MS paths to bonding angles provides also the possibility to use EXAFS to probe the 3D structure of the material rather than just radial distances.[66] This is especially relevant when advanced

approaches to data analysis such as reverse Monte Carlo simulations are used[23] (see Section 4.4).

3. XAS EXPERIMENT

3.1. Typical XAS Setup: Measurements in Transmission Mode

The XAS experiment consists of measuring the absorption coefficient for X-rays as a function of the energy of the incident X-ray photons. While conceptually simple, XAS experiments put stringent requirements on the X-ray source and optical elements, since a broad spectrum of the incident radiation is needed (with bandwidth of up to 1−2 keV), while simultaneously allowing for accurate energy selection with energy resolution up to a fraction of an eV. Moreover, a signal-to-noise ratio better than 1000 is required to extract the EXAFS component of the absorption spectra. Thus, to collect spectra in reasonable time, very high intensity of the incoming radiation is required, with ~10^{10} photons per second per eV or better.[67] Therefore, while there has been some noticeable progress with lab-based XAS setups during the last decades,[68−70] the majority of XAS studies, especially those conducted *in situ* and under *operando* conditions, still require synchrotron radiation (SR) sources.

At SR facilities, X-rays are produced by bending with magnetic fields the trajectories of electrons (or positrons) accelerated to relativistic velocities. The intensity of single bending magnet beamlines is usually sufficient for standard XAS experiments. However, for time-resolved studies, investigations of dilute samples or samples in attenuating environments, beamlines based on insertion devices are better suited. In the wiggler-type insertion devices, the X-rays are produced by arrays of magnets with alternating polarity, and the intensity of the X-ray radiation is several-times higher. Another type of insertion devices, undulators, can also be used at XAS beamlines. They can achieve even higher X-ray intensity by exploiting the interference effects and interactions between the emitted light and relativistic electrons but require tapering or scanning of the gap between arrays of magnets to expand the width of the emitted X-ray radiation spectrum to 1−2 keV needed for EXAFS data collection. In all cases, the produced X-ray beam is usually collimated in the synchrotron plane and strongly polarized, which may be exploited in advanced XAS studies of oriented samples.[71−73] The synchrotron radiation produced passes through a series of optical elements, such as X-ray mirrors with different coatings, which ensure further collimation of the X-ray beam and cutting off undesired portions of the emitted radiation to reduce the heat load on further beamline components and to remove higher harmonics contributions to the monochromatized spectrum.

In the commonly used setup schematically shown in Figure 2a, the X-ray radiation with desired energy is then selected using a monochromator, which consists of two parallel single crystals (normally Si), cut along a specific direction (e.g., (111), (220), or (311)). Alternatively, both diffraction planes can be produced from a single crystal by cutting in it a channel for the X-ray beam. By rotating the monochromator crystals, X-rays with wavelength λ are selected that fulfill the Bragg condition $n\lambda = 2d_m \sin \theta$, where d_m is the monochromator lattice spacing, and θ is the incidence angle for the X-rays (see Figure 2a). Higher harmonics (wavelengths corresponding to integers $n > 1$) need to be removed either by using X-ray
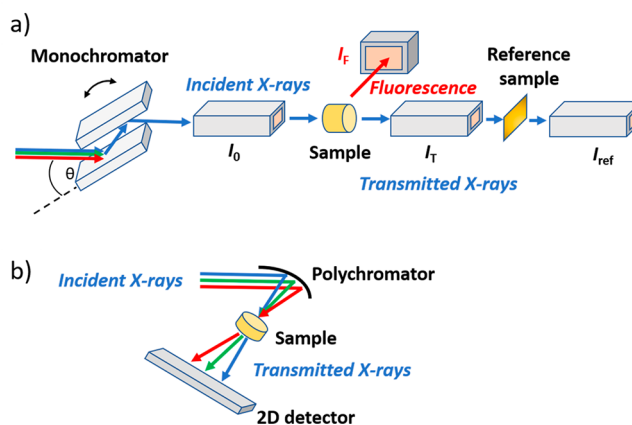

Figure 2. Schematics of a common setup for (a) XAS measurements with double crystal monochromator and for (b) energy-dispersive XAS experiments.

mirrors or by detuning of the double crystal monochromator by slightly tilting the second crystal with respect to the first crystal. Such misalignment of crystals reduces the intensity of all components in the monochromatized radiation, but the intensity of higher harmonics is suppressed much more strongly.

The monochromatized radiation is then passed through a series of detectors, which measure the intensity of the X-rays before (I_0 detector) and after the sample (I_T detector), as well as after the reference (I_{ref} detector). The absorption spectrum of the reference (e.g., metal foil containing the same absorbing element as the sample) is used for the precise alignment of the data collected. Ionization chambers filled with inert gas are typically used as I_0, I_T and I_{ref} detectors. The X-rays passing through these chambers ionize the gas atoms, and the drift of the released electrons and charged ions in the electric field applied across the ionization chamber electrodes results in a small current (ca. several pA), which is proportional to the intensity of the X-rays. Current amplifiers are then used to convert the current into the voltage signal. The filling gas is chosen so that the absorption in the ionization chamber (typically ca. 10% in I_0 detector) results in a detectable current, while ensuring that the intensity of the X-ray which passes through is not severely affected.

Once the signal from the I_0, I_T, and I_{ref} detectors is recorded, the XAS signal of the sample can be simply calculated according to eq 1 as $\mu d = \ln \frac{I_0}{I_T}$, while for the reference sample, the analogous expression is given by $\mu_{ref} d_{ref} = \ln \frac{I_T}{I_{ref}}$. The sample thicknesses d and d_{ref} do not need to be known explicitly since the contribution of these terms is canceled out during the standard XAS processing and normalization procedures.

Measurements in transmission mode normally ensure the best signal-to-noise ratio. However, such measurements impose significant requirements in terms of the sample quality. The sample thickness and the concentration of the absorbing atoms should be large enough so that significant X-ray absorption is ensured, with absorption jump values $\Delta\mu_0(E_0)d$ of ~0.1 or better. At the same time, the absorption cannot be too large since a significant number of X-ray photons needs to pass through the sample to be reliably detected by the I_T detector. The optimal $\Delta\mu_0(E_0)d$ value should be close to 1 and

the total absorption μd less than ~3.[67] Also essential for transmission measurements is the sample homogeneity, where the sample thickness and the concentration of the absorbing species are required to be uniform (on the scale of μm) within the whole X-ray irradiated area. Too strong X-ray attenuation and nonuniformity of the sample will result in the distortion of the XAS features, an increased relative contribution of higher harmonics, and incomplete cancellation of the I_0 signal variations due to, for example, monochromator glitches (spurious changes in I_0 due to the additional Bragg reflections from the monochromator crystals at certain energies).[74] Clearly, such conditions are not always possible to satisfy when *in situ* and *operando* studies are carried out. This is the case, for instance, when the absorbing species are diluted and nonuniformly distributed or when the matrix or support material and the elements in the sample environment (e.g., electrodes and electrolyte in an electrochemical cell) are too attenuating. In these situations, measurements in fluorescence mode are often helpful.

3.2. Measurements in Fluorescence and Total Electron Yield Modes

As stated by eq 3, the fluorescence intensity emitted by the sample absorbing the X-rays (total fluorescence yield) can be often considered proportional to the absorption coefficient. Some notable exceptions are known. For example, the fluorescence signal at the $L_{2,3}$ edges of 3d transition metals does not follow this rule due to the dominance of distinct decay channels in the total fluorescence signal.[75,76]

The fluorescence detector is usually located at 90° with respect to the X-ray beam (see Figure 2a). Such geometry minimizes the elastic scattering from the sample and hence reduces the background signal. To increase the solid angle from which the photons are collected by the fluorescence detector, the sample is often rotated by 45° with respect to the incoming beam to better face the detector.

A number of different detectors can be used for the collection of fluorescence data. The so-called Lytle detector (Stern-Heald detector)[67,77] is essentially an ionization chamber optimized for the collection of fluorescence photons. Photodiode detectors such as PIPS (passivated implanted planar silicon) detectors are based on a similar principle, but instead of creating electron−ion pairs (as in ionization chambers), in the photodiodes, the passing X-rays create electron−hole pairs in a semiconducting material. The aforementioned detectors collect photons regardless of their energy. As an alternative, one may use energy-discriminating detectors,[78] such as germanium and silicon multichannel detectors and silicon drift detectors, which allow one to distinguish and count the number of photons with the desired energy only, with energy resolution typically around 100 eV. Such detectors allow one to minimize the background signal. However, an important limitation is that these detectors have finite counting rates and get easily saturated if the total number of incident photons increases beyond a certain threshold. Because of the finite detector dead-time (time needed by the detector after registering a photon before the next photon can be counted), the number of registered photons is always lower than the true number of incident photons, and a detector dead-time correction[79] is needed. These issues are especially problematic in the case of dilute samples on strongly fluorescing supports, or in cases where the components of the sample environment, such as the electrolyte layer, produce a high intensity of

elastically scattered X-rays, which are also collected by the detector and have energies just slightly larger than the energy of the main fluorescence lines, thus cannot be filtered out or separated by energy-discriminating detectors.

Installing additional single crystal analyzers to disperse the fluorescent radiation provides the possibility to measure not just the total fluorescence yield, but the full spectrum of the emitted radiation (with energy resolution of a fraction of eV or better). It allows one to offset some of the above-mentioned issues (e.g., to better remove the background contribution) and enables advanced X-ray spectroscopies, such as HERFD-XAS and RIXS spectroscopy, discussed in Section 5.10. However, the low photon counts that are detected after such an additional energy selection require an especially intense X-ray source or long acquisition times for these methods to work.

An important factor to consider in XAS measurements in fluorescence mode is the self-absorption effect. For thick and concentrated samples, the energy-dependent attenuation of the incident and emitted X-ray photons results in distortions of the spectral features. Therefore, measurements in fluorescence mode are reliable only for thin or for dilute samples. While certain strategies are available to partially correct for the self-absorption effect in the collected data,[80] and some experimental geometries (e.g., so-called "grazing-exit" geometry) are less prone to this effect,[81,82] the only truly reliable option is to choose sample concentrations in a way such that the self-absorption is avoided. As a rule of thumb, self-absorption can be considered negligible if the absorption jump $\Delta\mu_0(E_0)d$ is below 0.1. It can be verified on a case by case basis by comparing the XAS signal collected in fluorescence mode with that from measurements in transmission mode in situations where both are available.

Conceptually similar to measurements in fluorescence mode are XAS measurements in total electron yield mode, where the X-ray absorption probability is also assessed indirectly through monitoring the intensity of a secondary process. In this case, the excitation created by the incident X-rays decays by the emission of Auger electrons. Similarly as with the fluorescence measurements, the emission intensity can be often considered proportional to the absorption coefficient. Because of the short mean free path of the Auger electrons emitted (ca. 1−5 nm, dependently on the energy[67,83]), the detected signal is limited to the sample surface (and not affected by self-absorption). For the method to work, the sample also needs to be electrically conductive, which is not usually a problem in the studies of electrocatalysts. Conventional total electron yield measurements require vacuum conditions for the electron detection, and thus, their applicability for *in situ* and *operando* investigations of catalysts, and electrocatalysts in particular, is limited. However, conversion electron yield measurements can be used in liquid environment, where the XAS spectrum is measured at the conductive surface that is in the contact with the liquid.[83] For example, Velasco-Velez et al. recently demonstrated the usefulness of *in situ* XAS in total electron yield mode to study the local structure of the electrolyte (water) near a gold electrode and its bias voltage dependence.[18,84] In their setup, a Si_3N_4 membrane was used to separate the electrolyte in the electrochemical cell from the vacuum of the detection system, allowing them to collect oxygen K-edge XAS data in fluorescence mode, as well as in total electron yield mode at a gold electrode, Figure 3a. As shown in Figure 3b, the fluorescence and total electron yield modes resulted in significantly different XAS spectra, signifying
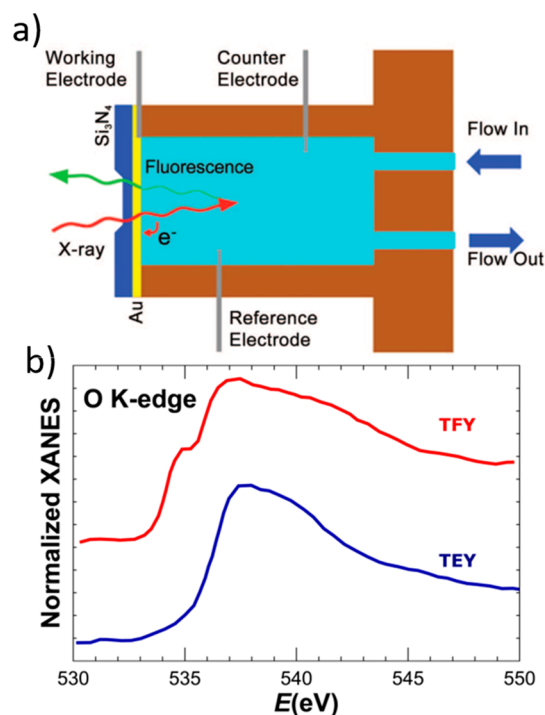
Figure 3. (a) Electrochemical cell for soft X-ray XAS data collection in fluorescence and total electron yield modes. (b) Experimental O K-edge XAS spectra collected in total fluorescence yield (TFY) and total electron yield (TEY) modes. Reproduced from ref 84. Copyright 2014 AAAS.

the importance of the surface-sensitivity of the total electron yield measurements as well as the strong interaction between the water molecules and the gold electrode at the interface.[84]

3.3. Energy Dispersive XAS Setup

An alternative approach to conventional XAS data collection with a scanning monochromator relies on an energy-dispersive (or optically dispersive) setup, as illustrated in Figure 2b. Instead of a monochromator, the X-ray beam is reflected in this scheme from a polychromator, which disperses the beam in space in a way so that photons with different energies travel along different paths. After passing through the sample, the entire spectrum is collected in a single shot using a 2D detector. This allows one to collect the XAS signal with unprecedented time resolution (down to the μs scale). Moreover, this setup provides much better beam stability since no moving components are involved. This makes it attractive for studies of very small samples, such as samples under extreme conditions (high temperatures, high pressures, strong magnetic fields), allowing one to extract unique information about *in situ* transformations of materials.[85−90] The applications of this method for the studies of catalysts under working conditions, are, however, limited by the fact that the data collection in fluorescence mode is normally not possible. Moreover, the quality and homogeneity of the sample are even more critical than in transmission measurements at a conventional XAS beamline because X-ray photons with different wavelengths travel through different parts of the sample. Normally, only relatively short spectra can be collected at energy dispersive beamlines, and defects in optics result in noticeable distortions of the spectral features.[90] Finally, sample exposure to the high intensity polychromatic X-ray beam can result in sample damage.

Nevertheless, while the popularity of energy-dispersive XAS setups at SR facilities is limited, they are finding new niche applications with the development of lab-based XAS spectrometers,[70] in studies under extreme conditions,[86,90,91] and in ultrafast XAS experiments with X-ray free electron lasers,[92] where the ability to collect spectra in a single shot is essential.

3.4. Time- and Spatially-Resolved XAS

While the possibilities provided by energy-dispersive XAS for *in situ* and *operando* studies of catalysts are limited, time-resolved measurements are often the key for understanding the working mechanism of catalysts and other functional materials, by allowing one to follow directly the transformations in the materials structure and composition, and detect the presence of intermediate species. The collection of a full XAS spectrum at a conventional monochromator-based SR beamline requires several minutes, which significantly limits the achievable time resolution. However, the recent progress in the so-called quick-XAFS (QXAFS) method, which relies on specially designed continuously scanning monochromators and rapid data acquisition schemes, has been considerable and allows one to achieve time-resolution down to the ms range.[93,94] This enables new experimental designs and access to previously unexplored details of the changes in the structure of the catalysts. For example, the QXAFS method with increasingly improving time-resolution has been instrumental for analyzing time-dependent processes at Pt electrodes during the ORR reaction, as demonstrated by Tada et al.[95−98]

For even better time-resolution, various pump-and-probe techniques can be used, where the spectrum is collected point-by-point, by repeating an experiment many times with fixed time delay between the sample perturbation ("pump" pulse) and the absorption measurements ("probe" pulse). Such studies are attractive, for instance, for the investigation of photocatalysts, where the excitation of the sample by the laser results in well-reproducible structural modifications with well-defined onset times. For example, Borfecchia et al. used this approach to follow light-induced excited state dynamics in photoactive metal complexes with 100 ps time resolution.[99] However, this approach is less common for the study of heterogeneous catalysts due to the challenge to repeatedly initiate the reaction at well-defined times in a typically macroscopic reactor with significant gradients of temperature, reactant concentrations, pH, etc.

The ability to collect XAS data quickly, combined with the advances in X-ray optics that allow now to focus the X-ray beam down to submicron dimensions, provides also the possibility to use XAS for 2D and 3D mapping of distributions of different species in nonhomogenous samples. A full XAS spectrum can be collected for each pixel and voxel in the image of the sample, using either a wide X-ray beam and a 2D detector (transmission measurements only) or point-by-point, by scanning the focused X-ray beam.[100] For example, Schroer et al. used tomography-based XAS and a scanning beam approach to map the 3D distributions of Cu species in different oxidation states in CuO/ZnO catalyst in a glass capillary,[101] and Grunwaldt et al. used a 2D detector to map the distribution of Rh species with different oxidation states in Rh/Al$_2$O$_3$ catalyst during CH$_4$ oxidation.[13,102,103] Clearly, the ability to probe and visualize directly inhomogeneities in the sample is especially relevant for complex multicomponent systems such as electrocatalysts at work. For example, Takao et

al. recently demonstrated the possibility to use QXAFS and a scanning X-ray beam to map the distribution of different Pt species at the cathode of polymer electrolyte fuel cells, where the increased Pt oxidation state was associated with the degradation of the catalyst and correlated in space with the presence of microcracks in the cathode layer (Figure 4).[104]
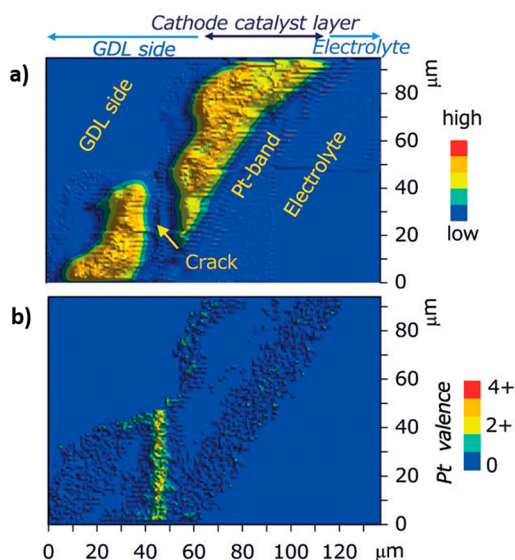

Figure 4. Mapping (a) Pt concentration and (b) valence state around a microcrack in a membrane-electrode assembly using QXAFS and a scanning X-ray beam. Reproduced with permission from ref 104. Copyright 2014 WILEY-VCH Verlag GmbH and Co. KGaA, Weinheim.

Without doubt, the importance of spatially- and time-resolved XAS studies for the understanding of catalyst under working conditions will further increase in the future. However, one of the challenges to be addressed in these experiments includes the very large data sets produced, which requires some further development in automatic data processing and analysis. This can be based on unsupervised machine learning methods[12] to fully exploit the potential provided by the new exciting experimental capabilities.

3.5. Sample Environments

The critical component of *in situ* and *operando* XAS measurements is the development of sample environments: furnaces, cryostats, reaction cells, etc. that enable the controlled exposure of the sample to the desired reaction conditions. In catalysis and electrocatalysis in particular, the challenge is to achieve a satisfying compromise between ensuring that the reaction conditions are close to those used in industry and lab-based investigations of catalyst performance, while simultaneously providing an unobstructed path for the incident X-rays, as well as transmitted or fluoresced X-ray photons or secondary electrons.[7,18]

For *operando* XAS studies of electrochemical processes, the catalyst is usually deposited on conducting carbon-based electrodes, which do not interfere with the data acquisition. The background from the carbon support to the XAS data is practically negligible, especially in the experiments within the hard X-ray regime. This constitutes an important advantage of the XAS method in comparison to other spectroscopies employed for studies of electrocatalysts. At the same time, the presence of an electrolyte layer in direct contact with the catalyst surface cannot be ignored. For example, a larger volume of the experimental cell may be beneficial for ensuring realistic experimental conditions, pH levels, distributions of reactants, and reaction products. A thick layer of electrolyte will, however, attenuate and scatter a significant fraction of the X-rays, hindering the XAS data acquisition. Moreover, bubble formation in the electrolyte in the case of electrochemical reactions at electrodes can result in significant noise problems in the experimental data.

Many different experimental cell designs have been proposed that are optimized for different applications and address the inevitable trade-off from different perspectives. Designs of several *in situ* cells for electrochemical measurements have been reviewed by Russell and Rose.[17] More recent
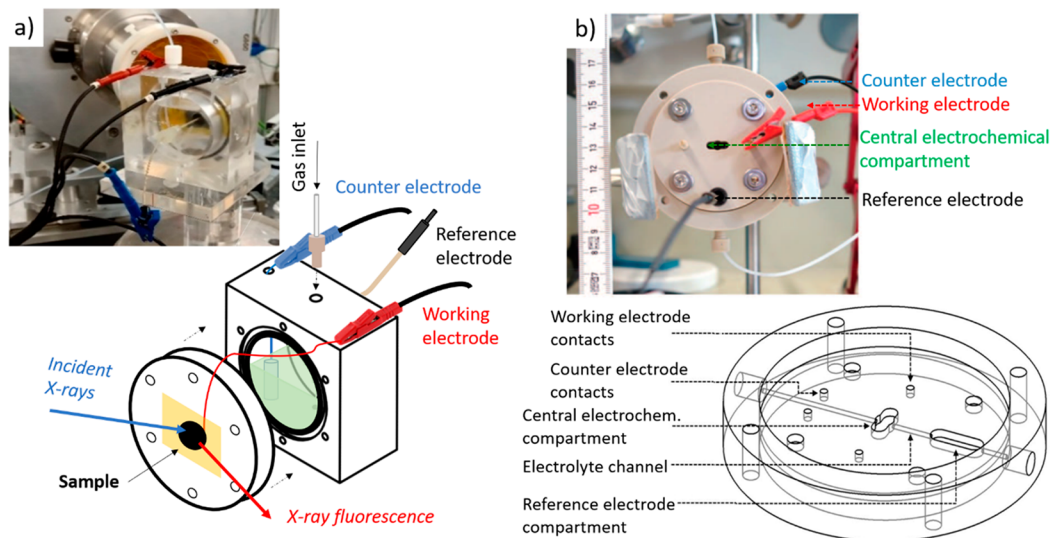

Figure 5. (a) Large volume electrochemical cell for XAS measurements in fluorescence mode used in refs 25, 106, and 111. (b) Electrochemical cell with continuous electrolyte flow for XAS measurements in transmission and fluorescence modes. Reproduced from ref 107 under Creative Commons Attribution 4.0 International License: https://creativecommons.org/licenses/by/4.0/.

examples can be found in refs 105−108. While single compartment cells are commonly used for *in situ* XAS measurements, two-compartment cells have also been employed.[108−110] Two proposed cell designs exemplifying alternative approaches are shown in Figure 5. Both cells are single compartment cells with a typical three electrode setup: reference electrode, counter electrode, and the sample as a working electrode. Figure 5a shows a large volume cell for XAS measurements in fluorescence mode, where the sample is mounted on the front panel of the cell facing the electrolyte, so that the working electrode simultaneously acts as an X-ray window. Incident X-rays and X-ray fluorescence thus pass through the back of the sample.[106]

At the same time, the approach illustrated in Figure 5b features a cell with a relatively small central electrochemical compartment to minimize the thickness of the electrolyte layer, allowing measurements both in transmission and fluorescence modes. The limitations due to the small volume of the cell and bubble formation are partially addressed by ensuring the continuous electrolyte flow through the cell using a syringe pump.[107] Degassing the electrolyte before the experiment to increase the solubility of the reactant gases in the electrolyte can further help to reduce the measurement problems related to bubble formation.

3.6. XAS in Soft X-ray Range

The high penetration depth of hard X-rays in the XAS method provides obvious advantages for *in situ* and *operando* studies by ensuring sufficient flexibility in the choice of sample environment geometry and materials used. However, in many cases, spectroscopical investigations in the soft X-ray range (with X-ray energies below 5 keV) can provide important clues about catalyst structure.[112,113] For example, L-edges (and even M-edges) of transition metals can be accessed in soft X-ray/UHV experiments, which may be more sensitive to the oxidation state of the catalyst than K-edges. This fact was employed by Kornienko et al. for the determination of the oxidation state of Co in CoS_x catalysts for water splitting (hydrogen evolution reaction)[114] and by Cheng et al. and Zhu et al. to determine the Ni oxidation state in Ni-based MOF catalysts for oxygen reduction/evolution reactions and urea oxidation reaction, respectively.[115,116] Hydride formation in the presence of hydrogen in Pd-based electrocatalysts for CO_2 electro-reduction, in turn, can be conveniently followed by using XAS at L-edges of Pd.[117] At the same time, information from the K-edges of light elements can provide important complementary insight about the structure of multielement catalysts,[114] or that of the electrolyte,[84] interactions between adsorbates and catalysts,[118,119] and structural motifs in carbon-based materials that are currently used as nonprecious metal catalysts for the CO_2 electroreduction and oxygen reduction reactions.[120−123] An excellent review on the measurements and interpretation of O K-edge XAS was recently published by Frati et al.[83]

The strong X-ray attenuation in the soft X-ray range puts significant additional constraints on the experimental design, where X-ray attenuation by air should be avoided. This complicates the design and assembly of the cells for *in situ* and *operando* measurements since the sample cell needs to be integrated into the beamline setup and separated from vacuum by thin windows made from X-ray transparent materials. For example, Ishihara et al. recently reported the design of an electrochemical cell for soft X-ray XAS, where the catalyst/

working electrode was a 15 nm layer of platinum deposited on a window made of silicon carbide.[124] A conceptually similar design with an Au film deposited on a Si_3N_4 window was also proposed by Velasco-Velez et al.[84] and is shown in Figure 3a.

Another issue to consider in the soft X-ray range is that the penetration depth of low energy X-rays is lower than that for hard X-rays, which makes soft X-ray XAS more surface sensitive. For example, the shift to lower energies of the Au M_5-edge XANES spectrum in Au NPs deposited on carbon nitride (C_3N_4) was observed by Zhang et al.,[125] whereas no changes at the Au L_3-edge were detected.[125] This difference was interpreted as an interface effect due to electron transfer from the support to the NP surface. The accompanying minor shifts of the nitrogen K-edge XAS features to higher energies observed allowed Zhang et al. to identify N atoms as the likely source of the transferred electrons. This negative charging of Au NPs on carbon nitride was correlated with an observed enhanced CO_2RR activity of these NPs with respect to similar NPs deposited on carbon.[125]

4. FROM SPECTRA TO DESCRIPTORS OF ELECTRONIC AND GEOMETRIC STRUCTURE

4.1. Qualitative and Semiquantitative Analysis of XANES Spectra

Spectral features in the XANES region of the absorption spectra are a result of transitions of photoelectrons excited by X-rays to unoccupied localized and delocalized states and are sensitive to both the materials atomic and electronic structure. However, due to the multitude of different possible transitions and the sensitivity of XANES to the details of the atomic bonding and density of on vacant states, the interpretation of XANES features is often nontrivial.[26]

A commonly used approach thus relies on simple finger-printing, where the XANES spectra for the sample of interest are compared with the spectra for reference materials. Nonetheless, this approach relies on the availability of such reference spectra and thus requires guessing *a-priori* which material structures may be the most relevant references. A possible alternative solution would be to create large publicly accessible databases of experimental data that can be used for the identification of the collected spectra. While there is some progress during the last decades in the development of such databases (e.g., https://cars.uchicago.edu/xaslib/,[126] www.cat.hokudai.ac.jp/catdb,[127] https://eelsdb.eu/),[128] currently they only contain a few hundred experimental spectra.[53] In many of the *in situ* and *operando* studies, the corresponding reference samples are also not easily available. In fact, some intermediate species and unique structural motifs that are present in catalysts under working conditions or ultradispersed NPs may not have analogues among bulk materials that are stable at ambient conditions. On the other hand, significant advances have also been made in *ab initio* XANES modeling, and codes like FEFF[42] and FDMNES[129] allow one to simulate XANES features for different structures with increasing accuracy and can be used to create large sets of reference spectra. For example, Zheng et al.[54] and Mathew et al.[53] used FEFF simulations to generate a database with ~800 000 XANES spectra for bulk material structures from the Materials Project database,[130−132] and developed tools for the automatic comparison of experimentally acquired spectra with theoretical data in the database, leading to the identification of the most likely structures. Despite this progress, the practical applica-
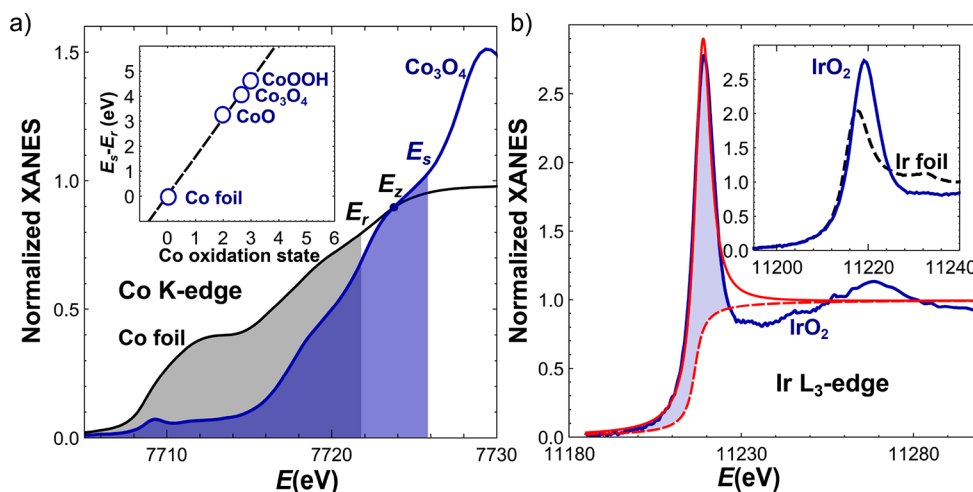
Figure 6. (a) Quantification of the shift between the absorption edge for metallic Co and Co_3O_4 following the procedure described by Capehart et al.[135] The areas of the shaded regions are equal and correspond to 80% of the total area under the pre- and near-edge part of the metallic Co XANES spectrum, integrated until $E = E_z$. The end of the near-edge region E_z here is defined as a point where the Co foil spectrum crosses the spectrum of Co_3O_4. The difference between the energy values corresponding to the boundaries of the shaded regions (E_s for Co_3O_4 and E_r for the Co foil) is used to characterize the absorption edge shift. The inset shows a nearly linear dependency of $E_s - E_r$ on the Co oxidation state. (b) Estimation of the WL intensity at the Ir L_3-edge in IrO_2 following the method reported by Clancy et al.[136] An arctangent function corresponding to the absorption jump (red dashed line) is subtracted, and the remaining area under the white line peak (shaded region) is numerically integrated. Alternatively, the WL is fitted as a combination of an arctangent function and a Lorentizan function (red solid line). The inset compares WLs for IrO_2 and for metallic Ir.

tions of this approach are still limited by the necessary trade-off between the accuracy of XANES modeling and the required computational resources to generate extensive databases, and, more critically, by the fact that only well-ordered crystalline materials with well-known and well-defined structures are typically considered.

In the absence of accurate theoretical models, the interpretation of XANES spectra often relies on semiempirical relationships. As the most important material descriptors that can be extracted from XANES data, one usually considers: (i) the position of the absorption edge, (ii) the intensity of the white line, and (iii) the presence and intensity of the pre-edge features.

As discussed in Section 2, the shift in the position of the absorption edge can often be directly linked to changes in the materials oxidation state and charge transfer. However, the differences in the shape of the XANES features for samples with different structures may result in ambiguities in the definition of the energy corresponding to the absorption edge, and a systematic approach is needed for quantitative analysis. In the simplest case, the energy corresponding to a certain inflection point (maximum of the first derivative) in the normalized XAS spectrum associated with the absorption threshold, pre-edge, or the main absorption feature can be used as a descriptor of the absorption edge position.[133] Alternatively, one can use integrated descriptors and determine the energy where the integrated absorption reaches a certain fixed value. For example, Capehart et al. suggested using as a descriptor of the absorption edge position an energy value corresponding to 80% of the integrated absorption spectrum area for the corresponding metal foil[134,135] (Figure 6a).

The integration of the area under the XANES features is also a useful descriptor of the white line intensity. At the L-edge of transition metals, the area under the WL is related to the density of unoccupied d-states and is thus sensitive to the oxidation state and changes in the electronic structure due to

the chemical bonding or charge transfer phenomena. Clancy et al. suggested to use as a descriptor of the WL intensity the integral area under the absorption spectrum after subtracting an arctangent function centered on the inflection point at the absorption edge (Figure 6b).[136] Sham et al. used a similar approach to characterize the charge transfer in gold alloys, and integrated the difference between the XAS spectra of alloys and those of a gold foil, where the latter has no WL due to the completely filled d-shell.[137,138] Alternatively, to characterize the intensity of the WL, one can use the fact that the shape of the WL is usually close to a Lorentzian line, and the experimental data can be fitted with such line shape and its integral area considered as the WL intensity.[136,139]

Fitting with one or a combination of several Lorentzian functions is also a common approach to characterize the shape, positions and intensities of the pre-edge features. The choice of Lorentzian line shape is based on the observation that if the broadening of the spectral features due to the instrumental resolution is low, the width of the features corresponding to a particular electronic transition is limited by the intrinsic lifetime of the excitation, which results in Lorentzian broadening. If the effect of the finite instrumental resolution cannot be neglected, Voigt or Gaussian functions can be a more meaningful approximations of the shapes of the observed peaks.[26,140] In all cases, however, caution is needed when a particular feature is attributed to a specific electronic transition. *Ab initio* XANES modeling can be a very valuable tool to verify such assignments.

Finally, note that a powerful technique to improve the sensitivity of the XANES method is differential, or "Δ-XANES" analysis, where the subtle variations in the XANES features, due to, e.g., the interactions with adsorbates in the catalyst under working conditions, are emphasized by subtracting the spectra of the pristine material or other suitable reference and analyzing the difference spectrum instead (by integration or peak-fitting methods).[21,140,141]

4.2. Qualitative Analysis of EXAFS Data: Identifying Neighboring Atoms

While XANES characterizes the chemical state of the absorbing atom and the symmetry of its environment, EXAFS analysis provides much more detailed information about the local atomistic structure. In particular, it allows one to identify quickly the type of atoms that are nearest to the absorbing atom and the interatomic distances to them. Often it is possible to identify the local environment of absorbing atoms just by looking at the first peak in the Fourier-transformed EXAFS spectra. In XAS data collected at absorption edges of some metals, the first peak in the FT-EXAFS at distances 1.5–2.0 Å typically corresponds to the low-Z neighbors (O, N, C, etc.), indicating the cationic nature of the absorbing site, Figure 1c. Because of the larger ionic size of the reduced ions, metal−metal bonds are normally longer and contribute to the FT-EXAFS at distances 2−2.5 Å (Figure 7). Thus, the presence of such a feature in the FT-EXAFS
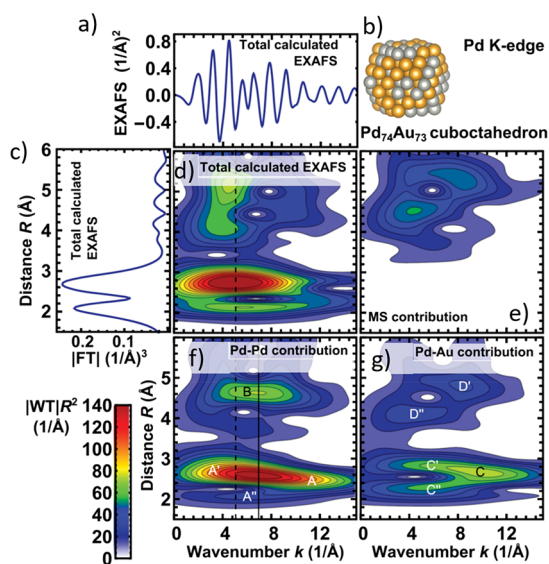

Figure 7. (a) Theoretically calculated Pd K-edge EXAFS spectrum for a (b) model $Pd_{74}Au_{74}$ NP, and its (c) Fourier and (d) wavelet transformations. (e) Wavelet transforms of partial multiple-scattering contributions, and those of the single scattering (f) Pd−Pd and (g) Pd−Au contributions are shown separately. Reprinted from ref 147 with permission of AIP Publishing.

spectra indicates the metallic nature of the absorbing species. It is important to note here that the positions of peaks in the FT-EXAFS spectra do not correspond to actual interatomic distances. Usually, the FT-EXAFS feature is located at an R value that is ∼0.5 Å shorter than the actual length of the corresponding bond. This can be noticed by comparing the position of the peaks in Figure 1c, which shows the FT-EXAFS spectrum for CuO, and in Figure 1d, which shows the actual RDF (histogram of bond-lengths). This difference arises due to the presence of a k-dependent phase function $\phi_p(k)$ in the sinusoid-term in eq 8, which effectively changes the apparent frequency by $\langle \phi_p(k)/2k \rangle$.

Although the visual examination of the FT-EXAFS data provides information about interatomic distances only, EXAFS features themselves are much more informative and provide the possibility to distinguish between different types of neighbors, even if they are located at the same interatomic

distance. The chemical sensitivity of EXAFS is based on the fact that the scattering functions F_p, and ϕ_p in eq 8 depend on the type of neighboring atoms. As a result, different neighbors contribute differently to the EXAFS spectrum. For example, for relatively light elements in the k-range relevant for EXAFS analysis, F_p is a function with a single maximum, whose position shifts to larger k values with increasing absorber atomic number Z. Much more complex F_p dependencies on the wavenumber k are characteristic for heavy elements such as Au due to the Ramsauer-Townsend effect.[142,143] Note here that the contrast between scattering functions for elements that are neighbors in the Periodic Table is small, making the discrimination of their respective contributions challenging.

A convenient way to visualize the neighbor-specific information is to rely on a wavelet transformation (WT) of the EXAFS spectra.[144−146] Similarly to Fourier transform, the wavelet transform is also an integral transformation that provides information about the frequency content in the analyzed spectrum. Unlike the FT, the WT provides a two-dimensional representation of the analyzed spectrum in k- and R-spaces simultaneously and shows not only what frequencies are present but also to which part of the spectrum they contribute, thus allowing one to capture the variations of the F_p and ϕ_p functions and directly distinguish between different types of neighbors. The Pd K-edge EXAFS signal and its Fourier and wavelet-transformation for $Pd_{74}Au_{73}$ NPs are shown in Figure 7.[147] Partial contributions of Pd−Au and Pd−Pd bonds to the WT-EXAFS spectrum are shown separately. Note that due to the random alloy structure of this model NP, the average number of Pd and Au neighbors around each Pd atom are roughly the same, and the corresponding Pd−Au and Pd−Pd distances are also similar. The wavelet transforms for Pd−Pd and Pd−Au bond contributions, however, are very different. In both cases, the main feature in the WT-EXAFS spectra (feature A in the Pd−Pd contribution and feature C in the Pd−Au contribution) due to the Ramsauer-Townsend effect is split in two branches. However, while for the Pd−Au contribution, both branches (C′ and C′′) have approximately the same intensity, for the Pd−Pd contribution branch, A′ at higher R values is much more intense. This difference thus allows an easy distinction between Pd-rich and Au-rich materials using their EXAFS spectra[147] and illustrates the usefulness of the WT method for the analysis of the materials composition.

During the last years, the use of the wavelet transform for the interpretation of experimental spectra has become increasingly popular, also in the studies of heterogeneous thermal- and electrocatalysts. For example, Grosse et al. used it to separate Cu−Cu, Cu−O and Cu−Cl contributions in Cu K-edge EXAFS for Cu nanocubes, a promising catalyst for the electrochemical CO_2 reduction.[148] In studies of nonprecious-metal catalysts for ORR, in turn, it was employed to distinguish between metal−metal and metal−nonmetal contributions in EXAFS spectra and to interpret distant coordination shell contributions,[20,149] while Zhang et al. used it for the interpretation of Pt L_3-edge EXAFS of singly dispersed Pt atoms for applications in hydrogen evolution reaction (HER).[150]

One should note, however, that while the wavelet transform is a very useful tool for XAS data visualization, it needs to be used with caution to avoid overinterpretation of the results. Similarly as with a Fourier transform, many effects can influence the appearance of features in the WT-EXAFS, and

their interpretation from their visual examination is straightforward only for the first or a first few peaks, which can be associated with distinct bonds. Contributions of more distant coordination shells, however, usually overlap and superpose with each other; thus, the corresponding features in the WT-EXAFS and FT-EXAFS spectra are impossible to interpret without modeling or data fitting. There have been some attempts in the literature to discriminate by wavelet analysis between the contributions to EXAFS spectra of light elements that are neighbors in the Periodic Table, as, for example, Co-based single-site catalysts for HER.[146,151] Nonetheless, in practice, such analysis may be very challenging because even small changes in the relative atomic positions and disorder can affect the WT-EXAFS features more significantly than the subtle difference between the scattering functions for similar elements.

4.3. Geometric Structure Descriptors: Coordination Numbers, Interatomic Distances, Disorder Factors

The popularity of the EXAFS method for quantitative structure analysis relies on the fact that eqs 7 and 8 provide an easy and accurate way to model the EXAFS spectrum. Note that such explicit equations do not exist for the description of the XANES region of the X-ray absorption spectra. To extract quantitative characteristics of the materials structure from EXAFS spectra, one needs to choose a proper model for $g_p(R)$ in eq 8 and then to fit the parameters of the distribution to match the experimental signal. Commonly, a Gaussian-shape is assumed for the distribution function $g_p(R)$. In this approach, which works well for relatively ordered materials, and which constitutes the workhorse of XAS data analysis in the overwhelming majority of the published studies, the EXAFS equation can be rewritten as[27]

$$\chi(k) = \sum_p \frac{C_p S_0^2}{k R_p^2} F_p(k, R_p) e^{-2R_p/\lambda(k)} e^{-2\sigma_p^2 k^2} \sin(2kR_p + \phi_p(k, R_p)) \tag{10}$$

where C_p is coordination number (number of atoms in a given coordination shell), R_p is the average interatomic distance (the radius of the coordination shell), and σ_p^2 is the disorder factor, known also as Debye−Waller factor or parallel mean-square relative displacement (MSRD) factor, which accounts for both thermal and static disorder in the material: $\sigma_p^2 = \sigma_{p,thermal}^2 + \sigma_{p,static}^2$. The MSRD factor from EXAFS analysis depends also on correlations between the atomic displacements and should not be confused with the Debye−Waller factor used in XRD data fitting or mean-square displacement (MSD) factor. For example, if the atomic displacements of neighboring atoms are large, but completely correlated, the EXAFS MSRD factor will be equal to 0, while the MSD extracted from XRD data can be quite significant.[152] Note also that the MSRD factor in eq 10 is responsible for the exponential damping of the EXAFS signal at high k-values, which is getting more pronounced upon an increase of the disorder (static or thermal), limiting the information content available from EXAFS data collected at high temperatures or for statically distorted materials. The thermal contribution to the disorder factor is related to the density of vibrational states and bond strengths:[27,152−154]

$$\sigma_{p,thermal}^2(T) = \frac{\hbar}{2\mu_p} \int_0^{\omega_{max}} \frac{d\omega}{\omega} \rho_p(\omega) \coth\left(\frac{\hbar\omega}{2k_B T}\right) \tag{11}$$

where μ_p is the reduced mass of atoms of the involved atomic pair, k_B is the Boltzmann's constant, and $\rho_p(\omega)$ is the local projected phonon density of states. For example, within the so-called correlated Debye model, $\rho_p(\omega) = \frac{3\omega^2}{\omega_{D,p}^3}\left(1 - \frac{\sin(\omega R_p/c_p)}{\omega R_p/c_p}\right)$, where $c = \omega_{D,p}/k_D$, $k_D = \left(\frac{6\pi^2 n}{V}\right)^{1/3}$, and V/n is the crystal volume per atom. The Debye model provides a physically meaningful description of the phonon spectrum for simple monometallic systems with one atom per unit cell.[155] Alternatively, the correlated Einstein model can be used where the density of phonon states is approximated with a Dirac delta-function $\rho_p(\omega) = \delta(\omega - \omega_{E,p})$, and eq 11 can be rewritten as[27,152−154]

$$\sigma_{p,thermal}^2(T) = \frac{\hbar}{2\mu_p\omega_{E,p}} \coth\left(\frac{\hbar\omega_{E,p}}{2k_B T}\right) \tag{12}$$

Here $\omega_{E,p}$ is a characteristic vibrational frequency (Einstein frequency), which can be associated with the centroid of a normal-mode frequency distribution.[155] The Einstein frequency can also be conveniently linked to the effective bond force constant as $\kappa_p = \mu_p\omega_{E,p}^2$. The Einstein model is believed to be more adequate than the Debye model for systems with strong contributions from optical phonons.[152] In practice, however, both the Debye and Einstein models can be used to describe the temperature-dependency of the Debye−Waller factor, and the difference between both approximations is typically less than the uncertainty of the $\sigma_{p,thermal}^2$ estimation from the experimental data.[155] In particular, the applicability of the Einstein model in a broad range of materials (including monometallic fcc materials) was demonstrated by Sanson et al.[154,156] Both Debye and Einstein frequencies (and the corresponding Debye and Einstein temperatures, defined as $\theta_{D,p} = \hbar\omega_{D,p}/k_B$ and $\theta_{E,p} = \hbar\omega_{E,p}/k_B$, correspondingly) can thus be used to describe the temperature dependencies of the Debye−Waller factor and bond strengths.

The parameters C_p, R_p, and σ_p^2 that characterize the materials structure and dynamics can then be obtained from nonlinear least-squares fitting of the experimental EXAFS data.[55] In addition, nonstructural parameters such as the E_0 and S_0^2 values need to be determined. The latter, due to its complete correlation with the C_p values, needs to be found in the analysis of EXAFS spectra for reference materials with known structure.

Functions F_p, ϕ_p, and λ_p can also be obtained experimentally from the analysis of EXAFS spectra in reference materials with known structure. This approach was mostly used in the older papers, when the accuracy of ab initio EXAFS simulations was limited. For example, this approach is applied in refs 157 and 158 to analyze EXAFS spectra of Pt catalysts for methanol oxidation and Ru-based catalysts for ORR. However, even nowadays it can provide better accuracy if very subtle effects need to be analyzed such as thermal expansion[159] or isotopic effects on EXAFS spectra.[160,161] Today a more common approach, however, is to calculate the functions F_p, ϕ_p, and λ_p theoretically, which can be achieved with a good accuracy with codes like FEFF[31,42,55] and GNXAS.[58,59]

The application of this conventional EXAFS data fitting approach to real catalysts under working conditions is nevertheless hindered by the fact that the disorder in such materials can exceed significantly the range where a Gaussian

approximation is valid. Small NPs, materials experiencing structural transformations, and materials operating at high temperature are catalytically relevant systems, and all exhibit significant static and thermal disorder. In addition, a non-Gaussian distribution of bond-lengths may be a result of a structure relaxation near the surface, interactions with adsorbates, particle-support interactions, or the coexistence of different populations of NPs with slightly different structures.[162−167] It has been demonstrated by Claussen and others that in this case EXAFS data fitting may result in significantly underestimated coordination numbers, interatomic distances, and disorder factors.[23,166−174] A dramatic illustration of this problem is the analysis of Zn K-edge EXAFS data of a bulk Zn foil, Figure 8. For this material,
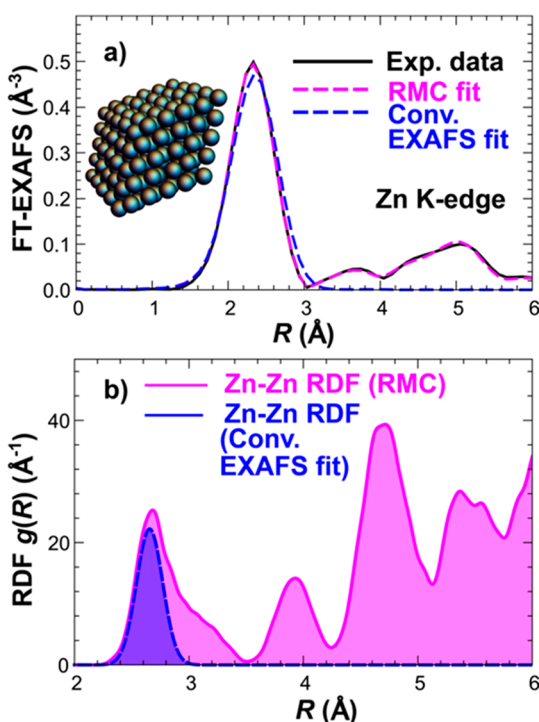

Figure 8. Zn K-edge EXAFS data fitting for a Zn foil using a conventional approach and RMC simulations. Experimental EXAFS and model spectra extracted following both approaches are compared in panel a, while the Zn−Zn RDFs obtained by both approaches are shown in panel b. Despite the fact that conventional EXAFS fitting provides almost as good description of the 1st coordination shell contribution as advanced RMC simulations, the number of nearest neighbors (the area under the 1st RDF peak) is underestimated by the conventional approach by ~50%. In addition to providing a more accurate RDF, the RMC analysis allows also fitting contributions of more distant coordination shells. Experimental data and RMC simulations taken from ref 25.

EXAFS fitting in Gaussian approximation applied to the first coordination shell contribution provides quite a good description of the experimental data (Figure 8a). The obtained coordination number value (6.4 ± 0.8), however, is very far from the actual number of nearest neighbors (12) in this material. Thus, the error in the coordination number estimation even in the case of a perfectly homogeneous bulk sample (Zn foil) and very good signal-to-noise ratio can be almost 50%. The reason for this effect is the distorted hcp-structure of bulk Zn, which results in a very asymmetric shape of the Zn−Zn RDF peaks. When results of conventional

EXAFS fitting are compared with those from more advanced reverse Monte Carlo (RMC) simulations (discussed in Section 4.5), one can note that the conventional EXAFS fitting tries to reproduce the region in the RDF around the most-probable interatomic distance, which has the largest influence on the agreement between experiment and simulations. Significant errors in the RDF further from the RDF peak maximum remain unnoticed by conventional analysis. This example illustrates that even a seemingly small misfit of the experimental data can actually indicate significant problems with the structure model. It also demonstrates clearly that coordination numbers and interatomic distances can be strongly underestimated by conventional EXAFS data fitting in the cases when large disorder (static or thermal) is present. This fact needs to be considered, when these EXAFS-derived descriptors are used, for instance, to determine particle sizes.

A possible approach to address this problem is to use in the analysis model $g_p(R)$ functions with a more complex shape. For example, for small NPs, liquids, and other disordered materials, the $g_p(R)$ function can be better described with a Γ-like function, which better accounts for the asymmetry of the RDFs in disordered matter.[175] This fitting approach was used, for instance, by Witkowska et al. in studies of Pt NPs for fuel cell cathodes.[176] A more general approach relies on the expansion of $g_p(R)$ in the so-called MacLaurin, or cumulant series:[152]

$$\ln \int_0^\infty \left[g_p(R) e^{-2R/\lambda_p(k)} / R^2 \right] e^{2ikR} \, \mathrm{d}R = \sum_{n=0}^\infty \frac{(2ik)^n c_{p,n}}{n!}$$

(13)

After integration in eq 8, one obtains

$$\chi_p(k) = \frac{C_p S_0^2}{k R_p^2} F_p(k) e^{-2R_p/\lambda(k)} e^{-2\sigma_p^2 k^2 + 2/3 c_{p,4} k^4 - 4/45 c_{p,6} k^6 + \ldots}$$

$$\times \sin\left(2k R_p - \frac{4}{3} c_{p,3} k^3 + \frac{4}{15} c_{p,5} k^5 + \ldots + \phi_p(k) \right)$$

with the coordination number $C_p = c_{p,1}^2 e^{c_{p,0} + 2c_{p,1}/\lambda}$, the average interatomic distance $R_p = c_{p,1}$, disorder factor $\sigma_p^2 = c_{p,2}$, while the $c_{p,3}$, $c_{p,4}$, etc. terms describe the asymmetry of the distribution and its deviation from the Gaussian shape.[152] In principle, by using the cumulant expansion, one can express the arbitrary complex shape of the RDF, and fit the parameters $c_{p,3}$, $c_{p,4}$, etc. to experimental data. In practice, however, due to the limited information content in the experimental spectrum and correlations between fitting variables, one can rarely fit reliably the terms beyond $c_{p,3}$. The latter is related to the skewness of the distribution and may be helpful for the interpretation of high-temperature data, which are affected by the strong anharmomic motion of atoms.

An alternatives to the cumulant expansion is the so-called regularization approach, where $g_p(R)$ is parametrized as a histogram and the bin-heights are new fitting variables.[177−182] This method, which approaches the reconstruction of $g_p(R)$ as an ill-defined problem, necessarily relies on additional assumptions about the RDF shape such as non-negativity and smoothness.

The correlations between fitting variables result also in another challenge in the EXAFS data fitting, namely the interpretation of contributions of distant coordination shells. As shown in Figure 1c, all peaks in the FT-EXAFS spectrum beyond the first one are a result of the superposition of

different SS and MS contributions. This means that the contributions of those photoelectron paths cannot be singled out by simple Fourier filtering, and it is necessary to fit them simultaneously. This results in an exponential increase in the number of required fitting variables with increasing R-range used for the fitting.[23,183] The correlations between these variables result in significant fit uncertainties. For simple monometallic systems, this problem can be addressed by using constraints that limit the number of degrees of freedom in the fit.[184,185] However, data of very good quality are required to fit reliably the contributions to EXAFS spectra from the coordination shells beyond the first one. Thus, such an analysis remains usually limited to the interpretation of *ex situ* EXAFS data, or EXAFS data collected at cryogenic conditions to reduce the EXAFS signal damping due to thermal disorder. The interpretation of more distant FT-EXAFS peaks using conventional fitting approaches, as well as the interpretation of EXAFS spectra in disordered materials, thus remain problematic. More advanced approaches may be useful to address these issues. Such approaches are discussed in Sections 4.4–4.6.

4.4. Structure Descriptors from XANES

The physical origin of the postedge structure in XANES is analogous to that in EXAFS. Therefore, this portion of the XANES spectra is sensitive to the same structure descriptors such as coordination numbers and average interatomic distances. In fact, due to the much larger sensitivity of XANES features to multiple-scattering contributions, and larger effective mean-free path lengths in the XANES region, XANES can be even more sensitive than EXAFS to the details of the materials structure, such as bonding angles and different crystallographic phases.[34,186] Deciphering the features in the postedge region of XANES is, however, challenging. For decades, they have been interpreted only via a comparison with those for reference materials with known structure, or via semiempirical relationships. For example, the shifts of the postedge features can be linked to changes in the interatomic distances:[187,188]

$$\frac{(E_2 - E_0)}{(E_1 - E_0)} = \frac{d_1^2}{d_2^2} \qquad (15)$$

where E_1 and E_2 are the positions of a certain XANES feature in similar materials with characteristic interatomic distances d_1 and d_2, respectively. See refs 188 and 189 for the derivation of this relationship, sometimes referred to as Natoli's rule.[190] Recently, Friebel et al. used this rule to monitor the changes in the interatomic distances around copper extracted from HERFD XANES data of a Cu monolayer deposited on a gold single crystal used as a catalyst for CO_2 electro-reduction[191] and to follow changes in metal–oxygen interatomic distances in Fe–Ni oxide catalysts for OER.[192]

Nevertheless, the use of XANES analysis for the interpretation of the interatomic distances in more complex situations became possible only recently after the development of XANES *ab initio* theory codes, like FDMNES[129] and FEFF,[42] that enable quick and accurate calculations of XANES spectra for many relevant systems, and codes such as FitIt[51] and MXAN[52] that allow the direct fit of the structure parameters to experimental XANES features. For example, Guda et al. used FDMNES simulations coupled with a machine-learning (ML)-based interpolation scheme to fit the structure around Ni atoms in CPO-27-Ni metalorganic frameworks upon adsorption of CO, CO_2, and NO molecules

(Figure 9a).[34,193] Figure 9b shows the difference (L_2-norm) between the calculated and experimentally measured XANES
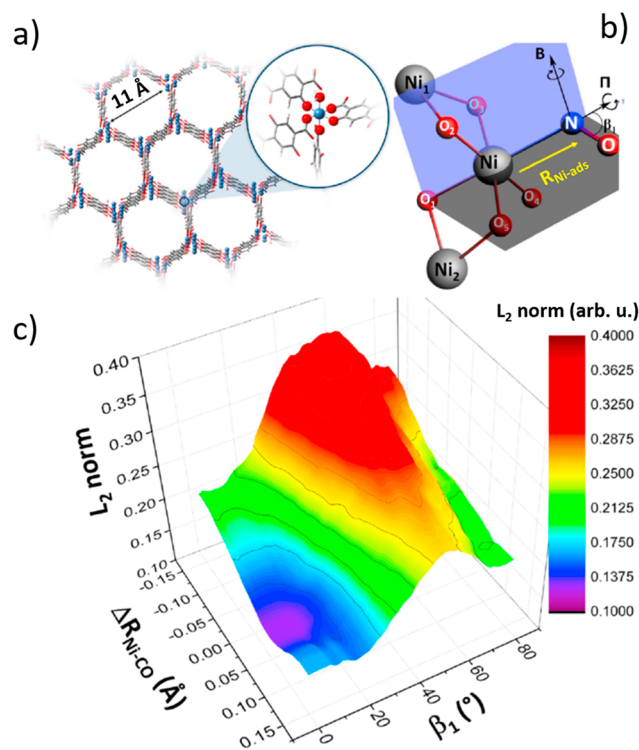
Figure 9. Schematic depiction of the (a) structure of CPO-27-Ni metalorganic framework and (b) adsorption of a NO molecule on the Ni site. (c) Difference between the experimental Ni K-edge XANES data and the theoretically calculated spectrum for different values of the Ni-adsorbate distance R_{Ni-CO} and adsorption angle β_1. Reproduced from ref 34 with permission from Elsevier.

as a function of the distance between the Ni site and the adsorbate, and the binding angle (e.g., Ni–C–O angle in the case of CO adsorption). A clear minimum in the residual plot allows one to identify the most likely values of these structure parameters. FDMNES simulations and fitting of XANES spectra using MXAN were also applied recently to find the structures of Fe–N–C, Ni–N–C, and Co–N–C catalysts for ORR from the corresponding Fe, Ni, and Co K-edge XANES spectra.[149]

Similarly, the sensitivity of the XANES spectra to particle sizes and shapes, and the reduction of the amplitude in XANES features (see Figure 10a) with increasing fraction of under-coordinated sites have been reported decades ago.[35,36,194–197] However, a practical approach to extract the coordination numbers from the XANES spectra was lacking. It was recently demonstrated that this problem can be addressed by supervised machine learning and artificial neural networks (NNs).[37,38] In this approach, instead of trying to write an explicit analytic relationship between XANES features and the structure descriptors, such a relationship is established numerically, by exposing an algorithm to many thousands of spectra (training data), for which the corresponding structure is known. Such spectra can be obtained in theoretical XANES simulations with FEFF or FDMNES codes. In the case of the NN method, the relationship between the spectral features and the structure is parametrized as a network of nodes, Figure 10b, where each of the nodes performs a simple mathematical

Figure 10. (a) Particle size effect in experimental Pt L_3-edge XANES data for well-defined Pt NPs supported on γ-Al$_2$O$_3$. The experimental data were extracted from refs [203] and [204]. (b) Schematic depiction of a neural network-based method for the interpretation of XANES data. (c) Comparison of coordination numbers for Pt NPs, as extracted from conventional EXAFS fitting and a NN-based XANES analysis. Adapted with permission from ref [38]. Copyright 2017 American Chemical Society.

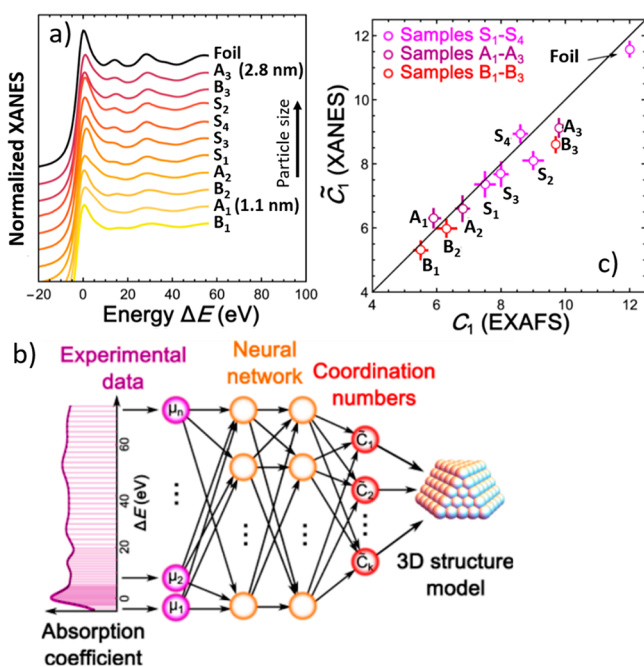operation $f(\{x_i\},\{\theta_i\})$ on its inputs $\{x_i\}$, subject to parameters (weights) $\{\theta_i\}$, and produces a single output that can be similarly processed by the nodes in the consequent layers. The values of the nodes in the first layer (input layer) are initialized by the normalized $\mu(E)$ values measured at a set of different energy points $\{E_i\}$. The values of the nodes in the last layer (output layer) correspond to the structure parameter of interest (e.g., average coordination numbers). During the training step, all weights $\{\theta_i\}$ are optimized via a back-propagation algorithm[198] so that for the training spectra, the NN yields the structure parameters that match their known true values. It was demonstrated in ref [38] that the coordination numbers extracted by NN from XANES data for the first four coordination shells for model Pt NPs are in a good agreement with the results of the EXAFS data analysis (Figure 10c). The ML-based approach, developed initially for the determination of coordination numbers in metallic NPs, was subsequently generalized for the determination of interatomic distances,[37] bonding angles,[34] the analysis of oxidized[199] and bimetallic[200] NPs, and the interpretation of polarization-dependent XANES spectra.[73] A similar approach was also used for the interpretation of EELS spectra.[201] See ref [12] for more details about ML-based XANES analysis and review of its recent applications.

Let us note here that both ML-based approaches and XANES data fitting rely on the accuracy of the *ab initio* XANES modeling, and therefore, caution is needed when interpreting the results. Contrary to the case of EXAFS modeling, where *ab initio* simulations provide a very good description of the experimental data, in the XANES region of the absorption spectra, systematic differences between

theoretical data and experimental XANES measurements are present, even if the most advanced codes are used for *ab initio* modeling. This systematic error can be propagated by the chosen data analysis method into significant inaccuracies in the values of the structure parameters. The accuracy of the ML-based approaches and XANES fitting thus always needs to be validated using sets of experimental data for samples with well-known structures.[12,202]

4.5. Atomistic Simulations for Interpretation of EXAFS Spectra

As discussed in Section 2.3, the large number of fitting variables, the strong correlations between them, and the nonlinear nature of the EXAFS equation can make EXAFS data fitting challenging in many cases, especially when contributions beyond the first coordination shell or very disordered materials are considered. At the same time, while this "inverse" problem is challenging, direct calculations of EXAFS spectra for an arbitrary complicated structure can be carried out easily and quickly by relying on eqs 6 and 8. Therefore, a viable alternative to EXAFS data fitting is to compare experimental spectra with theoretical spectra calculated for a given candidate structure. A good agreement between the experimental and theoretical spectra would then indicate a similarity between the simulated and experimentally probed structures. The recent impressive progress in the accuracy of *ab initio* simulations (e.g., within the DFT formalism) of catalysts structure[167,205,206] makes this approach attractive for the interpretation of EXAFS spectra. Note here, however, that the EXAFS spectra are sensitive to atomic displacements due to thermal motion. Therefore, such thermal vibrations need to be included in the theoretical models used to generate spectra for comparison with experimental measurements. Molecular dynamics (MD)[167,173,181,207−209] simulations or Monte Carlo sampling[210−213] can be used for this purpose. The interatomic forces required for such simulations[167,173] can be calculated either *ab initio* or based on empirical potential models.[181,207−209] A good agreement between time-averaged EXAFS spectra generated for MD structures has been demonstrated for bulk metals and alloys,[25,147,208,214] non-metallic bulk materials,[25,215−218] metal ion solutions in water and ionic liquids,[219−222] as well as for well-defined metal and oxide nanoparticles.[147,174,181,209,223−226]

Nevertheless, even the most sophisticated theoretical modeling approach cannot reproduce perfectly the complexity of the real materials structure, and even a small error in interatomic distances (few picometers) can result in a noticeable discrepancy between the experimental and modeled signals. A significantly better agreement with experimental data can be achieved if the atomic coordinates in the structure model are optimized to ensure an as good as possible match with the experimental measurements. This idea underlies a reverse Monte Carlo method for EXAFS data fitting. Originally employed by McGreevy and Puztai[227,228] for the interpretation of neutron and X-ray scattering data, the RMC is also getting increasingly popular for the interpretation of EXAFS data.[174,229−235] In this approach, atomic coordinates are optimized in an iterative stochastic process. At each iteration, an update to the structure is proposed, for example, small random displacements are applied to all atoms or a selected subset of atoms in the model, and the corresponding theoretical model-averaged EXAFS spectrum is recalculated and compared with the experimental data. If the agreement is
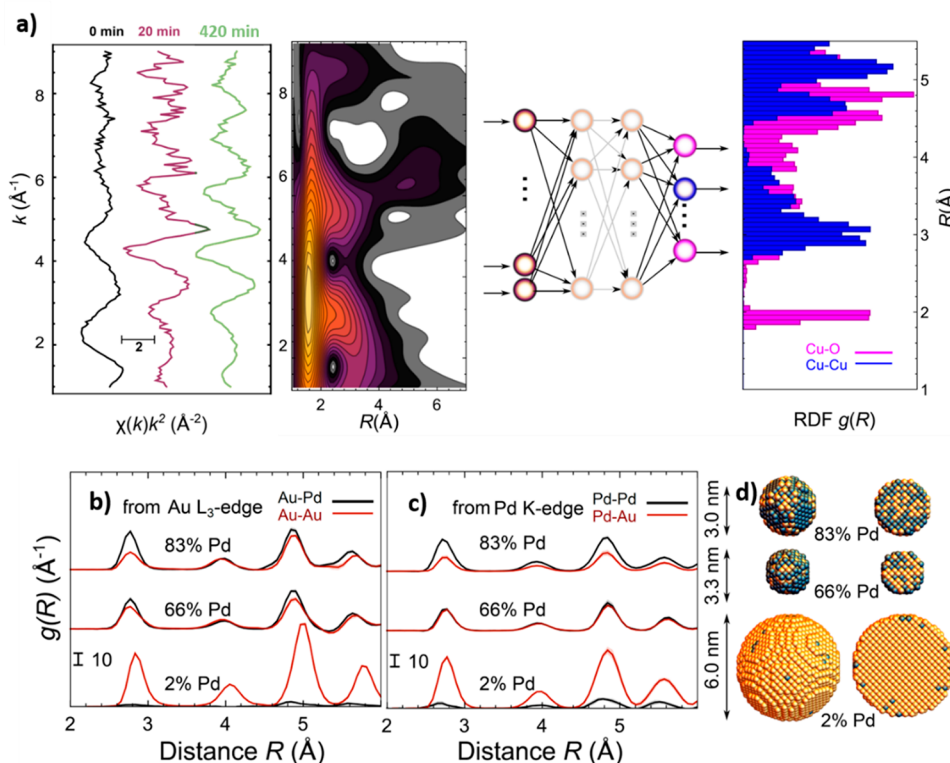
Figure 11. (a) Schematic depiction of the ML-EXAFS analysis method: *in situ* EXAFS data are processed via wavelet transform and fed into a neural network trained on theoretical EXAFS spectra. The NN then yields the corresponding partial RDFs. Data taken from ref 25. (b) Au−Pd and Au−Au and (c) Pd−Pd and Pd−Au partial RDFs, reconstructed by an NN from the corresponding experimental Au L$_3$-edge and Pd K-edge EXAFS data for PdAu NPs with different Pd concentration. The RDFs are integrated to obtain partial coordination numbers for the first four coordination shells, and the latter are used to model possible NP size and the distributions of metals (d). Reproduced with permission from ref 12. Copyright 2019 American Chemical Society.

improved, the proposed update is accepted. If the agreement gets worse, the proposed update can still be accepted with some probability to avoid being trapped in local minima, or else the model is returned to the previous state. After many thousands of such iterations, a good agreement between simulated and experimental data can be obtained, provided that the initial structure model was not too far away from the actual material structure. For bulk materials, a good strategy is to start with the equilibrium structure, known, for example, from XRD measurements. For nanomaterials and other disordered systems, however, the problem of having a relevant initial structure model is more severe and limits significantly the applications of the RMC method for studies of real catalysts. In some cases, a good result can be obtained by starting from ideal polyhedral structure models,[174] or structure models relaxed in MD-simulations.[147] A combination of MD and RMC is realized even more explicitly in the so-called hybrid-RMC approach, where the energy of the system and the discrepancy between experimental and simulated data are minimized simultaneously.[207,236,237]

Despite this limitation and the large computational times (several CPU days) required to process each spectrum, RMC remains a powerful tool for the interpretation of EXAFS spectra in a broad range of materials, by providing the possibility to fit the spectra for materials with non-Gaussian shapes of bond-length distributions,[174,232−234] also accounting for contributions of distant coordination shells,[217,229,230,238] as demonstrated in Figures 1c and 8. The extraction of interatomic distances and other structure parameters of

interest can then be done by performing statistical analysis of atomic coordinates in the final structure model. Unlike in conventional EXAFS data fitting, a key feature of the RMC method is that the obtained structural parameters are physically meaningful. The geometric constraints imposed by the fact that all fitting variables correspond to actual coordinates of atoms in a specific 3D structure model explain why in many cases RMC is able to provide an unambiguous structure model, despite the fact that the total number of fitting variables is much larger than that in the conventional fitting.

Another advantage of the RMC approach is its ability to integrate information from different experimental techniques because simultaneously with EXAFS one can also optimize, for instance, the agreement between simulated and experimental X-ray scattering data.[239] Such a combined approach was recently used by Triana et al. to refine the structure of complex Co-based electrocatalyst for oxidation reactions.[240] Ref 23 presents a recent review of the MD and RMC methods and their applications for studies of nanocatalysts.

4.6. Machine-Learning Based EXAFS Analysis

Because of the requirement to specify the initial structural model, and the large computational resources required to process each spectrum by the RMC method, it is challenging to apply this method to the interpretation of *in situ* and *operando* EXAFS data for catalysts at work. This is due to the fact that the structure of the material can be ill-defined and that one is often interested in processing in a systematic way large sets of data corresponding, for example, to different states of the catalyst at different moments of time or different

experimental conditions. In particular, it is challenging to apply the RMC method in the cases where different species coexist at the same time, that is, when the experimental signal cannot be interpreted in terms of a single structural component. Moreover, EXAFS data collected *in situ* or under *operando* conditions are often of limited quality, which may result in ambiguities of the structural models constructed by RMC.

The recently developed approach that addresses these issues and, similarly as RMC, takes into account the non-Gaussian shapes of bond length distributions and the contributions of distant coordination shells, is a machine-learning based analysis of the EXAFS data. Similarly as in the case of the XANES data analysis discussed in Section 4.4, here the mathematical model (e.g., an artificial neural network) is created and trained to establish the relationship between spectral features and the materials structure. In the case of the EXAFS analysis, much richer information about the materials structure can be extracted as compared to the case of the ML-based XANES analysis approach. In particular, the structure can be directly described with a set of partial RDFs, parametrized as a histogram of bond lengths. The output of each of the nodes of the neural network output layer can then be assigned to a height of the corresponding histogram bin, Figure 11a. Once the RDF is obtained, the corresponding structural parameters can be calculated simply by RDF integration using eq 9 (for coordination numbers) and analogous expressions for the average interatomic distances and disorder factors.[168]

Another important difference between the ML-based XANES and EXAFS data analysis is the construction of training structure models. Since EXAFS is more sensitive to the atomic displacements, and, in particular, to atomic thermal vibrations, such a disorder needs to be included in the theoretical models used for the training of the ML routine. Classical MD simulations with empirical force field models were found to be instrumental for this purpose due to their ability to generate realistic-looking structure models in relatively computationally cheap calculations. Computational efficiency is important because thousands of structure models are needed to reliably fit the complex relationship that links EXAFS features to the corresponding partial RDFs.[214]

Unlike for the RMC method, the only input that is required for the application of the trained ML routine for EXAFS analysis is the experimental EXAFS spectrum itself. Moreover, a very large number of spectra can be processed within seconds, making this approach highly attractive for high-throughput analysis. The issue of coexisting species can also be simply addressed in the ML approach by using for the ML training not just model spectra and RDFs for model compounds but their artificial linear combinations. Moreover, since the ML training is carried out with realistic MD structure models, the ML output is constrained to be some physically reasonable RDF, even for input spectra with limited data quality.

During the last years, the ML-based EXAFS data analysis approach has been proven successful in a wide range of studies such as the interpretation of EXAFS spectra of iron experiencing a temperature-induced phase-transition from the bcc to the fcc structure,[214] studies of composition effects on EXAFS spectra in bimetallic PdAu NPs (Figure 11b−d),[241] the thermal expansion of small Pt NPs,[168] and *operando* investigations of reduction and structural transformations in CuZn nanocatalysts during CO_2 electroreduction.[25] The

readers are referred to ref 12 for more details about the ML-EXAFS method and a review of its recent applications.

5. FROM DESCRIPTORS TO PHYSICAL MODELS OF ELECTROCATALYST STRUCTURE AND COMPOSITION

5.1. Absorber Concentrations

One of the first sample parameters that can be extracted from an XAS experiment is the concentration of the absorbing metal atoms. Indeed, both in transmission and fluorescence experiments, the intensity of the XAS signal before normalization is directly proportional to the number of absorbing atoms in the way of the X-ray beam and thus characterizes both the sample thickness and absorber concentration. This often serves as a convenient tool to quickly optimize the sample to ensure the best signal quality in transmission experiments and to avoid self-absorption effects in fluorescence-mode XAS. At the same time, this information can also be used to *in situ* monitor sample transformations due to metal deposition, dissolution in an electrochemical environment, or evaporation at high temperature. For example, the fluorescence line intensities associated with X-ray absorption at the Cu $L_{2,3}$ edges were recently used by Velasco-Velez et al. to *in situ* monitor the electrochemical deposition of Cu from $CuSO_4$ under −0.5 V (vs Ag/AgCl) applied potential (Figure 12).[75] The ability to
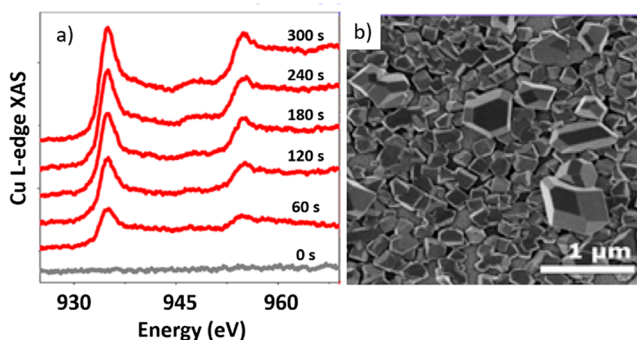
Figure 12. (a) Evolution of the XAS signal at the Cu L_2 and L_3-edges during the electrodeposition of Cu at −0.5 V versus Ag/AgCl in 5 mM $CuSO_4$. (b) SEM image of the deposited Cu electrode. Reproduced with permission from ref 75. Copyright 2019 American Chemical Society.

detect variations in the concentrations of the absorbing species is also critical for studies of heterogeneous samples, and is especially useful when combined with the possibility to scan the position of the X-ray beam. A good illustration of this is the study by Takao et al.,[104] where the spatial distribution of Pt species at the cathode of polymer electrolyte fuel cells was mapped, Figure 4a. The proportionality of the XAS signal to the number of absorbing species is also a useful tool to verify the relative concentrations of different metals in multielement systems such as bimetallic nanocatalysts. For example, Zhang et al. used the ratio of the Pt-L_3 and Au L_3 absorption jumps to estimate the thickness of the gold layer in Au-decorated Pt NPs for ORR.[242] While for atoms that are the neighbors in the Periodic Table (such as Pt and Au), the ratio of the corresponding absorption jumps can be directly linked to the ratio of the metals in the sample, for atoms with absorption edges separated by larger energy differences, one should also

take into account the energy-dependence of the X-ray absorption cross-sections.

5.2. Oxidation State

The oxidation state of the catalytically active species is one of the important parameters that determines the reactivity of a catalyst. It is also one of the parameters that most often changes under reaction conditions. Frequently, information about the oxidation state can be easily extracted from the examination of the absorption edge position since a higher oxidation state is associated with a shift of the absorption edge toward larger energies. For example, a nearly linear relationship between the Co K-edge position and the Co oxidation state has been reported (Figure 6a).[134,135] Using XAS spectra for reference materials with known oxidation state, the relationship between the oxidation state and the edge position can be established and used to find the oxidation state of the new material of interest. It should be however noted that instead of a nominal oxidation state, in some cases the absorption edge position rather characterizes the so-called coordination charge, which accounts for charge redistribution due to chemical bonding.[26,243]

The edge position is a commonly used descriptor for the oxidation state of electrocatalysts. For example, Bergmann et al. used in situ XANES at the Co K-edge to monitor the oxidation state of Co in Co_3O_4 catalysts during OER.[244] In addition, Friebel et al. used the position of the Ni K-edge to follow the changes in the Ni oxidation state under applied potential in Ni−Fe catalyst for electrochemical water splitting,[245] Velasco-Velez used the Cu $L_{2,3}$ edge to in situ monitor the generation of different Cu oxidation states by linear sweep voltammetry,[75] and Zhou et al. used the position of the Cu K-edge to confirm the effect of B-doping on the stabilization of cationic Cu species under CO_2RR conditions.[246]

While following the absorption edge position is a convenient tool for qualitatively tracking the changes in the oxidation state, one needs to be careful when applying this approach for quantitative analysis. As discussed in Section 4.1, the term "absorption edge position" does not have an unambiguous definition, and different authors use different conventions. One needs to pay especial attention when materials with very different structures are analyzed. For example, for nanostructured materials with different particle sizes, minor shifts of the absorption edge can be difficult to interpret because the particle size plays an important role in determining the edge position. In particular, for NPs, the increase in the Fermi level energy and the increase in the electronic screening lead to blue and red shifts of the X-ray absorption edge, respectively.[247]

For some systems, information about the oxidation state can be obtained from the analysis of pre-edge features. Because pre-edge features arise due to transitions to unoccupied localized states, XAS spectra for metals typically do not have them, while they are common for oxidized absorbing atoms, and are also quite sensitive to the oxidation state.[26] For example, Cu K-edge XANES has no pre-edge feature for Cu(I) species due to a completely filled 3d orbital (d^{10} state).[248] For the Cu(II) state, there is a single hole in the 3d orbital, and a pre-edge feature can be observed at ~8980 eV, Figure 1a, affected also by the distortion of the CuO_6 octahedron caused by the Jahn−Teller effect.[249] Similarly, the analysis of the shape and position of pre-edge features in the Fe K-edge is a

powerful tool to discriminate between Fe(II) and Fe(III) species and is used, for example, in environmental science.[26,250]

Independently, information about the materials oxidation state can be obtained also from EXAFS analysis. While EXAFS mostly probes the atomistic structure of the material, the E_0 factor in the EXAFS equation, eq 6, is sensitive to the absorption edge position and, hence, to the oxidation state. The quantitative interpretation of the E_0 from EXAFS data fitting with theoretical standards (e.g., FEFF program[31] and ARTEMIS software[55] that uses FEFF as a built-in code) is complicated by the fact that in the fitting, instead of the actual E_0 value, one refines the difference ΔE_0 between the value of the onset of the absorption edge in the experimental data and the photoelectron reference energy in the theoretical simulations. The numerical ΔE_0 value will thus depend on the beamline calibration, conventions used in EXAFS data alignment and extraction, the structure model used for the FEFF simulations, FEFF code parameters, and version. While the obtained ΔE_0 values themselves are noninformative, their systematic change in a series of similarly processed EXAFS spectra (e.g., time-dependent data for electrocatalysts under reducing/oxidizing conditions) hints toward changes in the sample oxidation state.

Another parameter, extracted from EXAFS data analysis, that can be used to track the changes in the sample oxidation state is the interatomic distance. A contracted bond length is commonly associated with an increased oxidation state.[245] This argument was used to confirm the changes in the Ni oxidation state in Ni−Fe catalysts during the electrochemical water splitting.[245] Gorlin et al.[251] also used Ni−O and Fe−O interatomic distances to determine Fe and Ni oxidation states in similar materials. Different Cu−O distances can also be used to distinguish between Cu_2O and CuO species.[252] In many cases, DFT calculations can be very helpful in establishing the relations between oxidation state and interatomic distances.[245] The use of EXAFS for the determination of the oxidation state can be especially helpful in the case of XAS data collected at high energies, where the XANES spectral features are broad and their interpretation is ambiguous. For example, XANES data analysis at the Sn K-edge may give ambiguous results due to the similarity of the spectra for Sn^0 and Sn^{2+} species, and therefore, the detection of Sn^{2+} species can be problematic. The Sn−O distance for SnO, however, is significantly longer than that in SnO_2 (2.22 vs 2.05 Å), thus allowing one to distinguish between 2+ and 4+ species based on EXAFS data analysis.[253] It is, of course, also always advantageous to contrast XAS findings with results from other techniques, as for example Raman spectroscopy, as illustrated in ref 254.

5.3. Particle Size

5.3.1. Coordination Number Analysis.

The particle size is one of the critical parameters that determine the catalytic properties of nanostructured catalysts. In many reactions, both in the gas phase and in an electrochemical environment, the catalyst particle size has a strong influence on the catalytic activity due to the increased number of undercoordinated sites or changes in the electronic structure in small NPs.[16,255−265]

A common approach for the determination of metal particle sizes from XAS relies on the analysis of the CNs. CNs are usually extracted from EXAFS data fitting but can be obtained also from XANES data interpretation using machine learning methods. For a particle of a given shape, there exists a unique relationship between the particle size and the CN in any

coordination shell of interest C_{nano}.[266] For example, for sufficiently large spherical particles, Calvin et al. proposed[267,268]

$$\frac{C_{nano}}{C_{bulk}} = \left[1 - \frac{3}{4}\left(\frac{R}{R_{nano}}\right) + \frac{1}{16}\left(\frac{R}{R_{nano}}\right)^3 \right] \quad (16)$$

where R_{nano} is the particle radius, C_{bulk} is the coordination number in the corresponding coordination shell in the bulk material, and R is the coordination shell radius. For particles of other shapes, similar relationships can be readily obtained from geometrical considerations.[268] However, it is often more convenient to analyze the relationship between coordination numbers and the particle sizes numerically, by generating simple models of NP clusters with different sizes, and calculating the coordination numbers for different shells explicitly (Figure 13a).[258,269,270] For example, Choi et al.
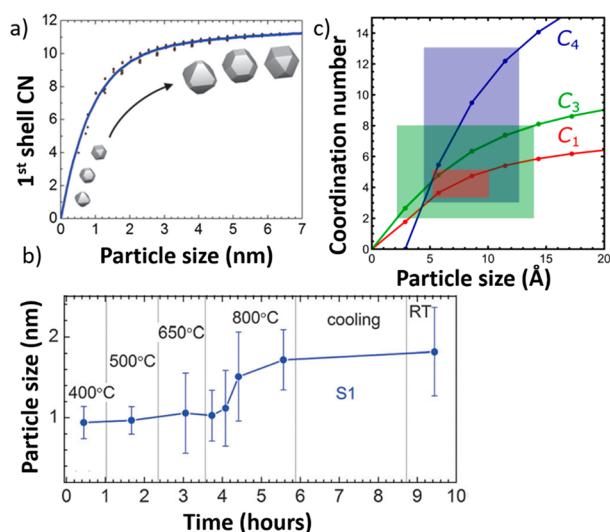

Figure 13. (a) Calculated dependency between the size of Pt clusters and the 1st shell CN. (b) Evolution of the NP size deduced from CNs obtained from EXAFS data fitting during the *in situ* coarsening in H_2 atmosphere of Pt NPs supported on Al_2O_3. Reproduced from ref 258 with permission from the PCCP Owner Societies. (c) Determination of the NP size for Fe NPs using CNs for the first (C_1), third (C_3), and fourth (C_4) coordination shells. Adapted from ref 273 with permission from the PCCP Owner Societies.

used this approach to interpret CNs extracted from EXAFS data to determine the size of Au NPs and found a good agreement with *ex situ* microscopy data. Interestingly, an increase in Au particle size was observed under reaction conditions during the electrochemical oxidation of 2-propanol.[271]

Since the accuracy of the coordination number estimations is rarely better than 5%, eq 16 indicates that coordination numbers for NPs will be undistinguishable from bulk values for R/Rnano ratios around 0.07. This sets the limit to the maximal particle sizes that can still be extracted reliably from XAS analysis. For example, for close packed Pt NPs (distance R between the nearest neighbors being 2.77 Å), size-effects can only be detected via XAS for particles smaller than ~4 nm.

It is important to note that XAS is an ensemble-averaging technique and that for heterogeneous samples with absorbing species coexisting in different environments, caution is needed in the interpretation of XAS data and the CNs extracted. In the

simplest case of a sample where metallic particles of different sizes coexist, the analysis of particle sizes by XAS will yield only an effective mean particle size averaged over all species. Nonetheless, knowledge of such effective particle size and tracking its evolution under reaction conditions can provide important clues about particle segregation/fragmentation trends, as demonstrated by Matos et al., who used the CNs extracted from the fitting of EXAFS data of Pt NPs to follow *in situ* their coarsening under high temperature treatments in different chemical environments (Figure 13b). However, in the samples with broad particle size distributions, the contribution of larger particles to the measured spectrum is effectively larger due to a larger fraction of atoms involved. Thus, the effective particle size obtained from XAS will be slightly larger than the true average particle size. See ref 268 for more details. If additional information about the particle size distribution is available (e.g., from TEM measurements), such information can be included in the interpretation of the coordination numbers; see ref 212. Another important case of heterogeneous samples, especially relevant for *in situ* catalysis studies, includes those with coexisting metallic and oxide phases. The interpretation of CNs here needs to be carried out with especial care, as discussed in Section 5.9.

While for the determination of the particle size in metallic NPs, information from the first coordination shell is, in principle, sufficient, the CNs extracted from further coordination shells can increase the confidence in the structure model. For example, Varnell et al. used CNs for the first four coordination shells, extracted from EXAFS data fitting, to determine the sizes of bcc-type Fe NPs formed in Fe-porphyrin-type catalyst during ORR,[272] while Bock et al. used a similar approach to track the sizes of Fe NPs during the electrochemical delithiation of Fe_3O_4 crystals (Figure 13c). These studies are also good examples where XAS data were used for the interpretation of particle sizes in systems with a structure different from the common fcc structure.

5.3.2. Interatomic Distance Analysis. The accuracy of the NP size determination from the CN analysis is always limited by the quite significant uncertainty of the CN values, especially in the case of the analysis of *in situ* and *operando* XAS data, which typically have lower signal-to-noise ratio. An alternative insight into the particle size can be obtained from the interpretation of interatomic distances. Note that due to surface tension effects, interatomic distances in NP near-surface layers tend to be shorter than those in the bulk material.[162,274] Because of the increasingly large surface-to-volume ratio in small NPs, this results in a reduction of the sample-averaged interatomic distances that can be detected by XAS.[275−277] Hence, accurately estimated interatomic distances can be used to determine particle sizes. Frenkel et al. used this approach for the determination of particle sizes in thiol-stabilized Au NPs from Au L_3-edge EXAFS data and demonstrated a good agreement between the particle sizes, as estimated from the CN analysis, and those obtained from interatomic distance analysis.[278] More recently, a linear relationship between the Au−Au bond contraction and the first shell coordination numbers was confirmed by Behafarid et al. for size-controlled Au NPs encapsulated in PS-P2PVP micelles (Figure 14a).[259] Moreover, the trend obtained based on the XAS data analysis was found to be in agreement with the results of DFT simulations for ligand-free NPs, highlighting the importance of theoretical modeling in the interpretation of the particle size/bond contraction relationship. Finally, it
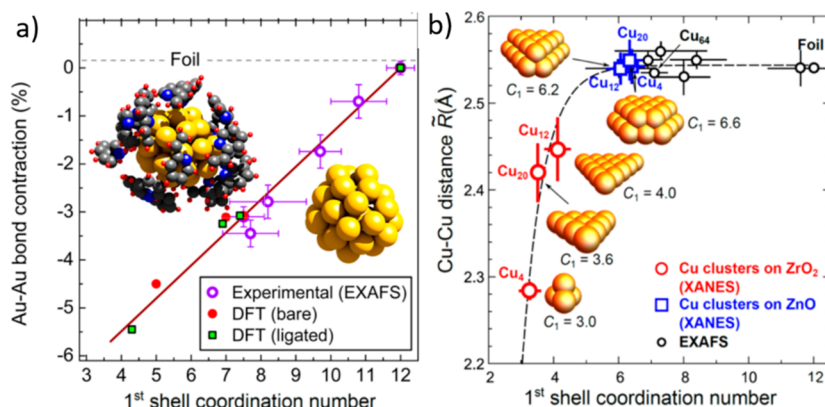
Figure 14. (a) Contraction of the Au−Au bond lengths in size-selected micellar Au NPs encapsulated by PS-P2VP ligands and supported on γ-Al₂O₃ compared to similar model Au NPs with and without the surface ligands as a function of the 1st shell CN. Structure models of NPs with and without ligands are shown in the insets. Reproduced with permission from ref 259. Copyright 2014 American Chemical Society. (b) Relation between the Cu−Cu interatomic distance and the 1st shell coordination numbers in ultrasmall soft-landed Cu clusters deposited on ZrO_2 and ZnO. Reproduced with permission from ref 37. Copyright 2018 American Chemical Society.

should be noted that similarly to the CN analysis, the interatomic distances can only provide insight into NP sizes in the case of very small particles (<2−3 nm) and are most informative for particles of subnanometer size. For example, Timoshenko et al. used interatomic distances extracted by neural networks from Cu K-edge XANES data to confirm the presence of ultrasmall NPs under a reactive atmosphere in samples containing size-selected Cu clusters, in agreement with the findings extracted from the analysis of NN-yielded CNs (Figure 14b).[37] Significant contraction of the interatomic distances was observed for Cu clusters with subnanometer size, while for larger particles, the interatomic distances were found to be close to the bulk value.[37,277]

5.3.3. Nonmetallic Nanoparticles. Previously discussed approaches are applicable to the extraction of particle sizes in metallic NPs only. The sensitivity of the XAS method to particle sizes in the case of oxidized NPs is much less pronounced. Because of the stability of metal−oxygen polyhedral structural units, even in the smallest oxidized NPs the metal atom is usually completely coordinated by oxygen atoms, and therefore, the first coordination shell does not contain any information on the particle size. The interpretation of contributions of more distant coordination shells in oxidized materials is thus necessary to obtain information about the particle sizes. For example, Figure 15a demonstrates that while the first coordination shell (1st peak in the Ni K-edge FT-EXAFS data) in NiO NPs is practically not affected by the particle size, contributions of more distant coordination shells are suppressed for smaller particles.[223] The interpretation of these distant shell contributions in oxide materials is, however, even more challenging than that in metallic systems. The few existing examples of NP size determination in oxidized systems rely on advanced data analysis approaches. The interpretation of size-effects in Ni K-edge XANES data for NiO NPs with sizes 1−4 nm was demonstrated by Anspoks et al. by directly matching to experimental data theoretically simulated EXAFS spectra for NPs of different sizes (Figure 15a,b).[223] To generate theoretical spectra, classical MD simulations were used. In addition to particle size, the other parameter that was varied in this study was the concentration of Ni vacancies. The latter is another factor that needs to be considered in the case of XAS data interpretation of oxide NPs since they may have
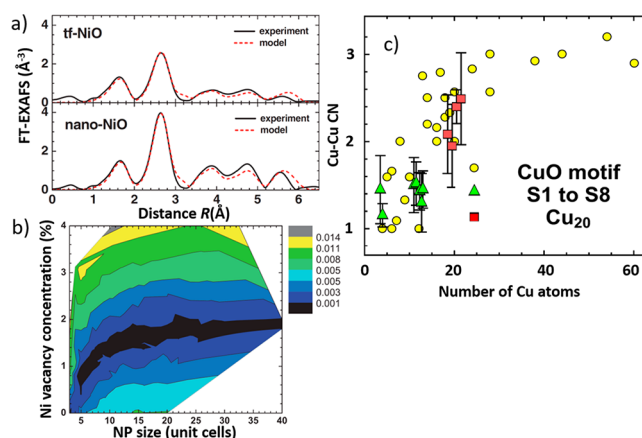
Figure 15. Determination of particle sizes for oxide NPs from XANES: (a, b) analysis of particle sizes in NiO nanostructures. (a) Experimental Fourier transformed Ni K-edge EXAFS data for a NiO thin film (tf) and nanocrystalline NiO are compared with the best matching theoretical EXAFS spectrum from MD simulations. (b) Differences between experimental and simulated EXAFS data for NP models with different sizes and Ni vacancy concentrations. Reproduced with permission from ref 223. Copyright 2012 by the American Physical Society. (c) Cu−Cu CNs yielded by a NN-based analysis of Cu K-edge XANES data are compared with the expected number of atoms in the mass-selected oxidized Cu clusters. Reproduced from ref 199 with the permission of AIP Publishing.

much more defective structures than their metallic analogues. The particle sizes obtained here from MD-EXAFS analysis were in good agreement with those extracted from XRD by the Scherrer's method.[223] One should note, however, that very high quality EXAFS data (with k_{max} up to 18 Å⁻¹) were available in this study, which is not a typical situation in the case of *operando* data analysis for catalysts. For these latter cases, a XANES-based method for particle size determination can be better suited. For example, Liu et al. recently demonstrated that the information on the second shell Cu−Cu coordination number, and hence, the particle size in oxidized Cu NPs can be extracted from neural network-based analysis of Cu K-edge XANES data for subnanometer size-selected Cu NPs (Figure 15c).[199]

5.4. Particle Shape

Catalyst particle shape is another important parameter for understanding not only the catalytic processes[279−281] but also the thermodynamic properties of NPs.[204,261] Differently shaped NPs expose different facets, which can significantly affect the catalyst interactions with adsorbates and reaction intermediates. For example, in studies of CO_2RR over PdH catalysts, Zhu et al. reported significantly higher selectivity toward CO_2 conversion to CO for octahedral NPs (exposing (111) facets) rather than for cubic NPs exposing (100) facets.[282] A change in the NP shape also results in a different number of active low-coordinated sites on the NP surface.[247] On the other hand, different particle shapes can also constitute evidence of different particle−support interactions. For example, the flattened, raft-like shape of Pt NPs on Al_2O_3 and TiO_2 supports can be a signature of strong particle− support interactions.[73,261,280]

Studies on shape-selected model NPs have demonstrated that small NPs with different shapes indeed exhibit different XAS spectra (Figure 16a,b).[184,185,204,261,283] The determination of the average NP shape from XAS data is usually based on coordination number analysis. As mentioned above, the relationships between CNs and particle size are somewhat different for particles of different shapes, giving the possibility
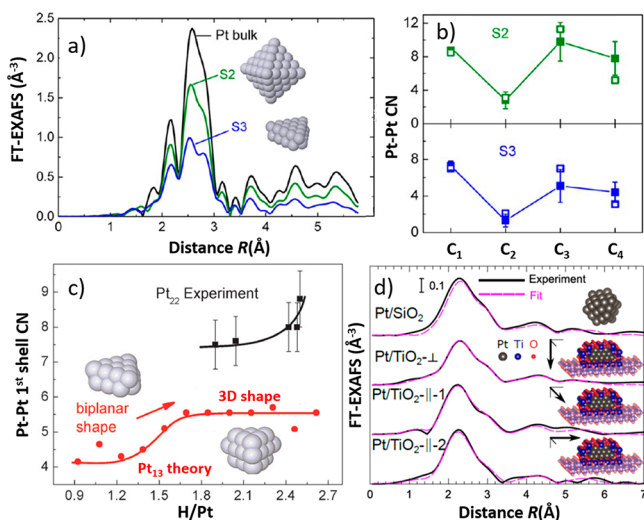
to discriminate between different shapes from the analysis of experimental XAS data, provided that the sample under investigation consists of size- and shape-selected particles. A common approach thus relies on generating a large library of cluster models of particles of different sizes and shapes, calculating for them coordination numbers in the first few coordination shells, and then selecting the model that gives the best agreement with the CNs extracted from experimental data.[204,261,269,283] If TEM data are available, the shape determination should also involve adding the TEM NP diameter as a relevant selection parameter together with the CNs for the first NN shells. Such an approach was used by Roldan et al. to solve the shape of Pt NPs on Al_2O_3.[279,284] It was also followed by Myers et al. for the determination of the shape of Pt electrocatalysts during ORR from in situ Pt L_3-edge EXAFS data.[285]

However, for the reliable determination of particle shapes from XAS data, several conditions need to be fulfilled. Similarly as with the interpretation of particle sizes, the NP geometry will affect significantly the XAS data only for small particles with sizes less than 4−5 nm. In the case of shape determination, this requirement is even more stringent because the number of different shapes that can fit the given set of CNs, within the analysis uncertainty, increases significantly with increasing particle size. Thus, without additional information, particle shapes can be determined only for particles smaller than 1−2 nm. Next, while for the determination of NP sizes information from the first coordination shell is, in principle, sufficient, information from at least a few coordination shells is required to resolve unambiguously the most representative NP shape, which means that high quality EXAFS data are required or advanced data approaches need to be used. Finally, the most critical requirement is the need of narrow particle size and shape distributions. Some of the synthesis methods that fulfill such requirement include colloidal chemistry approaches such as inverse micelle[284] and dendrimer encapsulation[2,286] methods. However, even if the as-prepared samples do have well-defined NP size and shape distributions, this may change under reaction conditions, rendering advanced XAS data analysis inapplicable.[280] Therefore, the extraction of particle shape information from XAS data is typically restricted to as-prepared model systems and a limited number of experimental conditions. In the case of in situ data interpretation, the analysis of NP shapes is usually limited to a simplified argument that a decrease (increase) in the first shell CNs can be an indication of the NPs becoming flatter (more spherical with less NP/support contact).[280,287,288] For example, Grunwaldt et al. used this approach and analysis of apparent coordination numbers from in situ EXAFS to demonstrate reversible changes in the shape of Cu/ZnO catalysts for methanol synthesis under wet and dry syngas conditions, resulting in more spherical and more disk-like NP shapes, correspondingly.[288] At the same time, Mistry et al. used in situ EXAFS to follow the transformation of Pt NPs on γ-Al_2O_3 from flattened (2D) to a more 3D-like shape as a result of an increase in the hydrogen coverage that also leads to a modified (weaker) NP/support interaction (Figure 16c).[287] In the case when different particle models may fit the obtained set of coordination numbers, information from other techniques, for instance, microscopy (e.g., STEM) measurements, becomes instrumental by providing an independent estimate of the NP size and helping to resolve the degeneracy.[73,279,283,284]

Figure 16. (a, b) Particle shape effect for ∼1 nm micellar Pt NPs supported on γ-Al_2O_3. Fourier-transformed Pt L_3-edge EXAFS data are shown in panel a, while panel b shows the CNs extracted for NPs with two different shapes (shown in the inset in panel a) for the first four coordination shells (filled squares) together with the corresponding CNs from NP shape models (open squares). Adapted with permission from ref 280. Copyright 2013 American Chemical Society. (c) Changes in the Pt 1st shell CNs as a function of hydrogen coverage due to a transformation in the NP shape. Results of experimental EXAFS measurements are compared with a theoretical model for a Pt_{22} cluster.[291] Adapted with permission from ref 287. Copyright 2013 WILEY-VCH Verlag GmbH and Co. KGaA, Weinheim. (d) Particle shapes obtained from NN-XANES analysis of polarization-dependent Pt L_3-edge XAS data for Pt NPs on SiO₂/Si(111) and TiO₂(110) supports, and fitting of the corresponding EXAFS data with the RMC method. The results from measurements acquired with three different X-ray polarizations (2 parallel (∥) and one perpendicular (⊥) to the substrate) are shown for the Pt/TiO₂ sample. Reproduced with permission from ref 73. Copyright 2019 American Chemical Society.

Because of the limited possibilities for multiple shell EXAFS analysis in the case of *in situ/operando* data with limited signal-to-noise ratio, an attractive alternative is to use XANES-based methods for NP shape determination. Neural network-based approaches were proven to provide reliable CNs values for the first four coordination shells in model Pt NPs, opening up the possibility to determine particle shapes.[38,73] In refs 289 and 290, Timoshenko et al. demonstrated the suitability of this approach for the analysis of *in situ* XANES data. An example involves the interpretation of Ag K-edge XANES data during the temperature-controlled particle aggregation. In the cases where EXAFS data are also available, particle shapes, constructed based on NN-XANES analysis, can further be validated by RMC-EXAFS simulations.[38,73] A recent example of this combined approach is the study by Ahmadi et al. of Pt NPs on $TiO_2(110)$ in UHV conditions, where the particle shapes were first determined by comparing CNs from NN-XANES analysis and conventional EXAFS data fitting with those for a large library of clusters of different sizes and shapes, and then the obtained structure model was further optimized using EXAFS data and RMC simulations, which refined the positions of the Pt atoms in the NP and Ti and O atoms at the interface between the NPs and the support. An additional feature of this study was that the XAS spectra were collected in ultrahigh vacuum (UHV) with three different X-ray polarizations and analyzed simultaneously. Because of the fact that the contribution to the X-ray absorption spectrum is different for bonds with different orientation with respect to the X-ray polarization, such polarization-dependent measurements provide a direct way to probe the anisotropic NP structure and shape (Figure 16d).[73] However, this approach is meaningful only for studies of oriented samples with narrow size and shape distributions; thus, its applicability to *in situ* and *operando* investigations of realistic catalysts is limited.

5.5. Alloying Motifs in Bimetallic NPs

5.5.1. Alloying Effect in XANES.
The interactions between the constituent metals in bimetallic systems provide many exciting possibilities to tune the catalyst properties. In general, the coexistence of atoms of different types, where each of them may have its own catalytic activity for the particular reaction, results in a plethora of possible effects such as the presence of unique heterometallic sites on the catalyst surface, changes in the lattice constant, increased disorder and heterogeneity, induced stress due to lattice mismatch, charge transfer, and change in the electronic properties.[292–297] For example, for CO_2RR applications, where CO_2 can be converted into a number of different reaction products, alloying Cu with secondary metals such as Zn, Co, Ag, or Au is a common route to control the selectivity of the catalyst.[2,25,111,252,298–307] For the same reaction, segregated Au-core Pd-shell NPs were proposed, where the selectivity for CO_2RR to different hydrocarbons can be tuned by controlling the Pd shell thickness.[2,308,309] At the same time, Au–Pd alloy NPs were found to be active for the production of CO.[310] For PdPt NPs, depending on the order of the deposition of the different metals on the carbon support (i.e., Pt/Pd/C or Pd/Pt/C), enhanced selectivity toward hydrogen or formate production was obtained, respectively.[311] Moreover, the composition, structure, and architecture (e.g., random alloy vs segregated structure) of catalyst often change under working conditions. *Operando* studies are thus indispensable for understanding the catalytic processes in these materials. The XAS method gives

unique capabilities in this case, being an element-specific method, and thus providing the possibility to probe independently the local structure around each of the constituent metals.

The pronounced effect of alloying on XANES spectra can be well seen in Figure 17a and b, where Cu K-edge XANES
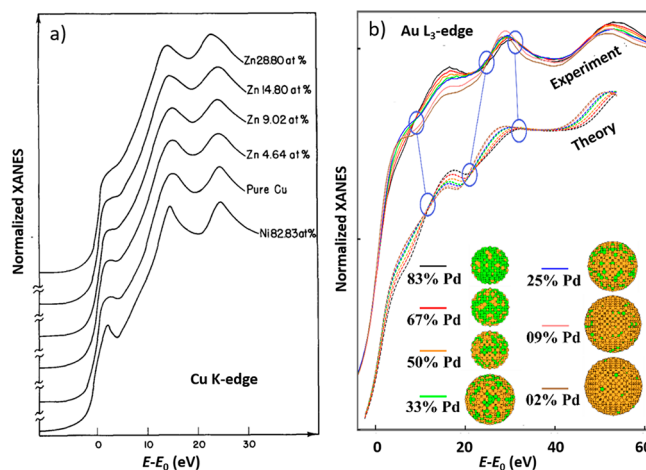
Figure 17. (a) Alloying effect in experimental Cu K-edge XANES data in CuZn and CuNi alloys. Reproduced from ref 312 with permission of AIP Publishing. (b) Alloying effect in experimental and theoretical Au L_3-edge XANES for PdAu alloy NPs with different composition. The corresponding models are shown below. Reproduced from ref 200 with permission from the PCCP Owner Societies.

spectra collected for CuZn and CuNi bulk alloys[312] and Au L_3-edge spectra for AuPd NPs[200] are compared. The observed differences between spectra for alloys with different compositions signify, in part, modifications in the electronic structure.[137,138] In particular, the intensity of pre-edge features at ~0−5 eV in Figure 17a was associated with the number of empty states in the vicinity of Cu, resulting in sharper features in the case of Ni-rich alloys, where Ni has no 4s electrons, and a less pronounced feature in the case of Zn-rich alloys (one extra 4s electron in comparison to metallic Cu).[312] Similar trends in *operando* Cu K-edge XANES spectra were recently observed for nanosized CuZn catalysts during CO_2RR.[25] Note here that because Ni, Cu, and Zn are neighbors in the Periodic Table, and have similar photoelectron scattering properties, it is difficult to distinguish between them using EXAFS-based analysis approaches. Insights from XANES can thus be very helpful to distinguish between Cu-rich and Zn-rich environments. One limitation of the XANES method here, however, is that modeling of alloying effects on the near-edge XAS features is currently challenging, as demonstrated in Figure 17b by comparing the trends in the experimental and simulated Au L_3-edge data in PdAu alloys, hindering applications of XANES for quantitative data analysis.

5.5.2. Partial Coordination Numbers.
A more common approach for the identification of alloying and ordering motifs in heterometallic compounds relies on the interpretation of coordination numbers. For example, for a homogeneous alloy formed by atoms of types A and B, the ratio of CNs for A−B bonds and A−A bonds should be equal to the ratio of the molar fractions of B and A atoms, $\frac{C_{AB}}{C_{AA}} = \frac{x_B}{x_A}$. Deviations from this relationship indicate segregation of the metals: the ratio $\frac{C_{AB}}{C_{AA}}$ being lower than $\frac{x_B}{x_A}$ means that the environment around

the A atoms is, on average, enriched by atoms of type A, and suggests a tendency of the A-type atoms to cluster.[184,313] C_{AB} equal to 0 indicates complete segregation of the metals. To further discriminate between a random alloy structure and an ordered material, one can calculate Cowley's short-range order parameter:

$$\alpha = 1 - \frac{C_{AB}}{x_B C_A} \tag{17}$$

Here $C_A = C_{AB} + C_{AA}$ is the total coordination number of atoms A. For random alloys, α is expected to be 0. Positive α values indicate segregation (clustering), while negative α values indicate ordering. For 3D fcc-type alloys, α can assume values between $-1/3$, for a perfectly ordered Cu_3Au-type alloy, and $+1$ for a completely segregated system.[184,313,314] The linear relationship between all coordination numbers extracted for PdAu NPs of different sizes and compositions, and the fraction of Pd atoms x_{Pd}, observed in ref 241 and shown in Figure 18a, indicates $\alpha = 0$ and a random alloy structure.
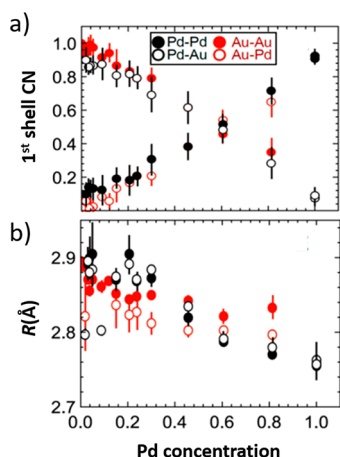

Figure 18. Changes in the 1st shell (a) coordination numbers and (b) interatomic distances in Pd−Pd, Pd−Au, Au−Pd, and Au−Au bonds in PdAu NPs with different Pd concentrations, as extracted from the analysis of Pd K-edge and Au L₃-edge EXAFS data. Reproduced with permission from ref 241. Copyright 2019 American Chemical Society.

In the situation, where significant fraction of atoms of type A is at the surface, one should also expect C_A being smaller than the corresponding value of nearest neighbors in the bulk material (12 in fcc metals). Two possible reasons for that are the high surface-to-volume ratio in small NPs and the segregation of A atoms to the material surface. To distinguish between these scenarios, EXAFS analysis at the absorption edge for the B-type atom, and analysis of the corresponding C_{BA} and C_{BB} coordination numbers are helpful. If C_A is lower than the bulk value, while $C_B = C_{BB} + C_{BA}$ is close to the bulk value, the segregation of A atoms to the particle surface is expected. If both C_A and C_B are smaller than the expected bulk value, this indicates the presence of small NPs. The effective coordination number, useful for the estimation of particle sizes as discussed in Section 5.3.1, can then be calculated as

$$C = x_B C_B + x_A C_A \tag{18}$$

As a side remark, note here that if EXAFS data both for atoms of type A and B are available due to the fact that the total number of A−B and B−A bonds is the same, $x_A C_{AB}$ should be equal to $x_B C_{BA}$, regardless of the material structure and the

segregation trends. This relation can be used as an additional way for the estimation of the ratio of the A and B metals, or, if the latter is known from independent measurements, as a helpful constraint for EXAFS data fitting. Additional obvious constraints that help to reduce the number of unknowns in structure refinement are those for interatomic distances (R) and disorder factors (σ^2): $R_{AB} = R_{BA}$ and $\sigma_{AB}^2 = \sigma_{BA}^2$.[184]

An alternative approach to these analytical considerations is to rely on simulations of the particle structure. Tupy et al. used simple RMC-like methods to fit the coordination numbers extracted from conventional in situ EXAFS data fitting of PtNi catalysts for ethylene glycol reforming. The starting model was a spherical particle with a random distribution of Pt and Ni atoms, which was then iteratively updated by swapping randomly chosen atoms until a good agreement between model-averaged and experimentally obtained coordination numbers was achieved, revealing the segregation of Ni to the particle surface under reaction conditions.[315] A similar approach was recently applied for deciphering the distribution of Pd and Au atoms in PdAu NPs.[241] The advantages of this simulation-based approach are (i) its ability to account for coordination number uncertainties (e.g., misfits between experiment and model can be differently weighted, dependently on the error bar associated with a particular partial coordination number) and (ii) the possibility to include in the analysis the information about coordination numbers in more distant coordination shells. The latter are very challenging to extract for bimetallic systems using conventional approaches but can be obtained from machine-learning based EXAFS analysis. The examples of the PdAu particle models constructed based on NN-EXAFS analysis are shown in Figure 11d.

However, in all the above-mentioned cases, caution needs to be taken if the coexistence of particles of different sizes and compositions cannot be excluded. The sample heterogeneity can result in significant artifacts in the interpretation of the coordination numbers, as demonstrated by Frenkel et al.[313]

5.5.3. Interatomic Distances and Disorder. The discussion in the previous paragraphs was limited to the cases where the metals that form the bimetallic material are substantially different in terms of their atomic number, so that they can be distinguished by EXAFS. In practice, many catalytically relevant alloy systems are formed by metals that are neighbors in the Periodic Table, limiting the amount of information that can be extracted from the CNs analysis. In this situation, to distinguish between different segregation/alloying motifs, one can rely on other structural parameters that can provide indirect insight. For example, due to the difference in sizes of the constituent atoms, the alloying may result in enhanced structural disorder and corresponding Debye−Waller factors. However, especially informative can be the analysis of the interatomic distances. According to Vegard's law, the lattice constant of a bimetallic alloy is expected to be in between those of the constituent pure metals and should change linearly with composition. This provides a possibility to distinguish between well-ordered alloys and segregated systems even for bimetallics consisting of atoms that are neighbors in the Periodic Table. For example, such a reasoning was employed to confirm the alloying of Pt with Au in ultradilute Pt−Au nanoalloys, which exhibited high electrocatalytic activity for the formic acid oxidation.[316] The dependency of Pd−Au, Pd−Pd, Au−Pd, and Au−Au bond lengths in random alloy PdAu NPs on the Pd concentration, as extracted from

advanced analysis of EXAFS data,[241] is shown in Figure 18b. The approximately linear relationship between the bond distance and the Pd concentration follows the Vegard's law. However, a more detailed look reveals some differences between the Au−Au and Pd−Pd bond-lengths, which, according to Vegard's law, should be the same. The observed difference was attributed to the difference in size of the Au and Pd atoms, together with the asymmetry of the interaction potential, which makes it easier to expand the Pd−Pd distance than to compress the Au−Au distance.[241] A similar effect was also observed for CuAu alloys.[314] This is just one example that demonstrates that caution is needed when the Vegard's law is applied to understand the structural motifs in the catalyst because interatomic distances are not only affected by the composition. For example, the surface segregation of atoms of one type may also result in compressed interatomic distances due to a surface tension effect,[162] as observed, for example, for ultradilute PdAu alloys.[241]

Regardless of the origin of the changes in the interatomic distances, in several important cases, the metal−metal bond length itself was established as a convenient descriptor of the catalyst properties. A nearly linear relationship between the contraction of the Pt−Pt bond distance (as extracted from *in situ* EXAFS analysis) and the specific catalytic activity for ORR in a broad range of Pt-based alloys was reported by Kaito et al.[317,318] The relationship between the Cu−Cu distance and the selectivity toward CO_2RR or competing HER in Cu-based alloys was discussed by Bernal et al.[319] For instance, using *operando* EXAFS, a pronounced switch in selectivity was observed for CuZn catalysts during CO_2RR from CH_4 production to CO and H_2. The observed change could be correlated with a change in the material structure and composition, from originally having Cu/ZnO_x to the formation of a CuZn brass alloy under reaction conditions, which led to an increase in the effective Cu-metal distance.[25,111]

5.6. 3D Structural Motifs in Non-Close-Packed Materials

Because of the large number of possible structures, learning about the 3D atomic arrangement and structural motifs in nonmetallic and non-close-packed materials is an even more challenging problem than the determination of the 3D structure of the metallic NPs with fcc-type structure. Information from EXAFS only usually concerns the radial atomic distribution of atoms (i.e., all information is projected onto one dimension) unless analysis can be extended to account for the contributions of distant coordination shells and bonding-angle sensitive MS effects. Thus, while EXAFS can provide enough information to distinguish different metal phases (e.g., fcc vs bcc structures)[214] and metallic from oxidized materials, a more specific identification of the non-close packed materials structure without additional information is challenging. As one successful example, we can mention the study of nanosized tungstates ($CoWO_4$ and $CuWO_4$) that are considered promising catalysts for photocatalytic oxidation of water. As shown in Figure 19a and b, by carrying out RMC-EXAFS optimization of four different candidate structure models, one could conclude that only the models with edge-sharing $Co−O_6$ octahedra can fit the available experimental data.[320] Such modeling, however, requires high-quality data and is not well-suited for the interpretation of *in situ* and *operando* experimental results.

Analysis of the XANES portion of the X-ray absorption spectra, in turn, seems to be more up to this task due its high
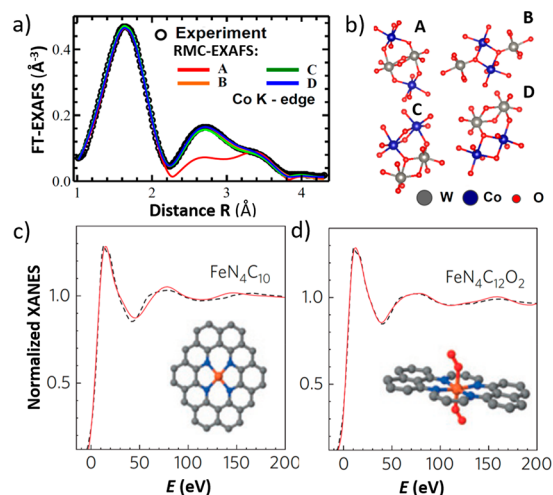
Figure 19. (a) Co K-edge EXAFS data of nanosized $CoWO_4$ and the accompanying fits with the RMC method and (b) four different candidate structure models: only the models with edge-sharing CoO_6 octahedra can fit the contribution of the distant coordination shells. Reproduced with permission from ref 320. Copyright 2015 WILEY−VCH Verlag GmbH and Co. KGaA, Weinheim. (c, d) Fe K-edge XANES data of Fe−N−C catalysts for ORR and fits with two different candidate structure models: additional axial Fe−O bonds are necessary to fit the experimental data. Reprinted by permission from Springer Nature, ref 327 (2015).

sensitivity to the 3D-geometry and symmetry of the environment around the absorbing atoms. As discussed above, pre-edge features in XANES spectra can allow one to easily distinguish between tetrahedrally and octahedrally coordinated structural motifs from K-edge spectra of transition metals.[321,322] For octahedrally coordinated cations (e.g., Cu^{2+} and Ti^{4+}), the intensity of the observed pre-edge is a commonly used descriptor of the distortion of the metal-O_6 octahedron due to the Jahn−Teller effect.[249,323] Analysis of the pre-edge features is also helpful to determine the symmetry around the active metal species in single-site catalysts for ORR and CO_2RR.[20,106,272,324,325] Note that due to different selection rules, different and highly complementary information can be extracted from the analysis of XANES data of the K- and L-edges of transition metals. For example, tetrahedral and octahedral environments have a much stronger effect on the Fe L_3-edge XANES than on the Fe K-edge XANES spectra, as demonstrated in studies of single-site Fe-based catalysts for ORR.[326]

The post-edge region in XANES spectra is equally informative. Zitolo et al. have demonstrated that XANES data fitting of iron- and cobalt-based nitrogen−carbon materials acquired during ORR provides important clues about the coordination of the active site, whereas EXAFS analysis yields ambiguous results.[327,328] In particular, Figures 19c and d show results of the Fe K-edge XANES data fitting for two candidate catalyst structures, and good agreement with experimental data can only be obtained with a model that features 6-coordinated Fe (planar Fe−N_4 motif, with two axially located oxygen atoms).

Even when the overall structure of the catalyst is known, the determination of the occupancies of different nonequivalent sites can still be a challenging and important task because tracking their evolution under reaction conditions can be the key for elucidating the nature of the active species. An

Figure 20. (a) Co K-edge spectra for a series of CoFe$_x$Al$_{2-x}$O$_4$ spinels. Adapted by permission from Springer Nature, ref 329 (2019). (b) Determination of the occupancies of non-equivalent sites avail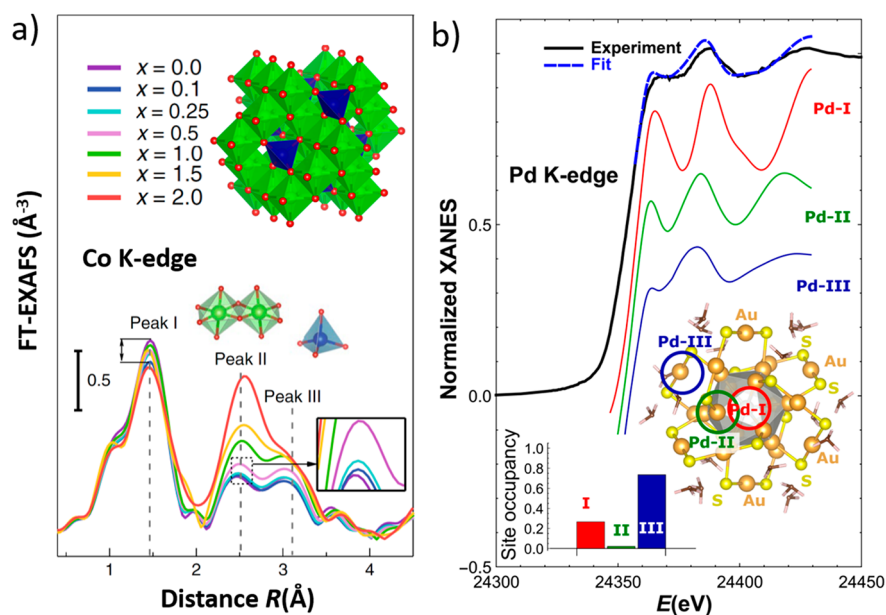able for Pd in ligand-protected PdAu$_{24}$ clusters. The experimental Pd K-edge XANES spectrum is compared with the result of LCA fitting with three ab initio calculated spectra corresponding to non-equivalent sites. The calculated site-specific spectra are shown separately. Corresponding nonequivalent sites Pd–I, Pd–II, and Pd–III, and their occupancies, are shown in the insets. Experimental and simulated data taken from ref 202.

illustrative example in this case includes the materials with Co-based spinel-like structures that currently are actively investigated for applications in OER and ORR.[329−331] In these materials, metal cations coexist in 2+ and 3+ states. Moreover, two crystallographically nonequivalent sites are available, with tetrahedral (Th) and octahedral (Oh) arrangement of oxygen atoms, correspondingly. In the normal spinel structure (such as that of Co$_3$O$_4$), Th sites are occupied by 2+ cations, while Oh sites are occupied by 3+ cations. In the inverse spinel structure, 2+ cations occupy half of the Oh sites, while the other half and all the Th sites are occupied by 3+ cations. In the spinels doped with different transition metals, the occupancies of Th and Oh sites can change. Moreover, the cations can get further oxidized under OER conditions and redistribute between Th and Oh sites. The actual active site for the OER in this material is still a matter of debate, with both octahedrally coordinated 3+ sites[330] and tetrahedrally coordinated 2+ sites[22,332] considered as candidates in the literature. Probing the occupancies of different sites under catalyst working conditions, and their correlation with catalytic activity, is a promising path to address this question. Because XAS is sensitive to both the oxidation state and the atomistic structure of the catalyst, it is a very suitable tool for this task.

The FT-EXAFS spectrum for a spinel-like structure features three distinct peaks (see Figure 20a), where the first broad feature at ∼1.5 Å corresponds to the superposition of all metal−oxygen contributions with different corresponding metal valences and tetrahedral/octahedral coordinations and is thus significantly distorted due to many nonequivalent metal−oxygen bonds contributing to it. The second peak at ∼2.5 Å corresponds to the bond between Oh cations, while the third peak ∼3.1 Å is attributed to the presence of absorbing atoms in a Th environment and is a superposition of contribution of bonds between Th−Oh metal species and Th−Th metal species. By following the changes in the

intensities of these peaks, Wu et al. were able to track the changes in the occupancy by Co of tetrahedral and octahedral sites with increasing the Fe doping in CoFe$_x$Al$_{2-x}$O$_4$ catalysts for OER.[329] The quantitative analysis of these trends is, however, challenging. While the aforementioned single-scattering contributions are dominating, MS contributions and additional metal−oxygen bonds also add to the second and third peaks in the FT-EXAFS, complicating its deciphering. A complex fitting scheme based on some significant simplifications and constraints for this class of materials was developed by Calvin et al.[333] However, caution is needed when such an approach is applied for the interpretation of *in situ* data with limited quality and limited *k*-range. One can envision that advanced data analysis approaches, such as those based on machine-learning methods, will be instrumental to address this challenging problem.

XANES can also be a powerful tool for the speciation of different site occupancies in complex materials. If the XANES spectra corresponding to each particular site are known, the site-occupancies can be found by simple linear combination analysis (LCA), that is, by fitting the experimental spectrum with a linear combination of spectra for different sites and chemical species. The obtained weights of different site-specific spectra will then correspond to site occupancies in the material. The challenge here is to obtain the site-specific reference spectra. It is often impossible to extract them from experimental measurements since well-ordered materials, where only sites of one given type are occupied, rarely exist. It has been demonstrated that the usage of theoretically simulated *ab initio* XANES spectra for different characteristic structural motifs is a viable alternative.[202] In particular, the occupancies of three possible locations of Pd atoms in ligand-protected PdAu$_{24}$ cluster (Figure 20b) can be refined by using linear combinations of *ab initio* calculated[42] site-specific XANES spectra, yielding a good agreement with experimental

Pd K-edge data. Findings from XANES were later corroborated by EXAFS measurements.[334] These molecular systems are considered to be highly promising and stable model catalysts in multiple reactions.[334] In particular, similar clusters were found to be highly active for CO_2RR.[2,335,336]

5.7. Strain, Defects, Disorder

Disorder effects can manifest differently in the XAS data and the extracted structural parameters. For example, a reduction of the average coordination numbers is expected in disordered systems due to a large number of vacancies in the structure. Nevertheless, in XAS analysis, one often considers disorder effects as the variations in the bond-length values, which are captured by the Debye–Waller factor σ^2. Importantly, the value of the XAS σ^2 parameter depends both on thermal $\sigma_{p,thermal}^2$ and static $\sigma_{p,static}^2$ disorders. The former is strongly linked to the dynamic properties of the material, such as correlations in the motion of neighboring atoms and bond strengths,[152,154,238] and characteristic vibrational frequencies commonly described by the correlated Einstein or Debye models (see Section 4.3). The $\sigma_{p,static}^2$ component in turn describes the static deviations from the average interatomic distances due to a structure relaxation at the interfaces or grain boundaries in polycrystalline materials, presence of defects, or increased structure roughness. These parameters can have a pronounced effect on the catalytic properties. For example, an increase in the structural microstrain (suggested by an increase in the EXAFS Debye–Waller factors) under aging treatment was linked to an improved methanol steam reforming activity for Cu/ZnO catalysts.[337] In electrocatalysis, the fabrication of rough surfaces via plasma treatment or dealloying processes is a common route to improve the electrocatalytic activity of polycrystalline materials.[263,338] On the other hand, the strain induced in the structure of multimetallic NPs due to the mismatch of the lattice parameters of the constituent metals provides the possibility to tune their electronic properties. This was for instance linked to the superior activity for ORR observed for NPs with an alloy core of varied composition surrounded by a monolayer of Pt.[339−341] A Volcano-type relation between the strain in Pt within such bimetallic systems and the catalyst activity for ORR was previously shown.[118]

Structural disorder can also change under catalyst working conditions due to interactions with adsorbates. For example, unusually large Debye temperatures, obtained from fitting Debye–Waller factors extracted from EXAFS data, were observed in the presence of hydrogen for Pt NPs with sizes ~1 nm supported on γ-Al_2O_3.[168,203,204,261,342] By comparing results for size- and shape-selected particles of different shapes prepared via a micelle-encapsulation method, a correlation between the surface-to-volume ratio and the Debye temperature was observed (Figure 21a).[204,261] Nevertheless, based on theoretical simulations, these anomalies were in part attributed to a decreasing hydrogen coverage on the NP surface with increasing measurement temperature.[261] Moreover, Small et al. reported larger Debye–Waller factors for γ-Al_2O_3-supported Pt NPs measured under CO atmosphere as compared to NPs measured under H_2 and observed also a dependency of the Debye–Waller factors on the gas partial pressure.[343] In this study, the elastic energy associated with the lattice strain was also estimated as $W = \frac{1}{2}C\kappa\sigma_{static}^2$, where C is the Pt–Pt coordination number, κ is the effective force constant obtained from the temperature-dependency of the Debye–Waller factors (see Section 4.3), and σ_{static}^2 is the static disorder.[344]
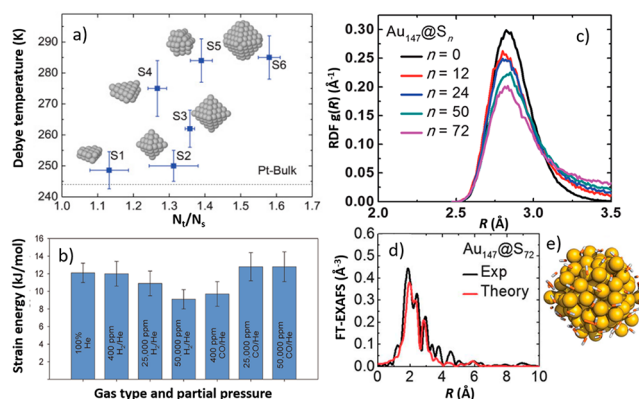
Figure 21. (a) Debye temperature for size- and shape-selected Pt NPs on γ-Al_2O_3 in H_2 environment as a function of the ratio of total number of atoms N_t and number of surface atoms N_s. Reproduced with permission from ref 261. Copyright 2011 American Physical Society. (b) Estimated strain energies for Pt NPs on γ-Al_2O_3 at different partial pressures of H_2 and CO. Reproduced with permission from ref 343. Copyright 2012 American Chemical Society. Ligand-induced disorder in a Au_{147} NP (c, d, e). (c) First shell RDF for an Au_{147} NP with different number of thiol ligands as obtained in ab initio MD simulations. (d) Comparison of Au L_3-edge experimental EXAFS data for Au_{147} NP functionalized with 72 thiols with the theoretical EXAFS data calculated for the corresponding MD model. (e) Snapshot of the MD model. Reproduced from ref 167 with permission from the Royal Society of Chemistry. Permission conveyed through Copyright Clearance Center, Inc.

All of these parameters can be obtained from EXAFS data fitting. While more work is still needed to determine the applicability of this approach, this study provides an interesting example of how EXAFS analysis can provide insight into the thermodynamic characteristics of the material. In particular, the results obtained by Small et al., Figure 21b, suggest significant differences in the strain energies for NPs under different environments that may affect the equilibrium geometry of the NPs as well as their thermodynamic properties.[343]

In addition to particle–adsorbates interactions, particle–support interactions and interactions with ligands can also have a pronounced effect on disorder, especially for small NPs. Anomalies due to particle–support interactions in the temperature-dependencies of the Debye–Waller factor for small supported Pt and PtSn NPs were investigated by Vila et al.[345−347] On the other hand, a systematic increase in the structural disorder of Au NPs with increasing number of ligands was described in the study by Yancey et al., where the results of experimental EXAFS measurements were confirmed also by ab initio MD modeling.[167] Broadening of the Au–Au bond-length distribution in the presence of ligands was observed and reproduced by DFT modeling also by Behafarid et al. As expected, the ligand effect on particle-averaged characteristics was more pronounced for smaller NPs.[259] Note here that the asymmetric shapes of the bond-length distributions, induced by particle-ligand or particle-support interactions observed in the aforementioned studies, were found to pose challenges for the conventional EXAFS data fitting approaches, and it was recently shown that more advanced data analysis methods may be required.[23,167,168,173,174,348]

Static disorder effects due to surface relaxation or interactions with adsorbates or support are most pronounced

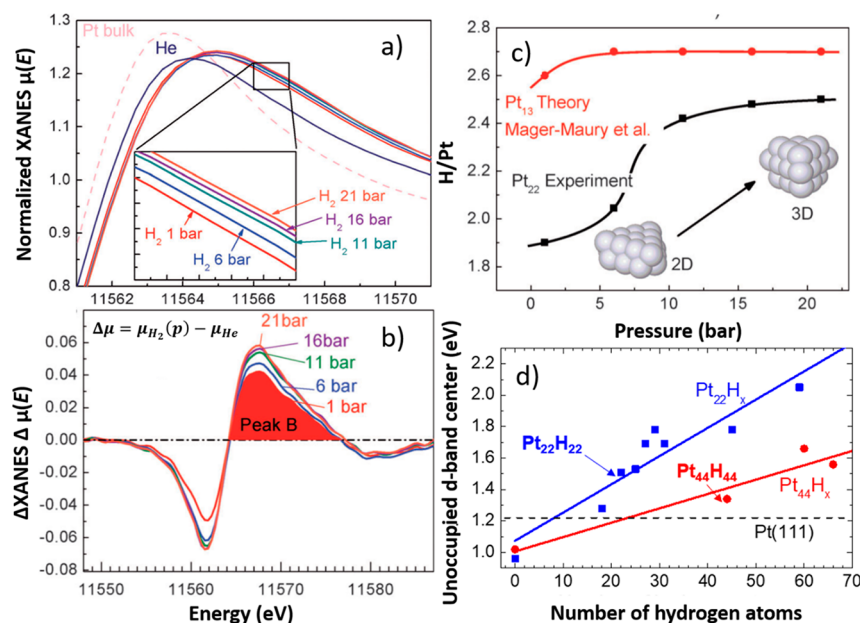**Figure 22.** (a) White line region of Pt L_3-edge XANES data for Al_2O_3-supported Pt_{22} NPs in H_2 atmosphere at pressures from 1 up to 21 bar. Spectra for a Pt foil and Pt NPs in He are also shown for comparison. (b) Difference spectra corresponding to different pressures, calculated by subtracting the spectrum acquired in He atmosphere. (c) H/Pt ratio calculated from the area of peak B in the difference spectra, compared with theoretical H/Pt ratios from ref 291. The proposed Pt_{22} NP model shapes are shown in the inset. Reproduced with permission from ref 287. Copyright 2013 WILEY−VCH Verlag GmbH and Co. KGaA, Weinheim. The shift in the Pt L_3-edge XANES peak shown in panel (a) correlates with the (d) hydrogen-coverage-dependent shift of the center of unoccupied d-band states, as obtained in DFT simulations. Reproduced from ref 357 with permission from the PCCP Owner Societies.

for atoms near the NP surface.[162,163] This limits the applicability of the XAS method for their investigation since the analysis of sample-averaged XAS spectra normally does not allow one to distinguish between the contributions of near-surface atoms and atoms in the NP core. As a result, the disorder at the NP surface (which is most relevant for understanding the catalytic properties) can in fact be much larger than that obtained from XAS data analysis since the latter weighs-in contributions of atoms at the surface but also those in the more ordered core. Nevertheless, in some special cases of very small NPs with well-defined geometry, the contributions of surface atoms can be elucidated, as described by Ericson et al. based on an *operando* study of Pt nanocatalysts during ORR. In such examples, the variations of bond lengths obtained due to surface relaxation effects can be directly compared with those yielded by surface-sensitive techniques.[349] In well-defined Au NPs prepared by a dendrimer encapsulations method, the challenge to discriminate between the disorder in the near-surface layers and that in the NP core was also addressed using the RMC method.[174]

5.8. Catalyst Interactions with the Environment

In situ and *operando* XAS studies are especially important for deciphering the working mechanism of catalysts including extracting in depth information concerning the interactions between the catalyst and its environment (support, ligands, adsorbates). The disorder effects, discussed above, are just one of the ways how these interactions manifest themselves in XAS data. For small metallic NPs, metal−metal bond lengths can also provide important information. For example, the lifting of the disorder in the near-surface layers observed in Pt NPs in the presence of CO or hydrogen adsorbates results in an increase in interatomic distances, detectable by EXAFS analysis. This means that despite the intrinsic surface

contraction, the Pt−Pt bond length in small NPs becomes closer to the bulk value in the presence of H_2.[168,261,287,343]

For small NPs and at large adsorbate coverages, the bond between the catalyst and the adsorbate can be directly observed. For example, the presence of a long Pt−O bond (ca. 2.5 Å) was tentatively associated with the presence of adsorbed 2-propanol on the surfaces of Pt NPs in an *in situ* study of 2-propanol oxidation by Paredis et al.[247] Simultaneously, the presence of a shorter Pt−O bond (ca. 2.0 Å) was attributed to chemisorbed oxygen or the formation of surface oxides.[247] Pt−O bonds are commonly detected also in ORR studies with Pt catalysts, and the difference in the bond length has been used in the past to distinguish between adsorbed oxygen and −OH species, the latter having longer bond lengths of ~2.2 Å.[350] In the *in situ* studies of CO electrooxidation, the formation of the Pt-CO bond was reported, with a corresponding bond length of ~1.9 Å.[351] Thus, by analyzing the differences in the interatomic distances revealed by XAFS, the identity of the adsorbed species can be sometimes revealed, while the comparison of the corresponding CNs can provide some estimate of the adsorbate coverages. Note here that for the determination of the expected interatomic distance for different types of absorbers, *ab initio* simulations of adsorbates within, for example, the DFT formalism or an *ab initio* molecular dynamics approach can be very helpful.[350,352−356]

In the case of strong particle−support interactions, the bonding between the catalyst particle and the corresponding support can also be detected. In fact, Pt−O bonds are often observed in the studies of oxide-supported metallic Pt NPs. For instance, Pt NPs supported on TiO_2 exhibited a significant Pt−O contribution even in the absence of any adsorbates (under UHV conditions), as recently reported by Ahmadi et al.[73] In the latter study, the oriented nature of the sample (Pt

NPs supported on a single crystal) and the fact that polarization-dependent XAS measurements could be implemented allowed the authors to directly probe the anisotropy of particle–support interactions and revealed the encapsulation of the Pt NPs by the TiO_2 support (Figure 16d).[73]

A sensitive tool to probe particle interactions with adsorbates and supports is XANES data analysis and, in particular, the analysis of the shape and intensity of the white line and shifts in the position of the absorption edge. Both are known to respond to the changes in the electronic structure or charge transfer between the catalyst and its environment. In particular, by performing XAS measurements at different temperatures for Al_2O_3-supported Pt NPs with different sizes and shapes in H_2 and He atmospheres, Behafarid et al. associated the blue shift and an increase in the integrated area of the differential Pt L_3-edge XANES spectrum with an increase in the hydrogen coverage.[357] The same approach was used by Mistry et al. to quantify the increase of the hydrogen coverage per surface Pt atom with increasing H_2 pressure, which was found to be in a good agreement with the predictions from theoretical models (Figure 22a–c).[287] Interestingly, the observed shift of the Pt L_3-edge XANES with increasing hydrogen coverage correlates with the shift of the center of the unoccupied d-band states, as obtained in DFT simulations by Behafarid et al. (Figure 22d).[357] The same method was used by Small et al.[343] to monitor temperature- and pressure-dependent CO and H_2 coverages on Pt NPs. During the last decades, the analysis of the shape and intensity of the Pt L-edge has turned to be a crucial tool for monitoring the catalyst interaction with adsorbates and reaction intermediates in *operando* studies of Pt-based catalysts for ORR,[17,141,358,359] as discussed in more detail in Section 6.2.2.

Unfortunately, in practice the effects of different particle interactions with the environment, either adsorbate or the NP support can be hard to distinguish. For example, a similar long Pt–O bond (ca. 2.5 Å), which was previously attributed to the interaction between Pt and adsorbed 2-propanol species, was subsequently assigned to the interaction between Pt NPs and the alumina support.[360] Moreover, the short Pt–O bond with a length of ∼2.0 Å can be attributed either to the presence of chemisorbed oxygen, or the formation of PtO_x oxides. Both of these processes can have also a similar effect on the shape of the XANES features. A similar controversy about the origin of the long metal–oxygen bond was also addressed by Paredis et al. in the study of zirconia-supported Pd catalysts for NO reduction with hydrogen.[361] To better distinguish between these processes, XAS measurements in HERFD mode can be beneficial, as demonstrated by Merte et al.[362]

Highly complementary information about the catalyst interaction with its environment can also be extracted from XAS measurements in the soft X-ray range, that is, addressing the problem from the perspective of the low-Z atoms in the support, ligands, or adsorbates. For example, the analysis of O K-edge XAS was used by Strasser et al. to demonstrate the filling of the O 2p/Pt 5d antibonding state, which signifies a weakening of the adsorption of oxygen species upon an increase of the lattice strain in a Pt–Cu catalyst for ORR.[118] Along the same line, Velasco-Velez et al. used the XAS O K-edge to probe the interactions between a gold electrode and water in the electrolyte.[84]

5.9. Analysis of Samples with Coexisting Species

X-ray absorbing atoms often coexist in the sample in different chemical state or environment. For example, under reaction conditions, the coexistence of reduced and oxidized species is common. In fact, in some cases it has been shown that the coexistence of metal atoms in different oxidation states is beneficial for the catalyst activity, as for example, in the case of Pt-based catalysts for ORR,[22,363] or oxide-derived Cu-based catalysts for CO_2RR.[364−366] The ability of the XAS method to quantify the populations of different species in heterogeneous mixtures is thus essential for studies of catalysts at work. At the same time, the need to disentangle contributions of different species to the sample-averaged XAFS spectrum is one of the most significant challenges for *in situ* and *operando* XAFS studies.

Because of the fact that the measured XAS spectrum is an average of contributions for all absorbing species, for a heterogeneous mixture, the obtained XAS signal $\mu_i(E)$ may be described as a combination of the corresponding spectra for the pure compounds $s_j(E)$, weighted by the concentration of the specific species w_{ij}:[26]

$$\mu_i(E) = \sum_{j}^{N} w_{ij} s_j(E)$$

(19)

If the spectra $s_j(E)$ are known, the concentrations of different species can be obtained via simple linear combination analysis (LCA), where the parameters w_{ij} are optimized to achieve a good match between the experimentally measured spectrum and the linear combination of reference spectra $s_j(E)$. For decades, this has been the most common approach for the analysis of XANES spectra for materials experiencing structural transformations or changes in composition. For example, it is a very common approach to monitor the reduction (oxidation) of catalysts during the activation or under reaction conditions.[111,367−369] By extracting LCA weights for different reference materials w_i, the average oxidation state can be obtained simply as $\sum_i w_i q_i$, where q_i is the charge state of the absorbing species in the reference samples.

Independently, information about fractions of different species can be obtained from EXAFS measurements. While, in principle, eq 19 is valid also for EXAFS spectra, due to the sensitivity of EXAFS to the details of the local structure, the suitable reference EXAFS spectra may be challenging to find and linear combination analysis of EXAFS spectra is problematic. A more flexible approach is to rely on the analysis of coordination numbers. For a two component system consisting of reduced and oxidized phases, where w_O is the concentration of the oxide phase (metal atoms have 0 metallic neighbors in the first coordination shell, but have n_O metal–oxygen bonds), and $w_M = (1 - w_O)$ is the concentration of the metallic phase (the metal atoms have n_M metallic neighbors in the first coordination shell and 0 metal–oxygen bonds), the total number of metal–metal and metal–oxygen bonds in the material with N metal atoms will be $n_{MM} = w_M n_M N$ and $n_{MO} = w_O n_O N$, respectively. Furthermore, the coordination numbers obtained from XAS will be[184]

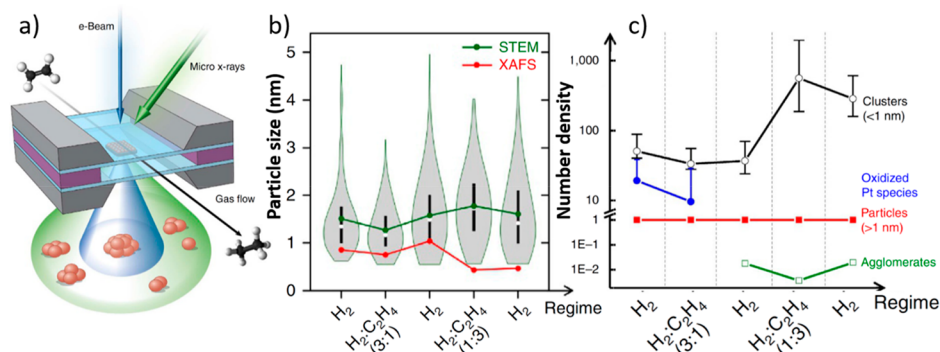$$C_{MM} = \frac{n_{MM}}{N} = w_M n_M$$

(20)

and

Figure 23. (a) Schematic of an experimental cell for multimodal characterization of Pt NPs, (b) particle size distribution and average particle sizes, as obtained from STEM and XAFS, and (c) evolution of the number density of Pt species, as obtained by contrasting the results in panel b. Reproduced from ref 379 under Creative Commons Attribution 4.0 International License: https://creativecommons.org/licenses/by/4.0/.

$$C_{MO} = \frac{n_{MM}}{N} = w_O n_O \qquad (21)$$

Knowing the coordination numbers C_{MM} and C_{MO} from EXAFS analysis, and the number of oxygen and metallic neighbors in the pure phases n_M and n_O, the concentrations of the metallic and oxidized phases can be easily calculated. For instance, a good agreement between the w_i values, extracted from EXAFS and LCA-based XANES analysis, was demonstrated in the recent *operando* study of oxide-derived Cu-based catalyst for CO$_2$RR.[369]

Eq 20 has important implications for the determination of particle sizes from EXAFS data. In the cases where oxidized and metallic phases of a catalyst coexist, the reduced metal–metal coordination numbers (with respect to bulk values) do not necessarily indicate a decrease in the particle size but may be an averaging effect due to the presence of the oxide phase. From eq 20, it follows that the *true* coordination number in the metallic phase, that is, the one that should be used for particle size determination, n_M, is not equal to the apparent CN C_{MM} extracted from XAS analysis but needs to be calculated as C_{MM}/w_M.[184]

LCA-XANES and EXAFS approaches are both limited by the fact that pure phases of the material need to correspond to well-defined bulk-like materials to determine the concentrations of the different species reliably. This implies being able to know in advance the reference spectra $s_j(E)$ or the number of neighbors in the pure phases (n_M and n_O). This is, however, not always the case for catalysts under working conditions, where the active phases are often significantly disordered and undercoordinated. In addition, XANES and EXAFS features can be distorted by self-absorption effects, resulting in systematic errors in LCA-XANES and EXAFS data fitting. In these situations, advanced linear-algebra based approaches such as principal component analysis (PCA),[370−373] multivariate curve resolution with alternating least-squares (MCR-ALS),[374−376] and other blind signal separation (BSS) methods can be more promising.[202,377,378] In all of these methods, instead of an individual spectrum, a series of spectra are analyzed where the weights of different components change, and where the total number of experimental spectra is normally much larger than the number of pure components, allowing one to find the approximations of concentrations and spectra for reference compounds (in BSS and MCR-ALS) or at least the total number of different species (in PCA) present in the sample. Refs 12 and 34 provide recent reviews of PCA, MCR-

ALS, and BSS techniques and examples of their applications in catalysis.

In addition to species in different oxidation state, particles of different sizes and composition can also coexist in the same sample. Without additional information, it is impossible or at least extremely challenging to disentangle the contributions of different species in these cases. However, when additional (even incomplete) information about the distributions of particles sizes is available, for example, from STEM, the fractions of different types of clusters can be identified, as demonstrated in a recent *operando* study of Pt NPs under ethylene hydrogenation conditions[379] (Figure 23), and a study of heterogeneous RhAu NPs synthesized via a microwave-assisted approach.[212]

5.10. Advanced X-ray Spectroscopies and Complementary Techniques

With the advances in synchrotron-based techniques, the set of tools available to researchers for studies of catalysts under working conditions is increasingly expanding. A prominent example includes photon-in/photon-out X-ray spectroscopies, which provide unique possibilities for probing electronic excitations in the material. By measuring the fluorescence spectrum at a fixed incident X-ray radiation energy, X-ray emission spectroscopy (XES) data are collected. In the case where the incident energy exceeds that of the absorption edge, the XES spectrum provides information about the occupied electronic states in the material and yields complementary information to that from XAS (which probes the density of unoccupied states).[118] Such nonresonant XES can be also used as a sensitive probe for the materials oxidation state.[18] For example, Gul et al. used XES to follow *in situ* changes in the oxidation state of Mn and Ni in MnNiO$_x$ catalyst for OER.[110] At the same time, when the energy of the incident radiation is just below the absorption edge, the excitation of the photoelectron is possible at the expense of the energy of the emitted X-ray photon through the so-called resonant inelastic X-ray scattering (RIXS) process. By collecting XES data corresponding to the RIXS transitions, high energy resolution off-resonant spectroscopy (HEROS) probes the density of occupied states and provides information that is equivalent to that in a XAS spectrum. Nevertheless, it proposed an important advantage versus conventional XAS, namely that it can be collected with a much better time-resolution because there is no need to scan the incident energy.[29] For instance, Szlachetko et al. used this approach to monitor changes in the oxidation state of Pt catalysts during CO oxidation with

subsecond time resolution.[380] Moreover, HEROS data do not suffer from self-absorption effects, which, as discussed above, plague XAS data acquisition in total fluorescence mode.[381] Nevertheless, the disadvantage of the HEROS approach is its requirement of a very high photon flux due to the low probability of RIXS processes.

By collecting XES data at different incidence energies, both at resonant and nonresonant conditions, exhaustive information about occupied and unoccupied states and the possible excitations in the material can be collected. For example, detailed information about electronic excitations in the d-band can be obtained. The latter are sensitive to the presence of ligands and the chemical environment around the absorbing atoms, as well as interactions with adsorbates, as demonstrated in recent studies of the interaction of Pt with CO[7,382] and with the CeO_2 support.[383] In the latter case, a significant similarity in the RIXS features for singly dispersed CeO_2-supported Pt catalysts and that of oxidized Pt was demonstrated, suggesting a more localized nature of the 5d states in ultradispersed catalyst than in metallic Pt (Figure 24).[383] At the same time, a
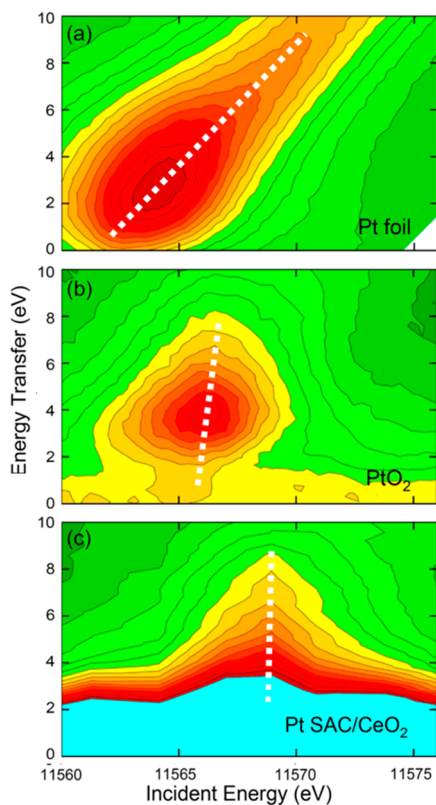

Figure 24. Comparison of RIXS patterns at the Pt L_3-edge in (a) Pt foil, (b) PtO_2, and (c) Pt single atom catalyst (SAC) on CeO_2. Reproduced with permission from ref 383. Copyright 2019 American Chemical Society.

better discrimination between different oxidation states of catalytic species (e.g., Co oxidation state in OER catalysts) can also be achieved through the analysis of the RIXS features.[192,384]

Measurements based on the detection of X-ray fluorescence photons corresponding only to a certain decay transitions (HERFD-XAS) can serve to remove the background contribution from elastic and Compton scattering, which is important for studies of very dilute samples and samples in

strongly scattering environments such as electrocatalysts in an electrolyte.[191,192] The HERFD-XAS approach also allows one to separate the XAS spectra of elements that are neighbors in the Periodic Table (so-called "range-extended" XAS), and thus, the collection of good quality Pt L_3-edge XAS is possible in the presence of Au atoms, while in the conventional XAS analysis the length of the Pt EXAFS spectrum is limited by the onset of the Au L_3-edge. Thus, measurements in HERFD-XAS mode are beneficial for studies of bimetallic catalysts.[385,386] One can also focus on a fluorescence channel with a particularly long lifetime, and thus improve significantly the energy resolution of the XAS method, which normally is limited by the finite lifetime of the created excitation. For example, HERFD-XAS was recently used by Friebel et al. at the Ni K-edge and Fe K-edge to detect changes in the structure and oxidation state of Ni−Fe catalysts under applied potential during the electrochemical water splitting,[245] and at the Cu K-edge HERFD to study the structure of monolayer and multilayer Cu on Au catalysts for CO_2RR.[191] Similarly, Merte et al. used Pt L_3-edge HERFD XAS to distinguish between chemisorbed oxygen species and different Pt oxides (PtO vs PtO_2).[362] Complementary applications of XAS and XES in the field of biological catalysis were recently reviewed by DeBeer et al.[387,388]

X-ray Raman scattering (XRS) is another photon-in/photon-out technique that provides information analogous to that from XAS. Here, the excitation of the core−electron is ensured not by the absorption, but by the nonresonant inelastic scattering of hard X-ray photons. Because of the high penetration depth of hard X-rays, XRS allows studies of materials at absorption edges of light elements (as well as L-edges of 3d transition metals) in strongly attenuating sample environments. The latter method has been shown useful for studies of Li-ion batteries.[389−392]

One of the main limitations of XAS-based methods is the ensemble averaging, that is, the collected signal is averaged over all absorbing species, which may exist in nonequivalent environments. This issue can be addressed by exploiting the anomalous X-ray diffraction phenomenon. In the latter, if the X-ray diffraction pattern is collected with X-rays whose energy is close to the absorption edge energy, the intensities of the XRD peaks are strongly energy-dependent. This observation is useful for element-specific analysis to discriminate between the contributions of different species to the total X-ray diffractogram and can be used for studies of multielement catalysts.[118] The sensitivity to the local structure can be further enhanced by scanning the energy of the incident X-rays. In this case, the intensity of the X-ray diffraction peaks is modulated analogously to the X-ray absorption coefficient. By following the variations in the intensity of an XRD peak that corresponds to a specific crystallographic site, site-specific diffraction anomalous fine structure (DAFS) signals can be collected, which can be then analyzed in the same way as a conventional XAFS spectrum. For instance, this approach allows one to analyze separately the structure of ordered and disordered states of the material,[393] separate contributions of tetrahedrally- and octahedrally-coordinated sites in catalysts with spinel-like structure,[394] or rationalize contributions of different Ni sites in Li−Ni−O batteries.[7,395]

While XRD studies are usually applied for studies of ordered materials, high-energy X-ray diffraction and the analysis of the intensity between the Bragg peaks enable the analysis of disorder and local structure. The so-called pair distribution function (PDF) analysis of X-ray (or neutron) scattering
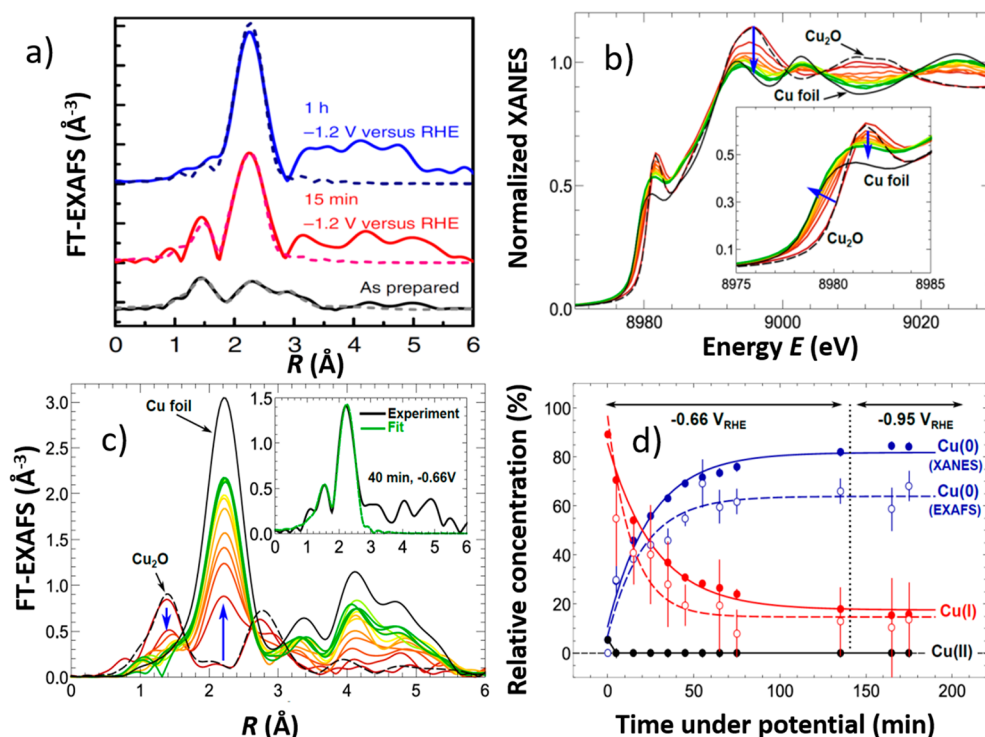
Figure 25. *Operando* Fourier transformed Cu K-edge EXAFS spectra showing the gradual reduction of Cu oxide films grown on a Cu foil via an oxygen-plasma treatment under CO_2RR conditions (in 0.1 M $KHCO_3$ and at −1.2 V vs RHE). Reproduced from ref 364 under Creative Commons Attribution 4.0 International License: https://creativecommons.org/licenses/by/4.0/. Time-resolved Cu K-edge (b) XANES and (c) FT-EXAFS spectra showing the reduction of unsupported Cu_2O nanocubes under CO_2RR conditions (in 0.1 M $KHCO_3$ and at −0.6 V or −0.95 V vs RHE). XANES LCA and EXAFS fits are shown in panel d and demonstrate that even after several hours under a reducing potential, a non-negligible fraction of Cu species remains in Cu(I) state. Reproduced with permission from ref 369.

patterns allows one to extract information about the interatomic distance distributions, analogous to that from EXAFS measurements. While the sensitivity of EXAFS is limited to short-range interactions, PDF analysis of scattering data allows one to probe atomic ordering at much longer length scales.[11,18,396−398] Normally, the X-ray scattering-based PDF analysis lacks the element-sensitivity of EXAFS. This issue, however, can be addressed by scanning the energy of the incident X-rays and employing the anomalous X-ray scattering, as discussed above.[399] Recently, PDF analysis was employed to probe the structure of Co_3O_4 catalysts for OER,[400] to probe rearrangements of the constituent atoms in Pt−Ni catalysts for ORR,[401,402] and distributions of different species in Pt−Ir−Co catalysts for ORR.[403]

6. EXAMPLES

6.1. CO₂ Electrochemical Reduction Reaction

6.1.1. Introduction. The electrochemical reduction of CO_2 (CO_2RR) is an important reaction in alternative energy schemes due to its promise to convert CO_2 into valuable chemicals and fuels under ambient conditions (ambient temperature, pressure and neutral pH).[263] However, it requires breaking the very stable C=O bond and is a complex multielectron process that results in multitude of different reaction products: C_1 products such as CO, CH_4, formic acid, and formaldehyde, and C_{2+} products such as ethane, ethylene, ethanol, n-propanol, etc. Used as fuels, C_{2+} products seem to be more attractive due to their higher value and higher energy densities.[15] The adsorption strength of H and CO, the protonation of CO, and the competing hydrogen evolution

reaction are limiting steps for this reaction.[2,256] Control over catalyst selectivity and stability, together with the need to reduce the high overpotential required (typically −1.0 V vs RHE), is the main challenge to address to make CO_2RR industrially viable. This stimulates the further development and research of suitable catalysts.[263]

When used as catalysts (electrodes), a number of metals convert CO_2 to CO or formic acid, which are the result of a simpler two electron reduction process. Metals like Sn, Cd, Hg, In, and Pb favor the formation of formic acid,[254,256,404−406] while Ag, Au, Zn, Ni, and Pd favor the production of CO.[256,264,338,407,408] However, copper-based catalysts are the only ones that can convert CO_2 to hydrocarbons and C_{2+} products with high efficiency, due, in part, to the optimal binding energy for H, CO, and COOH intermediates that facilitates C−C coupling and the further evolution of the intermediates into more complex products without poisoning the catalyst.[2,16,263,409,410] The poisoning by CO, for example, precludes the application of Pt as a catalyst for CO_2RR.[2]

The CO_2RR is highly sensitive to the catalyst structure and oxidation state, and the transformation or rearrangement of structural motifs at the catalyst surface under working conditions can result in significant changes in the catalytic properties. *In situ* and *operando* characterization tools such as XAS are therefore indispensable for the understanding of the details of the CO_2RR mechanism and the subsequent rational design of novel more efficient catalysts.

6.1.2. Oxidation State and Disorder Effects in CO₂RR. The unique ability of Cu-based catalysts to dimerize two adjacently adsorbed CO intermediates and, thus, convert CO_2 into more complex chemicals puts them into the focus of

CO_2RR investigations. Cu yields a variety of products,[2] with the selectivity often changing depending on subtle structure details. For example, the exploited strategies for the optimization of Cu-based catalyst properties include the synthesis of molecular catalysts/single atom catalysts, taking advantage of nanoscale effects, interparticle distance/loading effects, alloying Cu with other metals, exploiting particle shape (facet) effects, changing the catalyst surface roughness or concentration of defects, tuning particle−support interactions, exploiting electrolyte effects on the catalyst structure and activity, and controlling the electrode oxidation state.[15,16,263,411−413]

The latter aspect, namely, the role of the catalyst oxidation state, was especially debated in the recent literature and exemplifies a case where insight from *in situ* XAS may play a decisive role. While it is generally assumed that the active species for CO_2RR is metallic copper, it was observed that oxide-derived Cu catalysts have different catalytic properties than bulk metallic Cu.[263,414−419] In particular, lower reaction onset potential and higher selectivity toward C_{2+} products were observed on oxide-derived catalysts.[16,418] The reduction of the oxidized copper species to metallic copper under the typical CO_2RR conditions (e.g., −1.0 V vs RHE) is energetically favored, and therefore, the distinct catalytic properties of oxide-derived copper catalysts were explained by changes in the catalyst morphology and defect-rich structure.[16,414−417] However, *in situ* grazing incidence Cu K-edge XAS studies by Mistry et al. on O_2-plasma-treated Cu foils suggested that oxidized copper species can survive under CO_2RR conditions and may influence the formation of ethylene and alcohols.[8,15,16,364] In this study, a significantly enhanced selectivity toward ethylene production, as compared to an electropolished Cu foil, was observed for the plasma-treated sample. XANES and EXAFS spectra analysis of the as-prepared sample confirmed the presence of Cu(I) species and Cu−O bonds, respectively, in the oxygen-plasma treated Cu foils. *Operando* XAS measurements carried under CO_2RR reaction conditions showed that the Cu−O contribution gradually diminished but was still evident at least 15 min after the potential was applied. After 1 h under CO_2RR, the Cu−O contribution could not be discerned (Figure 25a). However, due to the fact that the XAS signal in this case was dominated by the underlying bulk copper after the expected significant reduction of the thickness of the Cu oxide layer under CO_2RR, the presence of oxidized species in the near-surface layers cannot be excluded. The importance of the residual oxidized species was confirmed based on catalytic selectivity studies. In particular, the catalytic performance of the O_2-plasma treated Cu foil was compared to that of an identical Cu foil similarly treated by O_2-plasma but subsequently exposed to a hydrogen plasma to reduce the oxidized species. Although the latter sample had a similarly rough morphology as the nonreduced sample, a drastic decrease in the ethylene selectivity was obtained.[364]

To limit the effect of sample-averaging in the XAS spectra and enhance the contribution of surface species, studies of nanostructured samples, rather than of polycrystalline foils, may be helpful. In the recent study by Möller et al.,[369] unsupported Cu NPs produced via a wet chemical synthesis with cubic shape and sizes ∼35 nm were investigated by *operando* XAS at the Cu K-edge under CO_2RR conditions. Similarly as in the former study,[364] the as-prepared sample was in Cu(I) state according to XANES analysis, see Figure 25b, and with a clear Cu−O contribution evident in the EXAFS

spectrum, see Figure 25c. Under reaction conditions, the contribution of oxidized Cu species also decreased, as evidenced by linear combination analysis of XANES spectra and changes in the Cu−O and Cu−Cu coordination numbers, as extracted by conventional EXAFS data fitting (Figure 25d). However, even after several hours under CO_2RR conditions, complete reduction was not achieved.[369] High selectivity toward ethylene was observed for this catalyst.

Nonetheless, the stability of oxidized Cu species during CO_2RR strongly depends on the nature of the investigated catalyst, its morphology, and support. Grosse et al. used *operando* XAS to monitor the evolution of the oxidation state and structure of 100 nm large Cu cubes electrochemically grown on carbon supports in the presence of chloride that stabilizes their cubic form.[148] As-prepared cubes showed the presence of Cu_2O and $CuCl_x$. However, the chloride contribution disappeared in the EXAFS spectra upon contact with the $KHCO_3$ electrolyte. After 1 h of CO_2RR, however, oxidized copper species were reduced and only metallic Cu was observed both by XANES, as well as by EXAFS analysis, including the wavelet transform analysis to enhance the chemical sensitivity.[148] Here, the changes in the oxidation state were accompanied by significant changes in the catalyst morphology under CO_2RR, namely, the reduction of the nanocube sizes and an increase of their porosity. The large disorder in the final catalyst structure was observed also in the XAS data, where reduced coordination numbers for Cu−Cu bonds were obtained from the fitting of the EXAFS spectra for the metallic catalyst phase. Findings from XAS regarding catalyst oxidation state supported by *quasi in situ* XPS/Auger measurements confirmed the lack of Cu(I) species in the Cu nanocube/C samples. In contrast, in the case where similar Cu cubes were grown on a copper foil (Cu cube/Cu), Cu-Auger data showed the presence of residual Cu(I) species after 1 h reaction. For this sample, enhanced production of C_{2+} products (ethylene) was observed as compared for the Cu cube/C samples, which mainly generated CH_4.[148,420]

Besides cubic-shaped catalysts, electrodeposited dendritic Cu catalysts were also investigated. For Cu dendrites electrodeposited on Ag and Pt foils, Cu(I) species were detected in the as-prepared catalysts via XAS and XPS but were found to be unstable. In fact, almost immediately after the exposure to CO_2RR conditions, linear combination analysis of the XANES spectra and EXAFS data fitting showed the complete reduction of the CuO_x species.[421] The oxidation state of Cu in electrodeposited Cu foams was also investigated in ref 422. First, *ex situ* studies of frozen Cu foams were carried out at 20K, where EXAFS analysis and LCA analysis of the XANES spectra suggested the presence of Cu(I) species. However, further *operando* XAS investigations showed no signs of the oxides and concluded that the Cu(I) species originally detected in cryo-XAS likely were a result of sample reoxidation.[422] This finding emphasizes the importance of *operando* studies in the determination of oxidation state and active species in electrocatalysts.

The evolution of the Cu oxidation state in electrochemically deposited Cu films, the role of the initial state of the electrode, and that of the electrolyte were studied also by Velasco-Velez et al.[75] using Cu $L_{2,3}$ and Cu K-edge XAS. It was shown that a Cu^0 electrode is stable under reaction conditions in $KClO_4$ but may get partially oxidized to Cu(I) in the presence of the CO_2-saturated $KHCO_3$ electrolyte. Electrodes prepared initially in the Cu(I) state got mostly reduced to Cu^0 under CO_2RR
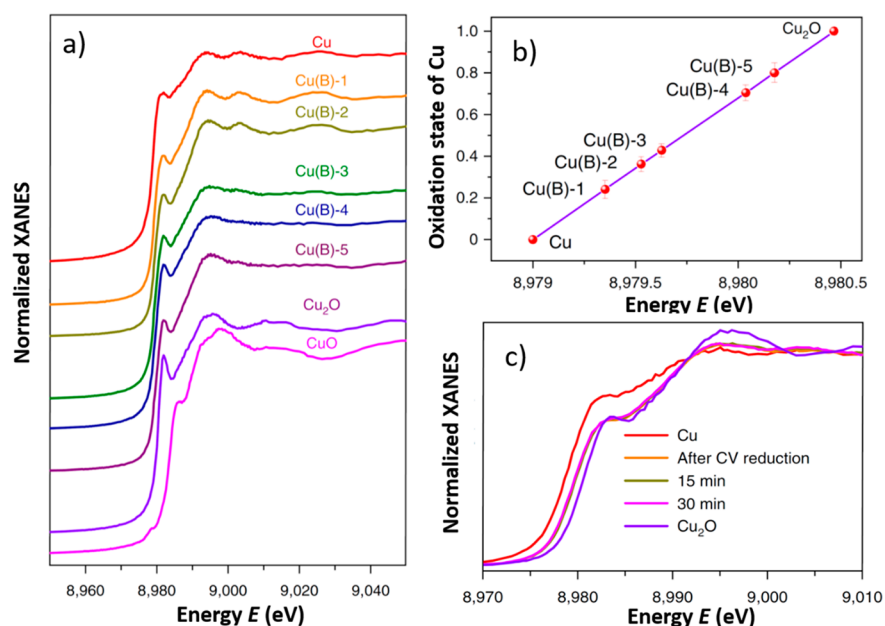
Figure 26. (a) Cu K-edge XANES data for Cu catalysts doped with different amounts of boron. (b) Increase of the Cu oxidation state as monitored by the absorption edge position with increasing boron concentration. Results in panels a and b are shown for catalysts after electrochemical reduction by cycling potential 5 times between −0.5 V to −2 V versus RHE. (c) *In situ* Cu K-edge XANES data collected under CO$_2$RR conditions (in 0.1 M KHCO$_3$ electrolyte at −1.1 V versus RHE) show the lack of further changes in catalyst composition and structure. Reprinted by permission from Springer Nature ref 246 (2018).
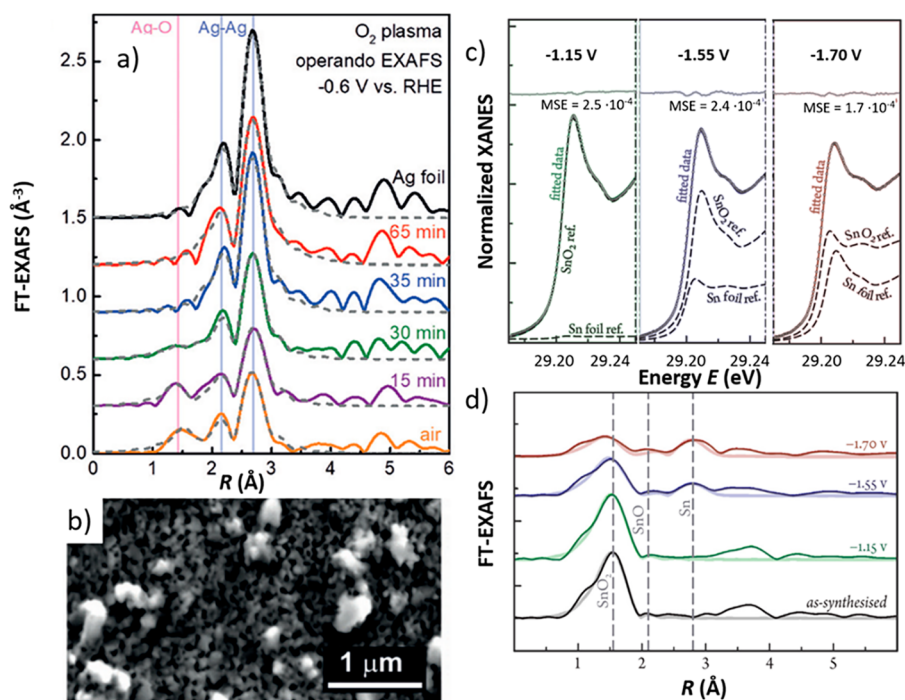
Figure 27. (a) Fourier-transformed Ag K-edge EXAFS spectra for O$_2$ plasma treated Ag foils, collected *operando* under CO$_2$RR conditions. (b) SEM image of an as-prepared O$_2$ plasma-treated Ag foil. Reproduced with permission from ref 338. Copyright 2017 WILEY-VCH Verlag GmbH and Co. KGaA, Weinheim. (c, d) *Operando* XAS at the Sn K-edge for SnO$_2$ nanoparticles on graphene: (c) XANES spectra and their linear combination analysis and (d) evolution of the EXAFS spectra. Reproduced with from ref with permission from Elsevier.[254]

conditions; however, a weak contribution of Cu−O bonds was discernible in Cu K-edge EXAFS. Electrodes that were initially in the Cu(II) state got reduced to Cu(I) and then Cu(0) in KClO$_4$ but formed an inert and stable carbonate layer in KHCO$_3$, as obtained from EXAFS data fitting, making it inactive for catalytic processes.[75]

The presence of specific anions can also affect the stability of Cu(I) species and the catalyst performance. In ref 423, nanostructured Cu catalysts prepared by cycling electropolished Cu foils in the presence of Cl$^-$, Br$^-$, I$^-$, and CO$_3^{2-}$ anions were investigated. While EXAFS analysis of all samples under CO$_2$RR conditions showed a predominantly metallic

structure, the HERFD-XANES method, more sensitive to the oxidation state of the catalyst, showed that Cu(I) species are present in some of the halide-modified catalysts. An especially high concentration of Cu(I) species was observed for the iodine-modified catalyst, where linear combination analysis of the HERFD-XANES data showed that ~15% of Cu remained in the Cu(I) state (ca. 8% as Cu_2O and 7% in CuI state). A positive correlation between the amount of Cu(I) species detected by HERFD-XANES, and the yield of C_{2+} products was observed.[423] In another recent study that focused on the effect of halide ions, Cu_2O microspheres were electroreduced in the presence of iodine, which resulted in porous Cu structures. When exposed to CO_2RR conditions, this catalyst yielded a significantly improved selectivity for C_{2+} products as compared to pristine metallic Cu. Analysis of the *ex situ* EXAFS spectra suggested that the structure of the porous Cu catalyst is predominantly metallic, but the amplitude of the spectral features (Cu−Cu coordination number) was reduced due to strong disorder or the presence of a small fraction of nonreduced species.[424]

The stabilization of cationic Cu species in the presence of boron was demonstrated via *in situ* XAS by Zhou et al.[246] In this study, nanostructured Cu powders with variable amounts of B dopants (1.3−2.2%) were prepared, and *ex situ* investigated by XAS after reduction at applied negative potentials (5 cycles with 0.1 V/s between −0.5 to −2 V_{RHE}), Figure 26a. A correlation between the amount of B introduced and the position of the Cu K-edge was observed, Figure 26b, signaling that the presence of B dopants stabilizes cationic Cu species, with a Cu average oxidation state up to 0.78 being achieved at the highest B concentration. *In situ* XAS measurements confirmed that the enhanced concentration of Cu(I) species was preserved also under CO_2RR conditions (Figure 26c). Importantly, the B-doped catalysts showed exceptionally high Faradaic efficiency toward C_2 hydrocarbon formation (80% FE) and complete suppression of C_1 products formation at the optimal copper valence state of +0.35.[246]

The effect of the catalyst oxidation state for CO_2RR was also investigated for other metal catalysts. For example, in ref 338, the possible role of oxidized silver species was studied. Silver is a popular catalyst for CO_2 conversion to CO. Similarly to Au, Ag binds CO too weekly, thus limiting the further reduction of the intermediate products, and exclusively CO and H_2 are produced.[2] In CO_2RR to CO conversion, Ag is less active than Au but is cheaper and can achieve nearly 100% selectivity.[338] Exceptional activity and selectivity for CO production at low overpotential was observed for Ag foils treated with oxygen plasma (Figure 27a,b).[338] Such samples showed an enhanced surface roughness, Figure 27b, and an oxidized surface. Thus, both the rough and defect-rich structure as well as the oxidized species could explain the enhanced catalytic properties. As mentioned above, XAS is a good tool to distinguish between them. XANES and EXAFS spectra collected at the Ag K-edge in the as-prepared sample confirmed the presence of oxidized silver species. *Operando* XAS measurements, however, showed that the AgO_x species are reduced within 35 min after the onset of the reaction, ruling out the role of AgO_x in the improved reactivity observed for this sample during the first 1−2 h (Figure 27a).[338] Also, the reduction of the AgO_x species could not be responsible for the observed decrease in the selectivity from making CO in favor of making H_2 with increasing reaction time since the AgO_x species were gone well before the change in the selectivity was detected. Decreased

coordination numbers, as obtained from EXAFS, could be linked to the enhanced structure roughness observed in microscopy measurements.[338] The former XAS results were also in agreement with *quasi in situ* XPS data. The latter, being a surface-sensitive technique, showed that oxidized species on the surface are depleted within 3 min under reaction conditions.[338] Importantly, no decrease in catalytic activity or selectivity was observed when the O_2-plasma treated Ag foil was subsequently exposed to a H_2-plasma, contrary to the Cu foil case in ref 364. This confirms that the activity and selectivity trends in the case of Ag are not related to the presence of residual AgO_x species but to the roughness and defects created by the O_2-plasma exposure. A similar enhancement of CO_2 conversion in preoxidized and then reduced Au catalyst was also observed and assigned to disorder effects.[407]

Similarly to Au and Ag, zinc is also selective for CO_2RR to CO[425] but is much cheaper and is thus promising for practical applications.[426] Zn, however, easily oxidizes upon contact with air and the electrolyte. *In situ/operando* studies are thus essential to understand the structure of the catalyst under working conditions. Using *operando* XANES and EXAFS data collected at the Zn K-edge, Rosen et al. showed that electrodeposited Zn dendrites deactivate during CO_2RR at potentials less negative than −0.7 V versus RHE due to oxidation of Zn at these potentials.[8,425] EXAFS data analysis suggested that the structure of oxidized Zn is more disordered than that in bulk references due to the lack of a contribution of distant coordination shells.[425] Remarkably, an order of magnitude higher catalytic activity was observed for this nanostructured sample than for bulk Zn.

Elsewhere, the presence of Zn^{2+} species at the catalyst surface was proposed to be beneficial for CO_2RR to CO.[408] Jeon et al. detected the stability of cationic Zn species during CO_2RR for Zn NPs < 7 nm synthesized via inverse micelle encapsulation.[264] In this case, the Zn K-edge position revealed that the as-prepared particles are completely oxidized. Nevertheless, the XANES and EXAFS features (and hence the materials structure) were different from those in bulk ZnO. Under reaction conditions at −1.1 V versus RHE, these Zn particles were not completely reduced, as suggested by the XANES and EXAFS analysis. In particular, a significant Zn−O contribution was clearly visible in the EXAFS spectra of catalysts under reaction conditions. Cationic species thus may contribute to the observed reactivity.[264] A strong correlation between the particle size and activity was observed, with 6.8 nm NPs exhibiting activity similar to that of bulk Zn and ~70% CO selectivity, and 1.7 nm NPs displaying four-times higher activity but also a large increase in the H_2 production at the expense of CO.[264]

Among the catalysts that convert CO_2 to formate or formic acid, Sn and SnO_x-derived catalysts have been investigated. The oxidation state of Sn seems to be one of the factors that significantly affects the observed catalytic activity.[254,405] In particular, a correlation between the formate production and the thickness of the oxide layer in the as-prepared catalysts was reported by Chen et al.[405] However, the reduction of the tin oxide is also expected under reaction conditions, with Sn^{4+} species undergoing a transformation to Sn^{2+} and then to the Sn^0 state.[254,406] The possibility to monitor the oxidation state of the Sn species under the catalyst actual working conditions, as provided by *operando* XAS, is very helpful. For instance, *in situ* XAS measurements at the Sn K-edge were used to monitor
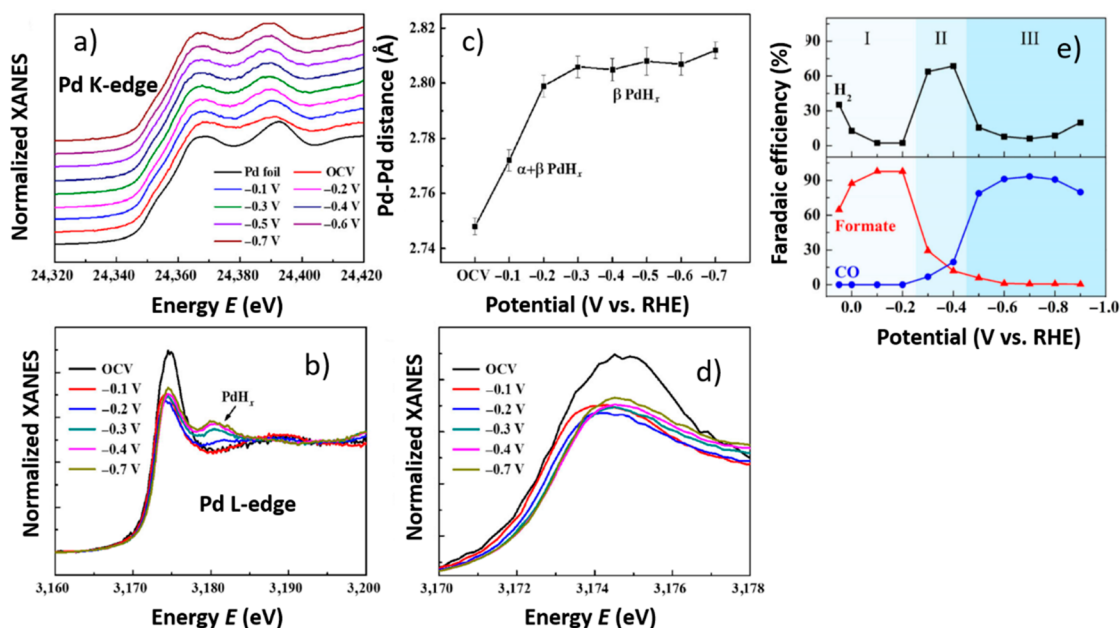
Figure 28. (a) *Operando* Pd K-edge and (b) Pd L_3-edge XANES for Pd NPs under CO_2RR conditions. (c) Changes in the Pd−Pd distance obtained from EXAFS data under applied potential, signaling the formation of Pd hydrides. This conclusion is supported also by prominent changes in the Pd L_3-edge XANES. (d) The white line intensity at the Pd L_3-edge changes nonmonotonically and (e) can be linked to a switch between different reaction regimes with distinct selectivity toward different products. Reproduced by permission from Springer Nature, ref 117 (2017).

changes in the Sn oxidation state of SnO_2 NPs supported on graphene.[254] The potential-dependent shift of the Sn K-edge XAS was observed under reaction conditions and is consistent with a gradual reduction of the Sn species (Figure 27c). Linear combination analysis of the XANES spectra showed the presence of Sn^0 and Sn^{4+} species, with the fraction of Sn^0 increasing for more negative applied potentials. EXAFS data analysis, Figure 27d, showed that the Sn−O coordination number decreased with increasing applied potential. The Sn−O bond length remained the same, ~2.0−2.1 Å, which was also consistent with SnO_2.[254] It is worth mentioning here that Sn^{2+} species were detected in complementary *operando* Raman measurements carried out for this sample. The difference between XAS and Raman results arises from the fact that XAS was probing the bulk phase of a relatively thick catalyst layer, while Raman was more sensitive to the interface between the catalyst and the electrolyte.[254]

As is clear from the examples summarized in this section, the role of oxidized species in CO_2RR selectivity remains controversial and is the topic of active research. Certainly, it is only one of several factors that affect the catalytic performance of CO_2RR catalysts. The survival of oxidized species under reducing CO_2RR conditions seems to depend on many subtle details of the experimental system and precatalyst preparation. *Operando* XAS studies will play a key role in the future to help link the catalyst performance to other parameters such as the catalyst composition, structure, and preparation.

6.1.3. Effect of Hydride Formation in Pd Catalysts for CO_2RR. Among other monometallic catalysts for CO_2RR, Pd-based catalysts attract attention due to the possibility to generate simultaneously CO and H_2 with tunable ratio, which is important to convert CO_2 to valuable syngas.[7,427] The peculiarity of Pd lies in its ability to absorb hydrogen within the Pd crystal lattice and to form different active phases such as

hydrides and carbides at ambient conditions.[117,282] The formation of hydrides changes the catalyst selectivity and can be used to tune the catalyst properties. For example, Sheng et al. correlated the formation of β-hydride, as detected by Pd K-edge XANES and EXAFS analysis, with a decrease in the adsorption energies for CO and H, and the consequent changes in the catalyst selectivity toward the simultaneous production of H_2 and CO under CO_2RR conditions.[7,427]

In general, the main products of the CO_2RR on Pd catalyst are CO and formic acid.[428] A correlation between changes in the catalysts structure and a switch between CO and formate production was observed by XAS for 4 nm Pd NPs.[117] Under applied negative potential, the Pd K-edge XANES features were found to shift toward lower energies, Figure 28a,[117,282,427] while the Pd−Pd interatomic distance extracted from EXAFS data fitting was found to increase from ~2.74 Å to 2.81 Å (Figure 28b). The observed expansion of the Pd lattice and changes in the Pd K-edge XANES features are due to the formation of Pd hydride and can be well reproduced in *ab initio* XAS simulations,[429,430] which can serve as a powerful tool for the quantitative interpretation of experimental data. In this case, the authors were able to estimate the concentration of absorbed hydrogen and observe directly the phase transition between $\alpha+\beta$ and β phases of Pd hydride.[429]

More direct evidence for hydride formation can be obtained from Pd L_3-edge XANES data, where an additional feature appears upon hydride formation due to the Pd−H antibonding states and the corresponding change in the d-density of electron states.[429,431] Changes in Pd L_3-edge XANES for Pd NPs under CO_2RR conditions observed by Gao et al.[117] are shown in Figure 28c. The formation of β phases of hydrides correlates with the switch from formate production at low negative potentials to the production of CO at more negative potentials (Figure 28e).[2] Interestingly, the intensity of the Pd L_3-edge white line changes in a nonmonotonic way, decreasing
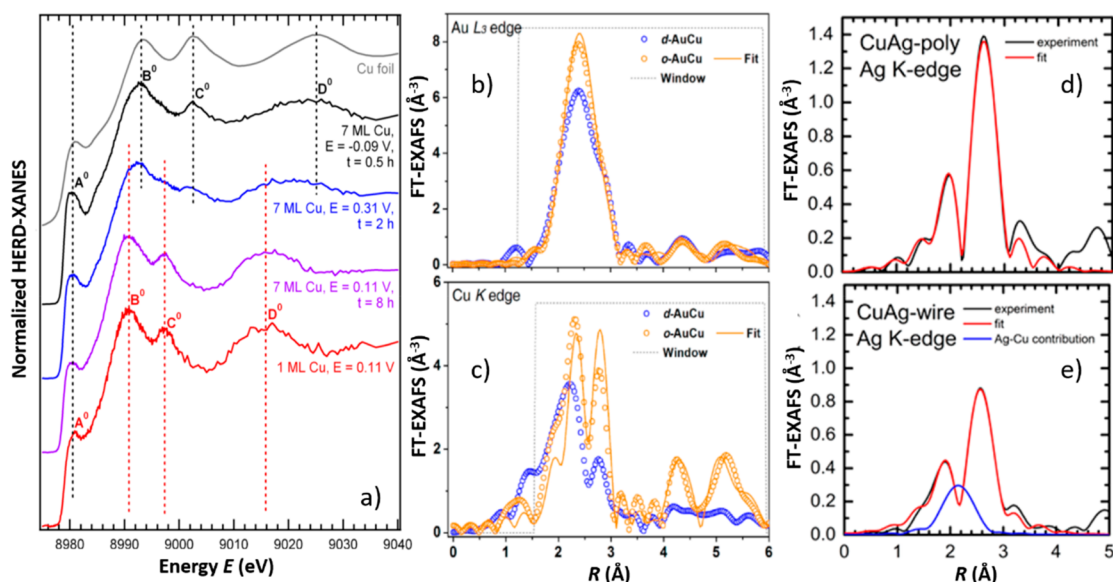
Figure 29. (a) *Operando* HERFD XANES, collected at the Cu K-edge for 1 and 7 monolayers of Cu deposited on an Au substrate. Reproduced with permission from ref 191. Copyright 2014 American Chemical Society. (b, c) *Ex situ* Fourier-transformed EXAFS spectra for disordered (d-AuCu) and ordered (o-AuCu) AuCu NPs, collected at the (b) Au L$_3$-edge and (c) Cu K-edge. Reproduced with permission from ref 306. Copyright 2017 American Chemical Society. (d, e) Fourier-transformed Ag K-edge EXAFS spectra for CuAg catalysts with (d) polycrystalline and (e) wire-like morphology. Results of EXAFS data fitting are also shown, with partial Ag−Cu contribution shown separately. Reproduced with permission from ref 252. Copyright 2018 American Chemical Society.

at potentials between −0.1 and −0.2 V, and increasing again at potentials between −0.2 V and −0.7 V (Figure 28d). This was attributed to different reaction regimes and, hence, different reaction intermediates adsorbed on the NP surface.[117]

As a side note, we would like to mention that the formation of carbides results in a similar expansion of the palladium lattice as the formation of hydrides, and these two effects can be hard to distinguish through the analysis of Pd K-edge EXAFS data, or even by XRD. The differences between these phases can be however detected from XANES data analysis, as demonstrated by Bugaev et al., highlighting the complementarity of EXAFS, XANES, and XRD techniques.[186]

6.1.4. Segregation and Ordering in Bimetallic Cu-Based Catalysts for CO$_2$RR. Alloying of two metals with different properties and interactions with adsorbates provides new ways to tune the catalytic properties through geometric effects, such as changes in the interatomic distances and surface strain, and ligand effects involving changes in the surface electronic structure. However, the bulk and surface structure of the bimetallic catalysts often change under reaction conditions; thus, the presence of the desired bimetallic structural motifs needs to be validated by *in situ* measurements. The element-specificity of XAS makes it well-suited for the investigations of multielement systems and their transformations because it provides the possibility to look independently at the local geometric and electronic structure around each of the constituent metals.

The Cu−Au system is considered a promising catalyst for CO$_2$RR. As mentioned above, pure Cu and Au have quite different catalytic properties in CO$_2$RR, with Cu being able to electrochemically convert CO$_2$ to hydrocarbons at high overpotentials, and Au being able to produce CO at moderate overpotential.[255] Experimental studies suggest that Cu−Au alloys are efficient for CO production. However, even a small addition of Au can lead to the suppression of hydrocarbon formation.[191,432] An increase of the Cu concentration generally

results in the increase of the selectivity toward hydrocarbons, although never exceeding that of pure Cu.[255] A possible explanation for this behavior is the segregation of Au under CO$_2$RR to the catalyst surface.

Ex situ EXAFS studies of as-prepared ligand-free CuAu NPs prepared via inverse micelle encapsulation indicated that Cu is oxidized in the as-prepared NPs, while the gold atoms are nearly completely coordinated by other gold atoms, without any significant Au−Cu interactions.[255] Some evidence of Au−Cu interaction in Cu−Au alloys can be gained from the changes in the shape of the Au L$_3$- and Cu K-edges XANES. Because of the charge transfer from Au to Cu in the alloy, the absorption intensity increases in the alloy at the Au L$_3$-edge, and decreases at the Cu K-edge with respect to that in the corresponding bulk monometallic foils.[26,433,434]

Friebel et al. employed grazing incidence HERFD-XANES measurements at the Cu K-edge to study the segregation trends of Au and Cu under CO$_2$RR conditions in monolayers of Cu deposited on Au.[191] Subtle signal changes due to absorption by a thin layer (1−7 monolayers) of Cu were detected. Depending on the number of Cu layers, the spectra exhibited different shifts with respect to that of a Cu foil (Figure 29a). While in the HERFD-XANES spectrum of a sample with seven layers of copper the positions of all features resembled those for a Cu foil, all features in the spectrum of the sample with 1 monolayer of Cu were shifted to lower energies. By using eq 15 to establish the relation between the shift of the XAS features and the interatomic distances, the observed shift was consistent with the difference in the interatomic distances in copper and gold, suggesting expanded interatomic distances due to the Cu−Au interactions. Interestingly, even the spectrum of the multilayer sample experienced changes with time, and after 8 h under reducing potential, it resembled strongly the spectrum of the monolayer sample. This was interpreted as an evidence that a significant fraction of the Cu atoms diffused into the Au substrate and
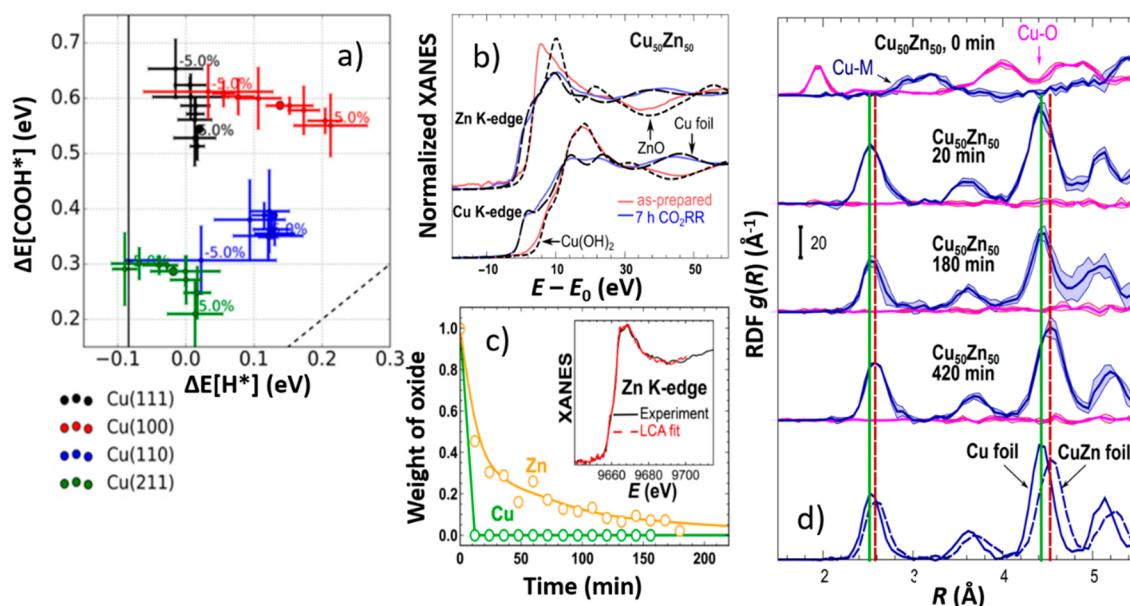
Figure 30. (a) Calculated binding energies of intermediate COOH* and H* on Cu(111), Cu(100), Cu(110), and Cu(211) facets with lattice expansion varied between −5 and +5%. The dashed line corresponds to $\Delta E[\text{COOH*}] = \Delta E[\text{H*}]$, which is a condition favorable for CO_2RR. Reproduced from ref 319 with permission from Elsevier. (b−d) Tracking expansion of interatomic distances in CuZn NPs by *operando* XAS and artificial neural network. (b) Changes in the Zn K-edge and Cu K-edge XANES spectra for $Cu_{50}Zn_{50}$ nanocatalysts under CO_2RR conditions. (c) The results of the linear combination of XANES data analysis. A representative Zn K-edge XANES spectrum and corresponding fit are shown in the inset. Adapted with permission from ref 111. (d) RDFs, extracted from operando Cu K-edge EXAFS data by artificial neural network analysis of Cu50Zn50 NPs and reference materials, showing time-dependent changes in the Cu-M distances. Reproduced with permission from ref 25 published by The Royal Society of Chemistry.

assumed the lattice constant of the surrounding Au matrix. For the same system under oxidizing (positive) potentials, the differences in the oxidation of monolayer versus multilayer systems were observed: at oxidizing potential, Cu in monolayer sample transformed directly to Cu(II), without the Cu(I) state, which was in fact observed for the multilayer system. This observation was confirmed also by cyclic voltammetry and highlights the importance of the Cu−Au interactions.[191]

Regarding the CuAu system, it is also worth mentioning that AuCu random alloys and intermetallics are expected to have different catalytic properties, with the more ordered intermetallic material showing higher selectivity toward CO_2 conversion to CO.[2,306] The possibility to distinguish by EXAFS between random alloys and ordered phases was demonstrated by Kim et al. in a study of AuCu NPs, Figure 29b and c,[306] and can be a useful tool, especially for smaller NPs, where XRD data are not available.

CuAg alloys were also investigated for applications in CO_2RR. Despite the fact that Cu and Ag have minimal miscibility, which results in strong segregation,[2] several reports describe that the addition of Ag may enhance the selectivity of Cu toward C_{2+} products.[252,304,305] For example, in ref 252, electrodeposited Cu and CuAg samples with different morphologies were analyzed. Addition of 3,5-diamino-1,2,4-triazole (DAT) during the electrodeposition changed the morphology of the Cu and CuAg samples from polycrystalline to wire-like. CuAg samples with wire-like morphology exhibited enhanced activity and selectivity for CO_2RR to C_2H_4 and C_2H_5OH with respect to that of polycrystalline CuAg and similarly prepared Cu samples. The difference in the atomistic structures of polycrystalline and wire-like CuAg became apparent after the analysis of *ex situ* Ag K-edge EXAFS data (Figure 29d,e). While for the polycrystalline sample no

Ag−Cu bonding was detected (thus, Cu and Ag were completely segregated in this sample), significant interaction between Ag and Cu and a more homogeneous distribution of these metals were observed for the wire-like sample. The EXAFS fits indicated a Ag−Cu coordination number of ∼2 for this sample, and a contraction of the Ag−Ag distance as a result of Ag alloying with Cu. The observed Ag−Cu alloying in this sample is believed to be responsible for its superior catalytic properties.[252]

For similarly synthesized CuSn catalysts,[435] the addition of Sn resulted in a higher concentration of adsorbed CO and higher selectivity for CO production. Also in this case, the use of the DAT additive resulted in a more nanostructured catalyst morphology, and good mixing of Sn in Cu, as confirmed by Sn K-edge EXAFS data analysis.[435] Enhanced CO selectivity was achieved also for Pd-rich CuPd NPs,[436] where alloying between Cu and Pd was similarly confirmed based on the analysis of Pd−Cu, Pd−Pd, Cu−Pd, and Cu−Cu coordination numbers and interatomic distances.[436]

Overall, the changes of the interatomic distances can have a significant impact on the catalytic activity of bimetallic catalysts. As discussed in ref 319, the expansion of Cu−Cu distances may result in suppressed HER and, hence, higher selectivity for CO_2RR (Figure 30a). From this viewpoint, the segregation of Cu to the surface of smaller alloy NPs, as observed, for example, in ref 319 for CuCo NPs from XPS and *operando* XAS analysis, is not beneficial for CO_2RR, because it often results in contracted, rather than expanded Cu-M distances due to surface tension effects. On the other hand, random mixing of Cu with, for example, Zn, as we discuss in the next example, can be helpful due to the expanded lattice constant in the CuZn brass alloy with respect to that of pure Cu.[307]

Enhanced reactivity of CuZn catalysts for CO_2RR was recently demonstrated.[111,298−303,437] Nanoporous CuZn showed significantly enhanced Faradaic efficiency for CO and formate production,[299] oxide-derived CuZn catalysts were found promising for the formation of C_2 products,[34] while Zn-coated Cu electrodes were shown to have higher selectivity for CH_4.[300] In particular, the higher yield of hydrocarbon products over CuZn catalysts was associated with the spillover of adsorbed CO from Zn to Cu sites.[301,302] However, recent *operando* XAS studies revealed that the dynamics of the Cu and Zn interactions can be significantly more intricate under CO_2RR conditions,[25,111] exemplifying the complexity of structural motifs and their rearrangements in bimetallic catalysts in general. In this study, Jeon et al. focused on size-selected colloidal CuZn NPs with sizes ∼5 nm and different Cu to Zn ratios. Catalytic activity studies showed a pronounced relationship between the catalyst composition and the selectivity of the reaction products, where Zn-rich NPs converted CO_2 mostly to CO, while Cu-rich NPs produced CH_4.[264] However, the selectivity of these catalysts was found to change significantly with time, and the initial CH_4 production was first replaced by CO and last mainly by H_2. Here, XAS data analysis served to clarify that CH_4 was formed when Cu/ZnO was present in the samples, while $CO+H_2$ was obtained once the Cu−Zn alloy was formed. Moreover, the findings in the former study revealed that not only different structural motifs are present in the CuZn NPs with different composition but also that these motifs changed with time as the structure of the catalysts transformed under reaction conditions.[25,111]

Operando XAS measurements carried out at the Cu K- and Zn K-edges showed a surprising difference in the reduction rates of Cu and Zn species under CO_2RR conditions. While both Cu and Zn are completely oxidized in the as-prepared samples and completely metallic in the final state, as evidenced by the similarity of the corresponding Cu K-edge and Zn K-edge XANES data with the spectra of reference oxides and metals, Figure 30b, linear combination analysis showed that the reduction of the Cu species takes place much faster than that of Zn (Figure 30c). Further insight into the transformations of the catalyst structure came from the advanced analysis of EXAFS data carried out with the artificial neural network method, which allows the inversion of the EXAFS spectrum, extracting the entire RDF (Figure 30d). In agreement with XANES data, RDFs extracted by neural network from Cu K-edge EXAFS data demonstrated that Cu was in a metallic state immediately after the potential was applied. However, the structure of this metallic phase continued evolving, as best evidenced by the shift of all RDF peaks toward slightly larger interatomic distances. For the $Cu_{50}Zn_{50}$ NP sample, the observed shift was in agreement with the difference between the interatomic distances in pure bulk Cu, and a bulk CuZn brass alloy. Thus, the shift of the RDF peaks is an evidence of the gradual CuZn alloying. By tracking the Cu−M interatomic distance, one can characterize the degree of alloying. For the $Cu_{50}Zn_{50}$ NPs, the complete transformation from a Cu-like to a brass-like structure was observed. Importantly, the characteristic time of the structural modification (several hours) matched well the time in which the selectivity of the catalyst changes from the production of CH_4 to the production of CO and hydrogen. Time-dependent structural changes and those of the catalyst selectivity were less pronounced for other Cu−Zn compositions. For Cu-rich NPs,

the interatomic distances plateaued at a value in-between those for metallic Cu and CuZn brass. For Zn-rich NPs, the CuZn alloy was formed soon after the potential was applied, without further pronounced changes in the structure. The extracted RDFs for this sample, however, marked deviations from the fcc-type structure characteristic for Cu-rich NPs. The NN-EXAFS results showed that not only the final state of the catalyst but also its transformation dynamics depend on the catalyst composition.

The switch in the catalytic behavior of this system was explained in refs 25 and 111 by the interplay of geometric and electronic effects. The expansion of the interatomic distances was found to result in a more favorable stabilization of the reaction intermediates, leading to the formation of products beyond *CO.[319] Furthermore, changes in the electronic structure due to Cu and Zn alloying resulted in a shift of the d-band center of Cu away from the Fermi level,[438] and a weakening of the *CO binding[111,439,440] during the gradual Cu and Zn reduction and alloying, leading to different catalytic selectivity and stability for Cu-rich and Cu-poor samples. In fact, it was suggested that the Cu-M interatomic distances might constitute a convenient descriptor of the catalyst properties in these bimetallic NPs, with NPs with shorter interatomic distances (similar to that in metallic Cu) favoring the production of CH_4, while NPs with longer Cu—M distances favor the production of CO.

6.1.5. Transition Metal- and Nitrogen-Doped Carbon Materials for CO_2 Conversion. In the past few years, transition metal- and nitrogen-doped carbon (TMNC) catalysts have attracted significant attention as promising catalysts for CO_2 conversion to CO. These catalysts, typically synthesized via pyrolysis of metal, nitrogen, and carbon precursors, are currently considered promising alternatives to the more expensive Au and Ag catalysts for CO production.[441−444] In TMNC catalysts, the nitrogen atom is incorporated into the carbon and forms a binding site for metal species. These singly dispersed metal sites are commonly considered to be the active species for CO_2RR.[441] However, the large number of different structural motifs that can coexist in TMNC materials (e.g., pyrollic and pyridinic nitrogen environments, coexistence of singly dispersed metal species with metal clusters, metal carbides, oxides and nitrides) complicates severely both the unambiguous identification of the main catalytic species and their structural characterization using sample-averaging spectroscopic methods.[441]

The catalytic activity and selectivity of TMNC materials is in a large part determined by the chosen transition metal, although other factors, such as the microstructure of carbon, also can play a role.[441] Ni-based TMCN catalysts show the highest selectivity toward CO_2 conversion into CO but are efficient only at high overpotentials. Therefore, Fe-based catalysts are often considered as the most promising catalysts in this class of materials, by ensuring the high selectivity to CO production at low overpotentials, and also due to their ability to convert CO_2 to small amounts of CH_4.[441,443] Significantly lower selectivity toward CO production is usually reported for highly dispersed Co and Cu-based TMCN materials, which exhibit high HER reactivity, although examples of highly active Co-based TMNCs and related single-site materials were also reported.[441,445,446] Regarding Cu-based (and, similarly, Zn-based) materials, the main issue seems to be the low stability of the metal−nitrogen structural motifs, which results in the formation of metallic clusters.[441,447,448] For example, surprising
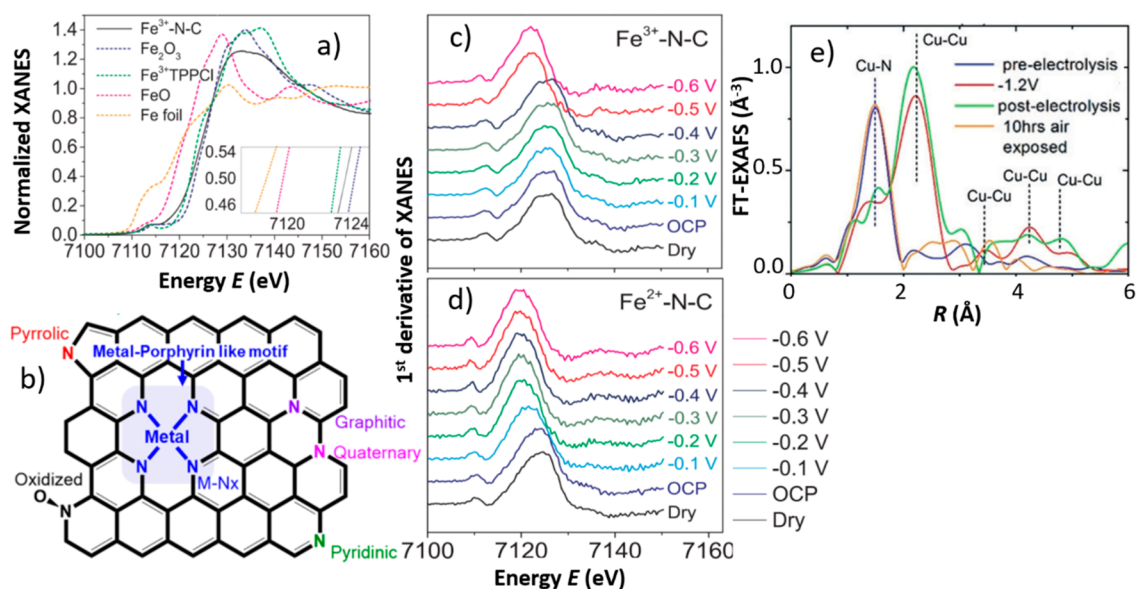
Figure 31. (a) Comparison of Fe K-edge XANES for pyrrolic Fe-based TMNC (Fe^{3+}−N−C) with those from references materials. (b) Different N-containing structural motifs available as metal anchoring sites. Derivatives of *operando* Fe K-edge XANES spectra for (c) pyrrolic Fe-based TMNC (Fe^{3+}−N−C) and for (d) pyridinic Fe-based TMNC (Fe^{2+}−N−C). Panels a, c, and d are from ref 455. Reprinted with permission from AAAS. Panel b was reproduced with permission from ref 441. Copyright 2019 American Chemical Society. (e) Fourier-transformed *operando* Cu K-edge EXAFS spectra showing reversible formation of Cu clusters in Cu-based TMCN. Reproduced with permission from ref 448. Copyright 2019 Wiley-VCH Verlag GmbH and Co. KGaA, Weinheim.

selectivity toward ethanol formation was observed for Cu-based TMNC catalysts. However, further investigations attributed it to the significant transformation of the catalyst under CO_2RR conditions leading to Cu cluster formation.[448] Selectivity toward formate production is observed with Sn-based TMNC materials.[449]

The sensitivity of the XAS method to the local environment around the metal atoms of interest makes it ideally suited for probing the structure of TMNC materials.[20,327,328] For example, the presence of the $M-N_4$ structural moiety in the active catalyst, which can be detected through the analysis of M-N coordination numbers from EXAFS, is commonly considered as an important indicator to which high CO_2RR activity is assigned.[441] Such motifs have been detected in Ni-based TMNC materials,[120,121,123,324,450,451] in Fe-based TMNC catalysts,[106,452−455] in Co-based TMNC materials,[452,454,456] in Cu-based TMNC materials,[324,448,457,458] in Zn-based materials,[459,460] and in Sn-based catalysts.[449] The presence of a pronounced metal−metal signal in the EXAFS spectra, in turn, has been interpreted as an evidence for the formation of metal clusters, which is usually associated with a diminished catalyst selectivity toward CO production.[122,453,461−463] The transformation of Ni NPs in carbon nanotubes back to singly dispersed Ni sites active for CO_2RR has been reported by Fan et al.[464] At the same time, Chen et al. reported the synergetic role of Fe−N_4 motifs and Fe clusters detected by EXAFS, in promoting CO_2RR.[465]

Moreover, coordinatively unsaturated Ni−N_x, Co−N_x, and Cu−N_x structural motifs with EXAFS M-N coordination numbers less than 4 have been found especially active and selective for CO_2 conversion to CO.[456,458,459,464,466−468] In particular, in the case of Co-based TMNC catalysts, Wang et al. demonstrated that the Co−N coordination number can be controlled by changing the pyrolysis temperature, where the decomposition of Co−N bonds in Co molecular precursors at elevated temperatures resulted in reduced Co−N coordination

numbers and enhanced CO selectivity. The Co−N coordination number can be increased back to 4 under treatment in a NH_3 atmosphere, resulting also in a suppressed CO selectivity.[456] Similar relation between the synthesis temperature, EXAFS M-N coordination numbers, and CO selectivity in Cu-based TMNCs was reported by Zheng et al.[458] Koshy et al., however, interpreted the increase of the CO selectivity in Ni-based TMNCs with increasing pyrolysis temperature by the encapsulation of Ni clusters with graphite. These clusters that may coexist with Ni−N_4 structural motifs in the materials, catalyze the competing HER reaction; thus, the restriction of electrolyte access to them improves the overall selectivity of the catalyst toward CO production.[123]

One should note here that the interpretation of EXAFS spectra in TMNC materials may be far for trivial due to the heterogeneity of their structure and coexistence of different structural motifs with different bond lengths, whose contribution to the EXAFS spectra cannot be easily separated. One approach that improves the chemical sensitivity of the EXAFS analysis is the wavelet transformation. WT was used by Zhang et al.[462] and Wen et al.[463] to better distinguish between metallic and nonmetallic contributions. However, even in this case, caution is needed in the assignment of different features to particular structural motifs. For example, M-O, M-N, and M-C contributions cannot be easily distinguished by EXAFS data analysis due to the similarity of the photoelectron scattering properties for atoms that are neighbors in the Periodic Table; thus, the contribution of oxidic species could be hard to distinguish from that of M−N−C motifs. Similarly, the commonly used argument that the lack of a M-M contribution in the Fourier-transformed EXAFS spectra signifies the lack of metallic clusters in the sample should be used with caution, because the presence of such structural motifs may be masked by the strong disorder or destructive interference of different contributions to the total EXAFS signal.

Further evidence for the presence of M-N$_x$ motifs might come from XANES data analysis (Figure 31a). The absorption edge in these materials is typically shifted to higher energies with respect to that in metallic reference materials, in agreement with the higher oxidation state of the metal in the TMNC catalysts.[120,122,123,324,449−452,454,455,457−459,462−469] A characteristic pre-edge feature in the K-edge XAS due to 1s-4p$_z$ transition can be used as a fingerprint of the broken square-planar M-N$_4$ configuration with D$_{4h}$ symmetry in a porphyrin-like structure.[449,453,467,469] For samples with M-N$_4$ motifs coexisting with metal clusters, linear combination analysis of the XANES spectra can be used to quantify the concentrations of the respective phases and link them with the trends in catalytic properties.[453]

Important additional clues about the nature of the active sites and metal−nitrogen interactions in TMNC materials come from the analysis of soft X-ray absorption data. For example, N K-edge XAS features exhibit characteristic fingerprints of pyridinic or pyrollic bonding motifs and shift to higher energies upon immobilization on transition metal cations.[120−123] The shapes of the transition metal L$_3$-edge XANES features can also be used to discriminate between planar and nonplanar structural motifs of the metal centers.[121,452,455,470]

Nonetheless, it appears that the single-site nature of the TMCN catalysts prevents them from forming more complex reaction products. A possible path to resolve this issue could be preparing catalyst with two metal sites next to each other.[441,454] Catalysts with diatomic metal nitrogen sites (Ni/Fe−N−C) were synthesized by Ren et al.[469] Unlike the case of the Ni−N−C and Fe−N−C samples, a pronounced peak in the Fourier-transformed EXAFS data attributed to metal−metal bonds was observed in the bimetallic sample, which was interpreted as a signature of the neighboring metal sites.[469]

The *ex situ* measurements discussed above are insufficient to address the issue of the structure of the active catalyst and to elucidate the nature of the active sites. Because of the expected structural and chemical transformations under reaction conditions, *in situ* and *operando* studies are necessary. Using *in situ* XAS, Leonard et al. demonstrated that the oxidation state of Fe in Fe-based TMNC is predominantly 3+, but under reaction conditions, a reduction of the Fe species was observed through the shift in the edge position. Moreover, while for the as-prepared samples the EXAFS analysis suggested that the Fe−N$_4$ structure motif fits well the experimental data, under reaction conditions the reduction of the Fe−N coordination number was observed. The changes in the catalyst structure coincided with an increase in the selectivity toward methane production.[106]

Interestingly, the structural changes in the oxidation state and local structure of Fe under reaction conditions seem to depend on the N-containing structural motifs in the Fe-anchoring site in Fe-based TMCNS, Figure 31b, as shown by a recent *operando* XAFS study by Gu et al.[455] In this study, two catalysts were prepared, one with pyrrolic-type nitrogen dopants, another with pyridinic-type nitrogen dopants. The N-containing structural motif was controlled by choosing the Fe precursor either with pyrrolic or with pyridinic ligands. It was found from *operando* XANES analysis at the Fe K-edge that under CO$_2$RR conditions with potentials as negative as −0.4 V versus RHE, the oxidation state of iron in the catalyst with pyrrolic-type motifs remained close to the initial value (ca.

3+) (Figure 31c). In the catalyst with pyridinic-type motifs, in turn, the Fe oxidation state was reduced when the potential was applied and was closer to 2+ (Figure 31d). In catalysts with pyrolic structural motifs, the reduction of the Fe^{3+} species was achieved only at potentials of −0.5 V versus RHE and more negative. Similarly as in the study by Leonard et al. described above, the reduction of Fe species was accompanied by the decrease of the Fe−N coordination number.[455] The stability of the Fe^{3+} species, as ensured by the pyrrolic structural motifs, was linked to the superior efficiency of this catalyst for CO production observed at potentials between −0.2 and −0.5 V versus RHE.

In contrast to Fe-based TMNCs, *in situ* XAS studies of Ni-based TMNCs show much less pronounced changes in the metal environment under reaction conditions. No changes in the Ni K-edge XAS were observed by Jiang et al.,[122] and only a minor change was reported by Wen et al.[463] In the latter case, a small shift of the Ni K-edge XAS to higher energies was observed in the electrolyte under open circuit potential, which was reversed under applied negative potential. No changes in the Ni K-edge EXAFS features were detected at potentials higher than −0.9 V versus RHE. A slight increase in the main FT-EXAFS feature amplitude and small shift toward larger interatomic distances (by ca. 0.03 Å) were observed at more negative potentials, which were interpreted as a signature of CO$_2$ activation, adsorption at a Ni site, and distortion of the Ni−N$_4$ motif due to Ni 3d electron redistribution.[463]

An instructive example of the importance of *operando* methods in studies of TMNCs is the recent study by Karapinar et al.[448] of Cu-based catalysts. While in general the Cu−N$_4$ motif in Cu-based TMNCs materials is not considered active for CO$_2$RR, the former study reported a surprising selectivity of this catalyst for CO$_2$ conversion to ethanol. *Ex situ* EXAFS data analysis for the as-prepared sample, as well as for the sample after reaction confirmed the presence of the Cu−N$_4$ moiety, and the lack of Cu clusters. However, when *operando* XAS measurements were performed, EXAFS data collected under applied potential showed the clear formation of Cu clusters and the disappearance of the Cu−N$_4$ species (Figure 31e). The latter, thus, cannot be responsible for the ethanol production. The observed catalytic activity hence should be attributed to the *in situ* formed Cu clusters, with sizes of at least 4 nm, as determined from EXAFS-yielded coordination number analysis. Intriguingly, the collected data suggested that after reaction and exposure to air, the Cu clusters could be dissolved, and the Cu−N$_4$-like motif returned to be the dominant Cu-containing species in the material.[448] While the reversibility of the Cu cluster formation certainly requires additional investigations, a similar process was previously observed by Weng et al. in the study of Cu(II)phthalocyanine-based catalysts under CO$_2$RR conditions.[447] Here the catalysts demonstrated selectivity toward CH$_4$. On the basis of *operando* XAS data, it was established that the actual active species were the 2 nm Cu nanoclusters formed under reaction conditions and disappearing after the potential was removed.[7,447] These intriguing examples clearly indicate the importance of *operando* studies for the identification of active species in TMNC materials and working electrocatalysts in general.

One can also note that other noncarbon-based single-atom catalysts have also been proposed for CO$_2$RR applications. For example, Sun et al. reported on singly dispersed Ir-based catalyst on a α-Co(OH)$_2$ support showing high selectivity toward CO production. In this case, the analysis of *operando*

XANES data confirmed the predominantly oxidized state of the Ir species and its stability under reaction conditions. The high dispersion of the Ir species was confirmed by EXAFS data analysis.[471]

6.2. Oxygen Reduction Reaction

6.2.1. Introduction. Fuel cells transform the chemical energy stored in hydrogen or organic fuels into electrical energy and have been widely explored as an alternative to internal combustion engines. They are thus considered to be a key transformative technology in the transportation sector. Operation of a fuel cell involves two electrochemical processes: oxidation of hydrogen (or other fuels) at the anode, and the oxygen reduction reaction that takes place at the cathode. Currently, platinum is commonly used as a catalyst for both of these processes. However, while the oxidation reaction at the anode occurs relatively easily and at low overpotentials, the ORR at the cathode is much more sluggish and requires higher overpotentials and much higher loadings of the expensive platinum catalyst.[2,472] The ORR step is currently the limiting factor for the widespread practical applications of fuel cells. It is therefore not surprising that major efforts in the advancement of fuel cell technology have been focused on the improvement of the ORR catalysts.

ORR can follow one of the two possible pathways. In the 2-electron (2e) process (partial reduction), hydrogen peroxide is formed as the reaction product. In the 4e process (full reduction), water is formed as the final product. Because of a higher efficiency of the 4e process, and due to the high reactivity of the peroxide formed in the 2e process, the 4e process is more attractive for practical applications.[2,472] The 4e process is facilitated by Pt and Pt-alloy catalysts, while the 2e process takes place, for instance, on Hg, Au, graphite, and different oxide-based materials.[263] For both processes, the first step is the adsorption of oxygen on the catalyst surface. The catalyst activity is thus determined by the balance between the binding energies of the adsorbed oxygen species, reaction intermediates, and products: oxygen species should be adsorbed tightly enough so that the reaction can occur. At the same time, a too strong interaction between the catalyst and intermediates will result in catalyst poisoning.[472] This principle is visualized in the famous "volcano" plots introduced by Norskov and others, which show that the near-optimal binding properties, and hence, maximal ORR activity is expected for Pt and Pt-based materials.[472,473] The sensitivity of *in situ* XAS to the presence of adsorbates, bond-lengths and bond-strengths between catalyst and adsorbate has been widely used to rationalize the structure−property relationship in the materials for ORR.[141] Strategies like the control of the particle size, control of the exposed facets, alloying of Pt with another metal to introduce lattice strain or to tune the catalyst electronic structure have been proposed for improving the adsorbate binding at Pt-based catalysts, and XAS has been very instrumental for understanding the effect of these parameters on the catalytic activity.[17,263] At the same time, due to the high costs of platinum, significant efforts have been invested in the development of nonprecious metal catalysts for ORR, including transition metal−nitrogen doped carbon materials. The sensitivity of XAS to the complex structural motifs encountered in these materials and their *in situ* transformations has been also widely exploited.[20]

6.2.2. Adsorbates and Oxidation in Pt Catalysts. Pioneered by O'Grady et al. in the 1980s, the application of *operando* XAS for the understanding of Pt catalysts for ORR has a long history.[358,359] Starting from these early works, the analysis of the shape and intensity of Pt L_3- and L_2-edge white lines was in the focus, providing important clues about the Pt oxidation state, adsorbates, and the d-band occupancy. Indeed, since the L_3 and L_2-edge WLs correspond to the excitations of the electrons from the $2p_{3/2}$ and $2p_{1/2}$-shells to partially vacant 5d-shells, the intensity of this feature is directly correlated with the number of holes in the d-shell, and can be used to probe the Pt oxidation and the charge transfer between Pt and adsorbed species. Generally, upon an increase in the applied potential, an increase in the WL magnitude is also observed, which is commonly associated with the 5d band becoming empty and electron withdrawing by the adsorbed oxygen species. The increase of the WL gets especially pronounced at potentials higher than 0.8 V versus RHE, where the formation of surface oxides is observed, as evidenced also by a Pt−O contribution appearing in the EXAFS spectra.[17,176,474−476] The relation between the WL intensity and the adsorption of oxygen species was demonstrated, for instance, by Erickson et al, who compared *in situ* Pt XAS data under N_2 and O_2 atmospheres.[141] It was found that at all applied potentials the sample under N_2 had a lower WL intensity than that of the same sample under O_2, highlighting the interaction between the catalyst and oxygen species. The enhancement in the WL intensity is especially pronounced for smaller Pt NPs, as observed by Mukerjee, McBreen et al.[17,475] suggesting stronger particle-adsorbate interactions (including poisoning) at the prevalent undercoordinated Pt sites. This finding allows one to rationalize the observation that the ORR activity decreases with decreasing particle size.[263,362] At the same time, a recent XANES study by Liu et al. demonstrated that the undesired oxidation of carbon-supported ultradispersed Pt species can be prevented by doping the carbon support with nitrogen, resulting in a more durable and highly efficient catalyst for ORR.

At lower potentials (ca. 0 V vs RHE and more negative), the WL intensity decreases, corresponding to a more metallic state of Pt. Additionally, a widening and an increase in the WL skewness is observed, which are attributed to the adsorption of hydrogen on the catalyst surface and the photoelectron transitions to the antibonding Pt−H orbitals.[17,475] The applications of XAS for studies of Pt−adsorbate interactions have been reviewed by Matthew and Russel[358] and Russel and Rose.[17]

The changes in the XANES features due to interactions with adsorbates and oxide formation are more easily distinguished in HERFD-XAS data, as demonstrated by Merte et al. in the study of size-selected Pt NPs with sizes ∼1.2 nm.[362] In this study, three distinct potential regimes were observed: (i) hydrogen chemisorption occurring between 0 V and ∼0.3 V versus RHE, as evidenced by a broad asymmetric white line with low amplitude; (ii) chemisorption of oxygen species (OH or O) as the potential was increased between 0.3 and 0.96 V, with the WL becoming narrower and its amplitude increasing; (iii) platinum oxide formation being observed at or above 0.9 V, as evidenced by an increase in the WL width (see Figure 32).[362] While the spectrum for the catalyst in as-prepared dry state resembled that of PtO_2, the intensity of the WL for the catalyst in its final state at 1.26 V versus RHE was lower, suggesting a lower average oxidation state of Pt in the obtained PtO_x structure.
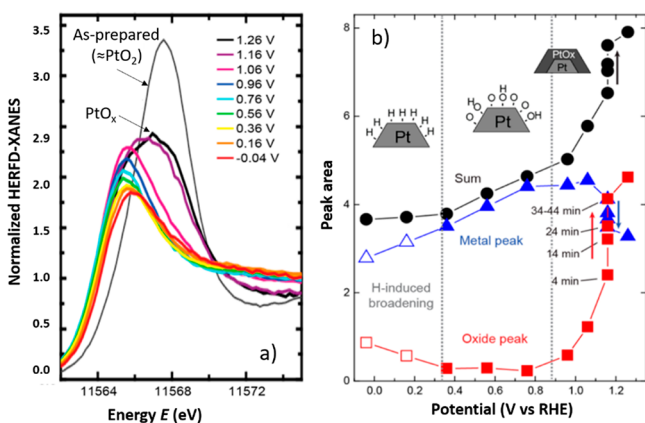
Figure 32. (a) Potential-dependent Pt L_3-edge HERFD-XANES for 1.2 nm Pt NPs on a carbon support. (b) Evolution of the metallic and oxide-like phases in the catalyst as a function of the applied potential in 0.1 M $HClO_4$ electrolyte obtained by fitting the HERFD XANES spectra with a combination of arctangent functions and two pseudo-Voigt peaks, corresponding to metallic (blue triangles) and oxidic (red squares) components, and integration of the peak areas. The evolution of the total area is also shown (black circles). Reproduced with permission from ref 362. Copyright 2012 American Chemical Society.

The presence of oxides is also important in the context of catalyst degradation since the catalyst oxidation was linked to

the dissolution of Pt and ripening of Pt NPs.[362,477] For example, recently Kim et al. reported the enhanced performance of Pt catalysts on carbon supports functionalized with oxygen-containing groups in comparison with that for the catalysts without such functionalization. However, more severe degradation was observed for the oxygen-functionalized sample. The analysis of Pt L_3-edge XANES data suggested an increased oxidation state for Pt atoms in this catalyst even at reducing potentials, which can explain both, the enhanced performance as well as poor durability of this material.[477]

6.2.3. Disorder in Pt Catalysts. Changes in the valence state, signified by the changes in the white line are typically accompanied by changes in the catalyst structure, for example, bond lengths, particle size, and induced strain.[141,285] EXAFS analysis can be used to follow these transformations in situ. For example, it was proposed that the analysis of Pt–O bond lengths can be used to discriminate between different adsorbates (e.g., Pt–O and Pt–OH).[350] However, in practice, data of very high quality are needed to determine reliably the interatomic distances with the accuracy required for such analysis. This requirement is rarely compatible with measurements under catalyst working conditions.[285] Another challenge is the sample-averaging nature of the EXAFS method and the heterogeneity of the catalyst structure, where the changes are often limited only to the surface. Studies of very small particles with sizes ~1–2 nm can be helpful in this case. For example, Myers et al. employed in situ XAS to investigate the changes in
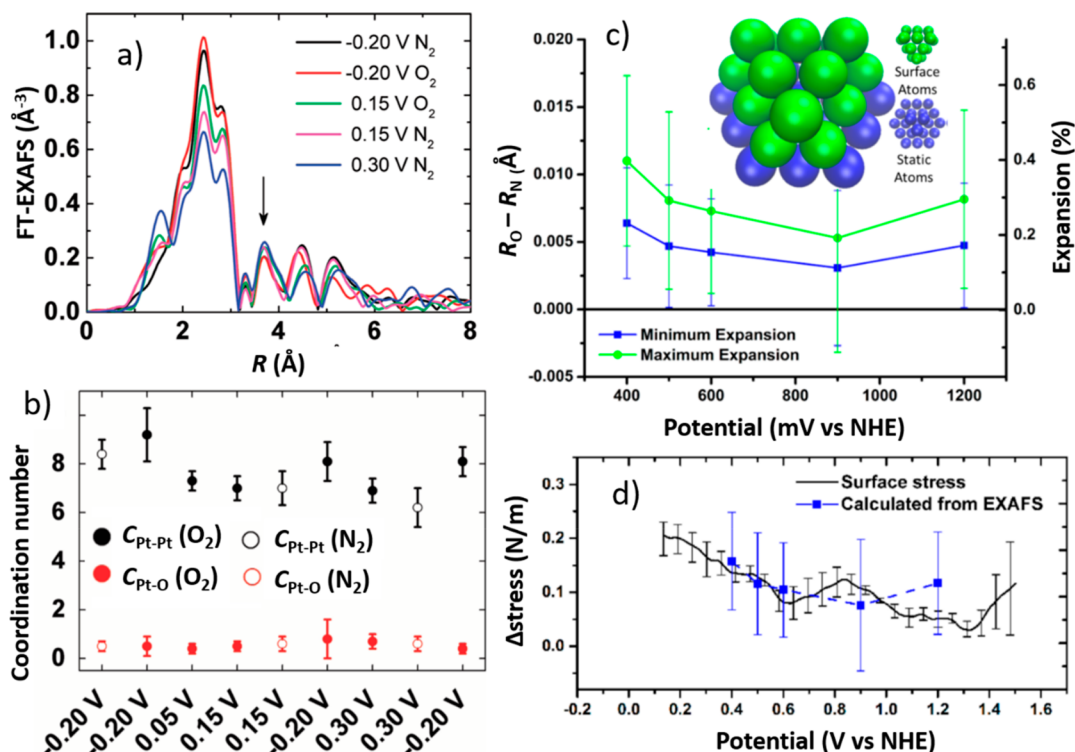
Figure 33. (a, b) Potential-dependent changes in the local structure of dendrimer-encapsulated Pt NPs immobilized on a carbon-paper electrode under ORR conditions in a 0.1 M $HClO_4$ electrolyte saturated either with N_2 or O_2. (a) Fourier transformed Pt L_3-edge EXAFS spectra. (b) Corresponding changes in the Pt–Pt ($C_{Pt–Pt}$) and Pt–O ($C_{Pt–O}$) coordination numbers in O_2 and N_2-saturated electrolyte. Reproduced with permission from ref 285. Copyright 2012 American Chemical Society. (c, d) Bond expansion under ORR conditions. (c) Minimum and maximum surface bond expansion in Pt NPs under ORR conditions as obtained from in situ EXAFS data analysis. The differences between Pt–Pt distances, measured in O_2 and N_2-saturated electrolyte are shown. The structure model of Pt NPs obtained from EXAFS-yielded CNs is shown in the inset. (d) Relative expansion of the interatomic distances obtained within the maximum surface bond expansion (surface-restricted expansion) model is compared with the in situ cantilever stress measurements. Reproduced with permission from ref 349. Copyright 2014 American Chemical Society.

1.8 nm dendritic Pt nanocatalysts for ORR.[285] Although the Pt precursors in the as-prepared samples were not completely reduced, the NPs were completely reduced *in situ* in the 0.1 M $HClO_4$ electrolyte when a -0.7 V (vs Hg/Hg_2SO_4) potential was applied. Through multiple-scattering EXAFS data fitting, the coordination numbers in the first few coordination shells were obtained and from them, information about the particle shape. With applied potential increasing between -0.2 and $+0.3$ V, a significant decrease in the first peak of the FT-EXAFS spectrum was observed, Figure 33a, corresponding to a reduction of the Pt−Pt CNs (Figure 33b). This effect was observed in both, N_2- and O_2-saturated electrolytes. At the same time, the more distant peaks in the FT-EXAFS spectra (dominated in fcc-type structures by multiple-scattering contributions) were relatively unaffected (Figure 33a). This was interpreted as an evidence of an increase in the NPs surface disorder, with the NP core relatively unaffected by potential changes. Myers et al. argued that MS contributions are more significantly suppressed by the disorder than single-scattering contributions. Therefore, even in the as-prepared sample, the surface layers (which in all NPs are expected to be less ordered) practically do not contribute to the MS-related component in particle-averaged EXAFS, and the total MS signal is dominated by the contribution from the ordered NP core region. The lack of changes in the MS contribution under applied potential can thus be interpreted as the lack of structural changes in the NP core.[285]

The effect of surface disorder and associated stress was also probed by Erickson et al.[349] with 1.2 nm Pt NPs prepared by an incipient wetness method. It was observed that upon exposure to oxygen, the Pt−Pt interatomic distances increase with increasing applied potential, and are longer that those at the same potential under N_2. This difference was attributed to the interaction between the Pt NPs and adsorbed oxygen species that resulted in an expansion of the interatomic distance. On the basis of the analysis of the CNs extracted from EXAFS data fitting, a 3D model of the NP structure was proposed (inset in Figure 33c), a truncated cuboctahedron. Two models of interatomic distance expansion were then compared: (i) uniform expansion, where all Pt−Pt distances were equally increased (minimum expansion), and (ii) a surface-restricted expansion, where only the distances between Pt atoms on the surface (green atoms in the inset in Figure 33c) were increased, representing the maximum expansion. The potential dependencies of the Pt−Pt distances for surface atoms calculated within both models are compared in Figure 33c. Strikingly, the bond expansion obtained within the second model was found to be in a good quantitative agreement with the direct *in situ* surface stress data obtained using optical cantilever stress measurements,[349,478] pointing thus to a surface-localized stress, Figure 33d. Such insight into the surface disorder is particularly important in catalysis applications since a linear correlation between the interatomic distances at the surface and the energy of the d-band center has been theoretically predicted and discussed to affect the adsorbate binding.[479] For instance, an expansion of the interatomic distances increases the energy of the electrons near the Fermi level that can be subsequently transferred to adsorbates.[349]

6.2.4. Time-Resolved Studies of Pt Catalysts. With the advances in XAS instrumentation, time-dependent information on the structural changes taking place at Pt electrodes during electrochemical reactions can be monitored on the time scale

of seconds. In 2007, a pioneering study by Tada et al.[96] employed time-grating QXAFS (essentially a pump-and-probe technique) to monitor the changes in the Pt valence and Pt−O and Pt−Pt bonds with 1 s time resolution. A comparable time resolution was achieved also by energy-dispersive XAFS.[96,350] In 2012−2013, technical advances in the QXAFS method allowed to improve the time-resolution first up to 500 ms,[480] and later on to 100 ms[98] and 20 ms in 2018.[97,481] Moreover, while in the earlier works a reasonable XAS signal could only be achieved for a catalyst loading several-times higher than that used in catalysis applications,[98] the loading could be subsequently reduced to more realistic values (e.g., 0.5 mg/ cm^2).

The former results demonstrate the complexity of the processes taking place at the surface of Pt electrodes. By following the time-dependency of the WL intensity, Pt−Pt and Pt−O coordination numbers (Figure 34a), it was observed that
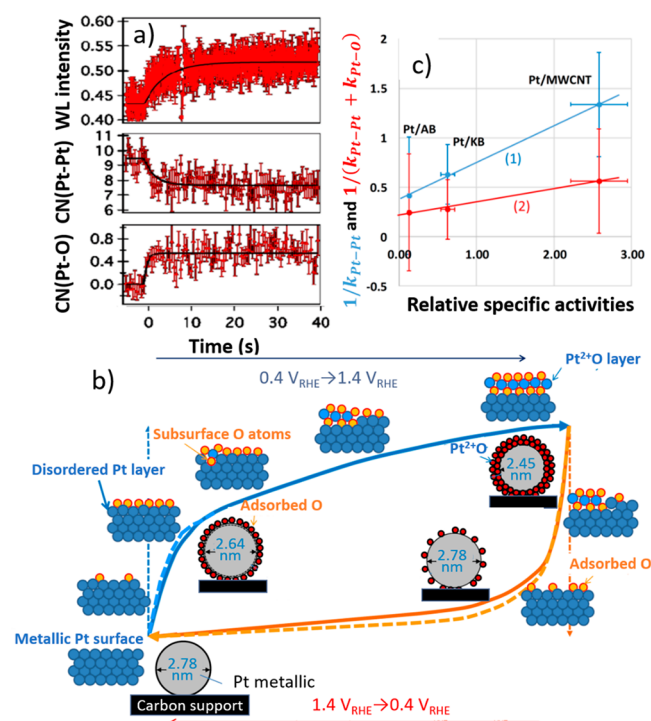
Figure 34. (a) Time-dependencies of the Pt L_3-edge WL intensity and Pt−Pt and Pt−O coordination numbers obtained from XAS data analysis upon an increase in the applied potential from 0.4 to 1.0 V. Reprinted by permission from Springer Nature, ref 97 (2018). (b) Reaction mechanism and kinetics for the events on the surface of a Pt cathode under voltage cycling from 0.4 to 1.4 V versus RHE. (c) Relationship between the specific activities and the rate constants for Pt−Pt and Pt−O coordination number changes under ORR conditions, obtained from the time-dependent EXAFS data. Reprinted by permission from Springer Nature, ref 481 (2018).

several seconds are needed until these parameters reach their stationary values after potential changes are applied, due to the final time needed for charge transfer, Pt−O bond formation and rearrangement of Pt atoms within the NPs. Moreover, the characteristic times (or, alternatively, rate constants k) for these processes, corresponding to different elementary steps in ORR, Figure 34b, were found to be different. In particular, it was found that the changes in the Pt−Pt coordination number are slower than those in the Pt−O CNs,[97] which can

contribute to the catalyst degradation during power-on/power-off cycles.[95−97] By comparing the time-dependent results for different Pt-based catalysts, the characteristic times of the changes in the XAFS-derived coordination numbers were found to be linearly correlated with the specific activity and the durability of the catalysts (Figure 34c).[481]

6.2.5. Alloys, Bimetallic and More Complex Catalysts.

The combination of Pt with another metal is a common route to tune the properties of the ORR catalysts, in particular, to improve its activity, stability, robustness toward poisoning, and to reduce the cost of the catalyst by minimizing the amount of Pt used. In terms of activity, Pt alloys with the first row transition metals (Ni, Co, Cr, Fe, Cu) are reported among the most active catalysts for ORR. In particular, the activity of Pt_3Ni catalysts exceeds that of pure Pt several times.[482,483] *In situ* XAS has been widely used to understand the origin of such enhaced performance. Mukerjee et al. investigated Pt−Ni, Pt−Co, Pt−Cr, Pt−Mn, and Pt−Fe alloy NPs with enhanced ORR activity in comparison to that of pure Pt via XAS.[17,474,484,485] The intensity of the Pt-L_3 WL within the double-layer region (0.54 V vs RHE) was enhanced in the alloy samples with respect to monometallic Pt, suggesting an increase in d-band vacancies. At the same time, under ORR conditions at a potential of 0.84 V, the intensity of the WL did not increase significantly for alloy catalysts, while for the platinum catalyst it was enhanced noticeably, surpassing that of the alloys. Analysis of the EXAFS spectra showed that a significant Pt−O contribution is present in the data of the Pt catalyst at 0.84 V, but not at 0.54 V and not for the alloy catalysts at any of these potentials. This suggests that the interactions between Pt and oxygen species in the alloy catalysts under ORR are suppressed. This, in turn, indicates that these catalysts are less prone to the poisoning by adsorbed OH, which may explain their enhanced catalytic activity. In fact, a nearly linear relationship between the intensity of the WL and the catalyst activity can be obtained, as observed by Antolini et al. in studies of Pt−Co catalysts with different particle sizes and different Co loadings.[139] Similar decreased Pt oxidation under ORR conditions has been observed also for other Pt-based bimetallic systems that were found to be promising for ORR, such as Pt NPs modified with gold clusters,[242] Pt−Ti intermetallic catalysts,[486] platinum−tungsten carbide catalysts,[487] platinum−vanadium alloys,[476] niobium oxide-supported Pt catalysts,[488] ordered PtFe nanocatalysts,[489] and others.

On the other hand, analysis of EXAFS spectra by Mukerjee et al. and others suggested that Pt−Pt distances in all alloy samples are lower than in pure Pt, thus changes in interatomic distances can also be responsible for the increased activity.[17,474,484,490] In fact, both effects seem to be correlated since an inverse relationship can be observed between the Pt−Pt bond distance and the Pt d-band occupation.[484] The effect of the reduced Pt−Pt bond length (compressive strain due to alloying) on the weakening of the adsorption of oxygen species is also well reproduced in theoretical simulations.[2,118,491]

Interestingly, the secondary metal itself in the aforementioned systems, does not seem to play an important role in the redox processes at the electrode surface, as evidenced by the lack of potential-dependent changes in the K-edge XAS spectra for these transition metals under reaction conditions.[474,484] The limitation of the alloy systems is that the secondary metal is typically less stable under ORR conditions than Pt and can be leached out, resulting in the loss of catalyst performance.

Moreover, the fraction of Pt in these catalysts is still significant; thus, they are not much cheaper than pure Pt catalysts. As a promising alternative, NPs with a non-noble metal alloy core covered with a monolayer of Pt have been proposed. A prominent example is Pd NPs decorated with a monolayer of Pt, which exhibit an ORR activity that surpasses that of pure Pt, and even more importantly, also show superior stability.[265,492,493] At the same time, Pt monolayers on Au, Ir, Rh, Ru, and Re cores show decreased activity, while preserving a good stability.[105] An attractive aspect of XAS for studies of these ORR catalysts is its ability to provide quantitative information about the Pt layer thickness, and distinguish between NPs with one and two monolayers of Pt by analyzing the EXAFS CNs. For example, for a single Pt monolayer on Pd(111), the expected Pt−Pt and Pt−Pd coordination numbers are 6 and 3, respectively, while for the system with two Pt monolayers the CNs are 9 and 1.5, respectively. Sasaki et al. demonstrated an excellent agreement of these theoretical values with the CNs extracted from experimental EXAFS data for Pt−Pd NPs where the thickness of the Pt shell was varied by Cu-mediated layer-by-layer Pt deposition.[105,265] It should be noted here that while the current associated with ORR increases upon addition of the second Pt monolayer, the specific activity decreases.[105]

A concern in the applications of Pd-containing catalysts in fuel cells is the possible uptake of hydrogen (used as fuel) that can crossover through the membrane to the cathode and form Pd hydride (as discussed in Section 6.1.3), thus affecting the durability of the catalyst. However, as demonstrated by Wise et al.,[494] a Pt monolayer on top of a Pd NP core provides efficient protection toward hydride formation. In fact, Pd hydride formation was prevented even if the Pt shell is incomplete (e.g., only a half monolayer of Pt is deposited). In their work, while in pure Pd NPs the Pd−Pd distance, extracted from *in situ* EXAFS data analysis at 0.0 V versus RHE, increased from 2.74 to 2.83 Å in the presence of hydrogen, indicating the formation of the beta hydride phase, much smaller changes in the Pd−Pd distances were observed in Pd NPs covered with a Pt shell.[494]

The properties of the monolayer Pt catalysts can be tuned in a broad range by choosing more complex core structures. Bimetallic alloy cores formed by metals with different lattice constants allow one to tune the strain induced in the Pt monolayer. For example, it was observed that the ORR activity of Pt monolayers on top of a PdAu alloy core depends significantly on the Pd to Au ratio, with optimal ORR performance achieved at a 9:1 Pd:Au ratio.[339−341] At the same time, Co−Pd core−shell NPs with Pt monolayer on the surface were also found to exhibit excellent catalytic properties, while containing a significantly lower amount of the noble metals.[495] IrNi bimetallic cores were also described to be promising in terms of the synthesis scalability and cost-efficiency.[496] Particles with even more complex core structure have been proposed, such as Pt monolayer-covered ternary PdNiMo core, where enhanced stability of the catalyst was ensured through the Pd−Mo interaction,[497] and Pt-covered NPs with PdNi core, where the core was stabilized by the incorporation of Au. The latter NPs exhibited a higher activity than Pt/Pd and Pt/PdNi catalysts.[498] On the other hand, an enhancement in ORR activity can also be obtained by replacing some of the Pt in the shell with other metals such as Re, Os, and Ir.[105,499] Clearly, the more complex the structure of the catalyst gets, the more important is to validate the presence of the desired structural

motifs in these systems using experimental measurements. In the aforementioned examples, XAS was very instrumental for this purpose, by providing information ranging from a simple estimate of the constituent metal ratios (either from absorption edge-step analysis or from EXAFS-derived coordination numbers), up to the determination of the particle morphology and alloying/segregation motifs.

For example, Pt monolayer-coated PdAu nanowires were studied in ref 341, and the insight from EXAFS data analysis was used to differentiate between different possible structural models and distributions of the metals. Pt atoms were found to be predominantly surrounded by Pt or Au, which allowed the authors to conclude that Pt atoms are located predominantly on the surfaces of the nanowires. More surprisingly, it was found that the coordination numbers for both Au−Au/Pt and Au−Pd atomic pairs were quite close to 6, despite the fact that the investigated particles were Pd-rich (a much larger Au−Pd CN is expected if the metals are uniformly mixed). This finding indicated that the Au atoms were also localized next to the surface, either directly underneath the Pt layer, or were mixed with Pt forming a PtAu shell on top of the Pd core. Such complex architecture was confirmed by DFT simulations. Notably, the segregation of Au to the nanowire surface in this case took place during the synthesis and pretreatment, and not during the ORR reaction itself.[341] In contrast, a reversible, potential-dependent exchange process involving Pd migrating between the core and the shell, within Pd−Au alloy (Pd-rich) NPs, was mentioned by Jirkovský et al. in ref 500. At potentials below 0.8 V versus RHE, the surface tended to be Au-rich, whereas at higher potentials (>1.0 V vs RHE) the surface was found to be Pd-rich.

In alkaline media, Pd alloys can be used for ORR without protective Pt shells. For example, pure Pd, PdCu and PdPt alloy NPs were investigated by Castegnaro et al.[501] Analysis of the coordination numbers extracted from EXAFS data together with Cowley's short-range parameter (see Section 5.5.2) were used to confirm the random distribution of the constituent metals. In turn, electrochemically prepared Pd−Au core−shell NPs were studied by Price et al. via *in situ* EXAFS.[502] The NPs were prepared by two electrochemical methods: (i) conventional Cu underpotential deposition (UPD) followed by a replacement of Cu with Pd, and (ii) by a Cu UPD-mediated process.[265] While no significant dependency of the NP structure on the applied potential was observed, significantly larger mixing of Pd and Au in the NP surface layer was observed for the NPs prepared via the Cu-UPD-mediated process.[502]

The attractiveness of alloy systems like PdAu for ORR applications relies on the fact that it consists of a combination of oxyphilic and oxyphobic metals. For example, Au (or Ag) binds oxygen species too weakly, while metals like Pd (and also Rh, Pd, and Ir) do it too strongly. Thus, by alloying Pd with Au, the surface binding energy can be tuned and the catalytic properties optimized.[17,503] While PdAu alloys are relatively well-known, other relevant combinations of metals are less explored. Recently, Li et al. proposed the RhAu system as a promising catalyst for ORR applications.[503] Unlike the Pd−Au system, Rh and Au are considered to be immiscible in their bulk phases. Nevertheless, Rh−Au alloying was demonstrated for NPs prepared via microwave assisted synthesis[504] or dendrimer encapsulation.[505] *In situ* XAS measurements from the dendrimer-encapsulated NPs revealed the incomplete reduction of the precursor species (XANES), and the surface

segregation of Au (EXAFS).[505] For RhAu NPs synthesized via a microwave-assisted method, significant discrepancy was obtained when comparing the NP sizes extracted from EXAFS and those obtained from TEM. This was explained by the coexistence of particles of different sizes and compositions. By combining the information from EXAFS with NP size distributions from TEM, a structure model was constructed consisting of a mixture of ultrasmall Rh NPs and larger RhAu NPs with Au segregated to surface. Further, by employing Monte Carlo simulations of the NP structure and dynamics, it was demonstrated that the *ab initio* EXAFS spectra, calculated following a model consisting of the NPs of these two types can reproduce reliably the experimental EXAFS data collected at both the Au L$_3$-edge and the Rh K-edges (Figure 35).[212]
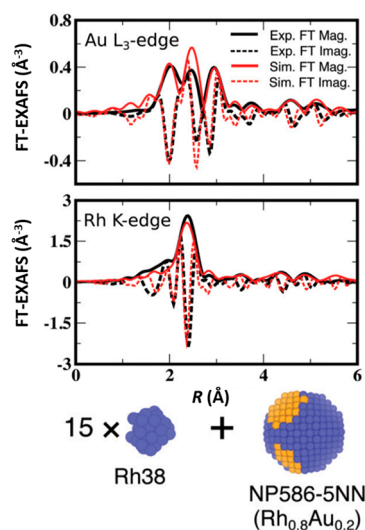
Figure 35. Comparison of the experimental and simulated Au L$_3$-edge and Rh K-edge EXAFS spectra for a Rh−Au NP system. Theoretical data are obtained from Monte Carlo modeling with classical MEAM force field models, and correspond to an ensemble consisting of NPs of two types: small Rh clusters and larger Rh−Au alloy NPs. A structure model is constructed based on the analysis of coordination numbers extracted from EXAFS, TEM measurements, as well as computational screening of different models until the best agreement between experiment and simulation was obtained. Reproduced from ref 212 with permission from The Royal Society of Chemistry.

6.2.6. Nonmetallic Catalysts for ORR. Among the nonmetallic catalysts for ORR, transition metal chalcogenides have been widely studied. For instance, Ru-based chalcogenide materials demonstrated good performance for ORR in direct methanol fuel cells (DMFC) when compared to Pt catalysts.[17,158,506] In particular, Ru−Se−Mo,[507−510] Ru−S,[158,508,509] Ru−Se,[158,508,509,511] and Ru−Te[158,508,510] have been investigated. The EXAFS data discussed in these references demonstrated the presence of metallic Ru−Ru bonds; thus, the actual structure of the investigated catalysts can be described as a chalcogenide-decorated metallic Ru. In all cases, Ru−O bonds were also observed. However, these bonds were attributed to adsorbed oxygen species rather than the formation of oxides.[508] By performing *in situ* XAS measurements at the Rh K-edge and the K-edges of the chalcogenide elements, it was concluded that only Ru species respond to the changes in the applied potential, suggesting that those are likely the active species. More specifically, a
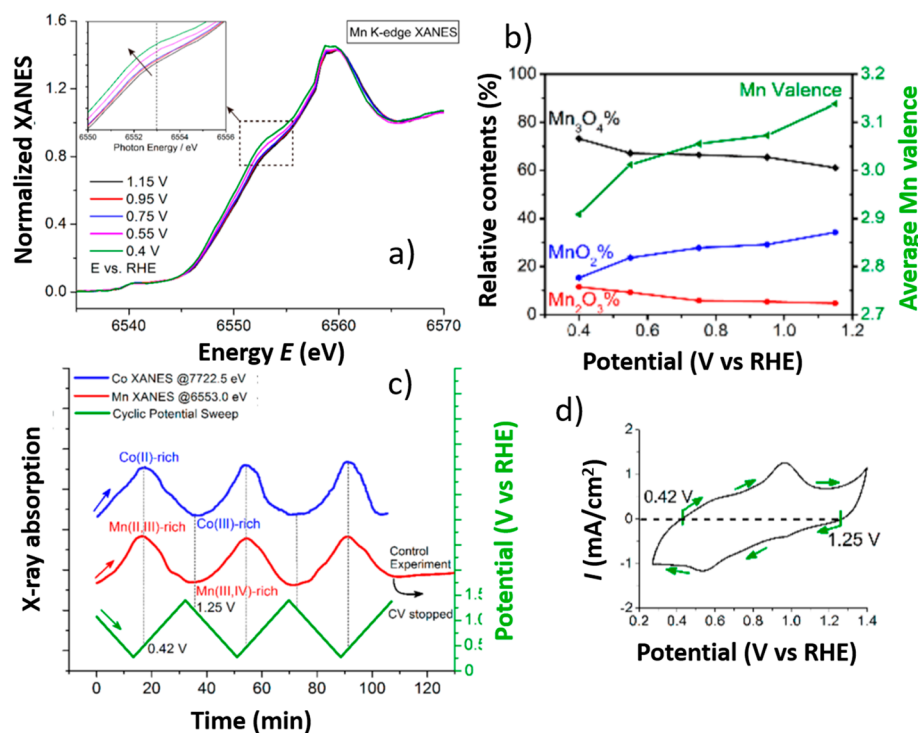
Figure 36. (a) Changes in the Mn K-edge XANES in $Co_{1.5}Mn_{1.5}O_4$ catalysts with applied potential in 1 M KOH electrolyte. (b) Results of linear combination analysis. (c) Periodic changes in the X-ray absorption at 7722.5 eV (Co K-edge) and 6553.0 eV (Mn K-edge) corresponding to changes in the Co and Mn oxidation state. (d) Corresponding CV. Reproduced with permission from ref 519. Copyright 2019 American Chemical Society.

significant increase in Rh−O contribution was observed via *in situ* EXAFS with increasing applied potential, and simultaneous reduction of the Rh−Rh coordination number and the corresponding bond length.[158] This effect is very pronounced in pure Ru electrodes, where the formation of oxides was observed at higher potentials.[510] The presence of the chalcogenides in Ru_xSe_y and $Ru_xSe_yMo_z$ catalysts, however, suppresses the oxidation of the electrode and the formation of the inactive RuO_2 phase, ensuring better catalytic activity.[510,511] Stronger Ru−O interactions (suggested by a larger Ru−O coordination number or shorter Ru−O bond length) were observed in Ru−S[508] and Ru−Te[510] catalysts, explaining the lower activity of these catalysts.

While promising for ORR, Ru-based materials are still expensive. Among various precious-metal-free catalysts for ORR, manganese-based oxides have attracted attention due to the high tunability of their structure and properties. At the same time, this diversity of possible structural motifs and valence states complicates the understanding of the actual active species and working mechanism of MnO_x-based catalysts. Commonly, the ORR activity of MnO_x-based materials is attributed to the cyclic redox reaction between Mn^{4+} species to Mn^{3+} species, where ORR occurs by oxidizing the Mn^{3+} species continuously produced by the reduction of Mn^{4+} species.[512−515] As a result, the coexistence and the ratio of Mn^{4+} and Mn^{3+} species seem to be the key for ensuring high ORR activity. Because of the high sensitivity of XANES to the Mn valence state, *in situ* measurements at the Mn K-edge have been used to gain insight into the working mechanism of MnO_x-based catalysts. For example, the reduction of a MnO_2-rich catalyst under ORR conditions was demonstrated through the linear combination analysis of Mn K-edge XANES data. High ORR activity was associated with a high MnO_2 content in

the material.[514,515] The importance of coexisting Mn^{3+} and Mn^{4+} species was confirmed also by Park et al., where the intercalation of layered Mn oxides with graphene oxide resulted in a reduced (closer to 3+) oxidation state of Mn-based catalysts and improved ORR activity.[516] The importance of fine-tuning the Mn^{3+} and Mn^{4+} ratio was emphasized in Mn K-edge XANES studies of mullite-type $SmMn_2O_{5-\delta}$ NPs prepared by laser irradiation of a $SmMn_2O_5$ micropowder suspension. Here, XANES data revealed that the concentration of oxygen vacancies and the ratio of Mn species in different oxidation states could be controlled by changing the laser energy. The maximal ORR activity was observed for an average Mn valence of ~3.36.[517] At the same time, the formation of disordered Mn^{2+}/Mn^{3+} mixed oxides in electrodeposited MnO_x catalysts under ORR conditions was reported by Gorlin et al. based on the positions of the Mn K-edge XANES features and the Mn−O interatomic distances extracted from EXAFS data.[513,518] Recently, even higher ORR activities have been reported in $Co_{1.5}Mn_{1.5}O_4$ catalysts,[519] where the reduction of Mn species from the +3/+4 state to +2/+3 state (as well as that of Co species from +3 to +2 state) has been suggested with increasing reaction time. (Figure 36). See also Section 6.3.6 for the discussion of Mn-based materials for bifunctional catalysts that combine activity for ORR and OER reactions.

Despite the progress in the development of transition metal chalcogenides and oxide-based ORR catalysts and interesting new work on carbides, nitrides and, phosphides-based catalysts,[506,520,521] the most actively investigated nonprecious metal catalysts for ORR are transition metal nitrogen-doped carbon catalysts, which are discussed in the next subsection.

6.2.7. Transition Metal- and Nitrogen Doped Carbon Catalysts. TMNC catalysts for ORR are currently the subject of vivid investigations, since they are considered promising

alternatives to Pt-based materials. The activity of Co-based macrocycles for ORR was pointed out already in 1960s, but the stability and the activity of these materials were low.[506,522] Later, it was found that both the stability and catalytic performance could be improved significantly upon pyrolysis of the transition metal-containing precursors.[506,523] Such high temperature treatment, however, results in significant changes in the TMNC materials, and heterogeneous structures with different coexisting species severely complicate the elucidation of the actual active sites for ORR. In particular, M-N_x moieties, metal carbides, metal NPs, and even metal-free CN_x structural motifs have all been proposed as possible active species, with the corresponding reports in the literature often providing contradicting evidence.[20,272,524,525] Moreover, the reason for the significant deactivation of the TMNC catalysts, one of the main issues for their transfer into practical applications, is still a controversial subject. The most popular types of TMNCs for ORR are Fe- and Co-based materials. Commonly, Fe-based TMNCs are believed to be more active for 4e ORR process, while Co-based TMNCs seem to favor 2e ORR process with H_2O_2 as the product.[506]

While sensitivity to the local structure around the metal center makes XAS an important tool for understanding the structure of TMNC materials, the heterogeneity of these catalysts and the sample-averaging nature of the XAS method is a serious obstacle. Commonly, Fe$-N_4$ species are considered to be important for the ORR activity of Fe-based TMNC materials, as demonstrated in refs 20, 149, 325, 327, and 526−533 using the XAS method and arguments similar to those presented in Section 6.1.5. In particular, a good agreement between experimental Fe K-edge XANES spectra for TMNC catalysts and the results of theoretical XANES modeling for the Fe$-N_4$ moiety was demonstrated.[20,149,327,526,534] At the same time, contrary reports also exist that emphasize the role of CN_x motifs and carbon-encapsulated Fe NPs. For example, Singh et al.[524] compared the ORR performance of two catalysts, Fe$-C-N$ and CN_x, where the latter was prepared by leaching the Fe-species with acid, although some Fe impurities still remained in the CN_x sample. Both catalysts exhibited activity toward ORR, although XANES and EXAFS analysis suggested very different local environment for Fe in both cases, namely, carbide- or nitride-like structures in the Fe$-C-N$ sample, and the presence of residual metallic Fe species in the CN_x catalyst. This observation revealed that the Fe$-N_4$ species are at least not the only possible active species in the Fe-based TMNC materials.[524] Similarly, linear combination analysis of Fe K-edge XANES spectra from Fe-based TMNC materials carried out by Kobayashi et al. to quantify the contributions of different Fe species before and after the acid leaching demonstrated that even when the Fe$-N_4$ motifs were leached out, the catalyst remained active for ORR.[535] Selective poisoning of these type of catalysts using Cl_2 and H_2 treatments was employed by Varnell et al. to find the active species.[272] It was discovered that the Cl_2 treatment deactivated the catalyst, while H_2 restored its activity. Mössbauer spectra showed no Fe$-N_4$ species in the active H_2-treated sample, while multiple Fe-containing species were present in the as-prepared sample. XANES and EXAFS analysis have shown that the Cl_2-treated inactive catalyst had a structure similar to that of $FeCl_3 \cdot (H_2O)_x$. XANES and EXAFS analyses of the active samples (as-prepared and reactivated by H_2-treatment) showed that Fe is predominantly metallic and has a bcc

structure. From multiple-shell EXAFS data fitting and analysis of Fe−Fe CNs, it was concluded that Fe is present as 1−2 nm NPs, which was confirmed with TEM. These findings suggest that carbon-encapsulated Fe NPs can be active for ORR even in the absence of Fe$-N_4$ structural motifs.[272]

An important insight toward resolving this controversy is extracted from *operando* XAS studies.[20,325,328,527] In particular, the analysis of *operando* Fe K-edge EXAFS spectra revealed that the Fe−N contribution changes with potential (i.e., is electrochemically active), while the Fe−Fe does not.[20,325] Moreover, the shift in the Fe K-edge XAS signal (Figure 37a)
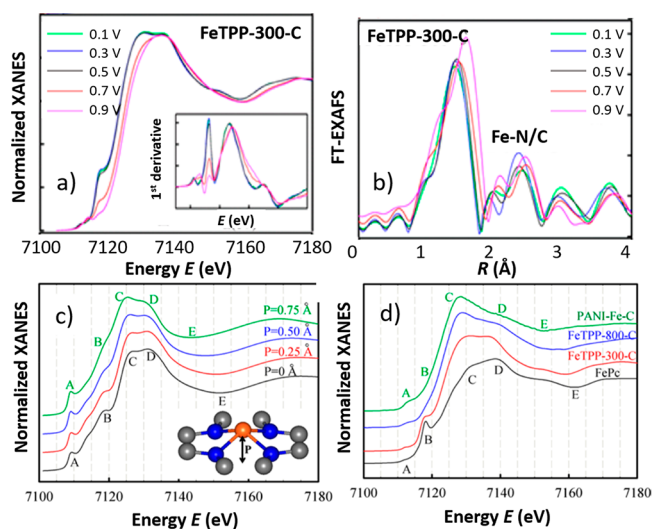
Figure 37. Changes in the Fe K-edge (a) XANES and (b) FT-EXAFS *operando* data in Fe-based TMNC catalyst for ORR with increasing applied potential. (c) Sensitivity of XANES features to the off-plane displacement of the Fe ion in the Fe$-N_4$ structural motif, as obtained in theoretical XANES simulations. (d) Changes in the simulated spectra describe well the trends in the experimental data collected at 0.1 V in N_2-saturated 0.1 M $HClO_4$ electrolyte for samples with different degree of distortion of the square-planar Fe$-N_4$ motif. Reproduced with permission from ref 325. Copyright 2015 American Chemical Society.

with increasing applied potential was attributed to the transition from the Fe 2+ to the 3+ state. The changes in the valence state were accompanied by the changes in the local structure. The Fe−N distance increased with increasing potential, Figure 37b, while the characteristic XANES feature that is a fingerprint for planar Fe$-N_4$ coordination (shoulder at 7117 eV) disappeared. These changes were attributed to the displacement of Fe from the in-plane to off-plane position (Figure 37c). Interestingly, the average displacement at 0.1 V was different for differently prepared samples, Figure 37d, and showed a positive correlation with the ORR activity, with the more distorted configuration corresponding to the catalyst with the highest activity.[325]

While generally considered less active than Fe-based TMNC materials, Co-based TMNC catalysts are believed to exhibit higher stability for ORR.[506] Their activity is also often associated with Co$-N_x$ moieties, as recently shown in refs 149 and 536−538 and others based on the analysis of Co K-edge XAS spectra. On the other hand, an *operando* XAS study by Zitolo et al.[328] revealed important differences in the behavior of Fe- and Co-based TMNC materials: unlike in the case of Fe, XAS spectra for Co-based TMNC catalysts showed

Figure 38. (a) Effective thicknesses of the oxide layers on Ir (blue) and Ru (red) thin films, estimated from a linear combination fitting of *operando* Ir L_3-edge and Ru K-edge XANES data. Representative spectra are shown in the insets. The data are reproduced with permission from ref 556. Copyright 2014 American Chemical Society. (b) Potential-dependent Ir−O interatomic distances, as obtained from the fitting of *operando* EXAFS data at the Ir L_3-edge for bulk-like IrO_x catalyst (IrO_2-30) NPs and for dispersed catalysts with NP size ~1.7 nm (IrO_2-150). The number in th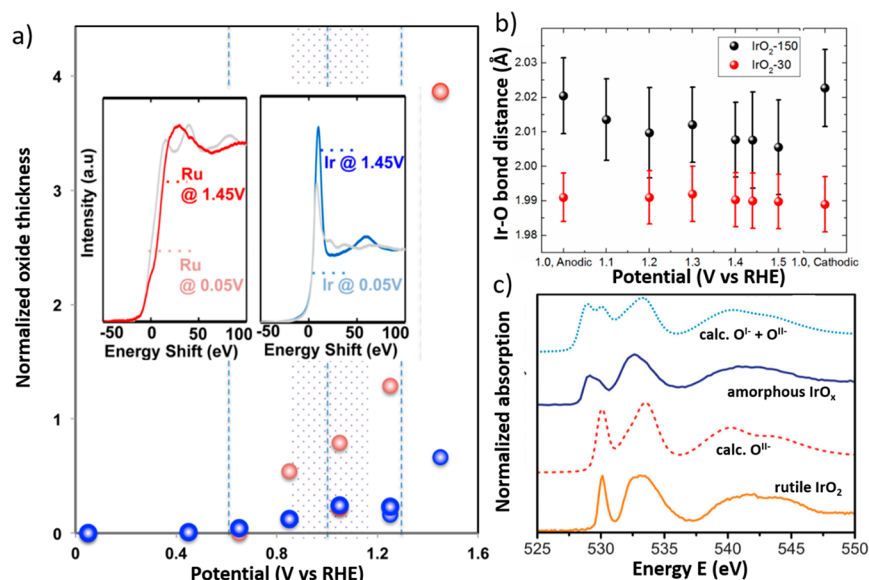e sample names refers to an approximate surface area of the catalyst (30 m^2/g and 150 m^2/g). Reproduced with permission from ref 564. Copyright 2016 American Chemical Society. (c) Experimentally acquired O K-edge XAS spectra for rutile-type IrO_2 and amorphous IrO_x catalysts, as well as ab initio calculated spectra for O^{II-} species in IrO_2, and a spectrum obtained as a linear combination of ab initio spectra for O^{II-} and O^{I-} species (with weights 60% and 40%, correspondingly). Reproduced with permission from ref 571 published by the PCCP Owner Societies.

practically no changes with applied potential in the range relevant for ORR, suggesting a significantly less pronounced structural change upon their interaction with adsorbates. At the same time, more pronounced differences in the Co K-edge XANES spectra could be detected when the spectra were collected in O_2-saturated versus N_2-saturated electrolytes. This suggests that Co-based sites are less prone to adsorb oxygen species and form Co−O bonds only in an O_2-saturated electrolyte.[328]

In addition to Co- and Fe-based TMNC materials, other analogous catalysts for ORR have been explored, such as Ni-,[149] Cu-,[539,540] and Zn-based TMNC catalysts,[541] with the presence of the M-N_x moiety inferred from EXAFS analysis and associated with the observed ORR activity. Ru-based TMNC materials (Ru on nitrogen-doped graphene) have also shown good ORR activity at low overpotentials.[542] The presence of singly dispersed Ru sites was demonstrated by Ru K-edge EXAFS analysis, including wavelet transform data, as well as theoretical XANES modeling for DFT-optimized structure models. At the same time, the presence of metallic Ru clusters was observed for three control samples which exhibited lower ORR activity: a sample, prepared without graphene doping by N, a sample with increased Ru loading, and a sample with increased annealing temperature.[542]

Coexistence of two or more active metal ion centers in close proximity has been demonstrated to further improve the catalyst activity. For example, a Co-based TMNC material synthesized from a bimetallic-organic framework precursor showed activity 12-times higher than that of a conventional Co−N_4-type catalyst, which was explained by the presence of Co_2N_5 structural motifs, and whose signature (shortened Co−Co bond) was detected in the analysis of Co K-edge EXAFS spectra.[543] Enhanced catalytic performance is expected also for catalysts containing metal-ion centers of different types,

especially those combining Fe and Co centers.[506,544] ORR catalysts prepared via high-temperature pyrolysis of a Co−Fe−N chelate complex were studied in ref 545. EXAFS measurements indicated that Fe−N_x and Co−N_x species do not survive the pyrolysis and form metallic clusters, which are removed during the subsequent acid treatment. The observed ORR activity was thus attributed to carbon species on the catalyst surface.[545] In contrast, more recent studies[546−548] revealed that coexisting Fe−N_x and Co−N_x moieties can be stabilized, resulting in enhanced activity. The indicators of the presence of heterometallic species can be sometimes observed in the EXAFS data,[547] although they are hard to discriminate from metal−metal contributions due to the formation of larger metallic clusters.

6.3. Oxygen Evolution Reaction

6.3.1. Introduction. The oxygen evolution reaction is at the heart and is often the limiting step of promising enabling technologies such as the electrochemical water splitting for hydrogen production, rechargeable metal-air batteries and reversible fuel cells that can resurge the fuel through electrocatalysis.[549,550] The electrochemical formation of molecular oxygen is a sluggish 4-electron process which requires an efficient electrocatalyst. Importantly, OER is strongly pH-dependent, and therefore, it proceeds differently in alkaline and acidic electrolytes, and different catalysts may be needed for the different conditions.[18,549,551]

Similarly as with other electrochemical reactions, the catalytic activity of a material for OER is determined by a balance between the adsorption strengths for oxygen and those of the reaction intermediates.[552] The most active catalysts which are currently used for OER are Ru- and Ir-based materials. However, these noble metal-based catalysts are expensive, and may suffer from dissolution problems at high overpotentials.[549] Therefore, alternatives are actively sought. In

particular, in alkaline media, transition metal-based oxides, hydroxides, and oxyhydroxides were shown to be promising and highly tunable catalysts, demonstrating activity comparable to that of traditional noble metal-based catalysts.[549,553−555] Moreover, nonoxide materials (phosphides, phosphates, chalcogenides, nitrides) have also been proposed as possible candidates for OER due to their better electrical conductivity, which often impairs applications of oxide-based catalysts.[551]

In many of these cases, the actual active species and the working mechanism of the catalysts remain actively debated. This is in part due to the coexistence of disordered species with different oxidation state and local environment, and because of the significant transformations of the materials electronic and atomistic structure that take place under reaction conditions. In fact, the most active OER catalysts are often those that are the least stable under reaction conditions.[19,556,557] *Operando* XAS studies can provide insight into the local changes around metal centers in the catalysts that can be used to gain mechanistic understanding of the OER process.[18,19]

6.3.2. Stability and Activity of Noble Metal-Based Catalysts. Ru- and Ir-based catalysts are the most common OER catalysts, especially in acidic media.[549,558] The activity of metallic Ru and Ir is higher than that of the respective oxides, but they show low stability under reaction conditions and therefore, oxide materials are typically used instead. More importantly, RuO_2 with a rutile-type structure is more active, but less stable than IrO_2 with the same structure. It should be noted that the dissolution of the catalyst has been previously associated with its oxidation to a higher oxidation state (>4+).[549,551]

The relationship between the catalyst activity and stability was explored by Danilovic et al. for thin metallic Ru and Ir films deposited by magnetron sputtering on glassy carbon substrate.[556] By using linear combination analysis of Ru K-edge and Ir L_3-edge XANES data collected under an applied potential they demonstrated that the oxidation of Ru is faster at the same potential (Figure 38a). Moreover, the appearance of signatures of high oxidation states (>4+) in the XANES spectra was found to coincide with both the onset of OER activity and also the dissolution of the deposited metals.[556] The discussion of the link between stability and activity was further extended to $SrRuO_X$ single crystal thin films with different orientation,[559,560] as well as sputtered Ru−Ir alloy films with different compositions and annealing pretreatments.[561] In all examples, the formation of Ru and Ir species with a high oxidation state was extracted from the Ir L_3-edge and Ru K-edge XANES data, and an inverse correlation between catalyst activity and stability was established. Analysis of spectral features at Ru $L_{3,2}$ edges can also be instrumental for tracking the changes in the oxidation state of Ru.[562]

Catalyst−support interactions can also be used to control the stability of the catalysts, as demonstrated by Oh et al.[563] In their work, the oxidation state of Ir NPs supported on antimony-doped tin oxide (ATO) after electrochemical oxidation was monitored by XAS. The observed shift of the Ir L_3-edge XANES features to lower energy values and lower area under the Ir L_3-edge WL for the ATO-supported catalyst with respect to that for carbon-supported suggested a different oxidation state of Ir in these two cases, namely ∼+ 3.3 and +4, correspondingly. The lower oxidation state of Ir in the ATO-supported catalyst was confirmed also by EXAFS analysis, which yielded a larger Ir−O interatomic distance. Note that an Ir−O bond length of ∼2.20 Å is expected for Ir^{3+} oxides, while

for IrO_2 the corresponding interatomic distance is 1.98 Å.[564,565] While no significant difference in OER activity was observed for the catalysts considered, ATO-supported Ir showed higher stability toward corrosive dissolution, which was attributed to particle-support interactions contributing to sustain a lower oxidation state of Ir.[563] The evolution of the oxidation state of Ir-based catalysts under OER conditions was demonstrated by Minguzzi et al. by using *in situ* time-resolved X-ray absorption measurements at a fixed energy, where the largest difference between the XAS spectra of Ir species in different oxidation state is expected.[566] Alternatively, energy-dispersive XAS can be used,[567] where subsecond time resolution was achieved while collecting *operando* Ir L_3-ege data for IrO_x catalysts.

In addition to stability, another issue hindering the application of the former noble metal-based catalysts is their high costs. A study of Abbott et al. on IrO_x NPs confirmed that with reducing particle size (i.e., increasing active surface area), an increase in the OER activity is observed. Nevertheless, the decrease in the NP size had also a concomitant detrimental effect on catalyst stability. XAS measurements at the Ir L_3-edge revealed that Ir was in a lower oxidation state (closer to 3+) in the smaller IrO_x NPs (ca. 1.7 nm) as compared to the bulk-like catalyst. This difference (and also the enhanced activity for smaller NPs) was attributed to surface-effects and in particular, to the formation of hydroxo- species at the particle surface. Under reaction conditions, the small IrO_x NPs were reversibly oxidized to the 4+ state, as suggested by the shift of the absorption edge to higher energy values and a reduction in the Ir−O interatomic distance (Figure 38b).[564] Similar trends were observed in an *operando* XAS study of 1−2 nm large IrO_x NPs deposited on TiO_2.[568] However, in this case, the oxidation of the IrO_x NPs under OER was irreversible, and this catalyst was more stable than the unsupported IrO_x NPs described above.[564]

Another approach to reduce the catalyst costs is the synthesis of core−shell NPs with the shell made of a noble metal and the core consisting of an earth-abundant materials. Tackett et al. proposed NPs with an Ir shell and a core consisting of Fe_4N. Because of the inability of iridium to form nitrides, Ir segregates to surface and a stable catalyst structure is expected. *Operando* XAS studies at the Ir L_3-edge and Fe K-edge confirmed that the nitride core remained stable under OER conditions, while Ir−Fe bonding was confined only to NP surface.[569] Alternatively, the catalysts price can be reduced by dispersing the IrO_x catalyst in a low-cost matrix, for example, the IrO_x-SnO_2−Ta_2O_5 catalyst.[570] Here *ex situ* EXAFS data collected at Ir L_3-edge showed that the majority of the Ir species in the resulting catalyst are in a highly distorted environment, consistent with the structure of rutile-type SnO_2, suggesting Ir-doped SnO_2 as an important active site in this material.[570]

Highly complementary information about noble metal-based OER catalysts can be extracted from O K-edge XAS data. By comparing spectra for rutile-type IrO_2, and those for more catalytically active amorphous and Ir-deficient IrO_x samples, substantial differences were observed by Pfeifer et al. (Figure 38c).[571,572] By employing *ab initio* simulations of XAS spectra, the additional feature at 529 eV was identified as originating from holes in O 2p-states resulting in formally a 1- oxidation state for the oxygen species. These species are believed to be highly active and directly involved in the formation of O−O bonds during OER. In a follow-up work, authors reported the
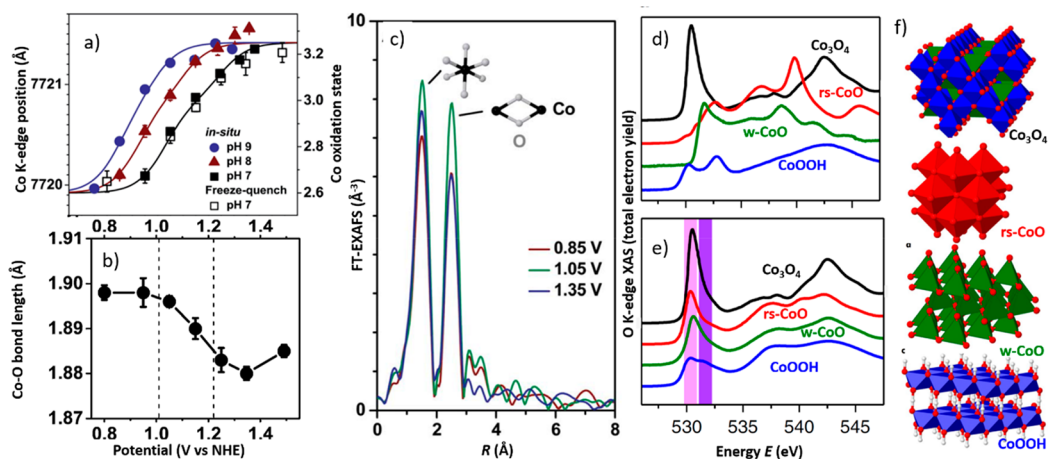
Figure 39. (a−c) *In situ* XAS results obtained at different pHs as well as results of freeze-quench measurements at pH = 7. (a) Changes in the Co K-edge XAS for amorphous CoO$_x$ catalysts. Potential-dependent changes in the Co K-edge position and corresponding estimated Co oxidation state are shown. (b) Evolution of the Co−O interatomic distance under applied potential as obtained from the fitting of Co K-edge EXAFS data collected with the freeze-quench approach at pH = 7. (c) Potential dependent changes in *in situ* Co K-edge EXAFS spectra acquired at pH = 9. Republished from ref 580 with permission of Royal Society of Chemistry; permission conveyed through Copyright Clearance Center, Inc. (d, e) Evolution of the O K-edge XAS spectra for four model catalysts. The spectra collected before and after OER conditioning are shown in panels d and e, respectively. Shaded regions in panel e highlight the XANES features at 530.5 and 531.5 eV. Corresponding structure models of the as-prepared catalysts are shown in panel f. Reprinted by permission from Springer Nature, ref 574 (2018).

formation of these species (and corresponding feature in the O K-edge XAS) also under an applied potential at the Ir electrode.[573] An alternative interpretation was, however, proposed by Frati et al., who suggested that the observed changes in the O K-edge XANES can be rather attributed to the formation of Ir^{5+} species in the presence of Ir vacancies.[83]

Ref 19 and the studies cited therein include additional examples of *operando* XAS studies of Ir-based catalysts.

6.3.3. Active Species in Transition Metal Oxides and (Oxy)hydroxides. Remarkable activity for OER was observed in transition metal-based oxides, hydroxides, and related materials. Moreover, the different oxidation states of the metal encountered in these materials (often coexisting within the same structure), and a multitude of possible different structures, phases, and structural motifs provide enormous possibilities to tune the properties of these catalysts.[549,551] Ni- and Co-based oxide materials are considered to be the most active for OER due to their optimal binding to oxygen species and reaction intermediates.[551] Because of their applicability for OER in neutral pH-conditions, Co-based materials are particularly attractive.[574]

Ordered pristine bulk Co oxides are believed to be inactive for OER, and the observed catalytic activity is commonly associated with the presence of defects, undercoordinated sites, and amorphous phases.[549] Good electrocatalytic performance requires also a good electrical conductivity, which may be insufficient in some bulk oxides. Therefore, different routes have been proposed to prepare efficient Co-based catalysts. Among recent examples, one can mention the formation of Co$_3$O$_4$-graphene composites[575] and Co$_3$O$_4$ nanocrystals supported on carbon nanotubes,[576] the activation of Co-species in metal−organic frameworks by plasma treatment,[577,578] and the preparation of amorphous CoO$_x$ clusters from biopolymers.[579] Nevertheless, the disordered nature of the active catalysts in all of these examples limits the applicability of many experimental tools, such as X-ray diffraction. At the same time, Co K-edge XAS data provided useful insight into the structures of the as-prepared catalysts

and confirmed the disordered structures of the Co−O structural motifs. However, significant structural changes in these catalysts are expected under working conditions, and, thus, *operando* measurements are essential.[549] An alternative, often used in the studies of OER catalysts, are *quasi in situ* measurements, that is, so-called freeze-quench approach where the catalyst is rapidly frozen under applied potential by immersing it in liquid nitrogen to preserve its state, and then disconnected from the electrodes. As shown in Figure 39a, at least for some material systems such an approach was demonstrated to yield similar results as the *in situ/operando* measurements but allows the collection of EXAFS data of better quality.[580] Both *operando* and *quasi in situ* XAS measurements have been instrumental for probing the active state of Co-based OER catalysts.

Distinguishing between different cobalt oxide structures by EXAFS analysis is often a challenging task. Because the difference in the number and lengths of Co−O bonds in the first coordination shell for different oxide phases is low, such an analysis often relies on the interpretation of contributions of further coordination shells, which, as discussed in Section 5.6, can be problematic. Interpretation of EXAFS data becomes especially challenging in a situation common in OER studies, where different disordered oxide phases coexist within the catalyst. Therefore, caution, is needed when a particular feature of the EXAFS spectrum (or a small change in this feature) is attributed to the development of a specific structural motif, and some of the published studies may suffer from the data overinterpretation.

Nevertheless, results of numerous EXAFS experiments for different Co-based oxides point to the same general trend, namely, the formation of CoOOH species consisting of edge-sharing CoO$_6$ structural units under reaction conditions (high pH or high anodic potential), which are believed to be the active phase for OER.[549,551] The fingerprints of these structural motifs in EXAFS spectra collected under OER conditions, namely, the characteristic interatomic distances and shapes of the main peaks in FT-EXAFS spectra are shown in Figure 39b
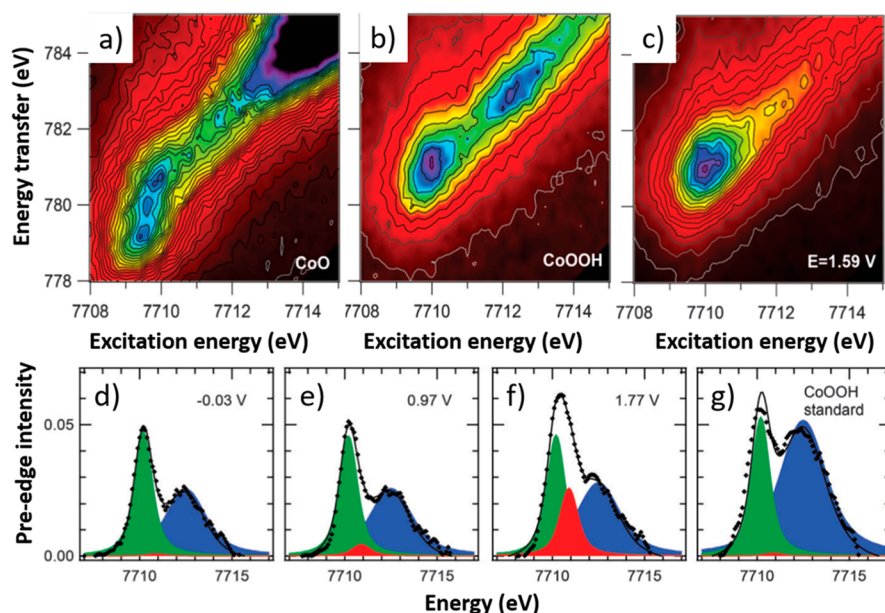
Figure 40. RIXS spectra of the 1s to 3d transition for (a) CoO, (b) CoOOH, and (c) CoO$_x$ catalyst under OER conditions at 1.59 V (RHE). (d−f) Experimental HERFD XAS pre-edge features acquired at the potentials indicated and (g) for CoOOH reference, and their fits with three pseudo-Voight profiles. Reproduced from ref 384 with permission of Royal Society of Chemistry; permission conveyed through Copyright Clearance Center, Inc.

and c. The importance of such structures for OER catalysis has been demonstrated in a number of *in situ* and *quasi in situ* studies of phosphate-derived amorphous cobalt oxide catalysts (Co-Pi),[580−582] Co-based perovskites,[583] oxychloride-derived Co oxide catalysts,[584] CoO$_x$ NPs,[585] Co$_3$O$_4$/CoO core−shell structures,[586] and pure Co$_3$O$_4$ spinel structures.[244,587] The latter case seems to be special because of the thermodynamic stability of the spinel structure. More importantly, by employing the freeze-quench XAS approach in combination with *in situ* X-ray diffraction, Bergmann et al.[244] showed that the transformation of Co$_3$O$_4$ to a CoOOH-like amorphous structure under OER conditions is reversible and that the spinel structure is recovered after reaction.[244] In a follow-up study from the same group,[574] by comparing the *in situ* transformations under OER conditions in four well-defined model catalysts (Co$_3$O$_4$ with spinel structure, CoO with rocksalt (rs-CoO) and wurtzite-type (w-CoO) structure, as well as CoOOH with low crystallinity[574]), the formation of a surface CoO$_x$(OH)$_y$ layer was observed in all cases. However, unlike the case of Co$_3$O$_4$, the structural changes in other model compounds were irreversible, and were especially pronounced in w-CoO. Considering the aforementioned ambiguity of the interpretation of distant coordination shell contributions to the Co K-edge EXAFS spectra, a useful complementary information can be extracted from O K-edge analysis. Here, the differences in the oxide structures result in significantly different spectral features (Figure 39d−f). Moreover, by collecting O K-edge data in the total electron yield mode, surface specific information about *operando* catalyst transformations can be obtained. For example, significant changes in the O K-edge XAS spectra for the Co$_3$O$_4$, rs-CoO, w-CoO, and CoOOH model catalysts were observed after OER conditioning. By using *ab initio* XAS simulations, the dominant feature visible in the spectra for all catalysts under reaction conditions at 530.5 eV, Figure 39e, was attributed to 3- or 4-coordinated O species characteristic for octahedral structural units. A second feature at ~531.5 eV was attributed to 2-fold

coordinated bridging oxygen species at the edges and corners of CoO$_x$(OH)$_y$ domains, which were found to be important for fast OER processes.[9,574]

The structural transformation of cobalt oxides under OER conditions is accompanied by an increase in Co oxidation state, which results in a potential- and pH-dependent shift of the Co K-edge XANES features (Figure 39a).[580−582] Under OER conditions, the oxidation state of Co within the catalytically active CoOOH units is believed to be close to 3+,[580−582,588] although reports showing oxidation state >3+ also exist.[582] However, the definition of the absorption edge position is ambiguous, and changes in materials structure can also result in the shift of the absorption edge position. For example, according to eq 15, a decrease of the interatomic distances will also result in a positive shift of the XANES features. Moreover, since the increase of the oxidation state is often accompanied by a reduction of the interatomic distances, Figure 39b, it might be hard to disentangle both contributions simply based on a comparison with reference compounds. Therefore, accurate quantitative determination of the Co oxidation state from Co K-edge XANES is challenging, especially if the increase in the oxidation state is paralleled by significant structural changes. In such cases, the observed spectra may not be directly fitted with a linear combination of reference spectra for standard compounds with well-defined oxidation states. Friebel et al. proposed the analysis of pre-edge features at the Co K-edge as a more robust tool to monitor the Co oxidation state.[384] By employing advanced RIXS spectroscopy, significant differences in the RIXS spectra for reference materials with different oxidation states were observed (Figure 40a,b). The RIXS spectrum for electrodeposited CoO$_x$ catalyst under OER conditions, Figure 40c, exhibited similarity with that of CoOOH. However, the broad feature observed in the CoOOH spectrum at an excitation energy ~7713 eV, attributed to the nonlocal transitions to 3d states, was less pronounced in the spectrum of the CoO$_x$ catalyst. Moreover, potential-dependent changes in the pre-edge in HERFD-XAS
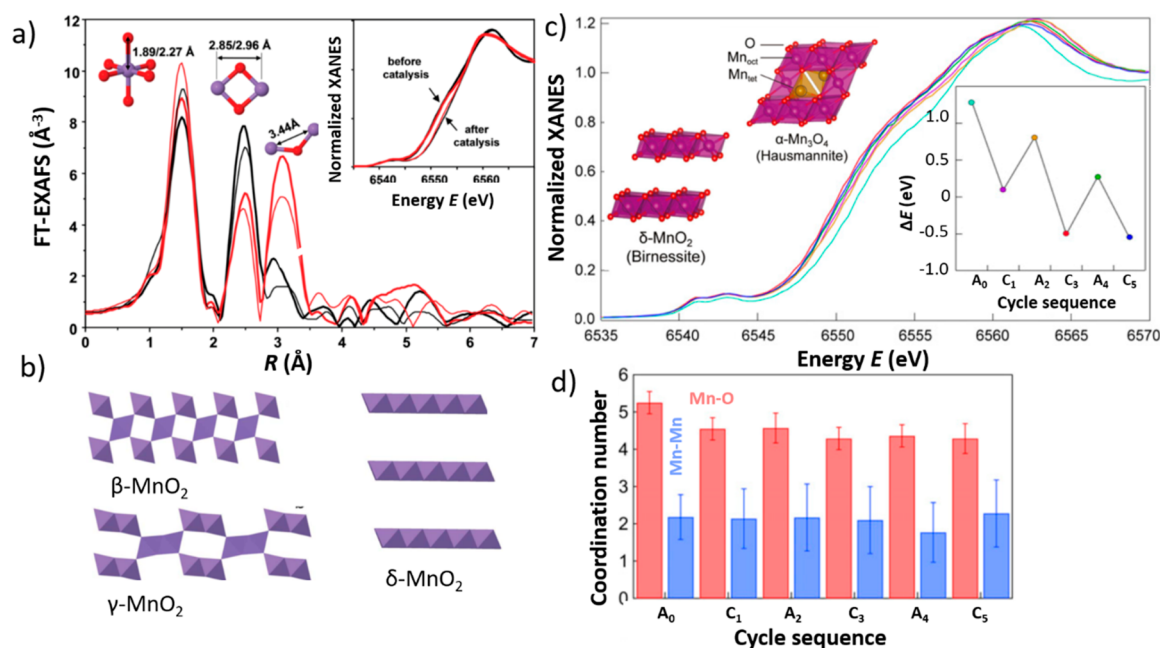
Figure 41. (a, b) Effect of the synthesis parameters on the structure of MnO_x catalysts for OER. (a) Mn K-edge EXAFS and XANES (inset) after deposition on the electrode (thick lines) and after 3 min at 1.76 V in 0.1 M K_2HPO_4 and 0.1 M KH_2PO_4 mixture for samples prepared via the synproportionation method (black lines) and impregnation-based synthesis (red lines). The former results in a structure dominated by edge-sharing octahedra, as in δ-MnO_2, while the latter leads to corner-sharing structure units as in β-MnO_2 and γ-MnO_2, as shown in panel b. Reproduced from ref 589 with permission of Royal Society of Chemistry; permission conveyed through Copyright Clearance Center, Inc. (c, d) Activation of δ-MnO_2 films by incorporation of Mn^{3+} species. (c) *In situ* Mn K-edge XANES after applying a sequence of potential pulses between 1.1 and −0.4 V (NHE). The inset shows the edge position after a sequence of pulses terminated at an anodic ("A") or a cathodic ("C") potential. (d) Changes in Mn−O (red) and Mn−Mn (blue) coordination numbers, as extracted from EXAFS data fitting signifying the transition from a δ-MnO_2-like structure to a spinel-like α-Mn_3O_4 phase (structure models are shown in the insets in panel c). Adapted with permission from ref 590.

were observed (Figure 40d−f). These changes were explained by a gradual increase in the intensity of an additional feature in the Co K-edge XAS that is not observed in the CoOOH spectrum (Figure 40g). The latter, based on DFT simulations, was attributed to a contribution of Co^{4+} species. Interestingly, the presence of Co^{4+} species was concluded to be rather detrimental for OER activity.[384]

Other transition metal oxides have also been investigated for applications in OER, and edge-sharing metal−oxygen octahedra are believed to be the key structural motifs in many of them.[589] For example, Mn-based oxides attract attention because of their potential for applications in acidic media, low toxicity, and the very large diversity of possible structure models.[549,590] For instance, the effect of the MnO_x catalyst synthesis route on its structure and OER performance was explored.[589] By comparing Mn K-edge EXAFS spectra, a significant difference in the contributions of distant coordination shells was observed for catalysts prepared by a chemical synproportionation method (i.e., from a solution containing Mn precursors in 2+ and 7+ oxidation states)[591] versus an impregnation-based synthesis (from Mn^{2+} precursors), Figure 41a, despite the fact that the resulting Mn oxidation state was similar in both catalysts (ca. 3.5, according to XANES analysis). Moreover, the EXAFS signal of the catalyst prepared by the former method was dominated by fingerprints of edge-sharing octahedral structural motifs, while for the catalysts prepared by impregnation, a significant number of corner-sharing octahedral units was suggested (Figure 41b). Interestingly, a higher intrinsic OER activity was observed for the catalysts prepared via the synproportionation method containing predominantly edge-sharing octahedra. Under

reaction conditions, the Mn average oxidation state increased up to ~4, paralleled by a decrease of the Mn−O interatomic distances. However, no significant changes in the catalyst structure were observed. Recently, the presence of edge-sharing MnO_6 structural units was detected by EXAFS analysis also in the study of OER-active mesoporous MnO_2 prepared by thermal treatment on manganese carbonate,[592] and in MnO_x catalysts prepared by a spray process.[593]

In all of these cases, a prominent role for ensuring high OER activity was attributed to Mn^{3+} species, with MnO_2 oxide considered catalytically inactive.[594] Unfortunately, Mn^{3+} species are thermodynamically unstable under reaction conditions. Recently, Chan et al. have demonstrated that Mn^{3+} can be introduced into MnO_2 films and be kinetically stabilized within tetrahedral sites through a synproportionation reaction between MnO_2 and $Mn(OH)_2$.[590] In their work, a MnO_2 film was electrodeposited, and Mn^{3+} species were introduced by alternating the potential between 1.1 and −0.4 V (NHE) in the presence of Mn^{2+} and NO_3^- ions in the electrolyte. Changes in the Mn K-edge position confirmed the incorporation of Mn^{3+} species, Figure 41c, while a gradual decrease of the Mn−O coordination number (from the original value of 6, Figure 41d), suggested that Mn is incorporated in tetrahedrally coordinated sites, forming a spinel-like structure.[590] The oxidation state of Mn can also be controlled by introducing another metal. For example, it was demonstrated that having Au NPs in the MnO_x films increases the Mn oxidation state in the as-prepared state as well as under OER conditions and promotes the OER activity.[595] More common are OER catalysts where a transition metal is combined with another 3d metal, resulting in unique structural
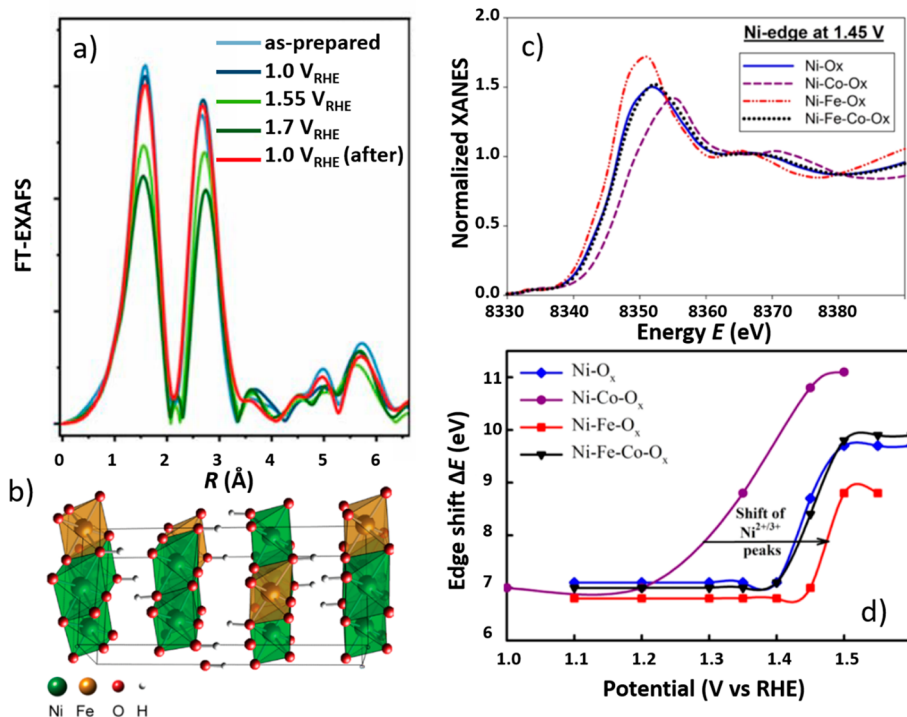
Figure 42. (a) Response of Ni−Fe oxide catalysts to OER conditions: changes in Ni K-edge EXAFS, signifying a partial transformation from the α-Ni(OH)$_2$-like phase to Fe-doped γ-NiOOH. Reproduced from ref 600 under Creative Commons Attribution 4.0 International License: https://creativecommons.org/licenses/by/4.0/. The corresponding structure model of the active catalyst phase is shown in panel b. Reproduced with permission from ref 245. Copyright 2015 American Chemical Society. (c, d) Effect of Co and Fe on the Ni oxidation state in Fe−Ni−Co oxide catalysts. (c) *In situ* XANES data collected at the Ni K-edge under OER conditions and (d) corresponding shifts of Ni K-edge as a function of the applied potential. Reproduced with permission from ref 601. Copyright 2016 American Chemical Society.

motifs. Examples of such catalysts are discussed in the next subsection.

6.3.4. Mixed Metal Oxide Catalysts. Adding a second metal in the transition metal-based OER catalyst can improve significantly its catalytic properties. In particular, bimetallic oxides have attracted significant attention by outperforming the corresponding monometallic counterparts.[549,551] Among others, Ni−Fe oxide electrocatalysts are considered very promising catalysts for OER in alkaline conditions. While the performance of pure iron oxides for OER is poor (in part, because of their low electrical conductivity),[551,552,596] the addition of iron to nickel oxides results in one of the most active catalysts among all nonprecious metal systems.[550] However, the nature of the actual active species in these catalysts remains controversial.[550,596]

This controversy, and insights from operando XAS to address it, are discussed in a great detail in the recent review by Zhu et al.[597] The problems related to the determination of the active sites in NiFe is discussed also in the recent reviews by Dionigi et al.,[598] Gong et al.,[550] Bandal et al.,[596] as well as featured in other excellent recent publications.[8,18,19,552,553] To avoid redundancy, we refer the reader to these reviews and the references therein. Briefly, the *operando* XAS studies carried out during the last decades have emphasized the role played by Ni-species, in particular, that of different phases of NiOOH.[245,599,600] The active role of Fe substitutions in NiOOH for tuning the oxidation state of Ni[251,601,602] as well as the response (further oxidation) of Fe species themselves under OER conditions were also discussed.[318,600,603−605]

The problem in obtaining conclusive answers from XAS studies of this class of materials stems, in part, from the

coexistence of different structural motifs within the catalyst, and the fact that only a fraction of the metal sites that contribute to the measured spectrum might contribute and in fact determine the catalytic activity. In this situation, a combination of *in situ* XAS with other techniques is very helpful. For example, very recently, the input from electrochemical measurements, *operando* wide-angle X-ray scattering (WAXS) and DFT simulations was used to interpret the changes in the *operando* Ni K-edge EXAFS data, namely, the decrease in the amplitude of the main FT-EXAFS peaks and the contraction of interatomic distances under applied potential (Figure 42a,b). The observed changes under OER conditions were attributed to a partial transformation from the α-Ni(OH)$_2$-like structure with intercalated water molecules and ions between the Ni(OH)$_2$ layers to a γ-NiOOH-like phase. However, the transformation was not complete, and a contribution of the α-Ni(OH)$_2$ phase was still present in WAXS data collected under OER conditions.[600] The need for complementary approaches that are sensitive to structural transformations on different length scales is expected to be even more pressing in the future due increased morphological, structural, and chemical complexity of the new OER catalysts that are being developed. This includes Fe−Ni catalysts such as nanotubes[606] and nanotube arrays,[607] supported NiFe clusters,[608] ultrathin films,[609] NiFe Prussian blue analogues,[610] hybrid catalysts combining Au single atoms with NiFe double hydroxide supports[611] and others.

Relatively less studied remain other multimetallic oxide catalysts for OER. Ni−Co and Fe−Ni−Co catalysts have attracted attention because of their high electrical conductivity and OER activity that surpassed that of pure Co oxides.[549] The

main role in their activity, is, however, played by Ni and Fe species, with Co species contributing indirectly by tuning the oxidation state and the local structure around the active sites. The passive role of Co species was suggested in several *in situ* XAFS studies revealing that while Ni species respond to the applied potential and get oxidized forming a NiOOH-like phase, none or only minor changes are visible in the local structure or oxidation state of Co.[601,612] At the same time, as demonstrated by Bates et al., the introduction of Co lowered the potential at which Ni oxidation occurred, Figure 42c and d,[601] and resulted also in a shortening of the Ni−O (as well as Fe−O in Ni−Fe−Co catalyst) bonds. In this study, among the catalysts compared, the highest OER activity was observed for the Fe−Ni−Co system, suggesting that while the presence of Co modifies the electronic state and local structure around Ni, and may induce the strain in the structure, the Fe species are the key to ensure the activity in this trimetallic catalyst.

Co−Fe oxides have been also proposed in several studies. However, the role of Fe and whether it really improves the catalytic properties of cobalt oxides remain under discussion.[596] The majority of the existing studies on Co−Fe systems highlight the role of edge-sharing CoO_6 octahedra, similarly as in pure CoO_x catalysts. For example, *ex situ* EXAFS analysis revealed a disordered arrangement of metal-O_6 octahedra as the main structural motif in acid-etched layered double Co−Fe hydroxides.[613] Amorphization and the formation of edge-sharing CoO_6 units under OER conditions were observed also in Ca_2FeCoO_5 perovskite-type catalysts.[614] Good agreement between Co K-edge XANES and EXAFS, and those for a CoOOH reference was observed also in the study of Pb−Co−Fe catalysts.[615]

At the same time, several studies emphasized the role of Fe species in Co−Fe oxide catalysts, reporting that CoOOH-like structural motifs were only needed to ensure sufficient electrical conductivity. An *operando* XAFS study comparing several electrodeposited CoO_x, FeO_x, and $CoFeO_x$ catalysts revealed that despite the clear differences observed in the catalytic activity, the Co K-edge XAFS spectra for materials with and without Fe were almost identical. At the same time, the Fe−O coordination number showed a correlation with the catalyst activity, with catalysts with a lower Fe−O CN exhibiting higher activity, suggesting the importance of undercoordinated Fe-based structural motifs for the catalyst working mechanism.[616] Moreover, the further oxidation of Fe^{3+} species to a higher oxidation state was described, implying a high electrochemical activity of these sites.[617,618]

However, several recent studies emphasized the importance of the synergy between Co and Fe species in ensuring high OER activity of the Co−Fe catalysts. EXAFS measurements for CoOOH nanosheets arrays suggested the incorporation of Fe-species within the CoOOH material,[619] and systematic changes in the Fe K-edge EXAFS spectra with increasing Co to Fe ratio in layered double hydroxide catalysts were observed, suggesting a strong interaction between the Fe and Co species.[555] A recent study also demonstrated that similar structural transformations take place in Co−Fe layered double hydroxide catalysts under OER conditions as in Ni−Fe catalysts, and DFT simulations revealed that Co−O−Fe centers in Co−Fe catalysts provide similar stabilization of OER intermediates as Ni−O−Fe centers in the Ni−Fe catalysts.[600] For Co−Fe catalysts with spinel-like structure, Smith et al. proposed an interesting model with multiple active sites, where the incorporation of Fe played a dual role.[620] First,

in the as-prepared samples the addition of Fe affected the oxidation state of Co, with the average oxidation state of the Co species being reduced (becoming closer to 2+) with increasing Fe concentration. Under OER conditions, the Co^{2+} species became oxidized, forming edge-sharing $Co^{3+}O_6$ structural units that are active for OER. At the same time, this catalyst was also shown to feature a second type of active site, where Fe played a more direct role, namely, edge-sharing $Fe^{3+}O_6$−$Co^{3+}O_6$ octahedra.[620]

Overall, the addition of a secondary metal in spinel-like Co_3O_4 is a common route to tune the catalyst properties. As discussed in Section 5.6, in pure Co_3O_4, the tetrahedral sites are occupied by Co^{2+} species, while the octahedral sites are occupied by Co^{3+}. However, this can be controlled by the addition of another metal such as Fe in the example above, Zn or Al. Oxidation states of Zn and Al are 2+ and 3+, respectively, and they are expected to replace Co species with the corresponding oxidation state. As a result, the addition of these OER-inactive metals results in an increased (in the case of Zn) and decreased (in the case of Al) average oxidation state of Co, as confirmed by XANES measurements.[332] Moreover, EXAFS analysis revealed that the spinel structure is preserved upon such a substitution, with Zn and Al displacing Co from tetrahedral and octahedral sites, respectively. This allows one to identify the more catalytically relevant site. Indeed, by performing *operando* XAS measurements, no changes at the Co K-edge in $ZnCo_2O_4$ were observed, while Co in $CoAl_2O_4$ was oxidized under OER conditions, suggesting the formation of the catalytically active CoOOH phase and highlighting the importance of tetrahedrally coordinated Co^{2+} species,[332] in accordance with the results for the Fe−Co spinel from ref 620. Interestingly, a previous study of $ZnCo_2O_4$ catalysts yielded somewhat conflicting results.[330] While in this case XANES and EXAFS analysis confirmed similar well-ordered normal spinel structure, and no changes in the Co and Zn oxidation states were observed under OER conditions, higher OER activity was observed for $ZnCo_2O_4$ than for Co_3O_4.[330] The enhanced activity in the bimetallic catalyst was partially attributed to the leaching of the Zn species, which resulted in a structure with a high number of vacancies, facilitating the formation of the active CoOOH phase at the catalyst surface.[330] The role of Zn in ensuring a defect-rich structure favorable for OER was observed also in the study of Co−Zn oxyhydroxides,[621] where it was also found that the presence of Zn facilitates the stabilization of higher oxidation states of Co, as follows from the systematic shifts in the Co K-edge XANES data with increasing Zn doping.[621]

6.3.5. Non-oxide Catalysts for OER.

In addition to transition metal oxides, phosphides, nitrides, chalcogenides and borides have also been proposed as promising catalysts for OER. The advantage of these systems is their significantly higher electrical conductivity. At the same time, due to the fact that these materials are thermodynamically less stable under OER conditions than the respective oxides, they might get oxidized under reaction conditions, and consequently, the actual active species might be again the oxides, hydroxides and oxyhydroxides formed on their surface.[551,596,622] XAS data available for these materials confirm this hypothesis. For example, a pronounced metal−P contribution was observed in the EXAFS spectra for the as-prepared highly conductive amorphous NiFeP,[623] Fe−Co−P,[624] and porous Fe−Co−P nanobox catalysts.[625] However, after their exposure to OER
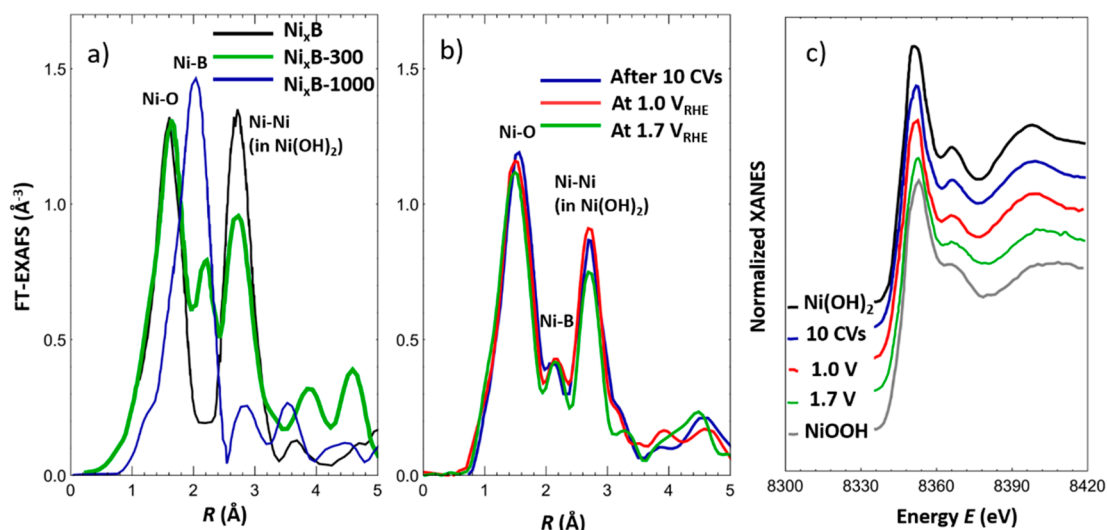
Figure 43. (a) Annealing effect on the Ni K-edge EXAFS spectra of Ni_xB catalysts: results from an as-prepared sample are compared with those for samples annealed in Ar at 300 °C (Ni_xB-300) and 1000 °C (Ni_xB-1000). *Operando* Ni K-edge (b) EXAFS and (c) XANES spectra for the Ni_xB-300 catalyst collected under OER conditions after conditioning (10 CVs) and at different applied potentials. Adapted with permission from ref 554. Copyright 2017 WILEY-VCH Verlag GmbH and Co. KGaA, Weinheim.

conditions, the formation of oxide and hydroxide species was observed, as evidenced by shifts in the respective absorption edges and the appearance of metal−oxygen contributions in the EXAFS spectra.[624,625] Similarly, the oxidation of the Co species and the formation of a CoOOH-like surface layer after exposure to reaction conditions were observed via XAS in another promising catalyst for OER, namely Co_4N nanowires.[626]

Good catalytic activity was demonstrated by Masa et al. also for cobalt-[627] and nickel borides.[554] In the cobalt boride sample, the Co K-edge EXAFS data of the as-prepared sample were dominated by metallic Co, with a relatively weak contribution of Co−B bonds.[627] However, the expanded interatomic distances detected confirmed the presence of the boride. Nevertheless, CoO_x species were detected by XPS on the catalyst surface after OER. However, since these measurements were done *ex situ*, reoxidation of the catalyst could not be excluded. For the Ni boride system, the contribution of metal-B bonds could be significantly enhanced with increasing annealing temperature, Figure 43a,[554] with the optimal OER activity observed for the Ni_xB sample heated at 300 °C. *Operando* XAS measurements for this sample carried out at 1.7 V revealed that the oxidation state of Ni increases from ∼2+ to ∼3+. In addition, the contribution of Ni−B to the EXAFS spectra was not affected by the exposure to the reaction conditions, while the contribution of the oxide phase changed (the corresponding Ni−O and Ni−Ni CNs were reduced), suggesting structural transformations involving an increase in the disorder and transformation of the original $Ni(OH)_2$-like phase to the active NiOOH (Figure 43b,c).[554]

6.3.6. Catalysts for Bifunctional Oxygen Electrocatalysis. For practical applications (for example, in rechargeable metal−air batteries), the design of a bifunctional catalyst which enables both OER and ORR reactions has attracted attention. One promising material is manganese oxide, which exhibits a large number of different phases, and allows one to tune its properties to find a balance between the requirements for OER and ORR processes.[18,110,518] Using *in situ* XAS at the Mn K-edge, Gorlin et al. investigated

electrodeposited MnO_x catalyst and demonstrated that Mn is present in different oxidation states and within different structures under ORR and OER regimes (at 0.7 and 1.8 V vs RHE, respectively). Under ORR conditions, the absorption edge of Mn could be well aligned with that of Mn_3O_4, and the corresponding EXAFS spectra featured fingerprints of the spinel-like structure. Under OER conditions, the oxidation state of Mn was increased, and both XANES and EXAFS features resembled those for birnessite, a mixed oxide containing Mn^{3+} and Mn^{4+} species, see Figure 44a.[518] In a related study, Gul et al. used *in situ* XAS and XES to investigate the structural and chemical transformations of $MnNiO_x$. The presence of Ni resulted in an increased oxidation state for Mn, and the birnessite-like structure and the +3/+4 valence for Mn species was already observed at ORR conditions, while under OER potentials the oxidation of Mn to the 4+ state and the formation of a MnO_2-like phase was observed in Mn K-edge XANES and EXAFS, respectively. Analysis of the Ni K-edge position suggested an average oxidation state between +2 and +3 under ORR conditions, and ∼+ 3.7 under OER conditions. The corresponding local structure around Ni probed by EXAFS revealed transformations similar to the transition between $Ni(OH)_2$ and γ-NiOOH.[110]

The incorporation of another metal to control the catalyst oxidation state is exploited also in another class of bifunctional catalysts such as complex perovskites. Jung et al. investigated nanostructured $La_x(Ba_{0.5}Sr_{0.5})_{1−x}Co_{0.8}Fe_{0.2}O_{3-d}$ materials and used EXAFS to study the effect of the calcination temperature on its structure, demonstrating that no significant structure degradation takes place after 100 charging/discharging cycles.[628] One can note here that the element-specificity of the XAS method is of great advantage for studies of such complex multielement systems.

Nevertheless, perovskite-based catalysts, have a relatively low ORR activity. An alternative class of materials that do not suffer from this limitation, but still preserve the high tunability of their properties are pyrochlore materials.[629] Park et al. investigated crystalline $Pb_2Ru_2O_{6.5}$ pyrochlore NPs, which exhibited metallic conductivity and good activity and stability
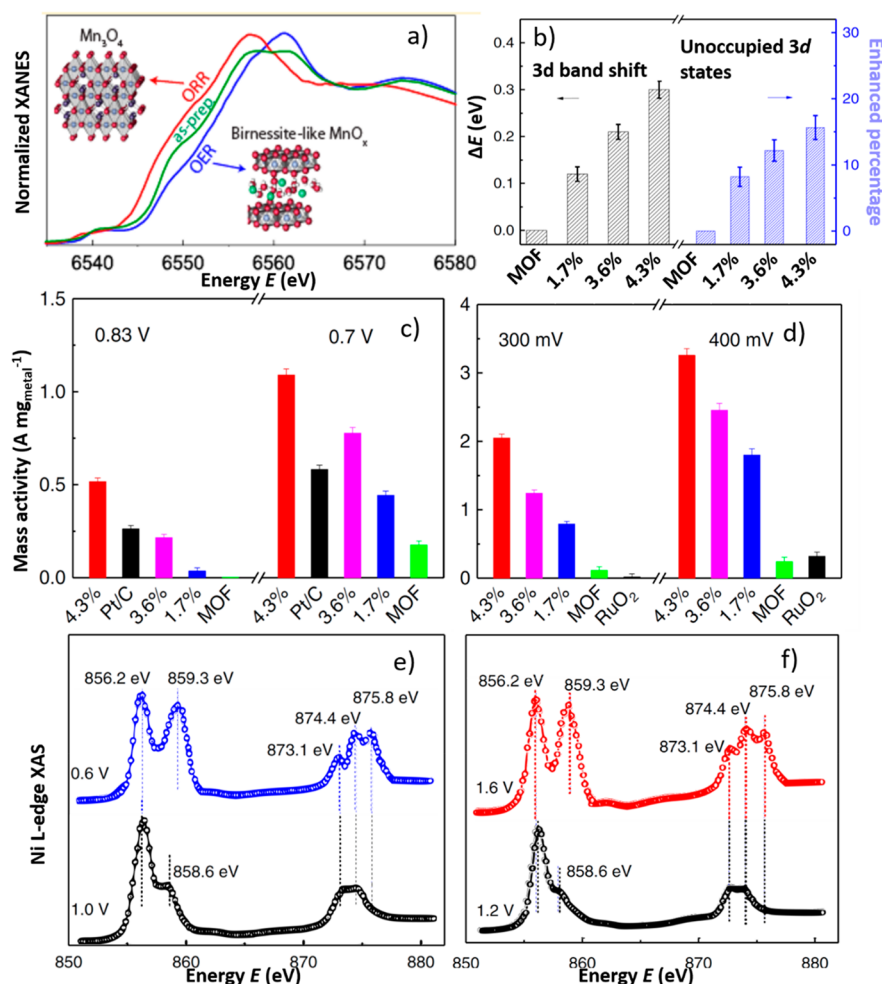
Figure 44. (a) Comparison of Mn K-edge XANES for as-prepared MnO_x catalyst and those for the catalyst under ORR and OER conditions, at 0.7 and 1.8 V (vs RHE) applied potentials, respectively, in 0.1 M KOH electrolyte. The corresponding structure motifs are shown in the insets. Reproduced with permission from ref 518. Copyright 2013 American Chemical Society. (b−f) Structure−property relationship in NiFe MOF bifunctional catalysts. (b) Shift and unoccupied states in the Ni 3d band for pristine MOF and lattice strained MOF with lattice expansion 1.7, 3.6 and 4.3% obtained from Ni XAS analysis. (c) Comparison of mass activities for the MOF catalysts and a Pt reference catalyst under ORR conditions and (d) of the MOF catalysts and RuO_2 reference catalyst under OER conditions. *Operando* Ni $L_{2,3}$-edge XAS collected under (e) ORR and (f) OER conditions, with characteristic features attributed to Ni^{4+} species appearing at ∼859 eV. Reprinted by permission from Springer Nature, ref 115 (2019).

both under ORR and OER conditions.[629] By comparing XANES data collected at the Ru K-edge and O K-edge of the $Pb_2Ru_2O_{6.5}$ catalysts, and of a much less catalytically active $Sm_2Ru_2O_7$, a stronger hybridization of the oxygen 2p orbitals and the Ru 4d states was detected in the more active catalyst, which was attributed to the higher covalency of the Ru−O bonds. Furthermore, shorter bonds (hence, higher oxidation state of Ru) were observed for the as-prepared $Pb_2Ru_2O_{6.5}$. However, no significant changes in the bond length were observed under reaction conditions, suggesting the high stability of the pyrochlore catalysts.[629]

Materials based on metalorganic frameworks were also considered as promising candidates for bifunctional oxygen electrocatalysis. The control of the catalyst properties can be ensured in this case through tuning the lattice strain. Recently, Cheng et al. investigated NiFe MOFs where the strain was controlled via UV irradiation for different amounts of time, which resulted in an expansion of the organic interlayers.[115] Using EXAFS, the octahedral local environment of the Ni species was established, with Ni−O interatomic distances

systematically changing with the induced strain. Moreover, positive shifts of the Ni K-edge XANES were observed with increasing strain, suggesting a charge transfer from Ni to neighboring O species. The Ni $L_{3,2}$-edge spectra, in turn, showed the white line with intensity gradually increasing upon induced strain. Both observations suggest a shift of the d-states energy, and an increasing number of d-state holes in Ni with increasing strain (Figure 44b). The changes in the Ni electronic structure were found to affect the interaction of Ni with the reaction intermediates, leading to an improvement in the catalytic activity for both, ORR and OER (Figure 44c,d). Under *operando* OER and ORR conditions, significant changes in the Ni L_3-edge XAS were observed, Figure 44e and f, which with the aid of theoretical simulations were interpreted as fingerprints of the catalytically relevant Ni^{4+} species.[115]

6.4. Other Electrochemical Reactions

In addition to CO_2RR, ORR and OER, catalysts for other electrochemical reactions have also been actively studied by XAS. For example, *operando* XAS studies have been carried out on catalysts used in the reactions taking place at the fuel cell

anode, that is, oxidation of hydrogen, alcohols, or other small organic molecules. Commonly, Pt-based catalysts are used for these reactions. Applications of XAS for studies of the electrochemical oxidation of ethanol over Pt-based catalysts recently were reviewed by Marinkovic et al.[21] Pt catalysts for methanol oxidation have also been investigated,[157,475] and potential-dependent changes in the shape of Pt L_3-edge WL were observed due to the interaction with adsorbates. At higher potentials, morphological modifications were also revealed for the Pt NPs.

Alloying of Pt with another metal (e.g., Sn or Rh) is a common route to enhance the activity of catalysts for alcohol electrooxidation, especially for ethanol oxidation, which requires breaking a strong C−C bond. The actual local composition of these bimetallic catalysts, the oxidation state of each of the constituent metals, and their respective roles in the catalytic processes, however, remain controversial, and insight from XAS is instrumental to gain fundamental understanding. For example, XAS studies have been employed to address the controversial role of SnO_x species in Pt−Sn and Pt−Sn−Rh catalysts.[21,263,630,631] Alloying of Pt with another metal can help also to reduce Pt poisoning by CO species. Pt−Mo and Pt−Ru catalysts have been actively investigated for this purpose.[632−635] XAS investigations revealed important difference between these catalysts: while the formation of a Pt−Ru alloy is often observed,[635] Pt and Mo usually segregate due to the low miscibility of Mo in Pt.[632,635] In addition to composition and oxidation effects, strain effects in these catalysts due to lattice mismatch can also be important to explain the electronic properties and activity of these catalysts, and can be probed by EXAFS analysis.[21,263,636]

Pd- and Au-based catalysts have also been considered for alcohol electrooxidation reactions due to their enhanced stability against CO poisoning. In particular, in a recent study of Au NPs for 2-propanol oxidation, *operando* XAS measurements revealed the presence of cationic Au species in the as-prepared samples due to a pretreatment in an O_2-plasma. The cationic species, however, quickly became reduced under reaction conditions. Moreover, an increase in the average NP size was observed under reaction conditions, which was linked to the observed decrease in activity.[271]

Another approach to avoid poisoning of fuel cell catalyst is to oxidize the adsorbed CO to CO_2. The electrochemical CO oxidation itself is an important model reaction, and has been extensively studied both theoretically and experimentally.[2,637] For example, *in situ* XAS was employed to probe the changes in the catalyst local structure during this process using size-selected Pt NPs (ca. 1.8 nm) as model catalysts. EXAFS analysis revealed no significant changes in the NP structure under working conditions. Nevertheless, the interactions with CO resulted in subtle changes in the Pt L_3-edge white line, affecting also the surface-induced disorder.[2,351]

Another technologically important reaction is the hydrogen evolution reaction, which takes place at the cathode during the electrochemical water splitting. Pt catalysts are most commonly used for this reaction due to the optimal hydrogen binding energy.[638] However, the high cost of Pt limits its large-scale application. One approach to address this problem is to improve Pt utilization efficiency by using ultradispersed catalysts. For example, in a recent study, a catalyst featuring singly dispersed Pt sites in a porous carbon matrix was found to exhibit good HER activity. Analysis of EXAFS features coupled to wavelet transform confirmed the presence of

isolated Pt sites, while the changes in the Pt L_3-edge WL revealed the charge transfer between Pt and the support, which based on DFT simulations was found to be important for ensuring the high HER activity.[150] Alternative approaches for reducing HER catalyst costs rely on using non-Pt-based catalysts. In particular, various phosphides, sulfides, carbides, nitrides and borides have been proposed.[18] XAS was found to be helpful in revealing the actual structure of these multielement catalysts, for example, the partially oxidized structure of a Co sulfide catalyst,[114] and the structures of Mo carbides, nitrides, and sulfides.[639−641] XAS measurements were helpful also to establish the oxidation states of Cr, Cu, and Ni in a recently proposed multisite CrO_x/Cu−Ni catalyst, which was found to be promising for HER in neutral media.[638]

In the last years, the electrochemical N_2 reduction reaction (NRR) for ammonia synthesis at ambient conditions has also attracted attention. The idea behind the intensive new research efforts on this extremely challenging electrochemical process is the possibility to replace or at least to complement the Haber-Bosch process that currently is used for industrial NH_3 production since the latter requires high pressures (200−350 atm), high temperatures (300−550 °C), and high-purity hydrogen that is currently produced from fossil fuels.[642] However, the inertness of the N_2 molecule and a competition with the kinetically favored HER limit the efficiency of NRR, requiring further improvements in the choice of catalyst and non-aqueous electrolyte.[643] Among others, transition metal-based single atom catalysts have been considered such as Au-based,[644] Ru-based,[645] Ni-based,[646] Fe-based,[647] and Co-based[648] TMNC materials. In all these examples, XANES and EXAFS analysis of the as-prepared samples confirmed the presence of M-N_x motifs that are believed to be important for NRR activity. In some cases, *operando* XAS investigations were also performed, confirming the stability of these moieties under catalyst working conditions.[649] However, further *operando* studies are needed to understand the roles of different species in NRR. More importantly, and as featured in a recent publication,[650] the majority of the ammonia yields reported to date for a variety of catalyst structures/compositions (other than a Li-based system[651]) could not be reproduced when measured under stringent experimental protocols to avoid the detection of other residual ammonia sources. Therefore, this is an open field where significant work will still be needed in the years to come not only to increase the production of ammonia but even more importantly, to ensure that the data collected correspond to ammonia really produced via the NRR process.

7. SUMMARY AND FUTURE OUTLOOK

The examples discussed in this Review illustrate the broad possibilities provided by the XAS method for catalysis research. In particular, XAS has become a method of choice for studies of electrocatalysts, often providing not only key information regarding the structural motifs in the as-prepared precatalysts but also in depth insight into the dynamic chemical, structural, and electronic transformations of the catalysts under reaction conditions.

The increasing popularity of XAS in the field of catalysis is attributed to the widespread availability of powerful X-ray sources, the improvements made in the instrumentation and sample environments as well as the new data analysis tools at our disposal. Moreover, even scientists with moderate XAS training can relatively quickly identify the main features of an XAS spectrum, such as the position of the absorption edge or

the main peaks in the FT-EXAFS data, both of which can immediately provide essential clues about the catalyst oxidation state and overall structure. Quite often such qualitative information is sufficient to gain key insight into the structure and oxidation state of material and its evolution under reaction conditions. At the same time, the availability of *ab initio* codes and user-friendly data analysis packages allows one to easily model and fit at least the EXAFS part of the absorption spectrum. Nevertheless, one needs to be well aware of possible artifacts in the analysis due, for example, to the correlation of different fitting parameters, or to an over-complicated fitting scheme with an excessively large number of fitting variables. Having an excellent fit to the experimental data does not necessarily mean that the chosen model is scientifically meaningful or in any way representative of the material under investigation.

Therefore, one of the most important messages that we hope to convey with this Review is that the seemingly simplicity of the XAS method is often misleading, especially, when *operando* XAS studies are undertaken to study transformations taking place in realistic catalysts under working conditions. The disordered nature of the catalysts, the coexistence of different species within the catalyst, possible multiple active sites, a limited signal-to-noise ratio of the XAS data collected under harsh reaction conditions or in strongly attenuating sample environments, or the lack of sufficient contrast in the XAS spectra for different structural motifs put stringent requirements on the instrumentation but also require that one exerts extreme caution during the data analysis steps.

One of the important consequences of the former complexity is that the findings of the XAS data analysis should be, whenever possible, complemented with the insight from other techniques, that is, other *in situ* and *ex situ* spectroscopic or microscopic methods as well as theoretical modeling. Only by combining the information obtained from the different perspectives provided by these methods can unambiguous answers be gained about the intricate processes that take place in (electro-)catalysts at work. An ongoing trend, which will continue without a doubt in the years to come, is the tighter integration of XAS with complementary techniques. For example, in depth information on functional materials can be gained through the simultaneous acquisition of XAS data and either XES, XRD, SAXS, or NRIXS[652] data in the hard X-ray range, or the collection of soft X-ray XAS in combination with near ambient pressure XPS data.

Furthermore, it is extremely important for *operando* studies to ensure that tools for the online monitoring of the reaction products and evaluation of the catalyst performance are directly available at the beamline. The demand for complementary techniques results also in the need of developing new reaction cells suitable for multimodal characterization, as, for example, XAS combined with *in situ* IR and Raman signal detection. Alternatively, in cases where multimodal characterization tools cannot be applied simultaneously at the beamline, reactor cells should be employed that are compatible with the sample transfer among different experimental techniques without breaking their original environment. An example here is to conduct XAS and TEM studies at different stages of a catalytic process on the same catalyst and within the same reactor cell.

On the data analysis part of the problem, an ongoing trend is the development of tools that allow the integration of the insight from theory (e.g., DFT modeling and molecular dynamics) into the XAS interpretation process. Recent progress in machine learning methods allows one to significantly simplify this process, and to employ artificial intelligence to identify the link between the theoretical models and features in the experimental data.[12] Equally important is the development of model optimization approaches (such as reverse Monte Carlo modeling) that allow one to combine insights from different experimental techniques to construct a single structure model of the catalyst consistent with all available information.

Another trend that we believe will be increasingly important in future *operando* XAS applications is the focus on time-resolved studies. As demonstrated in this Review, tracking the processes taking place in functional materials is within the possibilities of current XAS instrumentation when the characteristic times are on the order of seconds. Such experiments can provide important information about atomic rearrangements and in some cases the charge exchange in an electrochemical system and corresponding changes in the electronic structure of the catalysts. Time-resolved studies can also reveal the presence of short-lived intermediate species, identify reaction rate limiting steps, and, in general, provide clues about the catalyst working mechanisms. In principle, much faster processes can be tracked by XAS by relying on pump-and-probe approaches. There are already some known successful examples, where synchrotron-based XAS was used to monitor the dynamics of excited states in photocatalysts on the time scale of hundreds of picoseconds.[99] However, the requirement for reliable and highly reproducible reaction initiation currently limits the applicability of these approaches in heterogeneous catalysis.

While the fast and ultrafast time-resolved studies attract a lot of attention and excitement, we would like to emphasize also the need for studies of catalyst transformations on much longer time scales. The majority of the current *operando* XAS studies are limited in time by a few minutes or, maximum, a few hours. However, the activation and deactivation/degradation processes in real-world catalysts can take much longer times (hours, days, and even weeks). The understanding of these processes at the atomistic level that can be achieved by XAS is extremely important for practical industrial catalysis applications. The current user access model employed at synchrotron radiation facilities is, however, incompatible with such experiments. When dedicated beamlines are not available, alternative solutions might be provided by the ongoing development of laboratory-based XAS setups.

In addition to time-resolved studies, spatially resolved studies as well as experiments that combine spatial mapping with time-resolved investigations of the catalyst dynamics are also expected to gain importance in the future. This is due to the ability to partially lift one of the most important limitations of the XAS method, its sample-averaging nature. We believe that the potential of such experiments is currently severely underexploited. Despite the fact that proof-of-principle spatially resolved XAS studies of heterogeneous catalysts have been carried out more than a decade ago, the practical application of this approach is still rare. This can be in part attributed to problems of the data analysis. Both time-resolved and spatially-resolved experiments carried out at a modern beamlines can easily result in thousands of spectra and hundreds of gigabytes of data. The capabilities of presently popular XAS data analysis suites are still largely inadequate for even basic systematic analysis and visualization of such data

sets. Thus, the progress in this field will be strongly coupled to the progress in the automatization of data processing and interpretation.

Finally, let us note here that the emphasis on increasingly higher photon flux achievable at the next generation synchrotron radiation facilities will have less of an impact on conventional XAS, which is not considered a particularly "photon-hungry" technique. However, such improvements can be very helpful for advanced X-ray spectroscopies such as HERFD-XAS, RIXS, and XRS. As demonstrated in several examples in this Review, these techniques can provide unique information about the catalyst electronic structure and can be envisioned to become indispensable for understanding important aspects in catalysis such as catalyst−adsorbate interactions. Nevertheless, despite numerous success stories, the HERFD-XAS and RIXS methods remain currently underrepresented in catalyst research, and their full potential is not yet assessed. Again, the data analysis seems to be part of the problem since the interpretation of RIXS features, and even reliable quantitative analysis of features in conventional XANES spectra, is still a challenging task. As demonstrated during the last years, this problem can be successfully addressed via a combination of *ab initio* simulations (which nowadays provide increasingly accurate description of the near-edge part of the absorption spectra) with machine-learning techniques. The latter allow one to establish the relationship between spectral features and descriptors of atomistic and electronic structure even in the absence of explicit analytical models.

It should be clear from this Review that despite the long history of XAS-based *operando* catalyst research, many challenges still remain, making this an exciting field for the new generation of catalysis scientists and spectroscopists to jump in and contribute. The new developments in the field should encompass instrumentation improvements but also data analysis. The rich amount of information that can extracted from XAS data about the catalyst structure, composition, and dynamics under reaction conditions will make any effort in the advancement of new methods particularly rewarding. We envision that the most exciting contributions of *operando* XAS characterization to deciphering the working mechanisms of electrocatalysts are yet to come.

AUTHOR INFORMATION

Corresponding Authors

Janis Timoshenko − *Department of Interface Science, Fritz-Haber Institute of the Max-Planck Society, 14195 Berlin, Germany*; Email: janis@fhi-berlin.mpg.de

Beatriz Roldan Cuenya − *Department of Interface Science, Fritz-Haber Institute of the Max-Planck Society, 14195 Berlin, Germany*; ⓞ orcid.org/0000-0002-8025-307X; Email: roldan@fhi-berlin.mpg.de

Complete contact information is available at:
https://pubs.acs.org/10.1021/acs.chemrev.0c00396

Notes

The authors declare no competing financial interest.

Biographies

Janis Timoshenko is the leader of the "Operando Hard X-ray spectroscopy" group at the Department of Interface Science of the Fritz-Haber Institute of the Max-Planck Society in Berlin, Germany.

He received his PhD in solid state physics in 2015 from the University of Latvia, where he worked under the supervision of Prof. Alexei Kuzmin on the development of advanced approaches to EXAFS data analysis. He then went for postdoctoral positions at the Physics Department of Yeshiva University and the Department of Materials Science and Chemical Engineering of Stony Brook University, New York, USA, where he worked on the *in situ* investigation of nanomaterials using synchrotron radiation under the lead of Prof. Anatoly Frenkel. In 2018, he joined the Department of Interface Science at the Fritz-Haber Institute under the direction of Prof. Beatriz Roldan Cuenya. His primary research interests are synchrotron-based investigations of catalyst transformations under working conditions, as well as the development of simulation-based and machine learning-based approaches for XAS data interpretation.

Beatriz Roldan Cuenya is a Professor and Director of the Interface Science Department of the Fritz-Haber Institute of the Max-Planck Society in Berlin Germany. She received her PhD in solid state physics under the guidance of Prof. Werner Keune in 2001 from the University of Duisburg-Essen, Germany. She then went for a postdoctoral position at the Chemical Engineering Department of the University of California Santa Barbara (USA), where she worked under the supervision of Prof. Eric McFarland from 2001−2003. She joined the University of Central Florida (Orlando, USA) as an Assistant Professor of Physics in 2004, and in 2012 she became a full professor. In 2013, she moved back to Germany and became a Chair Professor of the Solid State Physics/Surface Physics group within the Department of Physics at the Ruhr University Bochum, Germany. In 2017, she became the director of the Interface Science Department at the Fritz Haber Institute. She is an honorary Professor at the Technical University of Berlin, Free University of Berlin, and Ruhr University Bochum (Germany), and distinguished Research Professor at the University of Central Florida (USA). Her research interests include studies of structural, electronic, vibrational, and chemical properties of size- and shape-selected nanostructures and their interfaces with gas and liquid environments using advanced synthesis methods and state-of-the-art *in situ* and *operando* microscopy and spectroscopy characterization techniques.

ACKNOWLEDGMENTS

REFERENCES

(1) Meirer, F.; Weckhuysen, B. M. Spatial and temporal exploration of heterogeneous catalysts with synchrotron radiation. *Nat. Rev. Mater.* **2018**, *3*, 324−340.

(2) Trindell, J. A.; Duan, Z.; Henkelman, G.; Crooks, R. M. Well-defined nanoparticle electrocatalysts for the refinement of theory. *Chem. Rev.* **2020**, *120*, 814−850.

(3) Dou, J.; Sun, Z.; Opalade, A. A.; Wang, N.; Fu, W.; Tao, F. F. Operando chemistry of catalyst surfaces during catalysis. *Chem. Soc. Rev.* **2017**, *46*, 2001−2027.

(4) Vimont, A.; Thibault-Starzyk, F.; Daturi, M. Analysing and understanding the active site by IR spectroscopy. *Chem. Soc. Rev.* **2010**, *39*, 4928−4950.

(5) Grajciar, L.; Heard, C. J.; Bondarenko, A. A.; Polynski, M. V.; Meeprasert, J.; Pidko, E. A.; Nachtigall, P. Towards operando computational modeling in heterogeneous catalysis. *Chem. Soc. Rev.* **2018**, *47*, 8307−8348.

(6) Shi, H.; Lercher, J. A.; Yu, X.-Y. Sailing into uncharted waters: recent advances in the in situ monitoring of catalytic processes in aqueous environments. *Catal. Sci. Technol.* **2015**, *5*, 3035−3060.

(7) Handoko, A. D.; Wei, F.; Yeo, B. S.; Seh, Z. W. Understanding heterogeneous electrocatalytic carbon dioxide reduction through operando techniques. *Nat. Catal.* **2018**, *1*, 922.

(8) Choi, Y.-W.; Mistry, H.; Roldan Cuenya, B. New insights into working nanostructured electrocatalysts through operando spectroscopy and microscopy. *Curr. Opin. Electrochem.* **2017**, *1*, 95−103.

(9) Bergmann, A.; Roldan Cuenya, B. Operando insights into nanoparticle transformations during catalysis. *ACS Catal.* **2019**, *9*, 10020−10043.

(10) Bordiga, S.; Groppo, E.; Agostini, G.; van Bokhoven, J. A.; Lamberti, C. Reactivity of surface species in heterogeneous catalysts probed by in situ X-ray absorption techniques. *Chem. Rev.* **2013**, *113*, 1736−1850.

(11) Billinge, S. J. L.; Levin, I. The problem with determining atomic structure at the nanoscale. *Science* **2007**, *316*, 561−565.

(12) Timoshenko, J.; Frenkel, A. I. Inverting" X-ray absorption spectra of catalysts by machine learning in search for activity descriptors. *ACS Catal.* **2019**, *9*, 10192−10211.

(13) Grunwaldt, J.-D.; Kimmerle, B.; Baiker, A.; Boye, P.; Schroer, C. G.; Glatzel, P.; Borca, C. N.; Beckmann, F. Catalysts at work: From integral to spatially resolved X-ray absorption spectroscopy. *Catal. Today* **2009**, *145*, 267−278.

(14) Seh, Z. W.; Kibsgaard, J.; Dickens, C. F.; Chorkendorff, I.; Nørskov, J. K.; Jaramillo, T. F. Combining theory and experiment in electrocatalysis: Insights into materials design. *Science* **2017**, *355*, No. eaad4998.

(15) Arán-Ais, R. M.; Gao, D.; Roldan Cuenya, B. Structure-and electrolyte-sensitivity in CO2 electroreduction. *Acc. Chem. Res.* **2018**, *51*, 2906−2917.

(16) Gao, D.; Arán-Ais, R. M.; Jeon, H. S.; Roldan Cuenya, B. Rational catalyst and electrolyte design for CO2 electroreduction towards multicarbon products. *Nat. Catal.* **2019**, *2*, 198−210.

(17) Russell, A. E.; Rose, A. X-ray absorption spectroscopy of low temperature fuel cell catalysts. *Chem. Rev.* **2004**, *104*, 4613−4636.

(18) Lassalle-Kaiser, B.; Gul, S.; Kern, J.; Yachandra, V. K.; Yano, J. In situ/Operando studies of electrocatalysts using hard X-ray spectroscopy. *J. Electron Spectrosc. Relat. Phenom.* **2017**, *221*, 18−27.

(19) Fabbri, E.; Abbott, D. F.; Nachtegaal, M.; Schmidt, T. J. Operando X-ray absorption spectroscopy: a powerful tool toward water splitting catalyst development. *Curr. Opin. Electrochem.* **2017**, *5*, 20−26.

(20) Jia, Q.; Liu, E.; Jiao, L.; Pann, S.; Mukerjee, S. X-ray absorption spectroscopy characterizations on PGM-free electrocatalysts: justification, advantages, and limitations. *Adv. Mater.* **2019**, *31*, 1805157.

(21) Marinkovic, N. S.; Li, M.; Adzic, R. R. Pt-based catalysts for electrochemical oxidation of ethanol. *Top. Curr. Chem.* **2019**, *377*, 11.

(22) Wang, M.; Árnadóttir, L.; Xu, Z. J.; Feng, Z. In situ X-ray absorption spectroscopy studies of nanoscale electrocatalysts. *Nano-Micro Lett.* **2019**, *11*, 47.

(23) Timoshenko, J.; Duan, Z.; Henkelman, G.; Crooks, R.; Frenkel, A. Solving the structure and dynamics of metal nanoparticles by combining X-ray absorption fine structure spectroscopy and atomistic structure simulations. *Annu. Rev. Anal. Chem.* **2019**, *12*, 501−522.

(24) Newville, M. Fundamentals of XAFS. *Rev. Mineral. Geochem.* **2014**, *78*, 33−74.

(25) Timoshenko, J.; Jeon, H. S.; Sinev, I.; Haase, F. T.; Herzog, A.; Roldan Cuenya, B. Linking the evolution of catalytic properties and structural changes in copper−zinc nanocatalysts using operando EXAFS and neural-networks. *Chem. Sci.* **2020**, *11*, 3727−3736.

(26) Benfatto, M.; Meneghini, C. A close look into the low energy region of the XAS spectra: the XANES region. In *Synchrotron Radiation*; Mobilio, S., Boscherini, F., Meneghini, C., Eds.; Springer: Berlin, Heidelberg, 2015; pp 213−240.

(27) Rehr, J. J.; Albers, R. C. Theoretical approaches to X-ray absorption fine structure. *Rev. Mod. Phys.* **2000**, *72*, 621−654.

(28) Singh, J.; Lamberti, C.; van Bokhoven, J. A. Advanced X-ray absorption and emission spectroscopy: in situ catalytic studies. *Chem. Soc. Rev.* **2010**, *39*, 4754−4766.

(29) Błachucki, W.; Hoszowska, J.; Dousse, J.-C.; Kayser, Y.; Stachura, R.; Tyrała, K.; Wojtaszek, K.; Sá, J.; Szlachetko, J. High energy resolution off-resonant spectroscopy: A review. *Spectrochim. Acta, Part B* **2017**, *136*, 23−33.

(30) Rehr, J. J.; Kas, J. J.; Prange, M. P.; Sorini, A. P.; Takimoto, Y.; Vila, F. Ab initio theory and calculations of X-ray spectra. *C. R. Phys.* **2009**, *10*, 548−559.

(31) Ankudinov, A. L.; Ravel, B.; Rehr, J. J.; Conradson, S. D. Real-space multiple-scattering calculation and interpretation of X-ray-absorption near-edge structure. *Phys. Rev. B: Condens. Matter Mater. Phys.* **1998**, *58*, 7565−7576.

(32) Kas, J. J.; Jorissen, K.; Rehr, J. J. Real-space multiple-scattering theory of X-ray spectra. In *X-Ray Absorption and X-Ray Emission Spectroscopy: Theory and Applications*; Van Bokhoven, J. A., Lamberti, C., Eds.; John Wiley & Sons, Ltd: Chichester (UK), 2016; Vol. 1.

(33) Rehr, J.; Ankudinov, A. Progress in the theory and interpretation of XANES. *Coord. Chem. Rev.* **2005**, *249*, 131−140.

(34) Guda, A. A.; Guda, S. A.; Lomachenko, K. A.; Soldatov, M. A.; Pankin, I. A.; Soldatov, A. V.; Braglia, L.; Bugaev, A. L.; Martini, A.; Signorile, M.; et al. Quantitative structural determination of active sites from in situ and operando XANES spectra: from standard ab initio simulations to chemometric and machine learning approaches. *Catal. Today* **2019**, *336*, 3−21.

(35) Bazin, D.; Rehr, J. Limits and advantages of X-ray absorption near edge structure for nanometer scale metallic clusters. *J. Phys. Chem. B* **2003**, *107*, 12398−12402.

(36) Bazin, D.; Sayers, D.; Rehr, J.; Mottet, C. Numerical simulation of the platinum L$_{III}$ edge white line relative to nanometer scale clusters. *J. Phys. Chem. B* **1997**, *101*, 5332−5336.

(37) Timoshenko, J.; Halder, A.; Yang, B.; Seifer, S.; Vajda, S.; Frenkel, A. I.; et al. Subnanometer substructures in nanoassemblies formed from clusters under reactive atmosphere revealed using machine learning. *J. Phys. Chem. C* **2018**, *122*, 21686−21693.

(38) Timoshenko, J.; Lu, D.; Lin, Y.; Frenkel, A. I. Supervised machine learning-based determination of three-dimensional structure of metallic nanoparticles. *J. Phys. Chem. Lett.* **2017**, *8*, 5091−5098.

(39) Glatzel, P.; Weng, T.-C.; Kvashnina, K.; Swarbrick, J.; Sikora, M.; Gallo, E.; Smolentsev, N.; Mori, R. A. Reflections on hard X-ray photon-in/photon-out spectroscopy for electronic structure studies. *J. Electron Spectrosc. Relat. Phenom.* **2013**, *188*, 17−25.

(40) Tsapatsaris, N.; Beesley, A. M.; Weiher, N.; Tatton, H.; Dent, A. J.; Mosselmans, F. J.; Tromp, M.; Russu, S.; Evans, J.; Harvey, I.; et al. High throughput in situ XAFS screening of catalysts. *AIP Conf. Proc.* **2006**, *882*, 597−599.

(41) Grunwaldt, J.-D.; Frenkel, A. I. Synchrotron studies of catalysts: from XAFS to QEXAFS and beyond. *Synchrotron Radiat. News* **2009**, *22*, 2−4.

(42) Rehr, J. J.; Kas, J. J.; Vila, F. D.; Prange, M. P.; Jorissen, K. Parameter-free calculations of X-ray spectra with FEFF9. *Phys. Chem. Chem. Phys.* **2010**, *12*, 5503−5513.

(43) Ankudinov, A.; Takimoto, Y.; Rehr, J. Combined Bethe-Saltpeter equations and time-dependent density-functional theory approach for x-ray absorption calculations. *Phys. Rev. B: Condens. Matter Mater. Phys.* **2005**, *71*, 165110.

(44) Tanaka, I.; Mizoguchi, T. First-principles calculations of x-ray absorption near edge structure and energy loss near edge structure: present and future. *J. Phys.: Condens. Matter* **2009**, *21*, 104201.

(45) Vinson, J.; Rehr, J.; Kas, J.; Shirley, E. Bethe-Salpeter equation calculations of core excitation spectra. *Phys. Rev. B: Condens. Matter Mater. Phys.* **2011**, *83*, 115106.

(46) Laskowski, R.; Blaha, P. Understanding the L 2,3 x-ray absorption spectra of early 3d transition elements. *Phys. Rev. B: Condens. Matter Mater. Phys.* **2010**, *82*, 205104.

(47) Stavitski, E.; De Groot, F. M. The CTM4XAS program for EELS and XAS spectral shape analysis of transition metal L edges. *Micron* **2010**, *41*, 687−694.

(48) Liang, Y.; Vinson, J.; Pemmaraju, S.; Drisdell, W. S.; Shirley, E. L.; Prendergast, D. Accurate X-ray spectral predictions: an advanced self-consistent-field approach inspired by many-body perturbation theory. *Phys. Rev. Lett.* **2017**, *118*, 096402.

(49) Shirley, E. L. Ab initio inclusion of electron-hole attraction: Application to x-ray absorption and resonant inelastic x-ray scattering. *Phys. Rev. Lett.* **1998**, *80*, 794.

(50) Suzuki, Y.; Hino, H.; Kotsugi, M.; Ono, K. Automated estimation of materials parameter from X-ray absorption and electron energy-loss spectra with similarity measures. *npj Comput. Mater.* **2019**, *5*, 39.

(51) Smolentsev, G.; Soldatov, A.; Feiters, M. Three-dimensional local structure refinement using a full-potential XANES analysis. *Phys. Rev. B: Condens. Matter Mater. Phys.* **2007**, *75*, 144106.

(52) Benfatto, M.; Congiu-Castellano, A.; Daniele, A.; Della Longa, S. MXAN: a new software procedure to perform geometrical fitting of experimental XANES spectra. *J. Synchrotron Radiat.* **2001**, *8*, 267−269.

(53) Mathew, K.; Zheng, C.; Winston, D.; Chen, C.; Dozier, A.; Rehr, J. J.; Ong, S. P.; Persson, K. A. High-throughput computational X-ray absorption spectroscopy. *Sci. Data* **2018**, *5*, 180151.

(54) Zheng, C.; Mathew, K.; Chen, C.; Chen, Y.; Tang, H.; Dozier, A.; Kas, J. J.; Vila, F. D.; Rehr, J. J.; Piper, L. F.; et al. Automated generation and ensemble-learned matching of X-ray absorption spectra. *npj Comput. Mater.* **2018**, *4*, 12.

(55) Ravel, B.; Newville, M. ATHENA, ARTEMIS, HEPHAESTUS: data analysis for X-ray absorption spectroscopy using IFEFFIT. *J. Synchrotron Radiat.* **2005**, *12*, 537−541.

(56) Newville, M.; Līviņš, P.; Yacoby, s. Y.; Rehr, J.; Stern, E. Near-edge x-ray-absorption fine structure of Pb: A comparison of theory and experiment. *Phys. Rev. B: Condens. Matter Mater. Phys.* **1993**, *47*, 14126.

(57) Zabinsky, S. I.; Rehr, J. J.; Ankudinov, A.; Albers, R. C.; Eller, M. J. Multiple-scattering calculations of x-ray-absorption spectra. *Phys. Rev. B: Condens. Matter Mater. Phys.* **1995**, *52*, 2995−3009.

(58) Di Cicco, A. EXAFS multiple-scattering data-analysis: GNXAS methodology and applications. *Phys. B* **1995**, *208*, 125−128.

(59) Filipponi, A.; Di Cicco, A.; Natoli, C. R. X-ray-absorption spectroscopy and n-body distribution functions in condensed matter. I. Theory. *Phys. Rev. B: Condens. Matter Mater. Phys.* **1995**, *52*, 15122.

(60) Stern, E. A.; Ma, Y.; Hanske-Petitpierre, O.; Bouldin, C. E. Radial distribution function in X-ray-absorption fine structure. *Phys. Rev. B: Condens. Matter Mater. Phys.* **1992**, *46*, 687−694.

(61) Stern, E. EXAFS theory. In *X-ray absorption: principles, applications, techniques of EXAFS, SEXAFS and XANES*; Koningsberger, D., Prins, R., Eds.; John Willey and Sons: New York, 1988.

(62) Jonane, I.; Cintins, A.; Kalinko, A.; Chernikov, R.; Kuzmin, A. Treatment of disorder effects in X-ray absorption spectra beyond the conventional approach. *Radiat. Phys. Chem.* **2020**, *175*, 108112.

(63) Jonane, I.; Anspoks, A.; Kuzmin, A. Advanced approach to the local structure reconstruction and theory validation on the example of the W L3-edge extended x-ray absorption fine structure of tungsten. *Modell. Simul. Mater. Sci. Eng.* **2018**, *26*, 025004.

(64) Campbell, L.; Hedin, L.; Rehr, J.; Bardyszewski, W. Interference between extrinsic and intrinsic losses in x-ray absorption fine structure. *Phys. Rev. B: Condens. Matter Mater. Phys.* **2002**, *65*, 064107.

(65) Kuzmin, A.; Purans, J. The influence of the focusing effect on the X-ray absorption fine structure above all the tungsten L edges in non-stoichiometric tungsten oxides. *J. Phys.: Condens. Matter* **1993**, *5*, 9423.

(66) Frenkel, A.; Stern, E.; Voronel, A.; Qian, M.; Newville, M. Buckled crystalline structure of mixed ionic salts. *Phys. Rev. Lett.* **1993**, *71*, 3485−3488.

(67) Bunker, G. *Introduction to XAFS: a practical guide to X-ray absorption fine structure spectroscopy*; Cambridge University Press: Cambridge, 2010.

(68) Seidler, G.; Mortensen, D.; Remesnik, A.; Pacold, J.; Ball, N.; Barry, N.; Styczinski, M.; Hoidn, O. A laboratory-based hard x-ray monochromator for high-resolution x-ray emission spectroscopy and x-ray absorption near edge structure measurements. *Rev. Sci. Instrum.* **2014**, *85*, 113906.

(69) Jahrman, E. P.; Holden, W. M.; Ditter, A. S.; Mortensen, D. R.; Seidler, G. T.; Fister, T. T.; Kozimor, S. A.; Piper, L. F.; Rana, J.; Hyatt, N. C.; et al. An improved laboratory-based x-ray absorption fine structure and x-ray emission spectrometer for analytical applications in materials chemistry research. *Rev. Sci. Instrum.* **2019**, *90*, 024106.

(70) Schlesiger, C.; Anklamm, L.; Stiel, H.; Malzer, W.; Kanngießer, B. XAFS spectroscopy by an X-ray tube based spectrometer using a novel type of HOPG mosaic crystal and optimized image processing. *J. Anal. At. Spectrom.* **2015**, *30*, 1080−1085.

(71) Benfatto, M.; Natoli, C.; Brouder, C.; Pettifer, R.; Lopez, M. R. Polarized curved-wave extended X-ray-absorption fine structure: theory and application. *Phys. Rev. B: Condens. Matter Mater. Phys.* **1989**, *39*, 1936−1939.

(72) Shirai, M.; Inoue, T.; Onishi, H.; Asakura, K.; Iwasawa, Y. Polarized total-reflection fluorescence EXAFS study of anisotropic structure analysis for Co oxides on α-Al2O3(0001) as model surfaces for active oxidation catalysts. *J. Catal.* **1994**, *145*, 159−165.

(73) Ahmadi, M.; Timoshenko, J.; Behafarid, F.; Roldan Cuenya, B. Tuning the structure of Pt nanoparticles through support interactions: an in situ polarized X-ray absorption study coupled with atomistic simulations. *J. Phys. Chem. C* **2019**, *123*, 10666−10676.

(74) Goulon, J.; Goulon-Ginet, C.; Cortes, R.; Dubois, J. On experimental attenuation factors of the amplitude of the EXAFS oscillations in absorption, reflectivity and luminescence measurements. *J. Phys. (Paris)* **1982**, *43*, 539−548.

(75) Velasco-Vélez, J.-J.; Jones, T.; Gao, D.; Carbonio, E.; Arrigo, R.; Hsu, C.-J.; Huang, Y.-C.; Dong, C.-L.; Chen, J.-M.; Lee, J.-F.; et al. The role of the copper oxidation state in the electrocatalytic reduction of CO2 into valuable hydrocarbons. *ACS Sustainable Chem. Eng.* **2019**, *7*, 1485−1492.

(76) Kurian, R.; Kunnus, K.; Wernet, P.; Butorin, S. M.; Glatzel, P.; de Groot, F. M. Intrinsic deviations in fluorescence yield detected x-ray absorption spectroscopy: the case of the transition metal L2,3 edges. *J. Phys.: Condens. Matter* **2012**, *24*, 452201.

(77) Stern, E. A.; Heald, S. M. X-ray filter assembly for fluorescence measurements of x-ray absorption fine structure. *Rev. Sci. Instrum.* **1979**, *50*, 1579−1582.

(78) Cramer, S.; Tench, O.; Yocum, M.; George, G. A 13-element Ge detector for fluorescence EXAFS. *Nucl. Instrum. Methods Phys. Res., Sect. A* **1988**, *266*, 586−591.

(79) Ciatto, G.; d'Acapito, F.; Boscherini, F.; Mobilio, S. Treatment of EXAFS data taken in the fluorescence mode in non-linear conditions. *J. Synchrotron Radiat.* **2004**, *11*, 278−283.

(80) Booth, C.; Bridges, F. Improved self-absorption correction for fluorescence measurements of extended X-ray absorption fine-structure. *Phys. Scr.* **2005**, *2005*, 202.

(81) Pfalzer, P.; Urbach, J.-P.; Klemm, M.; Horn, S.; Frenkel, A. I.; Kirkland, J.; et al. Elimination of self-absorption in fluorescence hard-x-ray absorption spectra. *Phys. Rev. B: Condens. Matter Mater. Phys.* **1999**, *60*, 9335.

(82) Meirer, F.; Pepponi, G.; Streli, C.; Wobrauschek, P.; Zoeger, N. Grazing exit versus grazing incidence geometry for x-ray absorption near edge structure analysis of arsenic traces. *J. Appl. Phys.* **2009**, *105*, 074906.

(83) Frati, F.; Hunault, M. O. J. Y.; de Groot, F. M. F. Oxygen K-edge X-ray absorption spectra. *Chem. Rev.* **2020**, *120*, 4056−4110.

(84) Velasco-Velez, J.-J.; Wu, C. H.; Pascal, T. A.; Wan, L. F.; Guo, J.; Prendergast, D.; Salmeron, M. The structure of interfacial water on gold electrodes studied by x-ray absorption spectroscopy. *Science* **2014**, *346*, 831−834.

(85) Kantor, I.; Labiche, J.-C.; Collet, E.; Siron, L.; Thevenin, J.-J.; Ponchut, C.; Borrel, J.; Mairs, T.; Marini, C.; Strohm, C.; et al. A new detector for sub-millisecond EXAFS spectroscopy at the European Synchrotron Radiation Facility. *J. Synchrotron Radiat.* **2014**, *21*, 1240−1246.

(86) Pascarelli, S.; Mathon, O.; Mairs, T.; Kantor, I.; Agostini, G.; Strohm, C.; Pasternak, S.; Perrin, F.; Berruyer, G.; Chappelet, P.; et al. The Time-resolved and Extreme-conditions XAS (TEXAS) facility at the European Synchrotron Radiation Facility: the energy-dispersive X-ray absorption spectroscopy beamline ID24. *J. Synchrotron Radiat.* **2016**, *23*, 353−368.

(87) Baudelet, F.; Kong, Q.; Nataf, L.; Cafun, J.; Congeduti, A.; Monza, A.; Chagnot, S.; Itié, J. ODE: a new beam line for high-pressure XAS and XMCD studies at SOLEIL. *High Pressure Res.* **2011**, *31*, 136−139.

(88) Kuzmin, A.; Anspoks, A.; Kalinko, A.; Timoshenko, J.; Nataf, L.; Baudelet, F.; Irifune, T. Origin of pressure-induced metallization in Cu3N: an X-ray absorption spectroscopy study. *Phys. Status Solidi B* **2018**, *255*, 1800073.

(89) Kuzmin, A.; Anspoks, A.; Kalinko, A.; Timoshenko, J.; Kalendarev, R.; Nataf, L.; Baudelet, F.; Irifune, T. High-pressure x-ray absorption spectroscopy study of tin tungstates. *Phys. Scr.* **2015**, *90*, 094003.

(90) Nataf, L.; Baudelet, F.; Polian, A.; Jonane, I.; Anspoks, A.; Kuzmin, A.; Irifune, T. Recent progress in high pressure X-ray absorption spectroscopy studies at the ODE beamline. *High Pressure Res.* **2020**, *40*, 82−87.

(91) Aquilanti, G.; Trapananti, A.; Karandikar, A.; Kantor, I.; Marini, C.; Mathon, O.; Pascarelli, S.; Boehler, R. Melting of iron determined by X-ray absorption spectroscopy to 100 GPa. *Proc. Natl. Acad. Sci. U. S. A.* **2015**, *112*, 12042−12045.

(92) Katayama, T.; Inubushi, Y.; Obara, Y.; Sato, T.; Togashi, T.; Tono, K.; Hatsui, T.; Kameshima, T.; Bhattacharya, A.; Ogi, Y.; et al. Femtosecond x-ray absorption spectroscopy with hard x-ray free electron laser. *Appl. Phys. Lett.* **2013**, *103*, 131105.

(93) Nachtegaal, M.; Müller, O.; König, C.; Frahm, R. QEXAFS: techniques and scientific applications for time-resolved XAS. In *X-Ray Absorption and X-Ray Emission Spectroscopy: Theory and Applications*; Van Bokhoven, J. A., Lamberti, C., Eds.; John Wiley & Sons, Ltd: Chichester (UK), 2016; Vol. *1*, p 155.

(94) Müller, O.; Nachtegaal, M.; Just, J.; Luetzenkirchen-Hecht, D.; Frahm, R. Quick-EXAFS setup at the SuperXAS beamline for in situ X-ray absorption spectroscopy with 10 ms time resolution. *J. Synchrotron Radiat.* **2016**, *23*, 260−266.

(95) Tada, M.; Uruga, T.; Iwasawa, Y. Key factors affecting the performance and durability of cathode electrocatalysts in polymer electrolyte fuel cells characterized by in situ real time and spatially resolved XAFS techniques. *Catal. Lett.* **2015**, *145*, 58−70.

(96) Tada, M.; Murata, S.; Asakoka, T.; Hiroshima, K.; Okumura, K.; Tanida, H.; Uruga, T.; Nakanishi, H.; Matsumoto, S. i.; Inada, Y.; et al. In situ time-resolved dynamic surface events on the Pt/C cathode in a fuel cell under operando conditions. *Angew. Chem., Int. Ed.* **2007**, *46*, 4310−4315.

(97) Ishiguro, N.; Tada, M. Structural kinetics of cathode events on polymer electrolyte fuel cell catalysts studied by operando time-resolved XAFS. *Catal. Lett.* **2018**, *148*, 1597−1609.

(98) Ishiguro, N.; Saida, T.; Uruga, T.; Sekizawa, O.; Nagasawa, K.; Nitta, K.; Yamamoto, T.; Ohkoshi, S.-i.; Yokoyama, T.; Tada, M. Structural kinetics of a Pt/C cathode catalyst with practical catalyst loading in an MEA for PEFC operating conditions studied by in situ time-resolved XAFS. *Phys. Chem. Chem. Phys.* **2013**, *15*, 18827−18834.

(99) Borfecchia, E.; Garino, C.; Gianolio, D.; Salassa, L.; Gobetto, R.; Lamberti, C. Monitoring excited state dynamics in cis-[Ru (bpy) 2 (py) 2] 2+ by ultrafast synchrotron techniques. *Catal. Today* **2014**, *229*, 34−45.

(100) Suzuki, Y.; Terada, Y. Space-resolved XAFS, instrumentations and applications. In *X-Ray Absorption and X-Ray Emission Spectroscopy: Theory and Applications*; Van Bokhoven, J. A., Lamberti, C., Eds.; John Wiley & Sons, Ltd: Chichester (UK), 2016; Vol. *1*.

(101) Schroer, C. G.; Kuhlmann, M.; Günzler, T. F.; Lengeler, B.; Richwin, M.; Griesebock, B.; Lützenkirchen-Hecht, D.; Frahm, R.; Ziegler, E.; Mashayekhi, A.; et al. Mapping the chemical states of an element inside a sample using tomographic x-ray absorption spectroscopy. *Appl. Phys. Lett.* **2003**, *82*, 3360−3362.

(102) Grunwaldt, J. D.; Wagner, J. B.; Dunin-Borkowski, R. E. Imaging catalysts at work: a hierarchical approach from the macro-to the meso-and nano-scale. *ChemCatChem* **2013**, *5*, 62−80.

(103) Grunwaldt, J.-D.; Hannemann, S.; Schroer, C. G.; Baiker, A. 2D-mapping of the catalyst structure inside a catalytic microreactor at work: Partial oxidation of methane over Rh/Al2O3. *J. Phys. Chem. B* **2006**, *110*, 8674−8680.

(104) Takao, S.; Sekizawa, O.; Nagamatsu, S. i.; Kaneko, T.; Yamamoto, T.; Samjeské, G.; Higashi, K.; Nagasawa, K.; Tsuji, T.; Suzuki, M.; et al. Mapping platinum species in polymer electrolyte fuel cells by spatially resolved XAFS techniques. *Angew. Chem., Int. Ed.* **2014**, *53*, 14110−14114.

(105) Sasaki, K.; Wang, J.; Naohara, H.; Marinkovic, N.; More, K.; Inada, H.; Adzic, R. Recent advances in platinum monolayer electrocatalysts for oxygen reduction reaction: Scale-up synthesis, structure and activity of Pt shells on Pd cores. *Electrochim. Acta* **2010**, *55*, 2645−2652.

(106) Leonard, N.; Ju, W.; Sinev, I.; Steinberg, J.; Luo, F.; Varela, A. S.; Cuenya, B. R.; Strasser, P. The chemical identity, state and structure of catalytically active centers during the electrochemical CO 2 reduction on porous Fe−nitrogen−carbon (Fe−N−C) materials. *Chem. Sci.* **2018**, *9*, 5064−5073.

(107) Binninger, T.; Fabbri, E.; Patru, A.; Garganourakis, M.; Han, J.; Abbott, D. F.; Sereda, O.; Kötz, R.; Menzel, A.; Nachtegaal, M.; et al. Electrochemical flow-cell setup for in situ x-ray investigations i. Cell for saxs and xas at synchrotron facilities. *J. Electrochem. Soc.* **2016**, *163*, H906−H912.

(108) Favaro, M.; Drisdell, W. S.; Marcus, M. A.; Gregoire, J. M.; Crumlin, E. J.; Haber, J. A.; Yano, J. An operando investigation of (Ni−Fe−Co−Ce)Ox system as highly efficient electrocatalyst for oxygen evolution reaction. *ACS Catal.* **2017**, *7*, 1248−1258.

(109) Morikawa, T.; Gul, S.; Nishimura, Y. F.; Suzuki, T. M.; Yano, J. Operando X-ray absorption spectroscopy of hyperfine β-FeOOH nanorods modified with amorphous $Ni(OH)_2$ under electrocatalytic water oxidation conditions. *Chem. Commun.* **2020**, *56*, 5158−5161.

(110) Gul, S.; Ng, J. W. D.; Alonso-Mori, R.; Kern, J.; Sokaras, D.; Anzenberg, E.; Lassalle-Kaiser, B.; Gorlin, Y.; Weng, T.-C.; Zwart, P. H.; et al. Simultaneous detection of electronic structure changes from two elements of a bifunctional catalyst using wavelength-dispersive X-ray emission spectroscopy and in situ electrochemistry. *Phys. Chem. Chem. Phys.* **2015**, *17*, 8901−8912.

(111) Jeon, H. S.; Timoshenko, J.; Scholten, F.; Sinev, I.; Herzog, A.; Haase, F. T.; Roldan Cuenya, B. Operando insight into the correlation between the structure and composition of CuZn nanoparticles and their selectivity for the electrochemical CO2 reduction. *J. Am. Chem. Soc.* **2019**, *141*, 19879−19887.

(112) Bazin, D.; Guczi, L. Soft X-ray absorption spectroscopy in heterogeneous catalysis. *Appl. Catal., A* **2001**, *213*, 147−162.

(113) Smith, J. W.; Saykally, R. J. Soft x-ray absorption spectroscopy of liquids and solutions. *Chem. Rev.* **2017**, *117*, 13909−13934.

(114) Kornienko, N.; Resasco, J.; Becknell, N.; Jiang, C.-M.; Liu, Y.-S.; Nie, K.; Sun, X.; Guo, J.; Leone, S. R.; Yang, P. Operando spectroscopic analysis of an amorphous cobalt sulfide hydrogen evolution electrocatalyst. *J. Am. Chem. Soc.* **2015**, *137*, 7448−7455.

(115) Cheng, W.; Zhao, X.; Su, H.; Tang, F.; Che, W.; Zhang, H.; Liu, Q. Lattice-strained metal−organic-framework arrays for bifunctional oxygen electrocatalysis. *Nat. Energy* **2019**, *4*, 115.

(116) Zhu, D.; Guo, C.; Liu, J.; Wang, L.; Du, Y.; Qiao, S.-Z. Two-dimensional metal−organic frameworks with high oxidation states for efficient electrocatalytic urea oxidation. *Chem. Commun.* **2017**, *53*, 10906−10909.

(117) Gao, D.; Zhou, H.; Cai, F.; Wang, D.; Hu, Y.; Jiang, B.; Cai, W.-B.; Chen, X.; Si, R.; Yang, F.; et al. Switchable CO2 electroreduction via engineering active phases of Pd nanoparticles. *Nano Res.* **2017**, *10*, 2181−2191.

(118) Strasser, P.; Koh, S.; Anniyev, T.; Greeley, J.; More, K.; Yu, C.; Liu, Z.; Kaya, S.; Nordlund, D.; Ogasawara, H.; et al. Lattice-strain

control of the activity in dealloyed core—shell fuel cell catalysts. *Nat. Chem.* **2010**, *2*, 454—460.

(119) Baturina, O. A.; Gould, B. D.; Northrup, P. A.; Swider-Lyons, K. E. SO2 adsorption products on Pt nanoparticles as a function of electrode potential and oxidative properties of carrier gas: In situ sulfur K-edge XANES approach. *Catal. Today* **2013**, *205*, 106—110.

(120) Bi, W.; Li, X.; You, R.; Chen, M.; Yuan, R.; Huang, W.; Wu, X.; Chu, W.; Wu, C.; Xie, Y. Surface immobilization of transition metal ions on nitrogen-doped graphene realizing high-efficient and selective CO2 reduction. *Adv. Mater.* **2018**, *30*, 1706617.

(121) Li, X.; Bi, W.; Chen, M.; Sun, Y.; Ju, H.; Yan, W.; Zhu, J.; Wu, X.; Chu, W.; Wu, C.; et al. Exclusive Ni—N4 sites realize near-unity CO selectivity for electrochemical CO2 reduction. *J. Am. Chem. Soc.* **2017**, *139*, 14889—14892.

(122) Jiang, K.; Siahrostami, S.; Zheng, T.; Hu, Y.; Hwang, S.; Stavitski, E.; Peng, Y.; Dynes, J.; Gangisetty, M.; Su, D.; et al. Isolated Ni single atoms in graphene nanosheets for high-performance CO_2 reduction. *Energy Environ. Sci.* **2018**, *11*, 893—903.

(123) Koshy, D.; Chen, S.; Lee, D. U.; Burke Stevens, M.; Abdellah, A.; Dull, S.; Chen, G.; Nordlund, D.; Gallo, A.; Hahn, C.; et al. Understanding the origin of highly selective CO2 electroreduction to CO on Ni, N-doped carbon catalysts. *Angew. Chem., Int. Ed.* **2020**, *59*, 4043—4050.

(124) Ishihara, T.; Tokushima, T.; Horikawa, Y.; Kato, M.; Yagi, I. Development of a spectro-electrochemical cell for soft X-ray photon-in photon-out spectroscopy. *Rev. Sci. Instrum.* **2017**, *88*, 104101.

(125) Zhang, L.; Mao, F.; Zheng, L. R.; Wang, H. F.; Yang, X. H.; Yang, H. G. Tuning metal catalyst with metal—C3N4 interaction for efficient CO2 electroreduction. *ACS Catal.* **2018**, *8*, 11035—11041.

(126) Newville, M.; Carroll, S.; O'day, P.; Waychunas, G.; Ebert, M. A web-based library of XAFS data on model compounds. *J. Synchrotron Radiat.* **1999**, *6*, 276—277.

(127) Asakura, K.; Ikemoto, I.; Kuroda, H.; Kobayashi, T.; Shirakawa, H. Dopant structure in FeCl3-doped polyacetylene studied by X-ray absorption spectroscopy and X-ray photoelectron spectroscopy. *Bull. Chem. Soc. Jpn.* **1985**, *58*, 2113—2120.

(128) Ewels, P.; Sikora, T.; Serin, V.; Ewels, C. P.; Lajaunie, L. A complete overhaul of the electron energy-loss spectroscopy and X-ray absorption spectroscopy database: eelsdb. eu. *Microsc. Microanal.* **2016**, *22*, 717—724.

(129) Bunău, O.; Joly, Y. Self-consistent aspects of X-ray absorption calculations. *J. Phys.: Condens. Matter* **2009**, *21*, 345501.

(130) Ong, S. P.; Cholia, S.; Jain, A.; Brafman, M.; Gunter, D.; Ceder, G.; Persson, K. A. The materials application programming interface (API): A simple, flexible and efficient API for materials data based on REpresentational State Transfer (REST) principles. *Comput. Mater. Sci.* **2015**, *97*, 209—215.

(131) Ong, S. P.; Richards, W. D.; Jain, A.; Hautier, G.; Kocher, M.; Cholia, S.; Gunter, D.; Chevrier, V. L.; Persson, K. A.; Ceder, G. Python Materials Genomics (pymatgen): A robust, open-source python library for materials analysis. *Comput. Mater. Sci.* **2013**, *68*, 314—319.

(132) Jain, A.; Ong, S. P.; Hautier, G.; Chen, W.; Richards, W. D.; Dacek, S.; Cholia, S.; Gunter, D.; Skinner, D.; Ceder, G.; et al. Commentary: The Materials Project: A materials genome approach to accelerating materials innovation. *APL Mater.* **2013**, *1*, 011002.

(133) Wong, J.; Lytle, F.; Messmer, R.; Maylotte, D. K-edge absorption spectra of selected vanadium compounds. *Phys. Rev. B: Condens. Matter Mater. Phys.* **1984**, *30*, 5596.

(134) Mejia Gomez, A. E.; Sacanell, J.; Huck-Iriart, C.; Ramos, C. P.; Soldati, A. L.; Figueroa, S. J.A.; Tabacniks, M. H.; Fantini, M. C.A.; Craievich, A. F.; Lamas, D. G. Crystal structure, cobalt and iron speciation and oxygen non-stoichiometry of La0. 6Sr0. 4Co1-yFeyO3-δ nanorods for IT-SOFC cathodes. *J. Alloys Compd.* **2020**, *817*, 153250.

(135) Capehart, T.; Herbst, J.; Mishra, R.; Pinkerton, F. X-ray-absorption edge shifts in rare-earth—transition-metal compounds. *Phys. Rev. B: Condens. Matter Mater. Phys.* **1995**, *52*, 7907.

(136) Clancy, J.; Chen, N.; Kim, C.; Chen, W.; Plumb, K.; Jeon, B.; Noh, T.; Kim, Y.-J. Spin-orbit coupling in iridium-based 5d compounds probed by x-ray absorption spectroscopy. *Phys. Rev. B: Condens. Matter Mater. Phys.* **2012**, *86*, 195131.

(137) Sham, T.; Yiu, Y.; Kuhn, M.; Tan, K. Electronic structure of ordered and disordered Cu 3 Au: The behavior of the Au 5d bands. *Phys. Rev. B: Condens. Matter Mater. Phys.* **1990**, *41*, 11881.

(138) Sham, T. X-ray absorption studies of unoccupied d-band states in gold and nickel metallic compounds. *Solid State Commun.* **1987**, *64*, 1103—1106.

(139) Antolini, E.; Salgado, J.; Giz, M.; Gonzalez, E. R. Effects of geometric and electronic factors on ORR activity of carbon supported Pt—Co electrocatalysts in PEM fuel cells. *Int. J. Hydrogen Energy* **2005**, *30*, 1213—1220.

(140) Stöhr, J. Analysis of K-shell excitation spectra by curve fitting. In *NEXAFS Spectroscopy*; Springer: Berlin, Heidelberg, 1992; pp 211—238.

(141) Erickson, E. M.; Thorum, M. S.; Vasić, R.; Marinković, N. a. S.; Frenkel, A. I.; Gewirth, A. A.; Nuzzo, R. G. In situ electrochemical X-ray absorption spectroscopy of oxygen reduction electrocatalysis with high oxygen flux. *J. Am. Chem. Soc.* **2012**, *134*, 197—200.

(142) Rabe, P.; Tolkiehn, G.; Werner, A. Investigation of the extended X-ray absorption fine structure (EXAFS) at L-edges of heavy elements. *J. Phys. C: Solid State Phys.* **1979**, *12*, 899.

(143) McKale, A.; Veal, B.; Paulikas, A.; Chan, S.-K.; Knapp, G. Generalized Ramsauer-Townsend effect in extended x-ray-absorption fine structure. *Phys. Rev. B: Condens. Matter Mater. Phys.* **1988**, *38*, 10919.

(144) Funke, H.; Scheinost, A.; Chukalina, M. Wavelet analysis of extended X-ray absorption fine structure data. *Phys. Rev. B: Condens. Matter Mater. Phys.* **2005**, *71*, 094110.

(145) Timoshenko, J.; Kuzmin, A. Wavelet data analysis of EXAFS spectra. *Comput. Phys. Commun.* **2009**, *180*, 920—925.

(146) Xia, Z.; Zhang, H.; Shen, K.; Qu, Y.; Jiang, Z. Wavelet analysis of extended X-ray absorption fine structure data: Theory, application. *Phys. B* **2018**, *542*, 12—19.

(147) Timoshenko, J.; Keller, K. R.; Frenkel, A. I. Determination of bimetallic architectures in nanometer-scale catalysts by combining molecular dynamics simulations with x-ray absorption spectroscopy. *J. Chem. Phys.* **2017**, *146*, 114201.

(148) Grosse, P.; Gao, D.; Scholten, F.; Sinev, I.; Mistry, H.; Roldan Cuenya, B. Dynamic changes in the structure, chemical state and catalytic selectivity of Cu nanocubes during CO2 electroreduction: size and support effects. *Angew. Chem., Int. Ed.* **2018**, *57*, 6192—6197.

(149) Fei, H.; Dong, J.; Feng, Y.; Allen, C. S.; Wan, C.; Volosskiy, B.; Li, M.; Zhao, Z.; Wang, Y.; Sun, H.; et al. General synthesis and definitive structural identification of MN4C4 single-atom catalysts with tunable electrocatalytic activities. *Nat. Catal.* **2018**, *1*, 63.

(150) Zhang, H.; An, P.; Zhou, W.; Guan, B. Y.; Zhang, P.; Dong, J.; Lou, X. W. D. Dynamic traction of lattice-confined platinum atoms into mesoporous carbon matrix for hydrogen evolution reaction. *Sci. Adv.* **2018**, *4*, No. eaao6657.

(151) Fei, H.; Dong, J.; Arellano-Jiménez, M. J.; Ye, G.; Kim, N. D.; Samuel, E. L.; Peng, Z.; Zhu, Z.; Qin, F.; Bao, J.; et al. Atomic cobalt on nitrogen-doped graphene for hydrogen generation. *Nat. Commun.* **2015**, *6*, 1—8.

(152) Dalba, G.; Fornasini, P. EXAFS Debye—Waller factor and thermal vibrations of crystals. *J. Synchrotron Radiat.* **1997**, *4*, 243—255.

(153) Sevillano, E.; Meuth, H.; Rehr, J. Extended x-ray absorption fine structure Debye-Waller factors. I. Monatomic crystals. *Phys. Rev. B: Condens. Matter Mater. Phys.* **1979**, *20*, 4908.

(154) Fornasini, P.; Grisenti, R. On EXAFS Debye-Waller factor and recent advances. *J. Synchrotron Radiat.* **2015**, *22*, 1242—1257.

(155) Vaccari, M.; Fornasini, P. Einstein and Debye models for EXAFS parallel and perpendicular mean-square relative displacements. *J. Synchrotron Radiat.* **2006**, *13*, 321—325.

(156) Sanson, A. On the Einstein model for EXAFS parallel and perpendicular mean-square relative displacements. *J. Synchrotron Radiat.* **2008**, *15*, 514—518.

(157) Lampitt, R.; Carrette, L. L.; Hogarth, M.; Russell, A. In situ and model EXAFS studies of electrocatalysts for methanol oxidation. *J. Electroanal. Chem.* **1999**, *460*, 80−87.

(158) Malakhov, I.; Nikitenko, S.; Savinova, E.; Kochubey, D.; Alonso-Vante, N. In situ EXAFS study of Ru-containing electro-catalysts of oxygen reduction. *Nucl. Instrum. Methods Phys. Res., Sect. A* **2000**, *448*, 323−326.

(159) Dalba, G.; Fornasini, P.; Grisenti, R.; Purans, J. Sensitivity of extended X-ray-absorption fine structure to thermal expansion. *Phys. Rev. Lett.* **1999**, *82*, 4240.

(160) Purans, J.; Afify, N.; Dalba, G.; Grisenti, R.; De Panfilis, S.; Kuzmin, A.; Ozhogin, V.; Rocca, F.; Sanson, A.; Tiutiunnikov, S.; et al. Isotopic effect in extended x-ray-absorption fine structure of germanium. *Phys. Rev. Lett.* **2008**, *100*, 055901.

(161) Purans, J.; Timoshenko, J.; Kuzmin, A.; Dalba, G.; Fornasini, P.; Grisenti, R.; Afify, N.; Rocca, F.; De Panfilis, S.; Ozhogin, I.; et al. Femtometer accuracy EXAFS measurements: Isotopic effect in the first, second and third coordination shells of germanium. *J. Phys. Conf. Ser.* **2009**, *190*, 012063.

(162) Yevick, A.; Frenkel, A. I. Effects of surface disorder on EXAFS modeling of metallic clusters. *Phys. Rev. B: Condens. Matter Mater. Phys.* **2010**, *81*, 115451.

(163) Huang, W.; Sun, R.; Tao, J.; Menard, L.; Nuzzo, R.; Zuo, J. Coordination-dependent surface atomic contraction in nanocrystals revealed by coherent diffraction. *Nat. Mater.* **2008**, *7*, 308.

(164) Lei, Y.; Zhao, H.; Rivas, R. D.; Lee, S.; Liu, B.; Lu, J.; Stach, E.; Winans, R. E.; Chapman, K. W.; Greeley, J. P.; et al. Adsorbate-induced structural changes in 1−3 nm platinum nanoparticles. *J. Am. Chem. Soc.* **2014**, *136*, 9320−9326.

(165) Petkov, V.; Prasai, B.; Ren, Y.; Shan, S.; Luo, J.; Joseph, P.; Zhong, C.-J. Solving the nanostructure problem: exemplified on metallic alloy nanoparticles. *Nanoscale* **2014**, *6*, 10048−10061.

(166) Clausen, B. S.; Norskov, J. K. Asymmetric pair distribution functions in catalysts. *Top. Catal.* **2000**, *10*, 221−230.

(167) Yancey, D. F.; Chill, S. T.; Zhang, L.; Frenkel, A. I.; Henkelman, G.; Crooks, R. M. A theoretical and experimental examination of systematic ligand-induced disorder in Au dendrimer-encapsulated nanoparticles. *Chem. Sci.* **2013**, *4*, 2912−2921.

(168) Timoshenko, J.; Ahmadi, M.; Roldan Cuenya, B. Is there a negative thermal expansion in supported metal nanoparticles? An in situ X-ray absorption study coupled with neural network analysis. *J. Phys. Chem. C* **2019**, *123*, 20594−20604.

(169) Clausen, B.; Grabaek, L.; Topsoe, H.; Hansen, L.; Stoltze, P.; Norskov, J.; Nielsen, O. A new procedure for particle size determination by EXAFS based on molecular dynamics simulations. *J. Catal.* **1993**, *141*, 368−379.

(170) Clausen, B. S.; Topsøe, H.; Hansen, L. B.; Stoltze, P.; Nørskov, J. K. Determination of metal particle sizes from EXAFS. *Catal. Today* **1994**, *21*, 49−55.

(171) Clausen, B. S.; Topsøe, H.; Hansen, L. B.; Stoltze, P.; Nørskov, J. K. The effect of anharmonicity on the EXAFS coordination number in small metallic particles. *Jpn. J. Appl. Phys.* **1993**, *32*, 95−97.

(172) Hansen, L. B.; Stoltze, P.; Nørskov, J. K.; Clausen, B.; Niemann, W. Is there a contraction of the interatomic distance in small metal particles? *Phys. Rev. Lett.* **1990**, *64*, 3155−3158.

(173) Chill, S. T.; Anderson, R. M.; Yancey, D. F.; Frenkel, A. I.; Crooks, R. M.; Henkelman, G. Probing the limits of conventional extended X-ray absorption fine structure analysis using thiolated gold nanoparticles. *ACS Nano* **2015**, *9*, 4036−4042.

(174) Timoshenko, J.; Frenkel, A. I. Probing structural relaxation in nanosized catalysts by combining EXAFS and reverse Monte Carlo methods. *Catal. Today* **2017**, *280*, 274−282.

(175) Filipponi, A. EXAFS for liquids. *J. Phys.: Condens. Matter* **2001**, *13*, R23.

(176) Witkowska, A.; Principi, E.; Di Cicco, A.; Dsoke, S.; Marassi, R.; Olivi, L.; Centazzo, M.; Albertini, V. R. Temperature and potential-dependent structural changes in a Pt cathode electrocatalyst viewed by in situ XAFS. *J. Non-Cryst. Solids* **2008**, *354*, 4227−4232.

(177) Babanov, Y. A.; Vasin, V.; Ageev, A. L.; Ershov, N. A new interpretation of EXAFS spectra in real space. I. General formalism. *Phys. Status Solidi B* **1981**, *105*, 747−754.

(178) Ershov, N.; Ageev, A.; Vasin, V.; Babanov, Y. A. A new interpretation of EXAFS spectra in real space: II. A comparison of the regularization technique with the Fourier transformation method. *Phys. Status Solidi B* **1981**, *108*, 103−111.

(179) Frenkel, A.; Stern, E.; Voronel, A.; Rubshtein, A.; Ben-Ezra, Y.; Fleurov, V. Redistribution of La-Al nearest-neighbor distances in the metallic glass Al0.91La0.09. *Phys. Rev. B: Condens. Matter Mater. Phys.* **1996**, *54*, 884−892.

(180) Kuzmin, A.; Purans, J. Dehydration of the molybdenum trioxide hydrates MoO3· nH2O: in situ x-ray absorption spectroscopy study at the Mo K edge. *J. Phys.: Condens. Matter* **2000**, *12*, 1959.

(181) Price, S. W.; Zonias, N.; Skylaris, C.-K.; Hyde, T. I.; Ravel, B.; Russell, A. E. Fitting EXAFS data using molecular dynamics outputs and a histogram approach. *Phys. Rev. B: Condens. Matter Mater. Phys.* **2012**, *85*, 075439.

(182) Anspoks, A.; Kalinko, A.; Timoshenko, J.; Kuzmin, A. Local structure relaxation in nanosized tungstates. *Solid State Commun.* **2014**, *183*, 22−26.

(183) Kuzmin, A.; Chaboy, J. EXAFS and XANES analysis of oxides at the nanoscale. *IUCrJ* **2014**, *1*, 571−589.

(184) Frenkel, A. Solving the 3D structure of metal nanoparticles. *Z. Kristallogr. - Cryst. Mater.* **2007**, *222*, 605−611.

(185) Frenkel, A. I. Solving the structure of nanoparticles by multiple-scattering EXAFS analysis. *J. Synchrotron Radiat.* **1999**, *6*, 293−295.

(186) Bugaev, A. L.; Guda, A. A.; Lazzarini, A.; Lomachenko, K. A.; Groppo, E.; Pellegrini, R.; Piovano, A.; Emerich, H.; Soldatov, A. V.; Bugaev, L. A.; et al. In situ formation of hydrides and carbides in palladium catalyst: when XANES is better than EXAFS and XRD. *Catal. Today* **2017**, *283*, 119−126.

(187) Bianconi, A.; Fritsch, E.; Calas, G.; Petiau, J. X-ray-absorption near-edge structure of 3d transition elements in tetrahedral coordination: The effect of bond-length variation. *Phys. Rev. B: Condens. Matter Mater. Phys.* **1985**, *32*, 4292−4295.

(188) Bianconi, A.; Dell'Ariccia, M.; Gargano, A.; Natoli, C. Bond length determination using XANES. In *EXAFS and near edge structure*; Bianconi, A., Incoccia, L., Stipcich, S., Eds.; Springer: Berlin, Heidelberg, 1983; pp 57−61.

(189) Natoli, C. Near edge absorption structure in the framework of the multiple scattering model. Potential resonance or barrier effects? In *EXAFS and near edge structure*; Bianconi, A., Incoccia, L., Stipcich, S., Eds.; Springer: Berlin, Heidelberg, 1983; pp 43−56.

(190) Rehr, J.; Ankudinov, A.; Zabinsky, S. New developments in NEXAFS/EXAFS theory. *Catal. Today* **1998**, *39*, 263−269.

(191) Friebel, D.; Mbuga, F.; Rajasekaran, S.; Miller, D. J.; Ogasawara, H.; Alonso-Mori, R.; Sokaras, D.; Nordlund, D.; Weng, T.-C.; Nilsson, A. Structure, redox chemistry, and interfacial alloy formation in monolayer and multilayer Cu/Au (111) model catalysts for CO2 electroreduction. *J. Phys. Chem. C* **2014**, *118*, 7954−7961.

(192) Friebel, D.; Ogasawara, H.; Nilsson, A. X-ray Spectroscopy at Electro-catalytic Interfaces. In *Surface and Interface Science*; Wandelt, K., Ed.; Wiley-VCH Verlag GmbH & Co. KGaA, 2020; Vol. 8, pp 733−772.

(193) Guda, A.; Guda, S.; Martini, A.; Bugaev, A.; Soldatov, M.; Soldatov, A.; Lamberti, C. Machine learning approaches to XANES spectra for quantitative 3D structural determination: The case of CO2 adsorption on CPO-27-Ni MOF. *Radiat. Phys. Chem.* **2020**, *175*, 108430.

(194) Ankudinov, A.; Rehr, J.; Low, J. J.; Bare, S. R. Sensitivity of Pt X-ray absorption near edge structure to the morphology of small Pt clusters. *J. Chem. Phys.* **2002**, *116*, 1911−1919.

(195) Ankudinov, A.; Rehr, J.; Low, J.; Bare, S. Theoretical interpretation of XAFS and XANES in Pt clusters. *Top. Catal.* **2002**, *18*, 3−7.

(196) Kuzmin, A.; Larcheri, S.; Rocca, F. Zn K-edge XANES in nanocrystalline ZnO. *J. Phys.: Conf. Ser.* **2007**, *93*, 012045.

(197) Patlolla, A.; Zunino, J.; Frenkel, A. I.; Iqbal, Z. Thermochromism in polydiacetylene-metal oxide nanocomposites. *J. Mater. Chem.* **2012**, *22*, 7028−7035.

(198) LeCun, Y.; Bengio, Y.; Hinton, G. Deep learning. *Nature* **2015**, *521*, 436.

(199) Liu, Y.; Marcella, N.; Timoshenko, J.; Halder, A.; Yang, B.; Kolipaka, L.; Pellin, M. J.; Seifert, S.; Vajda, S.; Liu, P.; et al. Mapping XANES spectra on structural descriptors of copper oxide clusters using supervised machine learning. *J. Chem. Phys.* **2019**, *151*, 164201.

(200) Marcella, N.; Liu, Y.; Timoshenko, J.; Guan, E.; Luneau, M.; Shirman, T.; Aizenberg, J.; Friend, C. M.; Frenkel, A. Neural network assisted analysis of bimetallic nanocatalysts using X-ray absorption near edge structure spectroscopy. *Phys. Chem. Chem. Phys.* **2020**, *22*, 18902−18910.

(201) Kiyohara, S.; Tsubaki, M.; Liao, K.; Mizoguchi, T. Quantitative estimation of properties from core-loss spectrum via neural network. *J. Phys.: Mater.* **2019**, *2*, 024003.

(202) Timoshenko, J.; Shivhare, A.; Scott, R. W. J.; Lu, D.; Frenkel, A. I. Solving local structure around dopants in metal nanoparticles with ab initio modeling of X-ray absorption near edge structure. *Phys. Chem. Chem. Phys.* **2016**, *18*, 19621−19630.

(203) Sanchez, S. I.; Menard, L. D.; Bram, A.; Kang, J. H.; Small, M. W.; Nuzzo, R. G.; Frenkel, A. I. The emergence of nonbulk properties in supported metal clusters: negative thermal expansion and atomic disorder in Pt nanoclusters supported on γ-Al_2O_3. *J. Am. Chem. Soc.* **2009**, *131*, 7040−7054.

(204) Roldan Cuenya, B.; Frenkel, A.; Mostafa, S.; Behafarid, F.; Croy, J.; Ono, L.; Wang, Q. Anomalous lattice dynamics and thermal properties of supported size-and shape-selected Pt nanoparticles. *Phys. Rev. B: Condens. Matter Mater. Phys.* **2010**, *82*, 155450.

(205) Anderson, R. M.; Yancey, D. F.; Zhang, L.; Chill, S. T.; Henkelman, G.; Crooks, R. M. A theoretical and experimental approach for correlating nanoparticle structure and electrocatalytic activity. *Acc. Chem. Res.* **2015**, *48*, 1351−1357.

(206) Anderson, R. M.; Zhang, L.; Loussaert, J. A.; Frenkel, A. I.; Henkelman, G.; Crooks, R. M. An experimental and theoretical investigation of the inversion of Pd@Pt core@shell dendrimer-encapsulated nanoparticles. *ACS Nano* **2013**, *7*, 9345−9353.

(207) Prasai, B.; Wilson, A.; Wiley, B.; Ren, Y.; Petkov, V. On the road to metallic nanoparticles by rational design: bridging the gap between atomic-level theoretical modeling and reality by total scattering experiments. *Nanoscale* **2015**, *7*, 17902−17922.

(208) Di Cicco, A.; Minicucci, M.; Principi, E.; Witkowska, A.; Rybicki, J.; Laskowski, R. Testing interaction models by using x-ray absorption spectroscopy: solid Pb. *J. Phys.: Condens. Matter* **2002**, *14*, 3365.

(209) Roscioni, O. M.; Zonias, N.; Price, S. W.; Russell, A. E.; Comaschi, T.; Skylaris, C.-K. Computational prediction of L3 EXAFS spectra of gold nanoparticles from classical molecular dynamics simulations. *Phys. Rev. B: Condens. Matter Mater. Phys.* **2011**, *83*, 115409.

(210) Metropolis, N.; Rosenbluth, A. W.; Rosenbluth, M. N.; Teller, A. H.; Teller, E. Equation of state calculations by fast computing machines. *J. Chem. Phys.* **1953**, *21*, 1087−1092.

(211) Narayan, O.; Young, A. P. Convergence of Monte Carlo simulations to equilibrium. *Phys. Rev. E: Stat. Phys., Plasmas, Fluids, Relat. Interdiscip. Top.* **2001**, *64*, 021104.

(212) Duan, Z.; Timoshenko, J.; Kunal, P.; House, S. D.; Wan, H.; Jarvis, K.; Bonifacio, C.; Yang, J. C.; Crooks, R. M.; Frenkel, A. I.; et al. Structural characterization of heterogeneous RhAu nanoparticles from a microwave-assisted synthesis. *Nanoscale* **2018**, *10*, 22520−22532.

(213) House, S. D.; Bonifacio, C. S.; Timoshenko, J.; Kunal, P.; Wan, H.; Duan, Z.; Li, H.; Yang, J. C.; Frenkel, A. I.; Humphrey, S. M.; et al. Computationally Assisted STEM and EXAFS Characterization of Tunable Rh/Au and Rh/Ag Bimetallic Nanoparticle Catalysts. *Microsc. Microanal.* **2017**, *23*, 2030−2031.

(214) Timoshenko, J.; Anspoks, A.; Cintins, A.; Kuzmin, A.; Purans, J.; Frenkel, A. I. Neural network approach for characterizing structural

transformations by X-ray absorption fine structure spectroscopy. *Phys. Rev. Lett.* **2018**, *120*, 225502.

(215) Kalinko, A.; Evarestov, R.; Kuzmin, A.; Purans, J. Interpretation of EXAFS in ReO3 using molecular dynamics simulations. *J. Phys. Conf. Ser.* **2009**, *190*, 012080.

(216) Kuzmin, A.; Evarestov, R. Quantum mechanics−molecular dynamics approach to the interpretation of x-ray absorption spectra. *J. Phys.: Condens. Matter* **2009**, *21*, 055401.

(217) Timoshenko, J.; Anspoks, A.; Kalinko, A.; Kuzmin, A. Temperature dependence of the local structure and lattice dynamics of wurtzite-type ZnO. *Acta Mater.* **2014**, *79*, 194−202.

(218) Timoshenko, J.; Kuzmin, A.; Purans, J. Molecular dynamics simulations of EXAFS in germanium. *Cent. Eur. J. Phys.* **2011**, *9*, 710−715.

(219) Palmer, B. J.; Pfund, D. M.; Fulton, J. L. Direct modeling of EXAFS spectra from molecular dynamics simulations. *J. Phys. Chem.* **1996**, *100*, 13393−13398.

(220) Migliorati, V.; Serva, A.; Terenzio, F. M.; D'Angelo, P. Development of Lennard-Jones and Buckingham potentials for lanthanoid ions in water. *Inorg. Chem.* **2017**, *56*, 6214−6224.

(221) Busato, M.; D'Angelo, P.; Lapi, A.; Tolazzi, M.; Melchior, A. Solvation of Co2+ ion in 1-butyl-3-methylimidazolium bis (trifluoromethylsulfonyl) imide ionic liquid: A molecular dynamics and X-ray absorption study. *J. Mol. Liq.* **2020**, *299*, 112120.

(222) Migliorati, V.; Caruso, A.; D'Angelo, P. Unraveling the hydration properties of the Ba2+ aqua ion: the interplay of quantum mechanics, molecular dynamics, and EXAFS spectroscopy. *Inorg. Chem.* **2019**, *58*, 14551−14559.

(223) Anspoks, A.; Kalinko, A.; Kalendarev, R.; Kuzmin, A. Atomic structure relaxation in nanocrystalline NiO studied by EXAFS spectroscopy: Role of nickel vacancies. *Phys. Rev. B: Condens. Matter Mater. Phys.* **2012**, *86*, 174114.

(224) Anspoks, A.; Kalinko, A.; Kalendarev, R.; Kuzmin, A. Probing vacancies in NiO nanoparticles by EXAFS and molecular dynamics simulations. *J. Phys.: Conf. Ser.* **2013**, *430*, 012027.

(225) Anspoks, A.; Kuzmin, A. Interpretation of the Ni K-edge EXAFS in nanocrystalline nickel oxide using molecular dynamics simulations. *J. Non-Cryst. Solids* **2011**, *357*, 2604−2610.

(226) Anspoks, A.; Kuzmin, A.; Kalinko, A.; Timoshenko, J. Probing NiO nanocrystals by EXAFS spectroscopy. *Solid State Commun.* **2010**, *150*, 2270−2274.

(227) McGreevy, R.; Pusztai, L. Reverse Monte Carlo simulation: a new technique for the determination of disordered structures. *Mol. Simul.* **1988**, *1*, 359−367.

(228) McGreevy, R. L. Reverse monte carlo modelling. *J. Phys.: Condens. Matter* **2001**, *13*, R877.

(229) Timoshenko, J.; Kuzmin, A.; Purans, J. EXAFS study of hydrogen intercalation into ReO_3 using the evolutionary algorithm. *J. Phys.: Condens. Matter* **2014**, *26*, 26.

(230) Timoshenko, J.; Kuzmin, A.; Purans, J. Reverse Monte Carlo modeling of thermal disorder in crystalline materials from EXAFS spectra. *Comput. Phys. Commun.* **2012**, *183*, 1237−1245.

(231) Gurman, S.; McGreevy, R. Reverse Monte Carlo simulation for the analysis of EXAFS data. *J. Phys.: Condens. Matter* **1990**, *2*, 9463.

(232) Di Cicco, A.; Iesari, F.; Trapananti, A.; D'Angelo, P.; Filipponi, A. Structure and atomic correlations in molecular systems probed by XAS reverse Monte Carlo refinement. *J. Chem. Phys.* **2018**, *148*, 094307.

(233) Di Cicco, A.; Trapananti, A. Reverse Monte Carlo refinement of molecular and condensed systems by x-ray absorption spectroscopy. *J. Phys.: Condens. Matter* **2005**, *17*, S135.

(234) Kraynis, O.; Timoshenko, J.; Huang, J.; Singh, H.; Wachtel, E.; Frenkel, A. I.; Lubomirsky, I. Modeling strain distribution at the atomic level in doped ceria films with extended X-ray absorption fine structure spectroscopy. *Inorg. Chem.* **2019**, *58*, 7527−7536.

(235) Jonane, I.; Anspoks, A.; Aquilanti, G.; Kuzmin, A. High-temperature X-ray absorption spectroscopy study of thermochromic copper molybdate. *Acta Mater.* **2019**, *179*, 26−35.

(236) Opletal, G.; Petersen, T.; O'Malley, B.; Snook, I.; McCulloch, D. G.; Marks, N. A.; Yarovsky, I. Hybrid approach for generating realistic amorphous carbon structure using metropolis and reverse Monte Carlo. *Mol. Simul.* **2002**, *28*, 927–938.

(237) Pethes, I.; Pusztai, L. Reverse Monte Carlo modeling of liquid water with the explicit use of the SPC/E interatomic potential. *J. Chem. Phys.* **2017**, *146*, 064506.

(238) Timoshenko, J.; Anspoks, A.; Kalinko, A.; Kuzmin, A. Thermal disorder and correlation effects in anti-perovskite-type copper nitride. *Acta Mater.* **2017**, *129*, 61–71.

(239) Krayzman, V.; Levin, I. Reverse Monte Carlo refinements of nanoscale atomic correlations using powder and single-crystal diffraction data. *J. Appl. Crystallogr.* **2012**, *45*, 106–112.

(240) Triana, C.; Moré, R.; Bloomfield, A. J.; Petrović, P. V.; Ferrón, S. G.; Stanley, G.; Zarić, S. D.; Fox, T.; Brothers, E. N.; Sheehan, S. W.; et al. Soft templating and disorder in an applied 1D cobalt coordination polymer electrocatalyst. *Matter* **2019**, *1*, 1354–1369.

(241) Timoshenko, J.; Wrasman, C. J.; Luneau, M.; Shirman, T.; Cargnello, M.; Bare, S. R.; Aizenberg, J.; Friend, C. M.; Frenkel, A. I. Probing atomic distributions in mono-and bimetallic nanoparticles by supervised machine learning. *Nano Lett.* **2019**, *19*, 520–529.

(242) Zhang, J.; Sasaki, K.; Sutter, E.; Adzic, R. Stabilization of platinum oxygen-reduction electrocatalysts using gold clusters. *Science* **2007**, *315*, 220–222.

(243) Cramer, S.; Eccles, T.; Kutzler, F.; Hodgson, K. O.; Mortenson, L. Molybdenum x-ray absorption edge spectra. The chemical state of molybdenum in nitrogenase. *J. Am. Chem. Soc.* **1976**, *98*, 1287–1288.

(244) Bergmann, A.; Martinez-Moreno, E.; Teschner, D.; Chernev, P.; Gliech, M.; De Araújo, J. F.; Reier, T.; Dau, H.; Strasser, P. Reversible amorphization and the catalytically active state of crystalline Co3O4 during oxygen evolution. *Nat. Commun.* **2015**, *6*, 8625.

(245) Friebel, D.; Louie, M. W.; Bajdich, M.; Sanwald, K. E.; Cai, Y.; Wise, A. M.; Cheng, M.-J.; Sokaras, D.; Weng, T.-C.; Alonso-Mori, R.; et al. Identification of highly active Fe sites in (Ni, Fe)OOH for electrocatalytic water splitting. *J. Am. Chem. Soc.* **2015**, *137*, 1305–1313.

(246) Zhou, Y.; Che, F.; Liu, M.; Zou, C.; Liang, Z.; De Luna, P.; Yuan, H.; Li, J.; Wang, Z.; Xie, H.; et al. Dopant-induced electron localization drives CO2 reduction to C 2 hydrocarbons. *Nat. Chem.* **2018**, *10*, 974.

(247) Paredis, K.; Ono, L. K.; Mostafa, S.; Li, L.; Zhang, Z.; Yang, J. C.; Barrio, L.; Frenkel, A. I.; et al. Roldan Cuenya, B. Structure, chemical composition, and reactivity correlations during the in situ oxidation of 2-propanol. *J. Am. Chem. Soc.* **2011**, *133*, 6728–6735.

(248) Baker, M. L.; Mara, M. W.; Yan, J. J.; Hodgson, K. O.; Hedman, B.; Solomon, E. I. K-and L-edge X-ray absorption spectroscopy (XAS) and resonant inelastic X-ray scattering (RIXS) determination of differential orbital covalency (DOC) of transition metal sites. *Coord. Chem. Rev.* **2017**, *345*, 182–208.

(249) Frenkel, A. I.; Korshin, G. V.; Ankudinov, A. L. XANES study of Cu2+-binding sites in aquatic humic substances. *Environ. Sci. Technol.* **2000**, *34*, 2138–2142.

(250) Wilke, M.; Farges, F.; Petit, P.-E.; Brown, G. E., Jr; Martin, F. Oxidation state and coordination of Fe in minerals: An Fe K-XANES spectroscopic study. *Am. Mineral.* **2001**, *86*, 714–730.

(251) Görlin, M.; Chernev, P.; Ferreira de Araújo, J.; Reier, T.; Dresp, S. r.; Paul, B.; Krähnert, R.; Dau, H.; Strasser, P. Oxygen evolution reaction dynamics, faradaic charge efficiency, and the active metal redox states of Ni–Fe oxide water splitting electrocatalysts. *J. Am. Chem. Soc.* **2016**, *138*, 5603–5614.

(252) Hoang, T. T.; Verma, S.; Ma, S.; Fister, T. T.; Timoshenko, J.; Frenkel, A. I.; Kenis, P. J.; Gewirth, A. A. Nano porous copper-silver alloys by additive-controlled electro-deposition for the selective electroreduction of CO2 to ethylene and ethanol. *J. Am. Chem. Soc.* **2018**, *140*, 5791–5797.

(253) Grandjean, D.; Benfield, R. E.; Nayral, C.; Maisonnat, A.; Chaudret, B. EXAFS and XANES study of a pure and Pd doped novel Sn/SnOx nanomaterial. *J. Phys. Chem. B* **2004**, *108*, 8876–8887.

(254) Dutta, A.; Kuzume, A.; Kaliginedi, V.; Rahaman, M.; Sinev, I.; Ahmadi, M.; Cuenya, B. R.; Vesztergom, S.; Broekmann, P. Probing the chemical state of tin oxide NP catalysts during CO2 electro-reduction: A complementary operando approach. *Nano Energy* **2018**, *53*, 828–840.

(255) Mistry, H.; Reske, R.; Strasser, P.; Roldan Cuenya, B. Size-dependent reactivity of gold-copper bimetallic nanoparticles during CO2 electroreduction. *Catal. Today* **2017**, *288*, 30–36.

(256) Lü, F.; Bao, H.; Mi, Y.; Liu, Y.; Sun, J.; Peng, X.; Qiu, Y.; Zhuo, L.; Liu, X.; Luo, J. Electrochemical CO2 reduction: from nanoclusters to single atom catalysts. *Sustainable Energy Fuels* **2020**, *4*, 1012.

(257) Reske, R.; Mistry, H.; Behafarid, F.; Roldan Cuenya, B.; Strasser, P. Particle size effects in the catalytic electroreduction of CO2 on Cu nanoparticles. *J. Am. Chem. Soc.* **2014**, *136*, 6978–6986.

(258) Matos, J.; Ono, L.; Behafarid, F.; Croy, J.; Mostafa, S.; DeLaRiva, A.; Datye, A.; Frenkel, A.; Roldan Cuenya, B. In situ coarsening study of inverse micelle-prepared Pt nanoparticles supported on γ-Al2O3: pretreatment and environmental effects. *Phys. Chem. Chem. Phys.* **2012**, *14*, 11457–11467.

(259) Behafarid, F.; Matos, J.; Hong, S.; Zhang, L.; Rahman, T. S.; Roldan Cuenya, B. Structural and electronic properties of micellar Au nanoparticles: Size and ligand effects. *ACS Nano* **2014**, *8*, 6671–6681.

(260) Mistry, H.; Reske, R.; Zeng, Z.; Zhao, Z.-J.; Greeley, J.; Strasser, P.; Roldan Cuenya, B. Exceptional size-dependent activity enhancement in the electroreduction of CO2 over Au nanoparticles. *J. Am. Chem. Soc.* **2014**, *136*, 16473–16476.

(261) Roldan Cuenya, B.; Ortigoza, M. A.; Ono, L.; Behafarid, F.; Mostafa, S.; Croy, J.; Paredis, K.; Shafai, G.; Rahman, T.; Li, L.; et al. Thermodynamic properties of Pt nanoparticles: Size, shape, support, and adsorbate effects. *Phys. Rev. B: Condens. Matter Mater. Phys.* **2011**, *84*, 245438.

(262) Roldan Cuenya, B. Synthesis and catalytic properties of metal nanoparticles: Size, shape, support, composition, and oxidation state effects. *Thin Solid Films* **2010**, *518*, 3127–3150.

(263) Mistry, H.; Varela, A. S.; Kuehl, S.; Strasser, P.; Roldan Cuenya, B. Nanostructured electrocatalysts with tunable activity and selectivity. *Nat. Rev. Mater.* **2016**, *1*, 16009.

(264) Jeon, H. S.; Sinev, I.; Scholten, F.; Divins, N. J.; Zegkinoglou, I.; Pielsticker, L.; Roldan Cuenya, B. Operando evolution of the structure and oxidation state of size-controlled Zn nanoparticles during CO2 electroreduction. *J. Am. Chem. Soc.* **2018**, *140*, 9383–9386.

(265) Wang, J. X.; Inada, H.; Wu, L.; Zhu, Y.; Choi, Y.; Liu, P.; Zhou, W.-P.; Adzic, R. R. Oxygen reduction on well-defined core–shell nanocatalysts: particle size, facet, and Pt shell thickness effects. *J. Am. Chem. Soc.* **2009**, *131*, 17298–17302.

(266) Jentys, A. Estimation of mean size and shape of small metal particles by EXAFS. *Phys. Chem. Chem. Phys.* **1999**, *1*, 4059–4063.

(267) Calvin, S.; Miller, M.; Goswami, R.; Cheng, S.-F.; Mulvaney, S.; Whitman, L.; Harris, V. Determination of crystallite size in a magnetic nanocomposite using extended x-ray absorption fine structure. *J. Appl. Phys.* **2003**, *94*, 778–783.

(268) Frenkel, A. I.; Yevick, A.; Cooper, C.; Vasic, R. Modeling the structure and composition of nanoparticles by extended X-ray absorption fine-structure spectroscopy. *Annu. Rev. Anal. Chem.* **2011**, *4*, 23–39.

(269) Glasner, D.; Frenkel, A. I. Geometrical characteristics of regular polyhedra: application to EXAFS studies of nanoclusters. *AIP Conf. Proc.* **2006**, *882*, 746–748.

(270) Frenkel, A. I.; Frenkel, S. C.; Liu, T. Structural stability of giant polyoxomolybdate molecules as probed by EXAFS. *Phys. Scr.* **2005**, *2005*, 721.

(271) Choi, Y.; Sinev, I.; Mistry, H.; Zegkinoglou, I.; Roldan Cuenya, B. Probing the dynamic structure and chemical state of Au

nanocatalysts during the electrochemical oxidation of 2-propanol. *ACS Catal.* **2016**, *6*, 3396−3403.

(272) Varnell, J. A.; Tse, E. C. M.; Schulz, C. E.; Fister, T. T.; Haasch, R. T.; Timoshenko, J.; Frenkel, A. I.; Gewirth, A. A. Identification of carbon-encapsulated iron nanoparticles as active species in non-precious metal oxygen reduction catalysts. *Nat. Commun.* **2016**, *7*, 12582.

(273) Bock, D. C.; Pelliccione, C. J.; Zhang, W.; Timoshenko, J.; Knehr, K.; West, A. C.; Wang, F.; Li, Y.; Frenkel, A. I.; Takeuchi, E. S.; et al. Size dependent behavior of Fe3O4 crystals during electrochemical (de) lithiation: an in situ X-ray diffraction, ex situ X-ray absorption spectroscopy, transmission electron microscopy and theoretical investigation. *Phys. Chem. Chem. Phys.* **2017**, *19*, 20867−20880.

(274) Tomanek, D.; Mukherjee, S.; Bennemann, K. Simple theory for the electronic and atomic structure of small clusters. *Phys. Rev. B: Condens. Matter Mater. Phys.* **1983**, *28*, 665−673.

(275) Apai, G.; Hamilton, J. F.; Stohr, J.; Thompson, A. Extended X-ray-absorption fine-structure of small Cu and Ni clusters - binding-energy and bond-length changes with cluster size. *Phys. Rev. Lett.* **1979**, *43*, 165−169.

(276) Montano, P.; Schulze, W.; Tesche, B.; Shenoy, G.; Morrison, T. Extended x-ray-absorption fine-structure study of Ag particles isolated in solid argon. *Phys. Rev. B: Condens. Matter Mater. Phys.* **1984**, *30*, 672−677.

(277) Montano, P. A.; Shenoy, G. K.; Alp, E. E.; Schulze, W.; Urban, J. Structure of copper microclusters isolated in solid argon. *Phys. Rev. Lett.* **1986**, *56*, 2076−2079.

(278) Frenkel, A.; Nemzer, S.; Pister, I.; Soussan, L.; Harris, T.; Sun, Y.; Rafailovich, M. Size-controlled synthesis and characterization of thiol-stabilized gold nanoparticles. *J. Chem. Phys.* **2005**, *123*, 184701.

(279) Mostafa, S.; Behafarid, F.; Croy, J. R.; Ono, L. K.; Li, L.; Yang, J. C.; Frenkel, A. I.; Cuenya, B. R. Shape-dependent catalytic properties of Pt nanoparticles. *J. Am. Chem. Soc.* **2010**, *132*, 15714−15719.

(280) Roldan Cuenya, B. Metal nanoparticle catalysts beginning to shape-up. *Acc. Chem. Res.* **2013**, *46*, 1682−1691.

(281) Mistry, H.; Behafarid, F.; Zhou, E.; Ono, L.; Zhang, L.; Roldan Cuenya, B. Shape-dependent catalytic oxidation of 2-butanol over Pt nanoparticles supported on γ-Al2O3. *ACS Catal.* **2014**, *4*, 109−115.

(282) Zhu, W.; Kattel, S.; Jiao, F.; Chen, J. G. Shape-controlled CO2 electrochemical reduction on nanosized Pd hydride cubes and octahedra. *Adv. Energy Mater.* **2019**, *9*, 1802840.

(283) Frenkel, A. I.; Hills, C. W.; Nuzzo, R. G. A view from the inside: complexity in the atomic scale ordering of supported metal nanoparticles. *J. Phys. Chem. B* **2001**, *105*, 12689−12703.

(284) Roldan Cuenya, B.; Croy, J. R.; Mostafa, S.; Behafarid, F.; Li, L.; Zhang, Z.; Yang, J. C.; Wang, Q.; Frenkel, A. I. Solving the structure of size-selected Pt nanocatalysts synthesized by inverse micelle encapsulation. *J. Am. Chem. Soc.* **2010**, *132*, 8747−8756.

(285) Myers, V. S.; Frenkel, A. I.; Crooks, R. M. In situ structural characterization of platinum dendrimer-encapsulated oxygen reduction electrocatalysts. *Langmuir* **2012**, *28*, 1596−1603.

(286) Myers, V. S.; Weir, M. G.; Carino, E. V.; Yancey, D. F.; Pande, S.; Crooks, R. M. Dendrimer-encapsulated nanoparticles: new synthetic and characterization methods and catalytic applications. *Chem. Sci.* **2011**, *2*, 1632−1646.

(287) Mistry, H.; Behafarid, F.; Bare, S. R.; Roldan Cuenya, B. Pressure-dependent effect of hydrogen adsorption on structural and electronic properties of Pt/γ-Al2O3 nanoparticles. *ChemCatChem* **2014**, *6*, 348−352.

(288) Grunwaldt, J.-D.; Molenbroek, A.; Topsøe, N.-Y.; Topsøe, H.; Clausen, B. In situ investigations of structural changes in Cu/ZnO catalysts. *J. Catal.* **2000**, *194*, 452−460.

(289) Roese, S.; Kononov, A.; Timoshenko, J.; Frenkel, A.; Hoevel, H. Cluster assemblies produced by aggregation of preformed Ag clusters in ionic liquids. *Langmuir* **2018**, *34*, 4811−4819.

(290) Timoshenko, J.; Roese, S.; Hövel, H.; Frenkel, A. I. Silver clusters shape determination from in-situ XANES data. *Radiat. Phys. Chem.* **2020**, *175*, 108049.

(291) Mager-Maury, C.; Bonnard, G.; Chizallet, C.; Sautet, P.; Raybaud, P. H2-induced reconstruction of supported Pt clusters: metal−support interaction versus surface hydride. *ChemCatChem* **2011**, *3*, 200−207.

(292) Liu, P.; Nørskov, J. K. Ligand and ensemble effects in adsorption on alloy surfaces. *Phys. Chem. Chem. Phys.* **2001**, *3*, 3814−3818.

(293) Gao, F.; Goodman, D. W. Pd−Au bimetallic catalysts: understanding alloy effects from planar models and (supported) nanoparticles. *Chem. Soc. Rev.* **2012**, *41*, 8009−8020.

(294) Chen, P.-C.; Liu, X.; Hedrick, J. L.; Xie, Z.; Wang, S.; Lin, Q.-Y.; Hersam, M. C.; Dravid, V. P.; Mirkin, C. A. Polyelemental nanoparticle libraries. *Science* **2016**, *352*, 1565−1569.

(295) Agarwal, N.; Freakley, S. J.; McVicker, R. U.; Althahban, S. M.; Dimitratos, N.; He, Q.; Morgan, D. J.; Jenkins, R. L.; Willock, D. J.; Taylor, S. H.; et al. Aqueous Au-Pd colloids catalyze selective CH4 oxidation to CH3OH with O2 under mild conditions. *Science* **2017**, *358*, 223−227.

(296) Wong, A.; Liu, Q.; Griffin, S.; Nicholls, A.; Regalbuto, J. Synthesis of ultrasmall, homogeneously alloyed, bimetallic nanoparticles on silica supports. *Science* **2017**, *358*, 1427−1430.

(297) Hwang, B.-J.; Sarma, L. S.; Chen, J.-M.; Chen, C.-H.; Shih, S.-C.; Wang, G.-R.; Liu, D.-G.; Lee, J.-F.; Tang, M.-T. Structural models and atomic distribution of bimetallic nanoparticles as investigated by X-ray absorption spectroscopy. *J. Am. Chem. Soc.* **2005**, *127*, 11140−11145.

(298) Yin, G.; Abe, H.; Kodiyath, R.; Ueda, S.; Srinivasan, N.; Yamaguchi, A.; Miyauchi, M. Selective electro-or photo-reduction of carbon dioxide to formic acid using a Cu−Zn alloy catalyst. *J. Mater. Chem. A* **2017**, *5*, 12113−12119.

(299) Hu, H.; Tang, Y.; Hu, Q.; Wan, P.; Dai, L.; Yang, X. J. In-situ grown nanoporous Zn-Cu catalysts on brass foils for enhanced electrochemical reduction of carbon dioxide. *Appl. Surf. Sci.* **2018**, *445*, 281−286.

(300) Keerthiga, G.; Chetty, R. Electrochemical reduction of carbon dioxide on zinc-modified copper electrodes. *J. Electrochem. Soc.* **2017**, *164*, H164−H169.

(301) Ren, D.; Ang, B. S.-H.; Yeo, B. S. Tuning the selectivity of carbon dioxide electroreduction toward ethanol on oxide-derived Cu x Zn catalysts. *ACS Catal.* **2016**, *6*, 8239−8247.

(302) Feng, Y.; Li, Z.; Liu, H.; Dong, C.; Wang, J.; Kulinich, S. A.; Du, X. Laser-prepared CuZn alloy catalyst for selective electrochemical reduction of CO2 to ethylene. *Langmuir* **2018**, *34*, 13544−13549.

(303) Lamaison, S.; Wakerley, D.; Montero, D.; Rousse, G.; Taverna, D.; Giaume, D.; Mercier, D.; Blanchard, J.; Tran, H. N.; Fontecave, M.; et al. Zn−Cu alloy nanofoams as efficient catalysts for the reduction of CO2 to syngas mixtures with a potential-independent H2/CO ratio. *ChemSusChem* **2019**, *12*, 511−517.

(304) Li, Y. C.; Wang, Z.; Yuan, T.; Nam, D.-H.; Luo, M.; Wicks, J.; Chen, B.; Li, J.; Li, F.; Garcia de Arquer, F. P. Binding site diversity promotes CO2 electroreduction to ethanol. *J. Am. Chem. Soc.* **2019**, *141* (21), 8584−8591.

(305) Lee, S.; Park, G.; Lee, J. Importance of Ag−Cu biphasic boundaries for selective electrochemical reduction of CO2 to ethanol. *ACS Catal.* **2017**, *7*, 8594−8604.

(306) Kim, D.; Xie, C.; Becknell, N.; Yu, Y.; Karamad, M.; Chan, K.; Crumlin, E. J.; Nørskov, J. K.; Yang, P. Electrochemical activation of CO2 through atomic ordering transformations of AuCu nanoparticles. *J. Am. Chem. Soc.* **2017**, *139*, 8329−8336.

(307) Owen, E.; Preston, G. X-ray analysis of zinc-copper alloys. *Proc. Phys. Soc. London* **1923**, *36*, 49.

(308) Humphrey, J. J.; Plana, D.; Celorrio, V.; Sadasivan, S.; Tooze, R. P.; Rodríguez, P.; Fermín, D. J. Electrochemical reduction of carbon dioxide at gold-palladium core−shell nanoparticles: product distribution versus shell thickness. *ChemCatChem* **2016**, *8*, 952−960.

(309) Kortlever, R.; Peters, I.; Balemans, C.; Kas, R.; Kwon, Y.; Mul, G.; Koper, M. Palladium−gold catalyst for the electrochemical reduction of CO2 to C 1−C 5 hydrocarbons. *Chem. Commun.* **2016**, *52*, 10229−10232.

(310) Bellini, M.; Folliero, M. G.; Evangelisti, C.; He, Q.; Hu, Y.; Pagliaro, M. V.; Oberhauser, W.; Marchionni, A.; Filippi, J.; Miller, H. A.; et al. A gold−palladium nanoparticle alloy catalyst for CO production from CO2 electroreduction. *Energy Technol.* **2019**, *7*, 1800859.

(311) Cai, F.; Gao, D.; Si, R.; Ye, Y.; He, T.; Miao, S.; Wang, G.; Bao, X. Effect of metal deposition sequence in carbon-supported Pd−Pt catalysts on activity towards CO2 electroreduction to formate. *Electrochem. Commun.* **2017**, *76*, 1−5.

(312) Yeh, H.; Azároff, L. V. Electronic structure of copper-zinc solid solutions deduced from their X-ray K-absorption spectra. *Appl. Phys. Lett.* **1965**, *6*, 207−208.

(313) Frenkel, A. I. Applications of extended X-ray absorption fine-structure spectroscopy to studies of bimetallic nanoparticle catalysts. *Chem. Soc. Rev.* **2012**, *41*, 8163−8178.

(314) Frenkel, A.; Machavariani, V. S.; Rubshtein, A.; Rosenberg, Y.; Voronel, A.; Stern, E. Local structure of disordered Au-Cu and Au-Ag alloys. *Phys. Rev. B: Condens. Matter Mater. Phys.* **2000**, *62*, 9364.

(315) Tupy, S. A.; Karim, A. M.; Bagia, C.; Deng, W.; Huang, Y.; Vlachos, D. G.; Chen, J. G. Correlating ethylene glycol reforming activity with in situ EXAFS detection of Ni segregation in supported NiPt bimetallic catalysts. *ACS Catal.* **2012**, *2*, 2290−2296.

(316) Duchesne, P. N.; Li, Z.; Deming, C. P.; Fung, V.; Zhao, X.; Yuan, J.; Regier, T.; Aldalbahi, A.; Almarhoon, Z.; Chen, S.; et al. Golden single-atomic-site platinum electrocatalysts. *Nat. Mater.* **2018**, *17*, 1033.

(317) Kaito, T.; Tanaka, H.; Mitsumoto, H.; Sugawara, S.; Shinohara, K.; Ariga, H.; Uehara, H.; Takakusagi, S.; Asakura, K. In situ X-ray absorption fine structure analysis of PtCo, PtCu, and PtNi alloy electrocatalysts: The correlation of enhanced oxygen reduction reaction activity and structure. *J. Phys. Chem. C* **2016**, *120*, 11519−11527.

(318) Wang, D.; Zhou, J.; Hu, Y.; Yang, J.; Han, N.; Li, Y.; Sham, T.-K. In situ X-ray absorption near-edge structure study of advanced NiFe (OH)x electrocatalyst on carbon paper for water oxidation. *J. Phys. Chem. C* **2015**, *119*, 19573−19583.

(319) Bernal, M.; Bagger, A.; Scholten, F.; Sinev, I.; Bergmann, A.; Ahmadi, M.; Rossmeisl, J.; Cuenya, B. R. CO2 electroreduction on copper-cobalt nanoparticles: Size and composition effect. *Nano Energy* **2018**, *53*, 27−36.

(320) Timoshenko, J.; Anspoks, A.; Kalinko, A.; Kuzmin, A. Local structure of nanosized tungstates revealed by evolutionary algorithm. *Phys. Status Solidi A* **2015**, *212*, 265−273.

(321) Carbone, M. R.; Yoo, S.; Topsakal, M.; Lu, D. Classification of local chemical environments from x-ray absorption spectra using supervised machine learning. *Phys. Rev. Mater.* **2019**, *3*, 033604.

(322) Jiang, N.; Su, D.; Spence, J. Determination of Ti coordination from pre-edge peaks in Ti K-edge XANES. *Phys. Rev. B: Condens. Matter Mater. Phys.* **2007**, *76*, 214117.

(323) Itié, J.; Couzinet, B.; Polian, A.; Flank, A.; Lagarde, P. Pressure-induced disappearance of the local rhombohedral distortion in BaTiO3. *EPL (Europhysics Letters)* **2006**, *74*, 706.

(324) Hou, Y.; Huang, Y.-B.; Liang, Y.-L.; Chai, G.-L.; Yi, J.-D.; Zhang, T.; Zang, K.-T.; Luo, J.; Xu, R.; Lin, H.; et al. Unraveling the reactivity and selectivity of atomically isolated metal−nitrogen sites anchored on porphyrinic triazine frameworks for electroreduction of CO2. *CCS Chem.* **2019**, *1*, 384−395.

(325) Jia, Q.; Ramaswamy, N.; Hafiz, H.; Tylus, U.; Strickland, K.; Wu, G.; Barbiellini, B.; Bansil, A.; Holby, E. F.; Zelenay, P.; et al. Experimental observation of redox-induced Fe−N switching behavior as a determinant role for oxygen reduction activity. *ACS Nano* **2015**, *9*, 12496−12505.

(326) Zhang, H.; Hwang, S.; Wang, M.; Feng, Z.; Karakalos, S.; Luo, L.; Qiao, Z.; Xie, X.; Wang, C.; Su, D.; et al. Single atomic iron catalysts for oxygen reduction in acidic media: particle size control and thermal activation. *J. Am. Chem. Soc.* **2017**, *139*, 14143−14149.

(327) Zitolo, A.; Goellner, V.; Armel, V.; Sougrati, M.-T.; Mineva, T.; Stievano, L.; Fonda, E.; Jaouen, F. Identification of catalytic sites for oxygen reduction in iron-and nitrogen-doped graphene materials. *Nat. Mater.* **2015**, *14*, 937−942.

(328) Zitolo, A.; Ranjbar-Sahraie, N.; Mineva, T.; Li, J.; Jia, Q.; Stamatin, S.; Harrington, G. F.; Lyth, S. M.; Krtil, P.; Mukerjee, S.; et al. Identification of catalytic sites in cobalt-nitrogen-carbon materials for the oxygen reduction reaction. *Nat. Commun.* **2017**, *8*, 1−11.

(329) Wu, T.; Sun, S.; Song, J.; Xi, S.; Du, Y.; Chen, B.; Sasangka, W. A.; Liao, H.; Gan, C. L.; Scherer, G. G.; et al. Iron-facilitated dynamic active-site generation on spinel CoAl2O4 with self-termination of surface reconstruction for water oxidation. *Nat. Catal.* **2019**, *2*, 763−772.

(330) Menezes, P. W.; Indra, A.; Bergmann, A.; Chernev, P.; Walter, C.; Dau, H.; Strasser, P.; Driess, M. Uncovering the prominent role of metal ions in octahedral versus tetrahedral sites of cobalt−zinc oxide catalysts for efficient oxidation of water. *J. Mater. Chem. A* **2016**, *4*, 10014−10022.

(331) Liang, Y.; Wang, H.; Zhou, J.; Li, Y.; Wang, J.; Regier, T.; Dai, H. Covalent hybrid of spinel manganese−cobalt oxide and graphene as advanced oxygen reduction electrocatalysts. *J. Am. Chem. Soc.* **2012**, *134*, 3517−3523.

(332) Wang, H.-Y.; Hung, S.-F.; Chen, H.-Y.; Chan, T.-S.; Chen, H. M.; Liu, B. In operando identification of geometrical-site-dependent water oxidation activity of spinel Co3O4. *J. Am. Chem. Soc.* **2016**, *138*, 36−39.

(333) Calvin, S.; Carpenter, E.; Ravel, B.; Harris, V.; Morrison, S. Multiedge refinement of extended x-ray-absorption fine structure of manganese zinc ferrite nanoparticles. *Phys. Rev. B: Condens. Matter Mater. Phys.* **2002**, *66*, 224405.

(334) Shivhare, A.; Scott, R. W. Au25 clusters as precursors for the synthesis of AuPd bimetallic nanoparticles with isolated atomic Pd-surface sites. *Molecular Catalysis* **2018**, *457*, 33−40.

(335) Kauffman, D. R.; Alfonso, D.; Matranga, C.; Qian, H.; Jin, R. Experimental and computational investigation of Au25 clusters and CO2: a unique interaction and enhanced electrocatalytic activity. *J. Am. Chem. Soc.* **2012**, *134*, 10237−10243.

(336) Kauffman, D. R.; Alfonso, D. R.; Tafen, D. N.; Wang, C.; Zhou, Y.; Yu, Y.; Lekse, J. W.; Deng, X.; Espinoza, V.; Trindell, J.; et al. Selective electrocatalytic reduction of CO2 into CO at small, thiol-capped Au/Cu nanoparticles. *J. Phys. Chem. C* **2018**, *122*, 27991−28000.

(337) Kniep, B.-L.; Girgsdies, F.; Ressler, T. Effect of precipitate aging on the microstructural characteristics of Cu/ZnO catalysts for methanol steam reforming. *J. Catal.* **2005**, *236*, 34−44.

(338) Mistry, H.; Choi, Y. W.; Bagger, A.; Scholten, F.; Bonifacio, C. S.; Sinev, I.; Divins, N. J.; Zegkinoglou, I.; Jeon, H. S.; Kisslinger, K.; Stach, E. A.; Yang, J. C.; Rossmeisl, J.; Roldan Cuenya, B. Enhanced carbon dioxide electroreduction to carbon monoxide over defect-rich plasma-activated silver catalysts. *Angew. Chem., Int. Ed.* **2017**, *56*, 11394−11398.

(339) Sasaki, K.; Naohara, H.; Choi, Y.; Cai, Y.; Chen, W.-F.; Liu, P.; Adzic, R. R. Highly stable Pt monolayer on PdAu nanoparticle electrocatalysts for the oxygen reduction reaction. *Nat. Commun.* **2012**, *3*, 1−9.

(340) Koenigsmann, C.; Sutter, E.; Adzic, R. R.; Wong, S. S. Size-and composition-dependent enhancement of electrocatalytic oxygen reduction performance in ultrathin palladium−gold (Pd1−x Au x) nanowires. *J. Phys. Chem. C* **2012**, *116*, 15297−15306.

(341) Liu, H.; An, W.; Li, Y.; Frenkel, A. I.; Sasaki, K.; Koenigsmann, C.; Su, D.; Anderson, R. M.; Crooks, R. M.; Adzic, R. R.; et al. In situ probing of the active site geometry of ultrathin nanowires for the oxygen reduction reaction. *J. Am. Chem. Soc.* **2015**, *137*, 12597−12609.

(342) Kang, J. H.; Menard, L. D.; Nuzzo, R. G.; Frenkel, A. I. Unusual non-bulk properties in nanoscale materials: thermal metal−

metal bond contraction of γ-alumina-supported Pt catalysts. *J. Am. Chem. Soc.* **2006**, *128*, 12068−12069.

(343) Small, M. W.; Sanchez, S. I.; Marinkovic, N. S.; Frenkel, A. I.; Nuzzo, R. G. Influence of adsorbates on the electronic structure, bond strain, and thermal properties of an alumina-supported Pt catalyst. *ACS Nano* **2012**, *6*, 5583−5595.

(344) Frenkel, A.; Stern, E.; Voronel, A.; Heald, S. Lattice strains in disordered mixed salts. *Solid State Commun.* **1996**, *99*, 67−71.

(345) Vila, F. D.; Rehr, J. J.; Nuzzo, R. G.; Frenkel, A. I. Anomalous structural disorder in supported Pt nanoparticles. *J. Phys. Chem. Lett.* **2017**, *8*, 3284−3288.

(346) Vila, F. D.; Hayashi, S. T.; Moore, J. M.; Rehr, J. J. Molecular dynamics simulations of supported pt nanoparticles with a hybrid sutton−chen potential. *J. Phys. Chem. C* **2016**, *120*, 14883−14891.

(347) Vila, F. D.; Rehr, J. J.; Kelly, S. D.; Bare, S. R. Operando effects on the structure and dynamics of PtnSnm/γ-Al2O3 from ab initio molecular dynamics and X-ray absorption spectra. *J. Phys. Chem. C* **2013**, *117*, 12446−12457.

(348) Duan, Z.; Li, Y.; Timoshenko, J.; Chill, S. T.; Anderson, R. M.; Yancey, D. F.; Frenkel, A. I.; Crooks, R. M.; Henkelman, G. A combined theoretical and experimental EXAFS study of the structure and dynamics of Au147 nanoparticles. *Catal. Sci. Technol.* **2016**, *6*, 6879−6885.

(349) Erickson, E. M.; Oruc, M. E.; Wetzel, D. J.; Cason, M. W.; Hoang, T. T.; Small, M. W.; Li, D.; Frenkel, A. I.; Gewirth, A. A.; Nuzzo, R. G. A comparison of atomistic and continuum approaches to the study of bonding dynamics in electrocatalysis: microcantilever stress and in situ EXAFS observations of platinum bond expansion due to oxygen adsorption during the oxygen reduction reaction. *Anal. Chem.* **2014**, *86*, 8368−8375.

(350) Imai, H.; Izumi, K.; Matsumoto, M.; Kubo, Y.; Kato, K.; Imai, Y. In situ and real-time monitoring of oxide growth in a few monolayers at surfaces of platinum nanoparticles in aqueous media. *J. Am. Chem. Soc.* **2009**, *131*, 6293−6300.

(351) Weir, M. G.; Myers, V. S.; Frenkel, A. I.; Crooks, R. M. In situ X-ray absorption analysis of∼ 1.8 nm dendrimer-encapsulated Pt nanoparticles during electrochemical CO oxidation. *ChemPhysChem* **2010**, *11*, 2942−2950.

(352) Poverenov, E.; Efremenko, I.; Frenkel, A. I.; Ben-David, Y.; Shimon, L. J.; Leitus, G.; Konstantinovski, L.; Martin, J. M.; Milstein, D. Evidence for a terminal Pt (IV)-oxo complex exhibiting diverse reactivity. *Nature* **2008**, *455*, 1093−1096.

(353) Seitsonen, A. P.; Zhu, Y.; Bedürftig, K.; Over, H. Bonding mechanism and atomic geometry of an ordered hydroxyl overlayer on Pt (111). *J. Am. Chem. Soc.* **2001**, *123*, 7347−7351.

(354) Jacob, T.; Goddard, W. A. Agostic interactions and dissociation in the first layer of water on Pt (111). *J. Am. Chem. Soc.* **2004**, *126*, 9360−9368.

(355) Li, T.; Balbuena, P. B. Computational studies of the interactions of oxygen with platinum clusters. *J. Phys. Chem. B* **2001**, *105*, 9943−9952.

(356) Singh, N.; Nguyen, M.-T.; Cantu, D. C.; Mehdi, B. L.; Browning, N. D.; Fulton, J. L.; Zheng, J.; Balasubramanian, M.; Gutiérrez, O. Y.; Glezakou, V.-A.; et al. Carbon-supported Pt during aqueous phenol hydrogenation with and without applied electrical potential: X-ray absorption and theoretical studies of structure and adsorbates. *J. Catal.* **2018**, *368*, 8−19.

(357) Behafarid, F.; Ono, L.; Mostafa, S.; Croy, J.; Shafai, G.; Hong, S.; Rahman, T.; Bare, S. R.; Cuenya, B. R. Electronic properties and charge transfer phenomena in Pt nanoparticles on γ-Al2O3: Size, shape, support, and adsorbate effects. *Phys. Chem. Chem. Phys.* **2012**, *14*, 11766−11779.

(358) Mathew, R. J.; Russell, A. E. XAS of carbon supported platinum fuel cell electrocatalysts: advances towards real time investigations. *Top. Catal.* **2000**, *10*, 231−239.

(359) McBreen, J.; O'Grady, W. E.; et al. EXAFS: a new tool for the study of battery and fuel cell materials. *J. Power Sources* **1988**, *22*, 323−340.

(360) Lira, E.; Merte, L.; Behafarid, F.; Ono, L.; Zhang, L.; Roldan Cuenya, B. Role and evolution of nanoparticle structure and chemical state during the oxidation of NO over size-and shape-controlled Pt/γ-Al2O3 catalysts under operando conditions. *ACS Catal.* **2014**, *4*, 1875−1884.

(361) Paredis, K.; Ono, L. K.; Behafarid, F.; Zhang, Z.; Yang, J. C.; Frenkel, A. I.; Roldan Cuenya, B. Evolution of the structure and chemical state of Pd nanoparticles during the in situ catalytic reduction of NO with H2. *J. Am. Chem. Soc.* **2011**, *133*, 13455−13464.

(362) Merte, L. R.; Behafarid, F.; Miller, D. J.; Friebel, D.; Cho, S.; Mbuga, F.; Sokaras, D.; Alonso-Mori, R.; Weng, T.-C.; Nordlund, D.; et al. Electrochemical oxidation of size-selected Pt nanoparticles studied using in situ high-energy-resolution X-ray absorption spectroscopy. *ACS Catal.* **2012**, *2*, 2371−2376.

(363) Li, Y.; Liu, J. H.-C.; Witham, C. A.; Huang, W.; Marcus, M. A.; Fakra, S. C.; Alayoglu, P.; Zhu, Z.; Thompson, C. M.; Arjun, A.; et al. A Pt-cluster-based heterogeneous catalyst for homogeneous catalytic reactions: X-ray absorption spectroscopy and reaction kinetic studies of their activity and stability against leaching. *J. Am. Chem. Soc.* **2011**, *133*, 13527−13533.

(364) Mistry, H.; Varela, A. S.; Bonifacio, C. S.; Zegkinoglou, I.; Sinev, I.; Choi, Y.-W.; Kisslinger, K.; Stach, E. A.; Yang, J. C.; Strasser, P.; Roldan Cuenya, B. Highly selective plasma-activated copper catalysts for carbon dioxide reduction to ethylene. *Nat. Commun.* **2016**, *7*, 12123.

(365) De Luna, P.; Quintero-Bermudez, R.; Dinh, C.-T.; Ross, M. B.; Bushuyev, O. S.; Todorović, P.; Regier, T.; Kelley, S. O.; Yang, P.; Sargent, E. H. Catalyst electro-redeposition controls morphology and oxidation state for selective carbon dioxide reduction. *Nat. Catal.* **2018**, *1*, 103−110.

(366) Eilert, A.; Cavalca, F.; Roberts, F. S.; Osterwalder, J. r.; Liu, C.; Favaro, M.; Crumlin, E. J.; Ogasawara, H.; Friebel, D.; Pettersson, L. G.; et al. Subsurface oxygen in oxide-derived copper electrocatalysts for carbon dioxide reduction. *J. Phys. Chem. Lett.* **2017**, *8*, 285−290.

(367) Frenkel, A.; Wang, Q.; Marinkovic, N.; Chen, J.; Barrio, L.; Si, R.; Camara, A. L.; Estrella, A.; Rodriguez, J.; Hanson, J. Combining X-ray absorption and X-ray diffraction techniques for in situ studies of chemical transformations in heterogeneous catalysis: advantages and limitations. *J. Phys. Chem. C* **2011**, *115*, 17884−17890.

(368) Newton, M. A. Time resolved operando X-ray techniques in catalysis, a case study: CO oxidation by O2 over Pt surfaces and alumina supported Pt catalysts. *Catalysts* **2017**, *7*, 58.

(369) Möller, T.; Scholten, F.; Thanh, T. N.; Sinev, I.; Timoshenko, J.; Wang, X.; Jovanov, Z. P.; Manuel, G.; Roldan Cuenya, B.; Varela, A. S.; Strasser, P. Electrocatalytic CO₂ reduction on CuOx nanocubes: Tracking the evolution of chemical state and geometric structure to catalytic selectivity using operando spectroscopy. *Angew. Chem.* **2020**. DOI: 10.1002/ange.202007136

(370) Wasserman, S. R. The analysis of mixtures: application of principal component analysis to XAS spectra. *J. Phys. IV* **1997**, *7*, C2-203−C2-205.

(371) Frenkel, A. I.; Kleifeld, O.; Wasserman, S. R.; Sagi, I. Phase speciation by extended x-ray absorption fine structure spectroscopy. *J. Chem. Phys.* **2002**, *116*, 9449−9456.

(372) Wang, X.; Hanson, J. C.; Frenkel, A. I.; Kim, J.-Y.; Rodriguez, J. A. Time-resolved studies for the mechanism of reduction of copper oxides with carbon monoxide: complex behavior of lattice oxygen and the formation of suboxides. *J. Phys. Chem. B* **2004**, *108*, 13667−13673.

(373) Manceau, A.; Marcus, M.; Lenoir, T. Estimating the number of pure chemical components in a mixture by X-ray absorption spectroscopy. *J. Synchrotron Radiat.* **2014**, *21*, 1140−1147.

(374) Ruckebusch, C.; Blanchet, L. Multivariate curve resolution: A review of advanced and tailored applications and challenges. *Anal. Chim. Acta* **2013**, *765*, 28−36.

(375) Voronov, A.; Urakawa, A.; van Beek, W.; Tsakoumis, N. E.; Emerich, H.; Rønning, M. Multivariate curve resolution applied to in

situ X-ray absorption spectroscopy data: An efficient tool for data processing and analysis. *Anal. Chim. Acta* **2014**, *840*, 20−27.

(376) Cassinelli, W. H.; Martins, L.; Passos, A. R.; Pulcinelli, S. H.; Santilli, C. V.; Rochet, A.; Briois, V. Multivariate curve resolution analysis applied to time-resolved synchrotron X-ray Absorption Spectroscopy monitoring of the activation of copper alumina catalyst. *Catal. Today* **2014**, *229*, 114−122.

(377) Lee, D. D.; Seung, H. S. Learning the parts of objects by non-negative matrix factorization. *Nature* **1999**, *401*, 788−791.

(378) Hyvärinen, A.; Oja, E. Independent component analysis: algorithms and applications. *Neural Networks* **2000**, *13*, 411−430.

(379) Li, Y.; Zakharov, D.; Zhao, S.; Tappero, R.; Jung, U.; Elsen, A.; Baumann, P.; Nuzzo, R. G.; Stach, E.; Frenkel, A. Complex structural dynamics of nanocatalysts revealed in Operando conditions by correlated imaging and spectroscopy probes. *Nat. Commun.* **2015**, *6*, 7583.

(380) Szlachetko, J.; Ferri, D.; Marchionni, V.; Kambolis, A.; Safonova, O. V.; Milne, C. J.; Kröcher, O.; Nachtegaal, M.; Sá, J. Subsecond and in situ chemical speciation of Pt/Al2O3 during oxidation−reduction cycles monitored by high-energy resolution off-resonant X-ray spectroscopy. *J. Am. Chem. Soc.* **2013**, *135*, 19071−19074.

(381) Błachucki, W.; Szlachetko, J.; Hoszowska, J.; Dousse, J.-C.; Kayser, Y.; Nachtegaal, M.; Sá, J. High energy resolution off-resonant spectroscopy for X-ray absorption spectra free of self-absorption effects. *Phys. Rev. Lett.* **2014**, *112*, 173003.

(382) Glatzel, P.; Singh, J.; Kvashnina, K. O.; van Bokhoven, J. A. In situ characterization of the 5d density of states of Pt nanoparticles upon adsorption of CO. *J. Am. Chem. Soc.* **2010**, *132*, 2555−2557.

(383) Kottwitz, M.; Li, Y.; Palomino, R. M.; Liu, Z.; Wang, G.; Wu, Q.; Huang, J.; Timoshenko, J.; Senanayake, S. D.; Balasubramanian, M.; et al. Local structure and electronic state of atomically dispersed Pt supported on nanosized CeO2. *ACS Catal.* **2019**, *9*, 8738−8748.

(384) Friebel, D.; Bajdich, M.; Yeo, B. S.; Louie, M. W.; Miller, D. J.; Casalongue, H. S.; Mbuga, F.; Weng, T.-C.; Nordlund, D.; Sokaras, D.; et al. On the chemical state of Co oxide electrocatalysts during alkaline water splitting. *Phys. Chem. Chem. Phys.* **2013**, *15*, 17460−17467.

(385) Asakura, H.; Kawamura, N.; Mizumaki, M.; Nitta, K.; Ishii, K.; Hosokawa, S.; Teramura, K.; Tanaka, T. A feasibility study of "range-extended" EXAFS measurement at the Pt L3-edge of Pt/Al2O3 in the presence of Au2O3. *J. Anal. At. Spectrom.* **2018**, *33*, 84−89.

(386) Li, Y.; Frenkel, A. I. Metal nanocatalysts. In *XAFS Techniques for Catalysts, Nanomaterials, and Surfaces*; Iwasawa, Y., Asakura, K., Tada, M., Eds.; Springer: 2017; pp 273−298.

(387) Van Stappen, C.; Decamps, L.; Cutsail, G. E.; Bjornsson, R.; Henthorn, J. T.; Birrell, J. A.; DeBeer, S. The spectroscopy of nitrogenases. *Chem. Rev.* **2020**, *120*, 5005−5081.

(388) DeBeer, S. X-ray absorption spectroscopy. In *Nitrogen Fixation*; Ribbe, M., Ed.; Humana Press, 2011; pp 165−176.

(389) Lelong, G. r.; Radtke, G.; Cormier, L.; Bricha, H.; Rueff, J.-P.; Ablett, J. M.; Cabaret, D.; Gélébart, F. d. r.; Shukla, A. Detecting non-bridging oxygens: non-resonant inelastic X-ray scattering in crystalline lithium borates. *Inorg. Chem.* **2014**, *53*, 10903−10908.

(390) Fister, T. T. Nonresonant Inelastic X-ray Scattering and X-ray Raman Scattering. In *XAFS Techniques for Catalysts, Nanomaterials, and Surfaces*; Iwasawa, Y., Asakura, K., Tada, M., Eds.; Springer: Cham, 2017; pp 237−250.

(391) Ketenoglu, D.; Spiekermann, G.; Harder, M.; Oz, E.; Koz, C.; Yagci, M. C.; Yilmaz, E.; Yin, Z.; Sahle, C. J.; Detlefs, B.; et al. X-ray Raman spectroscopy of lithium-ion battery electrolyte solutions in a flow cell. *J. Synchrotron Radiat.* **2018**, *25*, 537−542.

(392) Braun, A.; Wang, H.; Bergmann, U.; Tucker, M. C.; Gu, W.; Cramer, S. P.; Cairns, E. J. Origin of chemical shift of manganese in lithium battery electrode materials—a comparison of hard and soft X-ray techniques. *J. Power Sources* **2002**, *112*, 231−235.

(393) Frenkel, A. I.; Kolobov, A. V.; Robinson, I. K.; Cross, J. O.; Maeda, Y.; Bouldin, C. E. Direct separation of short range order in intermixed nanocrystalline and amorphous phases. *Phys. Rev. Lett.* **2002**, *89*, 285503.

(394) Frenkel, A. I.; Cross, J.; Fanning, D.; Robinson, I. DAFS analysis of magnetite. *J. Synchrotron Radiat.* **1999**, *6*, 332−334.

(395) Kawaguchi, T.; Fukuda, K.; Tokuda, K.; Sakaida, M.; Ichitsubo, T.; Oishi, M.; Matsubara, E.; et al. Roles of transition metals interchanging with lithium in electrode materials. *Phys. Chem. Chem. Phys.* **2015**, *17*, 14064−14070.

(396) Egami, T.; Billinge, S. J. *Underneath the Bragg peaks: Structural analysis of complex materials*; Elsevier: Oxford, 2003.

(397) Billinge, S. J. Nanoscale structural order from the atomic pair distribution function (PDF): There's plenty of room in the middle. *J. Solid State Chem.* **2008**, *181*, 1695−1700.

(398) Billinge, S.; Kwei, G. Probing the short-range order and dynamics of phase transitions using neutron powder diffraction. *J. Phys. Chem. Solids* **1996**, *57*, 1457−1464.

(399) Lamberti, C.; Borfecchia, E.; van Bokhoven, J. A.; Fernández-García, M. XAS Spectroscopy: related techniques and combination with other spectroscopic and scattering methods. In *X-Ray Absorption and X-Ray Emission Spectroscopy: Theory and Applications*; Van Bokhoven, J. A., Lamberti, C., Eds.; John Wiley & Sons, Ltd: Chichester (UK), 2016; pp 303−350.

(400) Cai, Z.; Bi, Y.; Hu, E.; Liu, W.; Dwarica, N.; Tian, Y.; Li, X.; Kuang, Y.; Li, Y.; Yang, X. Q.; et al. Single-crystalline ultrathin Co3O4 nanosheets with massive vacancy defects for enhanced electrocatalysis. *Adv. Energy Mater.* **2018**, *8*, 1701694.

(401) Tuaev, X.; Rudi, S.; Petkov, V.; Hoell, A.; Strasser, P. In situ study of atomic structure transformations of Pt−Ni nanoparticle catalysts during electrochemical potential cycling. *ACS Nano* **2013**, *7*, 5666−5674.

(402) Gan, L.; Cui, C.; Rudi, S.; Strasser, P. Core−shell and nanoporous particle architectures and their effect on the activity and stability of Pt ORR electrocatalysts. *Top. Catal.* **2014**, *57*, 236−244.

(403) Loukrakpam, R.; Shan, S.; Petkov, V.; Yang, L.; Luo, J.; Zhong, C.-J. Atomic ordering enhanced electrocatalytic activity of nanoalloys for oxygen reduction reaction. *J. Phys. Chem. C* **2013**, *117*, 20715−20721.

(404) Zhang, Z.; Ahmad, F.; Zhao, W.; Yan, W.; Zhang, W.; Huang, H.; Ma, C.; Zeng, J. Enhanced electrocatalytic reduction of CO2 via chemical coupling between indium oxide and reduced graphene oxide. *Nano Lett.* **2019**, *19*, 4029.

(405) Chen, Y.; Kanan, M. W. Tin oxide dependence of the CO2 reduction efficiency on tin electrodes and enhanced activity for tin/tin oxide thin-film catalysts. *J. Am. Chem. Soc.* **2012**, *134*, 1986−1989.

(406) Dutta, A.; Kuzume, A.; Rahaman, M.; Vesztergom, S.; Broekmann, P. Monitoring the chemical state of catalysts for CO2 electroreduction: an in operando study. *ACS Catal.* **2015**, *5*, 7498−7502.

(407) Kim, H.; Jeon, H. S.; Jee, M. S.; Nursanto, E. B.; Singh, J. P.; Chae, K.; Hwang, Y. J.; Min, B. K. Contributors to enhanced CO2 electroreduction activity and stability in a nanostructured Au electrocatalyst. *ChemSusChem* **2016**, *9*, 2097−2102.

(408) Nguyen, D. L. T.; Jee, M. S.; Won, D. H.; Jung, H.; Oh, H.-S.; Min, B. K.; Hwang, Y. J. Selective CO2 reduction on zinc electrocatalyst: the effect of zinc oxidation state induced by pretreatment environment. *ACS Sustainable Chem. Eng.* **2017**, *5*, 11377−11386.

(409) Kuhl, K. P.; Cave, E. R.; Abram, D. N.; Jaramillo, T. F. New insights into the electrochemical reduction of carbon dioxide on metallic copper surfaces. *Energy Environ. Sci.* **2012**, *5*, 7050−7059.

(410) Hansen, H. A.; Varley, J. B.; Peterson, A. A.; Nørskov, J. K. Understanding trends in the electrocatalytic activity of metals and enzymes for CO2 reduction to CO. *J. Phys. Chem. Lett.* **2013**, *4*, 388−392.

(411) Kortlever, R.; Shen, J.; Schouten, K. J. P.; Calle-Vallejo, F.; Koper, M. T. Catalysts and reaction pathways for the electrochemical reduction of carbon dioxide. *J. Phys. Chem. Lett.* **2015**, *6*, 4073−4082.

(412) Calle-Vallejo, F.; Koper, M. T. Theoretical considerations on the electroreduction of CO to C2 species on Cu (100) electrodes. *Angew. Chem., Int. Ed.* **2013**, *52*, 7282−7285.

(413) Xie, H.; Wang, T.; Liang, J.; Li, Q.; Sun, S. Cu-based nanocatalysts for electrochemical reduction of CO_2. *Nano Today* **2018**, *21*, 41−54.

(414) Li, C. W.; Kanan, M. W. CO2 reduction at low overpotential on Cu electrodes resulting from the reduction of thick Cu2O films. *J. Am. Chem. Soc.* **2012**, *134*, 7231−7234.

(415) Kim, D.; Lee, S.; Ocon, J. D.; Jeong, B.; Lee, J. K.; Lee, J. Insights into an autonomously formed oxygen-evacuated Cu2O electrode for the selective production of C2H4 from CO2. *Phys. Chem. Chem. Phys.* **2015**, *17*, 824−830.

(416) Kas, R.; Kortlever, R.; Milbrat, A.; Koper, M. T.; Mul, G.; Baltrusaitis, J. Electrochemical CO2 reduction on Cu2O-derived copper nanoparticles: controlling the catalytic selectivity of hydrocarbons. *Phys. Chem. Chem. Phys.* **2014**, *16*, 12194−12201.

(417) Ren, D.; Deng, Y.; Handoko, A. D.; Chen, C. S.; Malkhandi, S.; Yeo, B. S. Selective electrochemical reduction of carbon dioxide to ethylene and ethanol on copper (I) oxide catalysts. *ACS Catal.* **2015**, *5*, 2814−2821.

(418) Pander, J. E., III; Ren, D.; Huang, Y.; Loo, N. W. X.; Hong, S. H. L.; Yeo, B. S. Understanding the Heterogeneous Electrocatalytic Reduction of Carbon Dioxide on Oxide-Derived Catalysts. *ChemElectroChem* **2018**, *5*, 219−237.

(419) Lee, S.; Kim, D.; Lee, J. Electrocatalytic production of C3-C4 compounds by conversion of CO2 on a chloride-induced bi-phasic Cu2O-Cu catalyst. *Angew. Chem., Int. Ed.* **2015**, *54*, 14701−14705.

(420) Gao, D.; Zegkinoglou, I.; Divins, N. J.; Scholten, F.; Sinev, I.; Grosse, P.; Roldan Cuenya, B. Plasma-activated copper nanocube catalysts for efficient carbon dioxide electroreduction to hydrocarbons and alcohols. *ACS Nano* **2017**, *11*, 4825−4831.

(421) Scholten, F.; Sinev, I.; Bernal, D. M.; Roldan Cuenya, B. Plasma-modified dendritic Cu catalyst for CO2 electroreduction. *ACS Catal.* **2019**, *9*, 5496.

(422) Klingan, K.; Kottakkat, T.; Jovanov, Z. P.; Jiang, S.; Pasquini, C.; Scholten, F.; Kubella, P.; Bergmann, A.; Roldan Cuenya, B.; Roth, C.; et al. Reactivity determinants in electrodeposited Cu foams for electrochemical CO2 reduction. *ChemSusChem* **2018**, *11*, 3449−3459.

(423) Gao, D.; Sinev, I.; Scholten, F.; Arán-Ais, R. M.; Divins, N. J.; Kvashnina, K.; Timoshenko, J. Roldan Cuenya, B. Selective CO2 Electroreduction to Ethylene and Multicarbon Alcohols via Electrolyte-Driven Nanostructuring. *Angew. Chem., Int. Ed.* **2019**, *58*, 17047−17053.

(424) Zou, C.; Xi, C.; Wu, D.; Mao, J.; Liu, M.; Liu, H.; Dong, C.; Du, X. W. Porous copper microspheres for selective production of multicarbon fuels via CO2 electroreduction. *Small* **2019**, *15*, 1902582.

(425) Rosen, J.; Hutchings, G. S.; Lu, Q.; Forest, R. V.; Moore, A.; Jiao, F. Electrodeposited Zn dendrites with enhanced CO selectivity for electrocatalytic CO2 reduction. *ACS Catal.* **2015**, *5*, 4586−4591.

(426) Hori, Y.; Kikuchi, K.; Suzuki, S. Production of CO and CH4 in electrochemical reduction of CO2 at metal electrodes in aqueous hydrogencarbonate solution. *Chem. Lett.* **1985**, *14*, 1695−1698.

(427) Sheng, W.; Kattel, S.; Yao, S.; Yan, B.; Liang, Z.; Hawxhurst, C. J.; Wu, Q.; Chen, J. G. Electrochemical reduction of CO2 to synthesis gas with controlled CO/H2 ratios. *Energy Environ. Sci.* **2017**, *10*, 1180−1185.

(428) Lu, Q.; Jiao, F. Electrochemical CO2 reduction: Electrocatalyst, reaction mechanism, and process engineering. *Nano Energy* **2016**, *29*, 439−456.

(429) Bugaev, A. L.; Guda, A. A.; Lomachenko, K. A.; Srabionyan, V. V.; Bugaev, L. A.; Soldatov, A. V.; Lamberti, C.; Dmitriev, V. P.; van Bokhoven, J. A. Temperature-and pressure-dependent hydrogen concentration in supported PdHx nanoparticles by Pd K-edge X-ray absorption spectroscopy. *J. Phys. Chem. C* **2014**, *118*, 10416−10423.

(430) Bugaev, A.; Guda, A.; Lomachenko, K.; Lazzarini, A.; Srabionyan, V.; Vitillo, J. G.; Piovano, A.; Groppo, E.; Bugaev, L.; Soldatov, A.; et al. Hydride phase formation in carbon supported palladium hydride nanoparticles by in situ EXAFS and XRD. *J. Phys.: Conf. Ser.* **2016**, *712*, 012032.

(431) Tew, M. W.; Miller, J. T.; van Bokhoven, J. A. Particle size effect of hydride formation and surface hydrogen adsorption of nanosized palladium catalysts: L3 edge vs K edge X-ray absorption spectroscopy. *J. Phys. Chem. C* **2009**, *113*, 15140−15147.

(432) Christophe, J.; Doneux, T.; Buess-Herman, C. Electroreduction of carbon dioxide on copper-based electrodes: activity of copper single crystals and copper−gold alloys. *Electrocatalysis* **2012**, *3*, 139−146.

(433) Ma, X.; Shen, Y.; Yao, S.; Shu, M.; Si, R.; An, C. Self-supported nanoporous Au3Cu electrode with enriched gold on surface for efficient electrochemical reduction of CO2. *Chem. - Eur. J.* **2020**, *26*, 4143−4149.

(434) Kuhn, M.; Sham, T. Charge redistribution and electronic behavior in a series of Au-Cu alloys. *Phys. Rev. B: Condens. Matter Mater. Phys.* **1994**, *49*, 1647−1661.

(435) Chen, X.; Henckel, D.; Nwabara, U.; Li, Y.; Frenkel, A. I.; Fister, T. T.; Kenis, P. J.; Gewirth, A. A. Controlling speciation during CO2 reduction on Cu-alloy electrodes. *ACS Catal.* **2020**, *10*, 672.

(436) Yin, Z.; Gao, D.; Yao, S.; Zhao, B.; Cai, F.; Lin, L.; Tang, P.; Zhai, P.; Wang, G.; Ma, D.; et al. Highly selective palladium-copper bimetallic electrocatalysts for the electrochemical reduction of CO2 to CO. *Nano Energy* **2016**, *27*, 35−43.

(437) Yin, G.; Sako, H.; Gubbala, R. V.; Ueda, S.; Yamaguchi, A.; Abe, H.; Miyauchi, M. A Cu−Zn nanoparticle promoter for selective carbon dioxide reduction and its application in visible-light-active Z-scheme systems using water as an electron donor. *Chem. Commun.* **2018**, *54*, 3947−3950.

(438) Andrews, P.; Hisscott, L. X-ray photoelectron spectroscopy of some Cu-Zn alloys. *J. Phys. F: Met. Phys.* **1975**, *5*, 1568.

(439) Liu, K.; Ma, M.; Wu, L.; Valenti, M.; Cardenas-Morcoso, D.; Hofmann, J. P.; Bisquert, J.; Gimenez, S.; Smith, W. A. Electronic effects determine the selectivity of planar Au−Cu bimetallic thin films for rlectrochemical CO2 reduction. *ACS Appl. Mater. Interfaces* **2019**, *11*, 16546−16555.

(440) Kim, D.; Resasco, J.; Yu, Y.; Asiri, A. M.; Yang, P. Synergistic geometric and electronic effects for electrochemical reduction of carbon dioxide using gold−copper bimetallic nanoparticles. *Nat. Commun.* **2014**, *5*, 4948.

(441) Varela, A. S.; Ju, W.; Bagger, A.; Franco, P.; Rossmeisl, J.; Strasser, P. Electrochemical reduction of CO2 on metal-nitrogen-doped carbon catalysts. *ACS Catal.* **2019**, *9*, 7270−7284.

(442) Tripkovic, V.; Vanin, M.; Karamad, M.; Björketun, M. r. E.; Jacobsen, K. W.; Thygesen, K. S.; Rossmeisl, J. Electrochemical CO2 and CO reduction on metal-functionalized porphyrin-like graphene. *J. Phys. Chem. C* **2013**, *117*, 9187−9195.

(443) Ju, W.; Bagger, A.; Hao, G.-P.; Varela, A. S.; Sinev, I.; Bon, V.; Cuenya, B. R.; Kaskel, S.; Rossmeisl, J.; Strasser, P. Understanding activity and selectivity of metal-nitrogen-doped carbon catalysts for electrochemical reduction of CO2. *Nat. Commun.* **2017**, *8*, 1−9.

(444) Delafontaine, L.; Asset, T.; Atanassov, P. Metal-nitrogen-carbon electrocatalysts for CO2 reduction towards syngas generation. *ChemSusChem* **2020**, *13*, 1688−1698.

(445) Zhang, Z.; Xiao, J.; Chen, X. J.; Yu, S.; Yu, L.; Si, R.; Wang, Y.; Wang, S.; Meng, X.; Wang, Y.; et al. Reaction mechanisms of well-defined metal−N4 sites in electrocatalytic CO2 reduction. *Angew. Chem., Int. Ed.* **2018**, *57*, 16339−16342.

(446) Lin, S.; Diercks, C. S.; Zhang, Y.-B.; Kornienko, N.; Nichols, E. M.; Zhao, Y.; Paris, A. R.; Kim, D.; Yang, P.; Yaghi, O. M.; et al. Covalent organic frameworks comprising cobalt porphyrins for catalytic CO2 reduction in water. *Science* **2015**, *349*, 1208−1213.

(447) Weng, Z.; Wu, Y.; Wang, M.; Jiang, J.; Yang, K.; Huo, S.; Wang, X.-F.; Ma, Q.; Brudvig, G. W.; Batista, V. S.; et al. Active sites of copper-complex catalytic materials for electrochemical carbon dioxide reduction. *Nat. Commun.* **2018**, *9*, 415.

(448) Karapinar, D.; Huan, N. T.; Ranjbar Sahraie, N.; Li, J.; Wakerley, D.; Touati, N.; Zanna, S.; Taverna, D.; Galvão Tizei, L. H.; Zitolo, A.; et al. Electroreduction of CO2 on single-site copper-

nitrogen-doped carbon material: selective formation of ethanol and reversible restructuring of the metal sites. *Angew. Chem., Int. Ed.* **2019**, *58*, 15098−15103.

(449) Zu, X.; Li, X.; Liu, W.; Sun, Y.; Xu, J.; Yao, T.; Yan, W.; Gao, S.; Wang, C.; Wei, S.; et al. Efficient and robust carbon dioxide electroreduction enabled by atomically dispersed Snδ+ sites. *Adv. Mater.* **2019**, *31*, 1808135.

(450) Zheng, Y.; Han, J.; Takele, L.; Xie, F.; Zhang, Y.; Sun, J.; Han, B.; Chen, J.; Gao, Y.; Tang, Z. Poly-phenylenediamine-derived atomically dispersed Ni sites for the electroreduction of CO2 to CO. *Inorg. Chem. Front.* **2019**, *6*, 1729−1734.

(451) Yuan, C.-Z.; Liang, K.; Xia, X.-M.; Yang, Z. K.; Jiang, Y.-F.; Zhao, T.; Lin, C.; Cheang, T.-Y.; Zhong, S.-L.; Xu, A.-W. Powerful CO2 electroreduction performance with N−carbon doped with single Ni atoms. *Catal. Sci. Technol.* **2019**, *9*, 3669−3674.

(452) Pan, F.; Zhang, H.; Liu, K.; Cullen, D.; More, K.; Wang, M.; Feng, Z.; Wang, G.; Wu, G.; Li, Y. Unveiling active sites of CO2 reduction on nitrogen-coordinated and atomically dispersed iron and cobalt catalysts. *ACS Catal.* **2018**, *8*, 3116−3122.

(453) Zhang, C.; Yang, S.; Wu, J.; Liu, M.; Yazdi, S.; Ren, M.; Sha, J.; Zhong, J.; Nie, K.; Jalilov, A. S.; et al. Electrochemical CO2 reduction with atomic iron-dispersed on nitrogen-doped graphene. *Adv. Energy Mater.* **2018**, *8*, 1703487.

(454) Lin, L.; Li, H.; Yan, C.; Li, H.; Si, R.; Li, M.; Xiao, J.; Wang, G.; Bao, X. Synergistic catalysis over iron-nitrogen sites anchored with cobalt phthalocyanine for efficient CO2 electroreduction. *Adv. Mater.* **2019**, *31*, 1903470.

(455) Gu, J.; Hsu, C.-S.; Bai, L.; Chen, H. M.; Hu, X. Atomically dispersed Fe3+ sites catalyze efficient CO2 electroreduction to CO. *Science* **2019**, *364*, 1091−1094.

(456) Wang, X.; Chen, Z.; Zhao, X.; Yao, T.; Chen, W.; You, R.; Zhao, C.; Wu, G.; Wang, J.; Huang, W.; et al. Regulation of coordination number over single Co sites: triggering the efficient electroreduction of CO2. *Angew. Chem., Int. Ed.* **2018**, *57*, 1944−1948.

(457) Yang, H.; Wu, Y.; Li, G.; Lin, Q.; Hu, Q.; Zhang, Q.; Liu, J.; He, C. Scalable production of efficient single-atom copper decorated carbon membranes for CO2 electroreduction to methanol. *J. Am. Chem. Soc.* **2019**, *141*, 12717−12723.

(458) Zheng, W.; Yang, J.; Chen, H.; Hou, Y.; Wang, Q.; Gu, M.; He, F.; Xia, Y.; Xia, Z.; Li, Z.; et al. Atomically defined undercoordinated active sites for highly efficient CO2 electro-reduction. *Adv. Funct. Mater.* **2020**, *30*, 1907658.

(459) Yan, C.; Li, H.; Ye, Y.; Wu, H.; Cai, F.; Si, R.; Xiao, J.; Miao, S.; Xie, S.; Yang, F.; et al. Coordinatively unsaturated nickel−nitrogen sites towards selective and high-rate CO2 electroreduction. *Energy Environ. Sci.* **2018**, *11*, 1204−1210.

(460) Yang, F.; Song, P.; Liu, X.; Mei, B.; Xing, W.; Jiang, Z.; Gu, L.; Xu, W. Highly efficient CO2 electroreduction on ZnN4-based single-atom catalyst. *Angew. Chem., Int. Ed.* **2018**, *57*, 12303−12307.

(461) Huan, T. N.; Ranjbar, N.; Rousse, G.; Sougrati, M.; Zitolo, A.; Mougel, V.; Jaouen, F.; Fontecave, M. Electrochemical reduction of CO2 catalyzed by Fe-NC materials: A structure−selectivity study. *ACS Catal.* **2017**, *7*, 1520−1525.

(462) Zhang, M.; Wu, T.-S.; Hong, S.; Fan, Q.; Soo, Y.-L.; Masa, J.; Qiu, J.; Sun, Z. Efficient electrochemical reduction of CO2 by Ni−N catalysts with tunable performance. *ACS Sustainable Chem. Eng.* **2019**, *7*, 15030−15035.

(463) Wen, C. F.; Mao, F.; Liu, Y.; Zhang, X. Y.; Fu, H. Q.; Zheng, L.; Liu, P. F.; Yang, H. G. Nitrogen stabilized low-valent Ni motifs for efficient CO2 electrocatalysis. *ACS Catal.* **2020**, *10*, 1086−1093.

(464) Fan, Q.; Hou, P.; Choi, C.; Wu, T. S.; Hong, S.; Li, F.; Soo, Y. L.; Kang, P.; Jung, Y.; Sun, Z. Activation of Ni particles into single Ni−N atoms for efficient electrochemical reduction of CO2. *Adv. Energy Mater.* **2020**, *10*, 1903068.

(465) Chen, Y.; Zou, L.; Liu, H.; Chen, C.; Wang, Q.; Gu, M.; Yang, B.; Zou, Z.; Fang, J.; Yang, H. Fe and N co-doped porous carbon nanospheres with high density of active sites for efficient CO2 electroreduction. *J. Phys. Chem. C* **2019**, *123*, 16651−16659.

(466) Rong, X.; Wang, H. J.; Lu, X. L.; Si, R.; Lu, T. B. Controlled synthesis of a vacancy-defect single-atom catalyst for boosting CO2 electroreduction. *Angew. Chem., Int. Ed.* **2020**, *59*, 1961−1965.

(467) Mou, K.; Chen, Z.; Zhang, X.; Jiao, M.; Zhang, X.; Ge, X.; Zhang, W.; Liu, L. Highly efficient electroreduction of CO2 on nickel single-atom catalysts: atom trapping and nitrogen anchoring. *Small* **2019**, *15*, 1903668.

(468) Zhao, C.; Dai, X.; Yao, T.; Chen, W.; Wang, X.; Wang, J.; Yang, J.; Wei, S.; Wu, Y.; Li, Y. Ionic exchange of metal−organic frameworks to access single nickel sites for efficient electroreduction of CO2. *J. Am. Chem. Soc.* **2017**, *139*, 8078−8081.

(469) Ren, W.; Tan, X.; Yang, W.; Jia, C.; Xu, S.; Wang, K.; Smith, S. C.; Zhao, C. Isolated diatomic Ni-Fe metal−nitrogen sites for synergistic electroreduction of CO2. *Angew. Chem., Int. Ed.* **2019**, *58*, 6972−6976.

(470) Han, J.; An, P.; Liu, S.; Zhang, X.; Wang, D.; Yuan, Y.; Guo, J.; Qiu, X.; Hou, K.; Shi, L.; et al. Reordering d orbital rnergies of single-site catalysts for CO2 electroreduction. *Angew. Chem., Int. Ed.* **2019**, *58*, 12711−12716.

(471) Sun, X.; Chen, C.; Liu, S.; Hong, S.; Zhu, Q.; Qian, Q.; Han, B.; Zhang, J.; Zheng, L. Aqueous CO2 reduction with high efficiency using α-Co (OH)2-supported atomic Ir electrocatalysts. *Angew. Chem., Int. Ed.* **2019**, *58*, 4669−4673.

(472) Stacy, J.; Regmi, Y. N.; Leonard, B.; Fan, M. The recent progress and future of oxygen reduction reaction catalysis: A review. *Renewable Sustainable Energy Rev.* **2017**, *69*, 401−414.

(473) Nørskov, J. K.; Rossmeisl, J.; Logadottir, A.; Lindqvist, L.; Kitchin, J. R.; Bligaard, T.; Jonsson, H. Origin of the overpotential for oxygen reduction at a fuel-cell cathode. *J. Phys. Chem. B* **2004**, *108*, 17886−17892.

(474) Mukerjee, S.; Srinivasan, S.; Soriaga, M. P.; McBreen, J. Effect of preparation conditions of Pt alloys on their electronic, structural, and electrocatalytic activities for oxygen reduction-XRD, XAS, and electrochemical studies. *J. Phys. Chem.* **1995**, *99*, 4577−4589.

(475) Mukerjee, S.; McBreen, J. Effect of particle size on the electrocatalysis by carbon-supported Pt electrocatalysts: an in situ XAS investigation. *J. Electroanal. Chem.* **1998**, *448*, 163−171.

(476) Santos, L.; Freitas, K.; Ticianelli, E. Heat treatment effect of Pt−V/C and Pt/C on the kinetics of the oxygen reduction reaction in acid media. *Electrochim. Acta* **2009**, *54*, 5246−5251.

(477) Kim, J. H.; Cheon, J. Y.; Shin, T. J.; Park, J. Y.; Joo, S. H. Effect of surface oxygen functionalization of carbon support on the activity and durability of Pt/C catalysts for the oxygen reduction reaction. *Carbon* **2016**, *101*, 449−457.

(478) Zhang, X.; Cahill, D. G. Measurements of interface stress of silicon dioxide in contact with water− phenol mixtures by bending of microcantilevers. *Langmuir* **2006**, *22*, 9062−9066.

(479) Hyman, M. P.; Medlin, J. W. Effects of electronic structure modifications on the adsorption of oxygen reduction reaction intermediates on model Pt (111)-alloy surfaces. *J. Phys. Chem. C* **2007**, *111*, 17052−17060.

(480) Ishiguro, N.; Saida, T.; Uruga, T.; Nagamatsu, S.-i.; Sekizawa, O.; Nitta, K.; Yamamoto, T.; Ohkoshi, S.-i.; Iwasawa, Y.; Yokoyama, T.; et al. Operando time-resolved X-ray absorption fine structure study for surface events on a Pt3Co/C cathode catalyst in a polymer electrolyte fuel cell during voltage-operating processes. *ACS Catal.* **2012**, *2*, 1319−1330.

(481) Sekizawa, O.; Kaneko, T.; Higashi, K.; Takao, S.; Yoshida, Y.; Gunji, T.; Zhao, X.; Samjeské, G.; Sakata, T.; Uruga, T.; et al. Key structural transformations and kinetics of Pt nanoparticles in PEFC Pt/C electrocatalysts by a simultaneous operando time-resolved QXAFS−XRD technique. *Top. Catal.* **2018**, *61*, 889−901.

(482) Kim, C.; Dionigi, F.; Beermann, V.; Wang, X.; Möller, T.; Strasser, P. Alloy nanocatalysts for the electrochemical oxygen reduction (ORR) and the direct electrochemical carbon dioxide reduction reaction (CO2RR). *Adv. Mater.* **2019**, *31*, 1805617.

(483) Wu, J.; Zhang, J.; Peng, Z.; Yang, S.; Wagner, F. T.; Yang, H. Truncated octahedral Pt3Ni oxygen reduction reaction electro-catalysts. *J. Am. Chem. Soc.* **2010**, *132*, 4984−4985.

(484) Mukerjee, S.; Srinivasan, S.; Soriaga, M. P.; McBreen, J. Role of structural and electronic properties of Pt and Pt alloys on electrocatalysis of oxygen reduction An in situ XANES and EXAFS investigation. *J. Electrochem. Soc.* **1995**, *142*, 1409−1422.

(485) Murthi, V. S.; Urian, R. C.; Mukerjee, S. Oxygen reduction kinetics in low and medium temperature acid environment: correlation of water activation and surface properties in supported Pt and Pt alloy electrocatalysts. *J. Phys. Chem. B* **2004**, *108*, 11011−11023.

(486) Kim, J.; Yang, S.; Lee, H. Platinum−titanium intermetallic nanoparticle catalysts for oxygen reduction reaction with enhanced activity and durability. *Electrochem. Commun.* **2016**, *66*, 66−70.

(487) Garcia, A. C.; Ticianelli, E. A. Investigation of the oxygen reduction reaction on Pt−WC/C electrocatalysts in alkaline media. *Electrochim. Acta* **2013**, *106*, 453−459.

(488) Sasaki, K.; Zhang, L.; Adzic, R. Niobium oxide-supported platinum ultra-low amount electrocatalysts for oxygen reduction. *Phys. Chem. Chem. Phys.* **2008**, *10*, 159−167.

(489) Chung, D. Y.; Jun, S. W.; Yoon, G.; Kwon, S. G.; Shin, D. Y.; Seo, P.; Yoo, J. M.; Shin, H.; Chung, Y.-H.; Kim, H.; et al. Highly durable and active PtFe nanocatalyst for electrochemical oxygen reduction reaction. *J. Am. Chem. Soc.* **2015**, *137*, 15478−15485.

(490) Li, M.; Zhao, Z.; Cheng, T.; Fortunelli, A.; Chen, C.-Y.; Yu, R.; Zhang, Q.; Gu, L.; Merinov, B. V.; Lin, Z.; et al. Ultrafine jagged platinum nanowires enable ultrahigh mass activity for the oxygen reduction reaction. *Science* **2016**, *354*, 1414−1419.

(491) Henning, S.; Kühn, L.; Herranz, J.; Nachtegaal, M.; Hübner, R.; Werheid, M.; Eychmüller, A.; Schmidt, T. J. Effect of acid washing on the oxygen reduction reaction activity of Pt-Cu aerogel catalysts. *Electrochim. Acta* **2017**, *233*, 210−217.

(492) Adzic, R. R.; Zhang, J.; Sasaki, K.; Vukmirovic, M. B.; Shao, M.; Wang, J.; Nilekar, A. U.; Mavrikakis, M.; Valerio, J.; Uribe, F. Platinum monolayer fuel cell electrocatalysts. *Top. Catal.* **2007**, *46*, 249−262.

(493) Zhang, J.; Vukmirovic, M. B.; Xu, Y.; Mavrikakis, M.; Adzic, R. R. Controlling the catalytic activity of platinum-monolayer electrocatalysts for oxygen reduction with different substrates. *Angew. Chem., Int. Ed.* **2005**, *44*, 2132−2135.

(494) Wise, A. M.; Richardson, P. W.; Price, S. W.; Chouchelamane, G.; Calvillo, L.; Hendra, P. J.; Toney, M. F.; Russell, A. E. Inhibitive effect of Pt on Pd-hydride formation of Pd@Pt core-shell electrocatalysts: An in situ EXAFS and XRD study. *Electrochim. Acta* **2018**, *262*, 27−38.

(495) Shao, M.; Sasaki, K.; Marinkovic, N. S.; Zhang, L.; Adzic, R. R. Synthesis and characterization of platinum monolayer oxygen-reduction electrocatalysts with Co−Pd core−shell nanoparticle supports. *Electrochem. Commun.* **2007**, *9*, 2848−2853.

(496) Kuttiyiel, K. A.; Sasaki, K.; Choi, Y.; Su, D.; Liu, P.; Adzic, R. R. Bimetallic IrNi core platinum monolayer shell electrocatalysts for the oxygen reduction reaction. *Energy Environ. Sci.* **2012**, *5*, 5297−5304.

(497) Okoli, C.; Kuttiyiel, K. A.; Sasaki, K.; Su, D.; Kuila, D.; Mahajan, D.; Adzic, R. R. Highly dispersed carbon supported PdNiMo core with Pt monolayer shell electrocatalysts for oxygen reduction reaction. *ECS Trans.* **2018**, *85*, 67−89.

(498) Kuttiyiel, K. A.; Sasaki, K.; Su, D.; Vukmirovic, M. B.; Marinkovic, N. S.; Adzic, R. R. Pt monolayer on Au-stabilized PdNi core−shell nanoparticles for oxygen reduction reaction. *Electrochim. Acta* **2013**, *110*, 267−272.

(499) Zhang, J.; Vukmirovic, M. B.; Sasaki, K.; Nilekar, A. U.; Mavrikakis, M.; Adzic, R. R. Mixed-metal Pt monolayer electrocatalysts for enhanced oxygen reduction kinetics. *J. Am. Chem. Soc.* **2005**, *127*, 12480−12481.

(500) Jirkovský, J. S.; Panas, I.; Romani, S.; Ahlberg, E.; Schiffrin, D. J. Potential-dependent structural memory effects in Au−Pd nano-alloys. *J. Phys. Chem. Lett.* **2012**, *3*, 315−321.

(501) Castegnaro, M. V.; Paschoalino, W. J.; Fernandes, M. R.; Balke, B.; Alves, M. C.; Ticianelli, E. A.; Morais, J. Pd−M/C (M= Pd, Cu, Pt) Electrocatalysts for Oxygen reduction reaction in alkaline medium: correlating the electronic structure with activity. *Langmuir* **2017**, *33*, 2734−2743.

(502) Price, S. W.; Rhodes, J. M.; Calvillo, L.; Russell, A. E. Revealing the details of the surface composition of electrochemically prepared Au@Pd Core@Shell nanoparticles with in situ EXAFS. *J. Phys. Chem. C* **2013**, *117*, 24858−24865.

(503) Li, H.; Luo, L.; Kunal, P.; Bonifacio, C. S.; Duan, Z.; Yang, J. C.; Humphrey, S. M.; Crooks, R. M.; Henkelman, G. Oxygen reduction reaction on classically immiscible bimetallics: a case study of RhAu. *J. Phys. Chem. C* **2018**, *122*, 2712−2716.

(504) García, S.; Zhang, L.; Piburn, G. W.; Henkelman, G.; Humphrey, S. M. Microwave synthesis of classically immiscible rhodium−silver and rhodium−gold alloy nanoparticles: Highly active hydrogenation catalysts. *ACS Nano* **2014**, *8*, 11512−11521.

(505) Luo, L.; Timoshenko, J.; Lapp, A. S.; Frenkel, A. I.; Crooks, R. M. Structural characterization of Rh and RhAu dendrimer-encapsulated nanoparticles. *Langmuir* **2017**, *33*, 12434−12442.

(506) Chen, Z.; Higgins, D.; Yu, A.; Zhang, L.; Zhang, J. A review on non-precious metal electrocatalysts for PEM fuel cells. *Energy Environ. Sci.* **2011**, *4*, 3167−3192.

(507) Abadi, M.; Agarwal, A.; Barham, P.; Brevdo, E.; Chen, Z.; Citro, C.; Corrado, G. S.; Davis, A.; Dean, J.; Devin, M. Tensorflow: Large-scale machine learning on heterogeneous distributed systems. *arXiv:1603.04467*, **2015**.

(508) Alonso-Vante, N.; Malakhov, I.; Nikitenko, S.; Savinova, E.; Kochubey, D. The structure analysis of the active centers of Ru-containing electrocatalysts for the oxygen reduction. An in situ EXAFS study. *Electrochim. Acta* **2002**, *47*, 3807−3814.

(509) Alonso-Vante, N.; Fieber-Erdmann, M.; Rossner, H.; Holub-Krappe, E.; Giorgetti, C.; Tadjeddine, A.; Dartyge, E.; Fontaine, A.; Frahm, R. The catalytic centre of transition metal chalcogenides vis-à-vis the oxygen reduction reaction: an in situ electrochemical EXAFS study. *J. Phys. IV* **1997**, *7*, C2-887−C2-889.

(510) Malakhov, I.; Nikitenko, S.; Savinova, E.; Kochubey, D.; Alonso-Vante, N. In situ EXAFS study to probe active centers of Ru chalcogenide electrocatalysts during oxygen reduction reaction. *J. Phys. Chem. B* **2002**, *106*, 1670−1676.

(511) Loponov, K. N.; Kriventsov, V. V.; Nagabhushana, K. S.; Boennemann, H.; Kochubey, D. I.; Savinova, E. R. Combined in situ EXAFS and electrochemical investigation of the oxygen reduction reaction on unmodified and Se-modified Ru/C. *Catal. Today* **2009**, *147*, 260−269.

(512) Keisar, O.; Ein-Eli, Y.; Alfi, Y.; Cohen, Y. Insights into the surface and stress behavior of manganese-oxide catalyst during oxygen reduction reaction. *J. Power Sources* **2020**, *450*, 227545.

(513) Stoerzinger, K. A.; Risch, M.; Han, B.; Shao-Horn, Y. Recent insights into manganese oxides in catalyzing oxygen reduction kinetics. *ACS Catal.* **2015**, *5*, 6021−6031.

(514) Lima, F. H.; Calegaro, M. L.; Ticianelli, E. A. Electrocatalytic activity of manganese oxides prepared by thermal decomposition for oxygen reduction. *Electrochim. Acta* **2007**, *52*, 3732−3738.

(515) Lima, F. H.; Calegaro, M. L.; Ticianelli, E. A. Investigations of the catalytic properties of manganese oxides for the oxygen reduction reaction in alkaline media. *J. Electroanal. Chem.* **2006**, *590*, 152−160.

(516) Park, H.-Y.; Shin, T. J.; Joh, H.-I.; Jang, J. H.; Ahn, D.; Yoo, S. J. Graphene-oxide-intercalated layered manganese oxides as an efficient oxygen reduction reaction catalyst in alkaline media. *Electrochem. Commun.* **2014**, *41*, 35−38.

(517) Dong, C.; Liu, Z. W.; Liu, J. Y.; Wang, W. C.; Cui, L.; Luo, R. C.; Guo, H. L.; Zheng, X. L.; Qiao, S. Z.; Du, X. W.; et al. Modest oxygen-fefective amorphous manganese-based nanoparticle mullite with duperior overall rlectrocatalytic performance for oxygen reduction reaction. *Small* **2017**, *13*, 1603903.

(518) Gorlin, Y.; Lassalle-Kaiser, B.; Benck, J. D.; Gul, S.; Webb, S. M.; Yachandra, V. K.; Yano, J.; Jaramillo, T. F. In situ X-ray absorption spectroscopy investigation of a bifunctional manganese oxide catalyst with high activity for electrochemical water oxidation and oxygen reduction. *J. Am. Chem. Soc.* **2013**, *135*, 8525−8534.

(519) Yang, Y.; Wang, Y.; Xiong, Y.; Huang, X.; Shen, L.; Huang, R.; Wang, H.; Pastore, J. P.; Yu, S.-H.; Xiao, L.; et al. In situ X-ray absorption spectroscopy of a synergistic Co−Mn oxide catalyst for the oxygen reduction reaction. *J. Am. Chem. Soc.* **2019**, *141*, 1463−1466.

(520) Doan-Nguyen, V. V.; Zhang, S.; Trigg, E. B.; Agarwal, R.; Li, J.; Su, D.; Winey, K. I.; Murray, C. B. Synthesis and X-ray characterization of cobalt phosphide (Co2P) nanorods for the oxygen reduction reaction. *ACS Nano* **2015**, *9*, 8108−8115.

(521) Yu, Y.; Ma, J.; Chen, C.; Fu, Y.; Wang, Y.; Li, K.; Liao, Y.; Zheng, L.; Zuo, X. General method for synthesis transition-metal phosphide/nitrogen and phosphide doped carbon materials with yolk-shell structure for oxygen reduction reaction. *ChemCatChem* **2019**, *11*, 1722−1731.

(522) Jasinski, R. A new fuel cell cathode catalyst. *Nature* **1964**, *201*, 1212−1213.

(523) Scherson, D.; Gupta, S.; Fierro, C.; Yeager, E.; Kordesch, M.; Eldridge, J.; Hoffman, R.; Blue, J. Cobalt tetramethoxyphenyl porphyrin—emission Mossbauer spectroscopy and O2 reduction electrochemical studies. *Electrochim. Acta* **1983**, *28*, 1205−1209.

(524) Singh, D.; Tian, J.; Mamtani, K.; King, J.; Miller, J. T.; Ozkan, U. S. A comparison of N-containing carbon nanostructures (CNx) and N-coordinated iron−carbon catalysts (FeNC) for the oxygen reduction reaction in acidic media. *J. Catal.* **2014**, *317*, 30−43.

(525) Pylypenko, S.; Mukherjee, S.; Olson, T. S.; Atanassov, P. Non-platinum oxygen reduction electrocatalysts based on pyrolyzed transition metal macrocycles. *Electrochim. Acta* **2008**, *53*, 7875−7883.

(526) Buan, M. E.; Cognigni, A.; Walmsley, J. C.; Muthuswamy, N.; Rønning, M. Active sites for the oxygen reduction reaction in nitrogen-doped carbon nanofibers. *Catal. Today* **2019**. DOI: 10.1016/j.cattod.2019.01.018

(527) Tylus, U.; Jia, Q.; Hafiz, H.; Allen, R.; Barbiellini, B.; Bansil, A.; Mukerjee, S. Engendering anion immunity in oxygen consuming cathodes based on Fe-Nx electrocatalysts: Spectroscopic and electrochemical advanced characterizations. *Appl. Catal., B* **2016**, *198*, 318−324.

(528) Zhong, R.; Zhi, C.; Wu, Y.; Liang, Z.; Tabassum, H.; Zhang, H.; Qiu, T.; Gao, S.; Shi, J.; Zou, R. Atomic Fe-N4 sites on electrospun hierarchical porous carbon nanofibers as an efficient electrocatalyst for oxygen reduction reaction. *Chin. Chem. Lett.* **2020**, *31*, 1588.

(529) Zhang, Z.; Sun, J.; Wang, F.; Dai, L. Efficient oxygen reduction reaction (ORR) catalysts based on single iron atoms dispersed on a hierarchically structured porous carbon framework. *Angew. Chem., Int. Ed.* **2018**, *57*, 9038−9043.

(530) Li, Q.; Chen, W.; Xiao, H.; Gong, Y.; Li, Z.; Zheng, L.; Zheng, X.; Yan, W.; Cheong, W. C.; Shen, R.; et al. Fe isolated single atoms on S, N codoped carbon by copolymer pyrolysis strategy for highly efficient oxygen reduction reaction. *Adv. Mater.* **2018**, *30*, 1800588.

(531) Hu, B.-C.; Wu, Z.-Y.; Chu, S.-Q.; Zhu, H.-W.; Liang, H.-W.; Zhang, J.; Yu, S.-H. SiO2-protected shell mediated templating synthesis of Fe−N-doped carbon nanofibers and their enhanced oxygen reduction reaction performance. *Energy Environ. Sci.* **2018**, *11*, 2208−2215.

(532) Yang, L.; Cheng, D.; Xu, H.; Zeng, X.; Wan, X.; Shui, J.; Xiang, Z.; Cao, D. Unveiling the high-activity origin of single-atom iron catalysts for oxygen reduction reaction. *Proc. Natl. Acad. Sci. U. S. A.* **2018**, *115*, 6626−6631.

(533) Jia, Q.; Ramaswamy, N.; Tylus, U.; Strickland, K.; Li, J.; Serov, A.; Artyushkova, K.; Atanassov, P.; Anibal, J.; Gumeci, C.; et al. Spectroscopic insights into the nature of active sites in iron−nitrogen−carbon electrocatalysts for oxygen reduction in acid. *Nano Energy* **2016**, *29*, 65−82.

(534) Wan, X.; Chen, W.; Yang, J.; Liu, M.; Liu, X.; Shui, J. Synthesis and active site identification of Fe− N−C single-atom catalysts for the oxygen reduction reaction. *ChemElectroChem* **2019**, *6*, 304−315.

(535) Kobayashi, M.; Niwa, H.; Saito, M.; Harada, Y.; Oshima, M.; Ofuchi, H.; Terakura, K.; Ikeda, T.; Koshigoe, Y.; Ozaki, J.-i.; et al. Indirect contribution of transition metal towards oxygen reduction reaction activity in iron phthalocyanine-based carbon catalysts for polymer electrolyte fuel cells. *Electrochim. Acta* **2012**, *74*, 254−259.

(536) Zhang, H.; Zhou, W.; Chen, T.; Guan, B. Y.; Li, Z.; Lou, X. W. D. A modular strategy for decorating isolated cobalt atoms into multichannel carbon matrix for electrocatalytic oxygen reduction. *Energy Environ. Sci.* **2018**, *11*, 1980−1984.

(537) Nguyen-Thanh, D.; Frenkel, A. I.; Wang, J.; O'Brien, S.; Akins, D. L. Cobalt−polypyrrole−carbon black (Co−PPY−CB) electrocatalysts for the oxygen reduction reaction (ORR) in fuel cells: Composition and kinetic activity. *Appl. Catal., B* **2011**, *105*, 50−60.

(538) Chang, S.-T.; Wang, C.-H.; Du, H.-Y.; Hsu, H.-C.; Kang, C.-M.; Chen, C.-C.; Wu, J. C.; Yen, S.-C.; Huang, W.-F.; Chen, L.-C.; et al. Vitalizing fuel cells with vitamins: pyrolyzed vitamin B12 as a non-precious catalyst for enhanced oxygen reduction reaction of polymer electrolyte fuel cells. *Energy Environ. Sci.* **2012**, *5*, 5305−5314.

(539) Mou, X.; Wang, D.; Liu, X.; Liu, W.; Cao, L.; Yao, T. XAFS study on single-atomic-site Cu1/N-graphene catalyst for oxygen reduction reaction. *Radiat. Phys. Chem.* **2020**, *175*, 108230.

(540) Li, J.; Xia, W.; Wang, T.; Zheng, L.; Lai, Y.; Pan, J.; Jiang, C.; Song, L.; Wang, M.; Zhang, H.; et al. A facile route for constructing effective Cu− Nx active sites for oxygen reduction reaction. *Chem. - Eur. J.* **2019**, *26*, 4070−4079.

(541) Li, J.; Chen, S.; Yang, N.; Deng, M.; Ibraheem, S.; Deng, J.; Li, J.; Li, L.; Wei, Z. Ultrahigh-loading zinc single-atom catalyst for highly efficient oxygen reduction in both acidic and alkaline media. *Angew. Chem., Int. Ed.* **2019**, *58*, 7035−7039.

(542) Zhang, C.; Sha, J.; Fei, H.; Liu, M.; Yazdi, S.; Zhang, J.; Zhong, Q.; Zou, X.; Zhao, N.; Yu, H.; et al. Single-atomic ruthenium catalytic sites on nitrogen-doped graphene for oxygen reduction reaction in acidic medium. *ACS Nano* **2017**, *11*, 6930−6941.

(543) Xiao, M.; Zhang, H.; Chen, Y.; Zhu, J.; Gao, L.; Jin, Z.; Ge, J.; Jiang, Z.; Chen, S.; Liu, C.; et al. Identification of binuclear Co2N5 active sites for oxygen reduction reaction with more than one magnitude higher activity than single atom CoN4 site. *Nano Energy* **2018**, *46*, 396−403.

(544) Chu, D.; Jiang, R. Novel electrocatalysts for direct methanol fuel cells. *Solid State Ionics* **2002**, *148*, 591−599.

(545) Nallathambi, V.; Lee, J.-W.; Kumaraguru, S. P.; Wu, G.; Popov, B. N. Development of high performance carbon composite catalyst for oxygen reduction reaction in PEM Proton Exchange Membrane fuel cells. *J. Power Sources* **2008**, *183*, 34−42.

(546) Zhang, D.; Chen, W.; Li, Z.; Chen, Y.; Zheng, L.; Gong, Y.; Li, Q.; Shen, R.; Han, Y.; Cheong, W.-C.; et al. Isolated Fe and Co dual active sites on nitrogen-doped carbon for a highly efficient oxygen reduction reaction. *Chem. Commun.* **2018**, *54*, 4274−4277.

(547) Wang, J.; Huang, Z.; Liu, W.; Chang, C.; Tang, H.; Li, Z.; Chen, W.; Jia, C.; Yao, T.; Wei, S.; et al. Design of N-coordinated dual-metal sites: a stable and active Pt-free catalyst for acidic oxygen reduction reaction. *J. Am. Chem. Soc.* **2017**, *139*, 17281−17284.

(548) Cheon, J. Y.; Kim, T.; Choi, Y.; Jeong, H. Y.; Kim, M. G.; Sa, Y. J.; Kim, J.; Lee, Z.; Yang, T.-H.; Kwon, K.; et al. Ordered mesoporous porphyrinic carbons with very high electrocatalytic activity for the oxygen reduction reaction. *Sci. Rep.* **2013**, *3*, 2715.

(549) Tahir, M.; Pan, L.; Idrees, F.; Zhang, X.; Wang, L.; Zou, J.-J.; Wang, Z. L. Electrocatalytic oxygen evolution reaction for energy conversion and storage: a comprehensive review. *Nano Energy* **2017**, *37*, 136−157.

(550) Gong, M.; Dai, H. A mini review of NiFe-based materials as highly active oxygen evolution reaction electrocatalysts. *Nano Res.* **2015**, *8*, 23−39.

(551) Suen, N.-T.; Hung, S.-F.; Quan, Q.; Zhang, N.; Xu, Y.-J.; Chen, H. M. Electrocatalysis for the oxygen evolution reaction: recent development and future perspectives. *Chem. Soc. Rev.* **2017**, *46*, 337−365.

(552) Burke, M. S.; Enman, L. J.; Batchellor, A. S.; Zou, S.; Boettcher, S. W. Oxygen evolution reaction electrocatalysis on transition metal oxides and (oxy) hydroxides: activity trends and design principles. *Chem. Mater.* **2015**, *27*, 7549−7558.

(553) Cai, Z.; Bu, X.; Wang, P.; Ho, J. C.; Yang, J.; Wang, X. Recent advances in layered double hydroxide electrocatalysts for the oxygen evolution reaction. *J. Mater. Chem. A* **2019**, *7*, 5069−5089.

(554) Masa, J.; Sinev, I.; Mistry, H.; Ventosa, E.; de la Mata, M.; Arbiol, J.; Muhler, M.; Roldan Cuenya, B.; Schuhmann, W. Ultrathin high surface area nickel boride (NixB) nanosheets as highly efficient electrocatalyst for oxygen evolution. *Adv. Energy Mater.* **2017**, *7*, 1700381.

(555) Yang, F.; Sliozberg, K.; Sinev, I.; Antoni, H.; Bähr, A.; Ollegott, K.; Xia, W.; Masa, J.; Grünert, W.; Roldan Cuenya, B.; et al. Synergistic effect of cobalt and iron in layered double hydroxide catalysts for the oxygen evolution reaction. *ChemSusChem* **2017**, *10*, 156−165.

(556) Danilovic, N.; Subbaraman, R.; Chang, K.-C.; Chang, S. H.; Kang, Y. J.; Snyder, J.; Paulikas, A. P.; Strmcnik, D.; Kim, Y.-T.; Myers, D.; et al. Activity−stability trends for the oxygen evolution reaction on monometallic oxides in acidic environments. *J. Phys. Chem. Lett.* **2014**, *5*, 2474−2478.

(557) Grimaud, A.; Demortière, A.; Saubanère, M.; Dachraoui, W.; Duchamp, M.; Doublet, M.-L.; Tarascon, J.-M. Activation of surface oxygen sites on an iridium-based model catalyst for the oxygen evolution reaction. *Nat. Energy* **2017**, *2*, 1−10.

(558) Seitz, L. C.; Dickens, C. F.; Nishio, K.; Hikita, Y.; Montoya, J.; Doyle, A.; Kirk, C.; Vojvodic, A.; Hwang, H. Y.; Norskov, J. K.; et al. A highly active and stable IrOx/SrIrO3 catalyst for the oxygen evolution reaction. *Science* **2016**, *353*, 1011−1014.

(559) Chang, S. H.; Connell, J. G.; Danilovic, N.; Subbaraman, R.; Chang, K.-C.; Stamenkovic, V. R.; Markovic, N. M. Activity−stability relationship in the surface electrochemistry of the oxygen evolution reaction. *Faraday Discuss.* **2014**, *176*, 125−133.

(560) Chang, S. H.; Danilovic, N.; Chang, K.-C.; Subbaraman, R.; Paulikas, A. P.; Fong, D. D.; Highland, M. J.; Baldo, P. M.; Stamenkovic, V. R.; Freeland, J. W.; et al. Functional links between stability and reactivity of strontium ruthenate single crystals during oxygen evolution. *Nat. Commun.* **2014**, *5*, 1−9.

(561) Danilovic, N.; Subbaraman, R.; Chang, K. C.; Chang, S. H.; Kang, Y.; Snyder, J.; Paulikas, A. P.; Strmcnik, D.; Kim, Y. T.; Myers, D.; et al. Using surface segregation to design stable Ru-Ir oxides for the oxygen evolution reaction in acidic environments. *Angew. Chem., Int. Ed.* **2014**, *53*, 14016−14021.

(562) Stefan, I. C.; Mo, Y.; Antonio, M. R.; Scherson, D. A. In situ Ru LII and LIII edge X-ray absorption near edge structure of electrodeposited ruthenium dioxide films. *J. Phys. Chem. B* **2002**, *106*, 12373−12375.

(563) Oh, H.-S.; Nong, H. N.; Reier, T.; Bergmann, A.; Gliech, M.; Ferreira de Araújo, J.; Willinger, E.; Schlögl, R.; Teschner, D.; Strasser, P. Electrochemical catalyst−support effects and their stabilizing role for IrOx nanoparticle catalysts during the oxygen evolution reaction. *J. Am. Chem. Soc.* **2016**, *138*, 12552−12563.

(564) Abbott, D. F.; Lebedev, D.; Waltar, K.; Povia, M.; Nachtegaal, M.; Fabbri, E.; Copéret, C.; Schmidt, T. J. Iridium oxide for the oxygen evolution reaction: correlation between particle size, morphology, and the surface hydroxo layer from operando XAS. *Chem. Mater.* **2016**, *28*, 6591−6604.

(565) Mo, Y.; Stefan, I. C.; Cai, W.-B.; Dong, J.; Carey, P.; Scherson, D. A. In situ iridium LIII-edge X-ray absorption and surface enhanced Raman spectroscopy of electrodeposited iridium oxide films in aqueous electrolytes. *J. Phys. Chem. B* **2002**, *106*, 3681−3686.

(566) Minguzzi, A.; Lugaresi, O.; Locatelli, C.; Rondinini, S.; D'Acapito, F.; Achilli, E.; Ghigna, P. Fixed energy X-ray absorption voltammetry. *Anal. Chem.* **2013**, *85*, 7009−7013.

(567) Achilli, E.; Minguzzi, A.; Lugaresi, O.; Locatelli, C.; Rondinini, S.; Spinolo, G.; Ghigna, P. In situ dispersive EXAFS in electrocatalysis: the investigation of the local structure of IrOx in chronoamperometric conditions as a case study. *J. Spectrosc.* **2014**, *2014*, 480102.

(568) Oakton, E.; Lebedev, D.; Povia, M.; Abbott, D. F.; Fabbri, E.; Fedorov, A.; Nachtegaal, M.; Copéret, C.; Schmidt, T. J. IrO2-TiO2:

A high-surface-area, active, and stable electrocatalyst for the oxygen evolution reaction. *ACS Catal.* **2017**, *7*, 2346−2352.

(569) Tackett, B. M.; Sheng, W.; Kattel, S.; Yao, S.; Yan, B.; Kuttiyiel, K. A.; Wu, Q.; Chen, J. G. Reducing iridium loading in oxygen evolution reaction electrocatalysts using core−shell particles with nitride cores. *ACS Catal.* **2018**, *8*, 2615−2621.

(570) Minguzzi, A.; Locatelli, C.; Cappelletti, G.; Scavini, M.; Vertova, A.; Ghigna, P.; Rondinini, S. IrO2-based disperse-phase electrocatalysts: A complementary study by means of the cavity-microelectrode and ex-situ X-ray absorption spectroscopy. *J. Phys. Chem. A* **2012**, *116*, 6497−6504.

(571) Pfeifer, V.; Jones, T.; Vélez, J. V.; Massué, C.; Greiner, M.; Arrigo, R.; Teschner, D.; Girgsdies, F.; Scherzer, M.; Allan, J.; et al. The electronic structure of iridium oxide electrodes active in water splitting. *Phys. Chem. Chem. Phys.* **2016**, *18*, 2292−2296.

(572) Pfeifer, V.; Jones, T. E.; Velasco Vélez, J. J.; Massué, C.; Arrigo, R.; Teschner, D.; Girgsdies, F.; Scherzer, M.; Greiner, M. T.; Allan, J.; et al. The electronic structure of iridium and its oxides. *Surf. Interface Anal.* **2016**, *48*, 261−273.

(573) Pfeifer, V.; Jones, T. E.; Vélez, J. J. V.; Arrigo, R.; Piccinin, S.; Hävecker, M.; Knop-Gericke, A.; Schlögl, R. In situ observation of reactive oxygen species forming on oxygen-evolving iridium surfaces. *Chem. Sci.* **2017**, *8*, 2143−2149.

(574) Bergmann, A.; Jones, T. E.; Moreno, E. M.; Teschner, D.; Chernev, P.; Gliech, M.; Reier, T.; Dau, H.; Strasser, P. Unified structural motifs of the catalytically active state of Co (oxyhydr) oxides during the electrochemical oxygen evolution reaction. *Nat. Catal.* **2018**, *1*, 711−719.

(575) Leng, M.; Huang, X.; Xiao, W.; Ding, J.; Liu, B.; Du, Y.; Xue, J. Enhanced oxygen evolution reaction by Co-OC bonds in rationally designed Co3O4/graphene nanocomposites. *Nano Energy* **2017**, *33*, 445−452.

(576) Wu, J.; Xue, Y.; Yan, X.; Yan, W.; Cheng, Q.; Xie, Y. Co3O4 nanocrystals on single-walled carbon nanotubes as a highly efficient oxygen-evolving catalyst. *Nano Res.* **2012**, *5*, 521−530.

(577) Dou, S.; Dong, C. L.; Hu, Z.; Huang, Y. C.; Chen, J. l.; Tao, L.; Yan, D.; Chen, D.; Shen, S.; Chou, S.; et al. Atomic-scale CoOx species in metal−organic frameworks for oxygen evolution reaction. *Adv. Funct. Mater.* **2017**, *27*, 1702546.

(578) Yan, D.; Dong, C.-L.; Huang, Y.-C.; Zou, Y.; Xie, C.; Wang, Y.; Zhang, Y.; Liu, D.; Shen, S.; Wang, S. Engineering the coordination geometry of metal−organic complex electrocatalysts for highly enhanced oxygen evolution reaction. *J. Mater. Chem. A* **2018**, *6*, 805−810.

(579) Chen, D.; Dong, C.-L.; Zou, Y.; Su, D.; Huang, Y.-C.; Tao, L.; Dou, S.; Shen, S.; Wang, S. In situ evolution of highly dispersed amorphous CoOx clusters for oxygen evolution reaction. *Nanoscale* **2017**, *9*, 11969−11975.

(580) Risch, M.; Ringleb, F.; Kohlhoff, M.; Bogdanoff, P.; Chernev, P.; Zaharieva, I.; Dau, H. Water oxidation by amorphous cobalt-based oxides: in situ tracking of redox transitions and mode of catalysis. *Energy Environ. Sci.* **2015**, *8*, 661−674.

(581) Risch, M.; Khare, V.; Zaharieva, I.; Gerencser, L.; Chernev, P.; Dau, H. Cobalt− oxo core of a water-oxidizing catalyst film. *J. Am. Chem. Soc.* **2009**, *131*, 6936−6937.

(582) Kanan, M. W.; Yano, J.; Surendranath, Y.; Dinca, M.; Yachandra, V. K.; Nocera, D. G. Structure and valency of a cobalt−phosphate water oxidation catalyst determined by in situ X-ray spectroscopy. *J. Am. Chem. Soc.* **2010**, *132*, 13692−13701.

(583) Risch, M.; Grimaud, A.; May, K. J.; Stoerzinger, K. A.; Chen, T. J.; Mansour, A. N.; Shao-Horn, Y. Structural changes of cobalt-based perovskites upon water oxidation investigated by EXAFS. *J. Phys. Chem. C* **2013**, *117*, 8628−8635.

(584) Jiang, H.; He, Q.; Li, X.; Su, X.; Zhang, Y.; Chen, S.; Zhang, S.; Zhang, G.; Jiang, J.; Luo, Y.; et al. Tracking structural self-reconstruction and identifying true active sites toward cobalt oxychloride precatalyst of oxygen evolution reaction. *Adv. Mater.* **2019**, *31*, 1805127.

(585) Seo, B.; Sa, Y. J.; Woo, J.; Kwon, K.; Park, J.; Shin, T. J.; Jeong, H. Y.; Joo, S. H. Size-dependent activity trends combined with in situ X-ray absorption spectroscopy reveal insights into cobalt oxide/carbon nanotube-catalyzed bifunctional oxygen electrocatalysis. *ACS Catal.* **2016**, *6*, 4347−4355.

(586) Tung, C.-W.; Hsu, Y.-Y.; Shen, Y.-P.; Zheng, Y.; Chan, T.-S.; Sheu, H.-S.; Cheng, Y.-C.; Chen, H. M. Reversible adapting layer produces robust single-crystal electrocatalyst for oxygen evolution. *Nat. Commun.* **2015**, *6*, 8106.

(587) Wang, H.-Y.; Hung, S.-F.; Hsu, Y.-Y.; Zhang, L.; Miao, J.; Chan, T.-S.; Xiong, Q.; Liu, B. In situ spectroscopic identification of μ-OO bridging on spinel Co3O4 water oxidation electrocatalyst. *J. Phys. Chem. Lett.* **2016**, *7*, 4847−4853.

(588) Velasco-Velez, J. J.; Pfeifer, V.; Hävecker, M.; Weatherup, R. S.; Arrigo, R.; Chuang, C. H.; Stotz, E.; Weinberg, G.; Salmeron, M.; Schlögl, R.; et al. Photoelectron spectroscopy at the graphene−liquid interface reveals the electronic structure of an electrodeposited cobalt/graphene electrocatalyst. *Angew. Chem., Int. Ed.* **2015**, *54*, 14554−14558.

(589) Bergmann, A.; Zaharieva, I.; Dau, H.; Strasser, P. Electrochemical water splitting by layered and 3D cross-linked manganese oxides: correlating structural motifs and catalytic activity. *Energy Environ. Sci.* **2013**, *6*, 2745−2755.

(590) Morgan Chan, Z.; Kitchaev, D. A.; Nelson Weker, J.; Schnedermann, C.; Lim, K.; Ceder, G.; Tumas, W.; Toney, M. F.; Nocera, D. G. Electrochemical trapping of metastable Mn3+ ions for activation of MnO2 oxygen evolution catalysts. *Proc. Natl. Acad. Sci. U. S. A.* **2018**, *115*, E5261−E5268.

(591) Mette, K.; Bergmann, A.; Tessonnier, J. P.; Hävecker, M.; Yao, L.; Ressler, T.; Schlögl, R.; Strasser, P.; Behrens, M. Nanostructured manganese oxide supported on carbon nanotubes for electrocatalytic water splitting. *ChemCatChem* **2012**, *4*, 851−862.

(592) Lian, S.; Browne, M. P.; Domínguez, C.; Stamatin, S. N.; Nolan, H.; Duesberg, G. S.; Lyons, M. E.; Fonda, E.; Colavita, P. E. Template-free synthesis of mesoporous manganese oxides with catalytic activity in the oxygen evolution reaction. *Sustainable Energy Fuels* **2017**, *1*, 780−788.

(593) Walter, C.; Menezes, P. W.; Loos, S.; Dau, H.; Driess, M. Facile formation of nanostructured manganese oxide films as high-performance catalysts for the oxygen evolution reaction. *ChemSusChem* **2018**, *11*, 2554−2561.

(594) Zaharieva, I.; Chernev, P.; Risch, M.; Klingan, K.; Kohlhoff, M.; Fischer, A.; Dau, H. Electrosynthesis, functional, and structural characterization of a water-oxidizing manganese oxide. *Energy Environ. Sci.* **2012**, *5*, 7081−7089.

(595) Frydendal, R.; Seitz, L. C.; Sokaras, D.; Weng, T.-C.; Nordlund, D.; Chorkendorff, I.; Stephens, I. E.; Jaramillo, T. F. Operando investigation of Au-MnOx thin films with improved activity for the oxygen evolution reaction. *Electrochim. Acta* **2017**, *230*, 22−28.

(596) Bandal, H.; Reddy, K. K.; Chaugule, A.; Kim, H. Iron-based heterogeneous catalysts for oxygen evolution reaction; change in perspective from activity promoter to active catalyst. *J. Power Sources* **2018**, *395*, 106−127.

(597) Zhu, K.; Zhu, X.; Yang, W. Application of in situ techniques for the characterization of NiFe-based oxygen evolution reaction (OER) electrocatalysts. *Angew. Chem., Int. Ed.* **2019**, *58*, 1252−1265.

(598) Dionigi, F.; Strasser, P. NiFe-based (oxy) hydroxide catalysts for oxygen evolution reaction in non-acidic electrolytes. *Adv. Energy Mater.* **2016**, *6*, 1600621.

(599) Bediako, D. K.; Lassalle-Kaiser, B.; Surendranath, Y.; Yano, J.; Yachandra, V. K.; Nocera, D. G. Structure−activity correlations in a nickel−borate oxygen evolution catalyst. *J. Am. Chem. Soc.* **2012**, *134*, 6801−6809.

(600) Dionigi, F.; Zeng, Z.; Sinev, I.; Merzdorf, T.; Deshpande, S.; Bernal Lopez, M.; Kunze, S.; Zegkinoglou, I.; Sarodnik, H.; Fan, D.; Bergmann, A.; Drnec, J.; Ferreira de Araujo, J.; Gliech, M.; Teschner, D.; Zhu, J.; Li, W.-X.; Greeley, J.; Roldan Cuenya, B.; Strasser, P. In-situ crystal structure and synergistic reaction mechanism for NiFe and CoFe layered double hydroxide catalysts in the oxygen evolution reaction. *Nat. Commun.* **2020**, *11*, 2522.

(601) Bates, M. K.; Jia, Q.; Doan, H.; Liang, W.; Mukerjee, S. Charge-transfer effects in Ni−Fe and Ni−Fe−Co mixed-metal oxides for the alkaline oxygen evolution reaction. *ACS Catal.* **2016**, *6*, 155−161.

(602) Görlin, M.; Ferreira de Araújo, J.; Schmies, H.; Bernsmeier, D.; Dresp, S. r.; Gliech, M.; Jusys, Z.; Chernev, P.; Kraehnert, R.; Dau, H.; et al. Tracking catalyst redox states and reaction dynamics in Ni−Fe oxyhydroxide oxygen evolution reaction electrocatalysts: The role of catalyst support and electrolyte pH. *J. Am. Chem. Soc.* **2017**, *139*, 2070−2082.

(603) Landon, J.; Demeter, E.; Inoglu, N.; Keturakis, C.; Wachs, I. E.; Vasić, R.; Frenkel, A. I.; Kitchin, J. R. Spectroscopic characterization of mixed Fe−Ni oxide electrocatalysts for the oxygen evolution reaction in alkaline electrolytes. *ACS Catal.* **2012**, *2*, 1793−1801.

(604) Balasubramanian, M.; Melendres, C.; Mini, S. X-ray absorption spectroscopy studies of the local atomic and electronic structure of iron incorporated into electrodeposited hydrous nickel oxide films. *J. Phys. Chem. B* **2000**, *104*, 4300−4306.

(605) Chen, J. Y.; Dang, L.; Liang, H.; Bi, W.; Gerken, J. B.; Jin, S.; Alp, E. E.; Stahl, S. S. Operando analysis of NiFe and Fe oxyhydroxide electrocatalysts for water oxidation: detection of Fe4+ by Mossbauer spectroscopy. *J. Am. Chem. Soc.* **2015**, *137*, 15090−15093.

(606) Wu, G.; Chen, W.; Zheng, X.; He, D.; Luo, Y.; Wang, X.; Yang, J.; Wu, Y.; Yan, W.; Zhuang, Z.; et al. Hierarchical Fe-doped NiOx nanotubes assembled from ultrathin nanosheets containing trivalent nickel for oxygen evolution reaction. *Nano Energy* **2017**, *38*, 167−174.

(607) Yu, N.; Cao, W.; Huttula, M.; Kayser, Y.; Hoenicke, P.; Beckhoff, B.; Lai, F.; Dong, R.; Sun, H.; Geng, B. Fabrication of FeNi hydroxides double-shell nanotube arrays with enhanced performance for oxygen evolution reaction. *Appl. Catal., B* **2020**, *261*, 118193.

(608) Geerts, L.; Cosentino, S.; Liao, T.-W.; Yadav, A.; Lin, P.-C.; Zharinov, V. S.; Hu, K.-J.; Longo, A.; Pereira, L. M.; Grandjean, D.; et al. Highly active oxygen evolution reaction model electrode based on supported gas-phase NiFe clusters. *Catal. Today* **2019**, *334*, 59−67.

(609) Shi, Y.; Yu, Y.; Liang, Y.; Du, Y.; Zhang, B. In situ electrochemical conversion of an ultrathin tannin nickel iron complex film as an efficient oxygen evolution reaction electrocatalyst. *Angew. Chem., Int. Ed.* **2019**, *58*, 3769−3773.

(610) Su, X.; Wang, Y.; Zhou, J.; Gu, S.; Li, J.; Zhang, S. Operando spectroscopic identification of active sites in NiFe prussian blue analogues as electrocatalysts: activation of oxygen atoms for oxygen evolution reaction. *J. Am. Chem. Soc.* **2018**, *140*, 11286−11292.

(611) Zhang, J.; Liu, J.; Xi, L.; Yu, Y.; Chen, N.; Sun, S.; Wang, W.; Lange, K. M.; Zhang, B. Single-atom Au/NiFe layered double hydroxide electrocatalyst: probing the origin of activity for oxygen evolution reaction. *J. Am. Chem. Soc.* **2018**, *140*, 3876−3879.

(612) Wang, H. Y.; Hsu, Y. Y.; Chen, R.; Chan, T. S.; Chen, H. M.; Liu, B. Ni3+-induced formation of active NiOOH on the spinel Ni−Co oxide surface for efficient oxygen evolution reaction. *Adv. Energy Mater.* **2015**, *5*, 1500091.

(613) Zhou, P.; Wang, Y.; Xie, C.; Chen, C.; Liu, H.; Chen, R.; Huo, J.; Wang, S. Acid-etched layered double hydroxides with rich defects for enhancing the oxygen evolution reaction. *Chem. Commun.* **2017**, *53*, 11778−11781.

(614) Kowalski, D.; Kiuchi, H.; Motohashi, T.; Aoki, Y.; Habazaki, H. Activation of catalytically active edge-sharing domains in Ca2FeCoO5 for oxygen evolution reaction in highly alkaline media. *ACS Appl. Mater. Interfaces* **2019**, *11*, 28823−28829.

(615) Chatti, M.; Gardiner, J. L.; Fournier, M.; Johannessen, B.; Williams, T.; Gengenbach, T. R.; Pai, N.; Nguyen, C.; MacFarlane, D. R.; Hocking, R. K.; et al. Intrinsically stable in situ generated electrocatalyst for long-term oxidation of acidic water at up to 80° C. *Nat. Catal.* **2019**, *2*, 457.

(616) Gong, L.; Chng, X. Y. E.; Du, Y.; Xi, S.; Yeo, B. S. Enhanced catalysis of the electrochemical oxygen evolution reaction by iron

(III) ions adsorbed on amorphous cobalt oxide. *ACS Catal.* **2018**, *8*, 807−814.

(617) Yang, L.; Liu, H.; Shen, H.; Huang, Y.; Wang, S.; Zheng, L.; Cao, D. Physically adsorbed metal ions in porous supports as electrocatalysts for oxygen evolution reaction. *Adv. Funct. Mater.* **2020**, *30*, 1909889.

(618) Enman, L. J.; Stevens, M. B.; Dahan, M. H.; Nellist, M. R.; Toroker, M. C.; Boettcher, S. W. Operando X-ray absorption spectroscopy shows iron oxidation Is concurrent with oxygen evolution in cobalt−iron (oxy) hydroxide electrocatalysts. *Angew. Chem.* **2018**, *130*, 13022−13026.

(619) Ye, S. H.; Shi, Z. X.; Feng, J. X.; Tong, Y. X.; Li, G. R. Activating CoOOH porous nanosheet arrays by partial iron substitution for efficient oxygen evolution reaction. *Angew. Chem., Int. Ed.* **2018**, *57*, 2672−2676.

(620) Smith, R. D.; Pasquini, C.; Loos, S.; Chernev, P.; Klingan, K.; Kubella, P.; Mohammadi, M. R.; Gonzalez-Flores, D.; Dau, H. Spectroscopic identification of active sites for the oxygen evolution reaction on iron-cobalt oxides. *Nat. Commun.* **2017**, *8*, 1−8.

(621) Huang, Z.-F.; Song, J.; Du, Y.; Xi, S.; Dou, S.; Nsanzimana, J. M. V.; Wang, C.; Xu, Z. J.; Wang, X. Chemical and structural origin of lattice oxygen oxidation in Co−Zn oxyhydroxide oxygen evolution electrocatalysts. *Nat. Energy* **2019**, *4*, 329−338.

(622) Peng, L.; Shah, S. S. A.; Wei, Z. Recent developments in metal phosphide and sulfide electrocatalysts for oxygen evolution reaction. *Chin. J. Catal.* **2018**, *39*, 1575−1593.

(623) Hu, F.; Zhu, S.; Chen, S.; Li, Y.; Ma, L.; Wu, T.; Zhang, Y.; Wang, C.; Liu, C.; Yang, X.; et al. Amorphous metallic NiFeP: a conductive bulk material achieving high activity for oxygen evolution reaction in both alkaline and acidic media. *Adv. Mater.* **2017**, *29*, 1606570.

(624) Liu, K.; Zhang, C.; Sun, Y.; Zhang, G.; Shen, X.; Zou, F.; Zhang, H.; Wu, Z.; Wegener, E. C.; Taubert, C. J.; et al. High-performance transition metal phosphide alloy catalyst for oxygen evolution reaction. *ACS Nano* **2018**, *12*, 158−167.

(625) Zhang, H.; Zhou, W.; Dong, J.; Lu, X. F.; Lou, X. W. D. Intramolecular electronic coupling in porous iron cobalt (oxy) phosphide nanoboxes enhances the electrocatalytic activity for oxygen evolution. *Energy Environ. Sci.* **2019**, *12*, 3348−3355.

(626) Chen, P.; Xu, K.; Fang, Z.; Tong, Y.; Wu, J.; Lu, X.; Peng, X.; Ding, H.; Wu, C.; Xie, Y. Metallic Co4N porous nanowire arrays activated by surface oxidation as electrocatalysts for the oxygen evolution reaction. *Angew. Chem., Int. Ed.* **2015**, *54*, 14710−14714.

(627) Masa, J.; Weide, P.; Peeters, D.; Sinev, I.; Xia, W.; Sun, Z.; Somsen, C.; Muhler, M.; Schuhmann, W. Amorphous cobalt boride (Co2B) as a highly efficient nonprecious catalyst for electrochemical water splitting: oxygen and hydrogen evolution. *Adv. Energy Mater.* **2016**, *6*, 1502313.

(628) Jung, J.-I.; Risch, M.; Park, S.; Kim, M. G.; Nam, G.; Jeong, H.-Y.; Shao-Horn, Y.; Cho, J. Optimizing nanoparticle perovskite for bifunctional oxygen electrocatalysis. *Energy Environ. Sci.* **2016**, *9*, 176−183.

(629) Park, J.; Risch, M.; Nam, G.; Park, M.; Shin, T. J.; Park, S.; Kim, M. G.; Shao-Horn, Y.; Cho, J. Single crystalline pyrochlore nanoparticles with metallic conduction as efficient bi-functional oxygen electrocatalysts for Zn−air batteries. *Energy Environ. Sci.* **2017**, *10*, 129−136.

(630) Du, W.; Yang, G.; Wong, E.; Deskins, N. A.; Frenkel, A. I.; Su, D.; Teng, X. Platinum-tin oxide core−shell catalysts for efficient electro-oxidation of ethanol. *J. Am. Chem. Soc.* **2014**, *136*, 10862−10865.

(631) Du, W.; Wang, Q.; LaScala, C. A.; Zhang, L.; Su, D.; Frenkel, A. I.; Mathur, V. K.; Teng, X. Ternary PtSnRh−SnO2 nanoclusters: synthesis and electroactivity for ethanol oxidation fuel cell reaction. *J. Mater. Chem.* **2011**, *21*, 8887−8892.

(632) Liu, Z.; Hu, J. E.; Wang, Q.; Gaskell, K.; Frenkel, A. I.; Jackson, G. S.; Eichhorn, B. PtMo alloy and MoOx@Pt Core−shell nanoparticles as highly CO-tolerant electrocatalysts. *J. Am. Chem. Soc.* **2009**, *131*, 6924−6925.

(633) Wiltshire, R. J.; King, C. R.; Rose, A.; Wells, P. P.; Hogarth, M. P.; Thompsett, D.; Russell, A. E. A PEM fuel cell for in situ XAS studies. *Electrochim. Acta* **2005**, *50*, 5208−5217.

(634) Camara, G. A.; Giz, M. J. d.; Paganin, V. A.; Ticianelli, E. A. Correlation of electrochemical and physical properties of PtRu alloy electrocatalysts for PEM fuel cells. *J. Electroanal. Chem.* **2002**, *537*, 21−29.

(635) Russell, A. E.; Maniguet, S.; Mathew, R. J.; Yao, J.; Roberts, M. A.; Thompsett, D. In situ X-ray absorption spectroscopy and X-ray diffraction of fuel cell electrocatalysts. *J. Power Sources* **2001**, *96*, 226−232.

(636) Du, W.; Wang, Q.; Saxner, D.; Deskins, N. A.; Su, D.; Krzanowski, J. E.; Frenkel, A. I.; Teng, X. Highly active iridium/iridium−tin/tin oxide heterogeneous nanoparticles as alternative electrocatalysts for the ethanol oxidation reaction. *J. Am. Chem. Soc.* **2011**, *133*, 15172−15183.

(637) Luo, L.; Zhang, L.; Duan, Z.; Lapp, A. S.; Henkelman, G.; Crooks, R. M. Efficient CO oxidation using dendrimer-encapsulated Pt nanoparticles activated with < 2% Cu surface atoms. *ACS Nano* **2016**, *10*, 8760−8769.

(638) Dinh, C.-T.; Jain, A.; de Arquer, F. P. G.; De Luna, P.; Li, J.; Wang, N.; Zheng, X.; Cai, J.; Gregory, B. Z.; Voznyy, O.; et al. Multi-site electrocatalysts for hydrogen evolution in neutral media by destabilization of water molecules. *Nat. Energy* **2019**, *4*, 107.

(639) Chen, W. F.; Sasaki, K.; Ma, C.; Frenkel, A. I.; Marinkovic, N.; Muckerman, J. T.; Zhu, Y.; Adzic, R. R. Hydrogen-evolution catalysts based on non-noble metal nickel−molybdenum nitride nanosheets. *Angew. Chem., Int. Ed.* **2012**, *51*, 6131−6135.

(640) Chen, W.-F.; Iyer, S.; Iyer, S.; Sasaki, K.; Wang, C.-H.; Zhu, Y.; Muckerman, J. T.; Fujita, E. Biomass-derived electrocatalytic composites for hydrogen evolution. *Energy Environ. Sci.* **2013**, *6*, 1818−1826.

(641) Deng, J.; Li, H.; Xiao, J.; Tu, Y.; Deng, D.; Yang, H.; Tian, H.; Li, J.; Ren, P.; Bao, X. Triggering the electrocatalytic hydrogen evolution activity of the inert two-dimensional MoS2 surface via single-atom metal doping. *Energy Environ. Sci.* **2015**, *8*, 1594−1601.

(642) Chen, G. F.; Ren, S.; Zhang, L.; Cheng, H.; Luo, Y.; Zhu, K.; Ding, L. X.; Wang, H. Advances in electrocatalytic N2 reduction— strategies to tackle the selectivity challenge. *Small Methods* **2019**, *3*, 1800337.

(643) Martín, A. J.; Shinagawa, T.; Pérez-Ramírez, J. Electrocatalytic reduction of nitrogen: From Haber-Bosch to ammonia artificial leaf. *Chem.* **2019**, *5*, 263−283.

(644) Wang, X.; Wang, W.; Qiao, M.; Wu, G.; Chen, W.; Yuan, T.; Xu, Q.; Chen, M.; Zhang, Y.; Wang, X.; et al. Atomically dispersed Au1 catalyst towards efficient electrochemical synthesis of ammonia. *Science bulletin* **2018**, *63*, 1246−1253.

(645) Geng, Z.; Liu, Y.; Kong, X.; Li, P.; Li, K.; Liu, Z.; Du, J.; Shu, M.; Si, R.; Zeng, J. Achieving a record-high yield rate of 120.9 for N2 electrochemical reduction over Ru single-atom catalysts. *Adv. Mater.* **2018**, *30*, 1803498.

(646) Mukherjee, S.; Yang, X.; Shan, W.; Samarakoon, W.; Karakalos, S.; Cullen, D. A.; More, K.; Wang, M.; Feng, Z.; Wang, G.; et al. Atomically dispersed single Ni site catalysts for nitrogen reduction toward electrochemical ammonia synthesis using N2 and H2O. *Small Methods* **2020**, *4*, 1900821.

(647) Wang, M.; Liu, S.; Qian, T.; Liu, J.; Zhou, J.; Ji, H.; Xiong, J.; Zhong, J.; Yan, C. Over 56.55% Faradaic efficiency of ambient ammonia synthesis enabled by positively shifting the reaction potential. *Nat. Commun.* **2019**, *10*, 341.

(648) Liu, Y.; Xu, Q.; Fan, X.; Quan, X.; Su, Y.; Chen, S.; Yu, H.; Cai, Z. Electrochemical reduction of N2 to ammonia on Co single atom embedded N-doped porous carbon under ambient conditions. *J. Mater. Chem. A* **2019**, *7*, 26358−26363.

(649) Wang, M.; Liu, S.; Qian, T.; Liu, J.; Zhou, J.; Ji, H.; Xiong, J.; Zhong, J.; Yan, C. Over 56.55% Faradaic efficiency of ambient ammonia synthesis enabled by positively shifting the reaction potential. *Nat. Commun.* **2019**, *10*, 1−8.

(650) Andersen, S. Z.; Čolić, V.; Yang, S.; Schwalbe, J. A.; Nielander, A. C.; McEnaney, J. M.; Enemark-Rasmussen, K.; Baker, J. G.; Singh, A. R.; Rohr, B. A.; et al. A rigorous electrochemical ammonia synthesis protocol with quantitative isotope measurements. *Nature* **2019**, *570*, 504−508.

(651) Tsuneto, A.; Kudo, A.; Sakata, T. Efficient electrochemical reduction of N2 to NH3 catalyzed by lithium. *Chem. Lett.* **1993**, *22*, 851−854.

(652) Kunze, S.; Grosse, P.; Tlahuilcol, M.; Lopez, B.; Sinev, I.; Zegkinoglou, I.; Mistry, H.; Timoshenko, J.; Hu, M. Y.; Zhao, J.; Alp, E. E.; Chee, S. W.; Roldan Cuenya, B. *Angew. Chem., Int. Ed.* **2020**, DOI: 10.1002/anie.202010535.